Calibration of the ATLAS calorimeters and discovery potential for massive top quark resonances at the LHC

Calibration of the ATLAS calorimeters and discovery potential for massive top quark resonances at the LHC

Elin Bergeås Kuutmann

Stockholm
University

ISBN 978-91-7155-987-6

Printed in Sweden by Universitetsservice AB, Stockholm 2010
Distributor: Department of Physics, Stockholm University

Cover image: Event display of a dijet event in ATLAS, resulting from 900 GeV proton-proton collisions in the LHC, recorded on November 23, 2009. Event number 416712 from run 140541. Image created with the aid of the VP1 package.

Abstract

ATLAS is a multi-purpose detector which has recently started to take data at the LHC at CERN. This thesis describes the tests and calibrations of the central calorimeters of ATLAS and outlines a search for heavy top quark pair resonances.

The calorimeter tests were performed before the ATLAS detector was assembled at the LHC, in such a way that particle beams of known energy were targeted at the calorimeter modules. In one of the studies presented here, modules of the hadronic barrel calorimeter, TileCal, were exposed to beams of pions of energies between 3 and 9 GeV. It is shown that muons from pion decays in the beam can be separated from the pions, and that the simulation of the detector correctly describes the muon behaviour.

In the second calorimeter study, a scheme for local hadronic calibration is developed and applied to single pion test beam data in a wide range of energies, measured by the combination of the electromagnetic barrel calorimeter and the TileCal hadronic calorimeter. The calibration method is shown to provide a calorimeter linearity within 3%, and also to give a reasonable agreement between simulations and data.

The physics analysis of this thesis is the proposed search for heavy top quark resonances, and it is shown that a narrow uncoloured $t\bar{t}$ resonance, a Z', could be excluded (or discovered) at 95% CL for cross sections of 4.0 ± 1.6 pb (in the case of $M = 1.0$ TeV/c^2) or 2.0 ± 0.3 pb ($M = 2.0$ TeV/c^2), including systematical uncertainties in the model, assuming $\sqrt{s} = 10$ TeV and an integrated luminosity of 200 pb^{-1}. It is also shown that an important systematical uncertainty is the jet energy scale, which further underlines the importance of hadronic calibration.

Ej för de starka i världen
men de svaga

– Hjalmar Gullberg

List of Papers

The results of the calorimetry work presented in this thesis have also been published in the following papers

I *Very Low Energy Muons in ATLAS TileCal*
E. Bergeaas, S. Hellman and K. Jon-And
Refereed ATLAS public note, ATL-TILECAL-PUB-2005-001, CERN, 22 March, 2005

II *Testbeam Studies of Production Modules of the ATLAS Tile Calorimeter*
P. Adragna et al.
Nuclear Instruments and Methods **A606** (2009) 362-394, 21 July 2009.

III *Local Hadronic Calibration of Single Pion Data from the Combined ATLAS Testbeam of 2004*
E. Bergeaas, Ç. İşsever, K. Jon-And, B.T. King, K. Lohwasser and D. Milstead
Refereed ATLAS public note, ATL-CAL-PUB-2007-001, 18 December 2007.

IV *Local Hadronic Calibration*
T. Barillari, E. Bergeaas Kuutmann et al.
Refereed ATLAS public note, ATL-LARG-PUB-2009-001, 5 January 2009.

Chapter 6 of this thesis is largely based on paper I, and Chapter 7 is based on paper III.

Contents

Acknowledgements

> *THANK YOU*
> – Status label of the LHCb experiment during the hours of the first proton-proton collisions in the LHC, November 23, 2009

Research in experimental particle physics is a collaborative effort, and the work presented in this thesis is no exception. None of this would have been possible without the efforts of the entire ATLAS collaboration to design, build and install the detector.

In particular, I would like to thank my supervisors, Kerstin Jon-And, Jörgen Sjölin and Sten Hellman. Kerstin, thank you for recognising me as a potential particle physicist when I was but a 21-year-old undergraduate student, and for your constant encouragement since then. I would not even have begun writing this thesis without you. Jörgen, who has been my primary advisor for the last two years, deserves my deepest gratitude for all the work spent on the $t\bar{t}$ resonance analysis. Thank you for teaching me sound scientific thinking, for your refusal to compromise with quality even in the slightest and for forcing me to write decent code. And to Sten, thank you for your support and for making me answer all the tricky questions.

Since my very first days as a diploma student in the group, Barbro Åsman has supported and encouraged me. Thank you for all the well-needed pep talks!

Çiğdem İşsever's hard work and experience in the field made the hadronic calibration study possible. Thank you for long discussions and important counsel! Çiğdem also founded the Oxford-Stockholm TeV-top working group, which proved to be a most fruitful collaboration. Without all the long and useful discussions with Müge Karagöz, James Ferrando and Sasha Sherstnev, the $t\bar{t}$ study would have been much shorter.

I would like to thank Tomáš Davídek for raising the subject of the muon analysis and for having patience with all my beginner's questions, Andrea Dotti for running the Tile stand-alone test beam simulations, and Ilya Korolkov for demanding the extra answers that made the study so much more interesting. I would also like to thank Adrian Fabich, Vincent Giangiobbe, Per

Johansson, Lukáš Přibyl, Claudio Santoni, Sasha Solodkov and Bob Stanek for all the discussions, ideas and good advice.

To David Milstead for reading my drafts. Thank you for making me see the big picture of the research, and for keeping my abuse of the English language at a minimum.

Barry King simulated the one million and sixty thousand pions used to derive the weights and study the performance of the hadronic calibration in the test beam, a contribution for which I am very grateful.

I would like to thank Kristin Lohwasser for completing the jet analysis for the local hadronic calibration, thus making the hadronic calibration work deeper and richer, as well as sharing all those convenient scripting tricks and TEX templates.

Karl-Johan Grahn was kind enough to provide me with the code used to make the dead material corrections, which saved me several weeks of hard work.

I am grateful for all the beneficial discussions on hadronic calibration and its implications with Tancredi Carli, Peter Loch, Sven Menke and Peter Speckmayer.

To Martin Aleksa, Christophe Clément, Elizabeth Gallas, Vincent Giangiobbe, Ambreesh Gupta, Hayk Hakobyan, Ana Henriques, Nicolas Kerschen, Claudio Santoni, Peter Schacht, Sasha Solodkov and Francesco Spanó, thank you for miscellaneous input and suggestions regarding hadronic calibration, ATHENA and the test beam.

I want to thank Pierre Savard, Venkantesh Kaushik, Marcel Vos, Koji Terashi, Bertrand Chapleau and Jean-Raphael Lessard for valuable input regarding the top resonances.

Thanks also to all the nice people in the elementary particle physics group at Stockholm University, who make going to work a pleasure even when the jobs keep crashing and ROOT is a mess. In particular, I am greatly indebted to Thomas Burgess and Christin Wiedemann, who introduced me to the extremely useful world of shell scripts. Without your help the hadronic calibration presented in this thesis would have taken approximately 200 years to complete. I would also like to thank Christian Walck for all the encouragement and many useful discussions on statistics and Are Raklev, the theorist-next-door, for all the pedagogical explanations of particle physics phenomenology. I would like to thank Christian Ohm for crucial help in the creation of the front page image. Torbjörn Moa kept my computer running, for which I am very grateful. Karl Gellerstedt has been extremely nice and helpful, in particular in matters of C++ coding. For miscellaneous help of matters great and small, I thank Stefan Sjörs, Maja Tylmad, Zhaoyu Yang, Sonja Hillert and Aras Papadelis.

To my office mate since many years, the brilliant Marianne Johansen, thank you for keeping me sane. Other office mates of past and present; Anneli Södergren, Yulia Minaeva, Jakob Gyllenpalm, Christian Ohm, Björn Nord-

kvist, Matthias Danninger, Narendra Yamdagni, Gustav Wikström and Svante Windblad, thank you for the shared candy, the shared laughs and the good times.

I would like to thank the silent heroes of the department, our administrators Elisabet Oppenheimer, Marieanne Holmberg and Mona Holgerstand. You make things work.

AlbaNova would have been a much more boring place without Gemma Vall-llosera, Sara Rydbeck and Mia Werner. Thank you for dragging me out of the office once in a while!

My parents, Lena and Lars Bergeås, gave me the courage needed to set out on this journey. Thank you for teaching me to follow my own ideas, for your endless support and for always believing in me.

And, most of all, to my beloved Andrej, thank you for making me dinner when I forget to eat, for debugging my code when it doesn't compile, and for constantly and whole-heartedly supporting every aspect of my work.

About this thesis

The thesis is organised as follows.

A general introduction to concepts, theory and experiment is given in Part I. The aim is that this part should be understandable to someone who does not have very much prior knowledge about particle physics.

In Chapter 2, an overview of the theoretical background to the LHC project is given, as well as a brief discussion of the importance of hadronic calibration for the discovery of new physics. In Chapter 3, the ATLAS detector is described.

Part II is devoted to calorimetry, the measurements of energy depositions. In Chapter 4, some basic concepts of calorimetry are explained, and the different properties of the interactions of high-energy hadrons, electrons and muons with calorimeter materials are discussed, providing the motivation for hadronic calibration. Chapter 5 describes the technique to test calorimeter modules with particle beams. In Chapter 6 a study of the behaviour of very low-energetic muons in the ATLAS hadronic calorimeters is presented, and in Chapter 7, a method to calibrate the ATLAS calorimeters to the hadronic scale is described.

An outline of how to search for top resonances (heavy hypothetical particles that decay into a top quark and a top anti-quark) is given in Part III. In Chapter 8 an overview of the theoretical motivation for top resonances is given, and in Chapter 9, the analysis strategy is described. The discovery potential is discussed in Chapter 10, where the expected production cross section limit is deduced.

Part IV finally summarises the key ideas and results of this thesis.

Author's contribution

I started my work in the ATLAS collaboration as a diploma student in January 2004, by studying the behaviour of very low energy muons in the hadronic calorimeter of ATLAS. When I was accepted as a graduate student in the summer of 2004, I extended and completed the muon analysis, which is presented in Chapter 6. The work presented in this chapter is largely my own, except for the simulation needed for Figure 6.5 in Chapter 6.3, which has been made by Sten Hellman.

In the summer of 2005, I began the work on hadronic calibration of the calorimeter system, where I specifically studied the reactions of pions in the central parts of the calorimeter (the "barrel" part), that were measured in the combined test beam runs of 2004. This work is described in detail in Chapter 7. I have made all the computations needed for the work in this chapter, except for the material presented in Chapter 7.8, which has been made by Kristin Lohwasser at the University of Oxford.

After the completion of the hadronic calibration, I turned my attention to the preparation of a physics analysis for LHC data, and the search for top resonances in the semi-leptonic channel seemed like the natural choice to continue working with calorimetry objects, as well as offering an interesting physics prospect. The top resonance analysis is presented in Part III of the thesis. Although I have written the text and made the plots of this part myself, it should be pointed out that the underlying analysis code has been written by Jörgen Sjölin and me in collaboration.

Part I:
Introduction

1. Physics at high energies

Måtte det verk, du i människors vimmel
skapar från morgon- till aftonglöd
stå som en lyra mot tidens himmel,
sedan du själv och din gud är död!
– Hjalmar Gullberg: "Vid Kap Sunion", Kärlek i tjugonde seklet, 1933.

Experimental particle physics addresses questions that are alluringly simple to ask, but deeply complex to answer: what is everything made of? how does it hold together? where did it all begin? Fundamental curiosity is a powerful driving force of mankind. The urge to see what is beyond the current horizon has launched expeditions to cross oceans or empty space, always exploring new aspects of knowledge, and often finding a multitude of new intriguing questions to answer the original one. The questions of elementary particle physics are often answered with the aid of energy. In the collisions of particles at high energies, the sub-structure of matter can be studied, new particles are created from the collision energy and the interactions between the particles are probed with better and better precision.

At the particle physics laboratory CERN, outside Geneva in Switzerland, the Large Hadron Collider (LHC) has been built[1, 2]. In the LHC, protons are accelerated and collided at high energies. In November 2009, the first collisions occurred in the LHC, which can accelerate hadrons to energies higher than what is achieved at comparable laboratories. At the collision points of the LHC, detectors have been built in order to observe the high-energy collisions in a controlled environment. One of these detectors is ATLAS[3], a general-purpose detector designed to fully explore the physics possibilities offered by the LHC.

The physics program of ATLAS comprises the precision measurements which test what is currently the best description of matter and forces, the Standard Model. Furthermore, open-minded searches for physics beyond the current theories will also be made. One example of a topic to be investigated is the study of the heaviest known elementary particle, the top quark[4, 5]. A possible extension to the Standard Model could for example contain a new heavy particle that decays into top quark pairs, a top pair resonance.

When working in a high-energy environment, the ability to measure energy is one of the fundamental requirements of a detector. Calorimeters are detectors used to measure the energy of particles through their total absorption in

the calorimeter material. They are very important detectors to use in high energy experiments, because as opposed to, for example, spectrometers, their performance improves with higher energy and they can be used to measure the energy of neutral particles such as neutrons. Furthermore, the signal readout of a calorimeter is fast, which makes triggering on calorimeter signals possible[6, 7].

In this thesis, studies of the calorimeter system of the ATLAS detector are described. Before ATLAS was installed at the LHC, its sub-detectors were tested, both separately and together with other sub-detectors. Some of the tests involved exposing the detector parts to high energy particle beams, so called *test beams*[8]. In Part II of this thesis, the study of the behaviour of very low-energy muons from a test beam targeted at the hadronic calorimeter is described. The second half of Part II has been devoted to the hadronic calibration of the central parts of the ATLAS detector, the so-called "barrel" part. The hadronic calibration scheme was developed and tested within the frame of the combined ATLAS barrel test beam, performed in 2004. In this thesis, an introduction to calorimetry is given, as well as a motivation to why there is need for a special scheme for hadronic calibration in addition to the electromagnetic calibration.

With a correctly calibrated detector, and the LHC providing high-energy collisions, the search for new physics can begin. In Part III, an analysis designed to search for top pair resonances is presented and tested on computer simulations of LHC collision data, resulting in an investigation of the discovery (or exclusion) potential for such resonances.

2. Theoretical and experimental overview

Everything makes sense a bit at a time. But when you try to think of it all at once, it comes out wrong.
– Terry Pratchett: "Only You Can Save Mankind", 1992.

In this chapter, an introduction to the theoretical background and an overview of the experimental set-up of the analysis presented in the thesis are given. Starting with a description of the Standard Model of elementary particle physics, the known problems of the Standard Model are outlined, and the motivation for physics experiments at multi-TeV energies is explained. The ATLAS detector at the LHC, as described later in this and the next chapter, might provide the framework for the discovery of new physics at previously unexplored energies. However, in order to carry out the ATLAS physics program, the various sub-detectors must be well-understood and properly calibrated. The research topic for Part II of this thesis is the tests and calibrations of the calorimeters of ATLAS. The importance of correctly calibrated calorimeters, especially with respect to hadronic showers, is therefore underlined.

2.1 The Standard Model of elementary particle physics

Currently, the model that most correctly describes matter and forces is the Standard Model of elementary particle physics. According to this model, all known matter is built from quarks and leptons. The most well-known lepton is the electron. Quarks are the building blocks of for example protons and neutrons. The quarks have been given the names **u**p, **d**own, **c**harm, **s**trange, **t**op and **b**ottom, and the charged leptons are called **e**lectron, muon (μ) and tau lepton (τ). Each charged lepton has an uncharged companion, a neutrino (ν). The neutrinos are very light compared to the charged leptons, but experiments have shown that they have different masses[9], so they cannot all be massless.

Every quark and lepton has an anti-particle, which is named by adding anti- to the particle name (e.g. anti-muon, anti-quark). The anti-electron is also called positron. In Table 2.1 the quarks and leptons are listed. The quarks

	1st generation	2nd generation	3rd generation	Electric charge[a]
Quarks (mass, GeV/c^2)[b]	up, u (≈ 0.003)	charm, c (≈ 1.2)	top, t (173.1 ± 1.3)	$+\frac{2}{3}$
	down, d (≈ 0.007)	strange, s (≈ 0.1)	bottom, b (≈ 4.5)	$-\frac{1}{3}$
Leptons (mass, GeV/c^2)[b]	e neutrino, ν_e ($< 2 \cdot 10^{-9}$)	μ neutrino, ν_μ ($< 2 \cdot 10^{-4}$)	τ neutrino, ν_τ (< 0.02)	0
	electron, e^- ($5.11 \cdot 10^{-4}$)	muon, μ^- (0.106)	tau, τ^- (1.78)	-1

[a] *The electric charge is given in fractions of the proton charge.*
[b] *1 GeV/c^2 is approximately the mass of a proton.*

Table 2.1: Quarks and leptons, the elementary fermions, according to the Standard Model of elementary particle physics. Every quark and lepton has an anti-particle, denoted by a bar above its symbol (e.g. $\overline{\nu_e}$, $\overline{u}$) or by a plus sign for the charged leptons (e.g. e^+). The masses of the quarks, except the top quark, are estimated, since no free quarks have been observed. The top mass is obtained from observation of top quark decays[10]. The neutrino masses are not known (except that they cannot all be 0), but the experimental upper limits are given[9].

and the leptons are spin[1] $1/2$ particles, and the common name for half-integer spin particles is *fermions*.

The quarks carry "colour charge" – red, green or blue[2]. The anti-quarks have "anti-colours". A colour-charged particle cannot exist in an unbound state, due to *colour confinement*, so the quarks form "white" (i.e. colourless) states, colour singlets, by combining into baryons (three quarks, one of each colour) or mesons (one quark and one anti-quark). All particles that are built from quarks are called *hadrons*. As of today, no free quarks have been observed[11]. The most recently discovered quark, the top quark, is the heaviest known elementary particle and some of its properties are outlined in Section 2.2.

In the Standard Model, the forces are also described as particles, force carriers, and we distinguish four fundamental forces of nature: gravity, electromagnetism, the strong force and the weak force. Of these four, the first two are

[1] Spin, measured in units of $\hbar$, is a quantum number, a fundamental particle property that conceptually is similar to an object's rotation around its own axis. However, as far as we know, leptons and quarks are elementary, lack substructure and have no spatial extension, so "rotation around the axis" lack meaning.

[2] The name "colour" is only a crude way of trying to describe this property of the quarks with a word known to us in everyday life. The quarks do not have real colours, that is, they do not emit photons of certain wavelengths, which is what a colour is in the macroscopic world.

Force	Particle name	Electric charge[a]	Mass (GeV/c^2)[b]	Particles sensitive to the force
Weak	W^+	$+1$	80.4	all quarks and leptons
	W^-	-1	80.4	
	Z^0	0	91.2	
Electro-magnetic	γ *photon*	0	0	electrically charged leptons and quarks
Strong	g *gluon*	0	0	quarks

[a] *The electric charge is given in fractions of the proton charge.*
[b] *1 GeV/c^2 is approximately the mass of a proton.*

Table 2.2: The experimentally verified force carriers, according to the Standard Model of particle physics, and the quarks and leptons that experience the force in question[9].

familiar to us in our everyday life, while the effects of the two latter have very limited range, which makes them less important in the understanding of phenomena in our macroscopic world. They are, however, very important on the sub-atomic level. A summary of the force carriers can be found in Table 2.2. The force carriers are spin 1 particles, and the common name for particles that carry integer spin is *bosons*.

The most obvious force in our everyday life, gravity, is not described in the Standard Model. This is not a huge problem for the description of the elementary particles, since gravity is almost totally negligible on the sub-atomic level. However, it is a problem for the Standard Model, which is evidently not the final theory of all fundamental physics. The theoretically predicted gravity force carrier, the graviton, has not been detected experimentally[9].

Another familiar force is electromagnetism. This is the force that binds electrons to atom nuclei and makes it possible for molecules and crystals to form. Many macroscopic properties of matter can be described in terms of electromagnetic interactions. The electromagnetic force carrier is the photon, a massless particle that we experience as, for example, light or radio waves.

The weak and the strong forces have very short ranges. The strong force is the one that binds the quarks in protons and other hadrons, and the residuals of the strong force also keeps the protons and the neutrons together in the atomic nucleus. The strong force carriers are called gluons, and the "charge" of the strong force is the colour charges of the quarks. The strong force is very strong within a hadron, but its effects are small outside the hadron and negligible outside the nucleus. Only the quarks, not the leptons, experience the strong force.

The force carriers of the weak force, the W^+, W^- and Z^0 particles, are very massive, making the weak interactions short-ranged. The most well-known example of weak interactions is the radioactive process known as β-decay, in which a neutron decays to a proton, an electron and an anti-electron neutrino, or a proton decays to a neutron, a positron and an electron neutrino. The neutrinos, being electrically uncharged and colourless, interacts weakly only, thus becoming hard to detect.

In the 1960's, Glashow, Salam and Weinberg managed to describe the weak and electromagnetic interactions at high energies with one single theory, the "unified electroweak theory"[7]. The theory was experimentally verified when physicists at the Gargamelle bubble chamber experiment at CERN detected neutral current reactions (reactions involving the Z^0 boson) in 1973[12, 13]. In 1983 the Z^0 and $W^\pm$ bosons themselves were discovered in the UA1 and UA2 experiments at CERN[14, 15, 16].

2.2 The top quark

The top quark is the heaviest known elementary particle, and one of the most recently discovered. The first direct observation of the top quark was made at the CDF and D0 experiments at the Tevatron accelerator at Fermilab in the U.S. in the early 1990s[4, 5].

Top quarks can be produced either through the strong interaction (as top and anti-top pairs, $t\bar{t}$) or through the electroweak interaction (so called single top production)[17, 18]. Feynman diagrams of leading order $t\bar{t}$ production are drawn in Figure 2.1 and of single top production in Figure 2.2.

Decay of the top quark

The estimated lifetime of a top quark is $5 \cdot 10^{-23}$ s, which is too short for a hadron to form. The top quark thus decays essentially as a free quark. The decay is almost exclusively to a W boson and a b quark. The properties of the final state recorded in the detector is determined by the decay of the W. To the first order, the W boson decays with equal probability either to a charged lepton-neutrino pair (for example $W^- \to e^- \bar{\nu}_e$) or into a quark anti-quark pair (for example $W^- \to \bar{u}d$) of a particular colour. Due to the three colour charges of the quarks, a W decay into a particular quark family is three times as probable as a decay into a particular leptonic family. The decay of a real W into quarks of the third generation is heavily suppressed for kinematical reasons, since the top mass is larger than the W mass. At higher order, the exact symmetry of the W decay vanishes, but approximately 33% of the W bosons decay into leptons and 67% decays hadronically.

If the lepton is a τ, it decays either into an electron and neutrinos, a muon and neutrinos or hadronically (mainly through processes involving pions). See Table 2.3 for branching fractions.

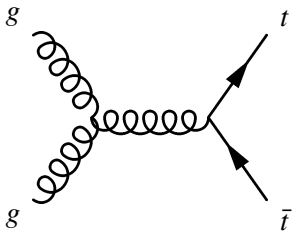

(a) s-channel (1)

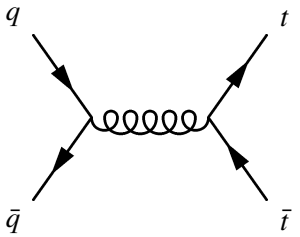

(b) s-channel (2)

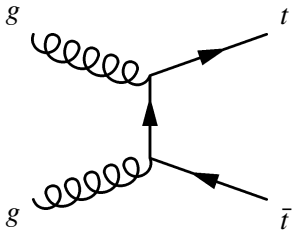

(c) t-channel (1)

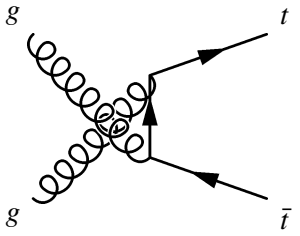

(d) t-channel (2)

Figure 2.1: Leading order $t\bar{t}$ production. Diagrams (a), (c) and (d) are gluon fusion processes, while (b) represent quark annihilation.

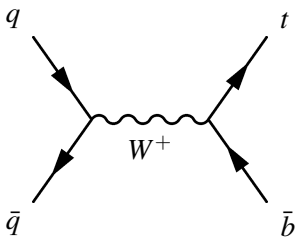

(a) s-channel

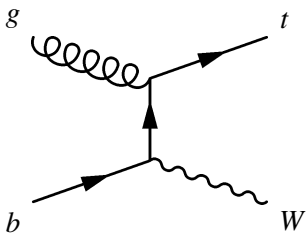

(b) Associated W production

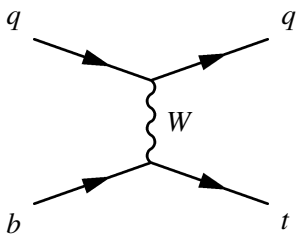

(c) t-channel

Figure 2.2: Representative examples of leading order single top production.

$\tau^- \rightarrow$	Branching fraction
$e^- + \bar{\nu}_e + \nu_\tau$	$17.85 \pm 0.05\%$
$\mu^- + \bar{\nu}_\mu + \nu_\tau$	$17.36 \pm 0.05\%$
hadrons	$64.79 \pm 0.07\%$

Table 2.3: Decays of the τ^- lepton[9]. τ^+ are charge conjugates of these processes. The hadronic decays mostly involve pions.

The final states of the W decays, as reconstructed in the detector, thus contain either an electron, a muon or hadrons. The branching ratios of these final states are listed in Table 2.4. By finally combining the different possible final states of the two W bosons of the $t\bar{t}$ decay, we arrive at the branching fractions given in Table 2.5.

$W \rightarrow$	Branching fraction
$e + \nu_e$	$12.76 \pm 0.13\%$
$\mu + \nu_\mu$	$12.52 \pm 0.15\%$
hadrons	$74.89 \pm 0.30\%$

Table 2.4: Decays of the W bosons. Only final states, after subsequent τ decays are listed.

$t\bar{t} \rightarrow$	Branching fraction	Total
$e\nu_e + e\nu_e + b\bar{b}$	$1.63 \pm 0.03\%$	$6.39 \pm 0.10\%$
$\mu\nu_\mu + \mu\nu_\mu + b\bar{b}$	$1.57 \pm 0.04\%$	
$e\nu_e + \mu\nu_\mu + b\bar{b}$	$3.20 \pm 0.05\%$	
$e\nu_e +$ jets	$19.11 \pm 0.22\%$	$37.87 \pm 0.34\%$
$\mu\nu_\mu +$ jets	$18.76 \pm 0.24\%$	
jets	$56.08 \pm 0.45\%$	$56.08 \pm 0.45\%$

Table 2.5: Branching fractions for the different final states of $t\bar{t}$ decays. τ decays into leptons or hadrons are included. $e\nu_e$ is shorthand for either of the states $e^- + \bar{\nu}_e$ and $e^+ + \nu_e$ and similarly for $\mu\nu_\mu$.

2.3 Problems of the Standard Model, and the need for the LHC

The Standard Model of particle physics has been tremendously successful in its description of the elementary particles and the forces governing them. However, the Standard Model is still not completely experimentally verified, and it cannot be the final theory of particle physics. One of the most evident reasons for this is the concept of *mass*: the mass of elementary particles, and the mass of galaxies.

In the most fundamental formulation of the Standard Model, all the particles are massless[19]. Particle masses cannot simply be added to the theory without disrupting it[3]. The only consistent way to describe the particle masses is by the spontaneous symmetry breaking of the electroweak theory, in which the Higgs field emerges. Particles gain mass through the interaction with the Higgs field, and the field itself can be manifested through the Higgs boson. Although predicted by the Standard Model, no Higgs boson has yet been observed[9].

The second aspect of mass is that observations of the rotation curves of galaxies indicate that they are much more massive than they should be, had all their mass come from ordinary observable matter such as stars and black holes. According to the observations, the excess matter in the galaxies is spread out like a halo that extends far beyond the visible rim of the galaxy. Furthermore, the mass discrepancy is not a minor correction; of the mass in the galaxies, only about one tenth consists of stars and interstellar gas[4][20]. For some time, there was a debate whether the mass observation discrepancies were due to some new, unknown particle(s) ("dark matter"), or simply a modification in the Newtonian theory of gravity at very large distances. However, in 2006 observations were made of colliding galaxy clusters, which clearly show that the mass discrepancy cannot be explained by a modification of the laws of gravity[21].

The excess mass in the galaxies could consist of massive, weakly interacting, stable particles, so called "dark matter" particles. But the Standard Model does not provide any such particles[5]. There exist several theories, none of them experimentally verified, that propose dark matter candidates. One of the theories is the supersymmetry model (SUSY), in which each Standard Model particle is assigned a supersymmetric partner. In several SUSY scenarios, the quantum number R-parity emerges, which is $+1$ for ordinary particles and -1 for supersymmetric particles. If the R-parity is conserved, the lightest supersymmetric particles must be stable. In certain supersymmetric models, the

[3] "Disrupt" meaning destroying the gauge-invariance and the renormalisability of the theory.

[4] The dark matter and the visible ordinary matter combined do only contribute to about 30% of the energy in the universe[20]. The rest is a totally unknown substance called "dark energy".

[5] The neutrinos are weakly interacting, but not very massive, and there is not enough of them to explain the entire observed mass discrepancy[22].

lightest SUSY particle is the supersymmetric partner of the neutral weak force carriers and the Higgs boson, the *neutralino*. This makes it a strong candidate for dark matter, since it would be heavy, electrically uncharged and only interact through the weak force (and gravity)[23].

As previously mentioned, the gravitational force is not described in the Standard Model, and a unification of all the forces is desirable for a final grand unified theory of all fundamental physics. An obstacle on the way is the so called hierarchy problem: why is gravity so much weaker than the weak force? Or differently formulated: why is the expected Higgs mass ($\sim 10^2$ GeV/c^2) so much smaller than the Planck mass ($\sim 10^{19}$ GeV/c^2). In order to find the Higgs at the mass we expect, based on previous observations of the other particles of the Standard Model, the theory must be extremely fine-tuned, which challenges its robustness and universality. The existence of supersymmetrical partners to the Standard Model particles could solve the hierarchy problem through pairwise cancellation of the higher order corrections.

Another suggested solution to the hierarchy problem is the existence of extra dimensions. If all the Standard Model fields and particles are confined to our familiar 4-dimensional spacetime, but gravity is free to propagate in an extra dimension, the gravitational force would seem "diluted" and thus weak to us. If the extra dimensions are warped, that is curled up and curved within themselves, and the standard model particles can excite into the extra dimension, the excitations would seem massive while viewed from the normal 4-dimensional spacetime[24, 25]. In the presence of a warped extra dimension, the mass hierarchy can get a purely geometrical explanation. Extra dimensions could have a most direct consequence for experimental particle physics, as the effects of the additional dimensions could potentially be observed at the LHC, maybe as the excitation of Standard Model particles. This is further elaborated in Chapter 8.1.

The observation of the colliding galaxy clusters revealed the existence of something that behaves like a particle which cannot be described by the Standard Model. Astronomical observations are important for the understanding of dark matter, but not enough. In order to understand the properties of these yet unknown particles, we must either devise a way to study them as they pass us, or we must create them here, in a controlled environment, so that we can measure their properties. This is why we need high-energy physics; by colliding high energy particles within a detector, measurements of the collision products, which may contain new, heavy particles, can be made.

At the particle physics laboratory CERN, in Switzerland, the Large Hadron Collider, LHC, is currently being started. An aerial view of the accelerator area is given in Figure 2.3. The LHC experiments recorded the first proton-proton collisions on November 23, 2009[27], when two proton beams, each of energy 450 GeV were brought in collision, giving a centre-of-mass energy of 900 GeV. As of the time of writing, November 2009, the LHC schedule is to provide colliding beams of 1.2 TeV each before Christmas 2009,

Figure 2.3: Aerial view of the LHC accelerator at CERN. The accelerator tunnel is marked in the photography. The tunnel is 100 m below ground level, and not visible from the ground. (Photography from [26]).

and from there gradually increase the energy, first to 3.5 TeV per beam, and then onwards to higher energies. The LHC was originally designed for a 14 TeV centre-of-mass energy (7 TeV per beam). The design luminosity is 10^{34} cm^{-2} s^{-1}, with collisions occuring every 25 ns [1]. The LHC is designed be the largest accelerator in the world, providing physicists with the opportunity to study physics at the TeV scale.

In order to measure the high-energy collision products, several detectors are being built at the LHC. One of them, ATLAS (A Toroidal LHC ApparatuS) is a general-purpose detector, designed to fully take advantage of the discovery potential of new physics at the high energies of the LHC[28]. The design of the ATLAS detector is described in Chapter 3. The work presented in Part II of this thesis has been performed on the calorimeters of the ATLAS detectors. A large part of the work is devoted to the hadronic calibration of the calorimeters, that is, the means to retrieve the correct energy of hadronic objects. In the next section, the importance of correctly calibrated calorimeters when searching for new physics is explained. The work presented in Part III, a suggested search for heavy particles decaying into top quarks, has been done using simulations of 10 TeV centre-of-mass energy collisions in ATLAS.

2.4 Hadronic calibration, heavy quarks and the discovery potential of new physics

As described in the previous section, the Standard Model is neither completely experimentally verified, nor the final theory of particle physics. High energy physics experiments, such as ATLAS, might provide us with information on new physics at higher energies.

The search for the Higgs boson is one of the most important motivations of the construction of the LHC. Previous experiments have excluded a Standard Model Higgs boson with a mass less than 114.4 GeV/c^2[29]. Theoretical and experimental constraints[30, 31] suggest that the Higgs boson should be light. If its mass is less than about 200 GeV/c^2, one of the Higgs decays that might be possible to detect is $H \to \gamma\gamma$. The electromagnetic calorimeter of ATLAS is designed to be able to detect this decay[32].

If the mass of the Higgs boson is high, one of the detectable processes might be its decay into two W bosons, which in turn could decay into two leptons and two jets[6], $H \to WW \to \ell\nu$ jet jet, which requires a good reconstruction of the $W \to$ jet jet process[32]. In order to correctly measure the jets, the energy scale for hadrons must be well-known, and the energy resolution must be good. The means of achieving hadronic calibration are described in Chapter 7.

The heaviest known elementary particle, the top quark, was discovered at Fermilab in 1995, but many of its properties have still not been precisely measured. Examples of these are the coupling between the top and the bottom quarks. Precision measurements of the decay products of the singly produced top could potentially reveal the existence of a fourth generation of quarks[7].

The large mass of the top quark brings it to the energy scale of the electroweak symmetry breaking, where the Higgs boson emerges. The top is also expected to have a large coupling to the Higgs boson, due to its mass, and the top quark and Higgs boson masses are linked[30, 31].

At the LHC, top quarks will be produced at a much higher rate than in previous colliders. The sheer abundance of top quarks at the LHC facilitates the search for signatures within the top quark spectrum. In particular, extended searches for top resonances, i.e. heavy particles that decay (primarily) into top anti-top pairs, are made possible. Part III of this thesis outlines how such a search could be made.

For the dark matter candidate searches, some important features can be outlined: there are theoretical indications, as previously stated, that the dark matter particles should be heavy, stable and weakly interacting. The latter statement implies that it will *not* react with the detector, thus remaining undetected. However, since momentum and energy are conserved in physical reactions, the "invisible" particles can be indirectly detected by looking for missing transverse energy, $E_{\mathrm{T}}^{\mathrm{miss}}$. This also requires a very good knowledge of the calorimeter signals.

The ATLAS detector recorded the first proton-proton collisions from the LHC on November 23, 2009, which marks the transition from the commissioning and calibration phase of the detector installation, to the data taking era.

[6] A *jet* is a collimated spray of hadrons, which is the result of the hadronisation of a high energy quark or gluon from the proton-proton collisions. See Chapters 4.1.3 and 7.8.

[7] This can be done by precision measurements of the element V_{tb} of the CKM matrix[9]. If this 3-by-3 matrix, which relates the basis of the weak eigenstates of the quarks with the mass eigenstates, is not unitary, the existence of a fourth generation of quarks is indicated[17, 18].

But the collisions would have no meaning to ATLAS without the many years of work performed by the almost 3000 ATLAS physicists to install and calibrate the detector. As we have just seen, a good understanding of the calorimeters is necessary for several important expected physics discoveries. The work presented in Part II of this thesis is a small part of the great effort that has been spent on testing and calibrating the calorimeter system of ATLAS. In Part III, one possible scenario for the discovery of new physics at the LHC is outlined.

3. The ATLAS detector at the LHC

> *The detectors in the end are the key informants of this study; physicist and nature meet in the detector, where knowledge and passion are one.*
> – Sharon Traweek: "Beamtimes and Lifetimes: The World of High Energy Physicists", 1988.

As described in the previous chapter, there are good reasons to believe that new fundamental physics might be discovered in the high-energy proton-proton collisions at the LHC. The general-purpose detector ATLAS is designed to take full advantage of the discovery potential for the new physics [28]. ATLAS has a cylindrical shape, centered around the LHC beam pipe, with an outer radius of approximately 11 metres, a length of 46 metres and a total weight of 7000 tonnes. The main sub-systems are, in order from smaller to

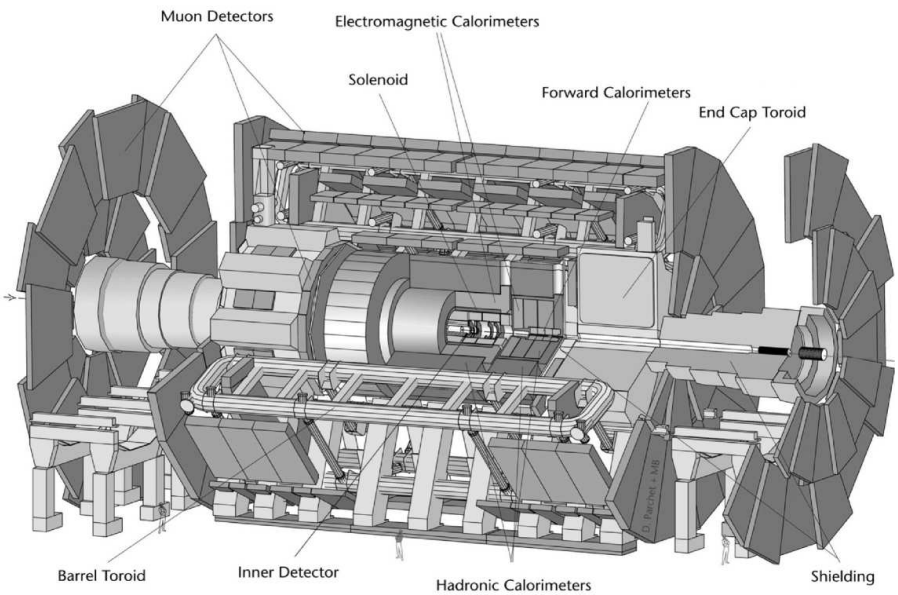

Figure 3.1: Overall layout of the ATLAS detector (Figure from [26].) The sub-detectors are, from smaller to larger radii: the inner detector, the electromagnetic calorimeter, the hadronic calorimeters and the muon system. The overall diameter is 22 metres and the total weight is approximately 7000 tonnes.

larger radii, the inner detector, the electromagnetic calorimeters, the hadronic calorimeters and the muon system[33], as indicated in Figure 3.1.

In this chapter, a brief overview of the ATLAS detector is given. Since the analysis work presented in Part II has been done on calorimeter data only, the detector description is emphasised on the calorimeter system. Much more detailed descriptions of all sub-detectors can be found in the ATLAS detector paper[3] and in the ATLAS performance book[34].

In the coordinate system of ATLAS, the z-axis is defined to lie along the beam pipe, the x-axis points towards the center of the LHC ring and the y-direction is upwards. These directions form a right-handed coordinate system. In polar coordinates, the angle θ is the polar angle to the beam pipe, and ϕ is the angle in the x-y-plane. The polar angle can be used to compute the pseudorapidity η, where

$$\eta = -\ln\left(\tan\left(\frac{\theta}{2}\right)\right). \tag{3.1}$$

For high-energy particles, the pseudorapidity is a good approximation of the rapidity y_r,

$$y_r = \frac{1}{2}\ln\left(\frac{E+p_L}{E-p_L}\right) \tag{3.2}$$

where E is the energy of the particle and p_L the momentum component along the beam. The pseudorapidity is a convenient approximation, because it can be measured even if the exact mass and momentum of the particle is unknown[35], and particle production constant per unit rapidity. η, ϕ, r are the most important coordinates of the detector. $|\eta| = 0$ is perpendicular to the beam and $|\eta| \to \infty$ is along the beam-pipe.

3.1 Inner detector

Closest to the collision point, the inner detector is placed. It has a cylindrical shape of radius 1.15 m and length 5.5 m, and it is immersed in a solenoidal magnetic field of 2 T. The innermost part of the inner detector is the high-granularity semiconductor pixel detector, that measures the vertex of the particles created in the collisions. Outside the pixel detector, the semiconductor tracker (SCT) is placed, were impact parameters and vertex positions can be measured. The outermost part of the inner detector is the transition radiation tracker (TRT), that uses straw detectors to measure particle tracks and identify electrons. An overview of the inner detector is given in Figure 3.2.

The most central parts of the beam pipe, which houses the protons during the collisions, is installed together with the inner detector. It is made out of 0.8 mm thick beryllium and has an inner diameter of 58 mm. Beryllium, with its low atomic number, is used in order to minimise interactions between the collision products and the beam pipe. Outside the inner detector, the beam pipe is made out of the cheaper and more robust material stainless steel[3].

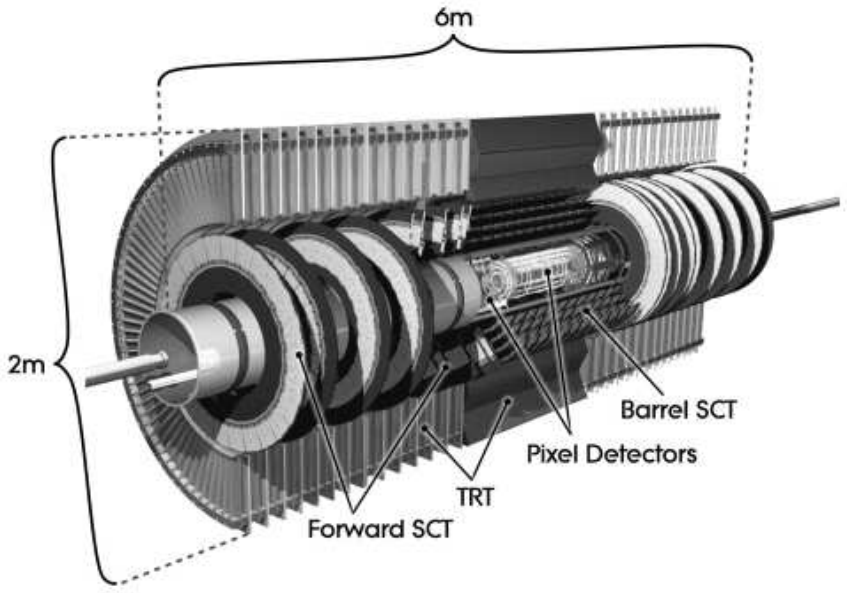

Figure 3.2: Overall layout of the inner detector of ATLAS, with the approximate length and diameter indicated. (Figure from [36].)

3.2 Calorimeter system

The calorimeter system of ATLAS consists of several non-compensating sampling calorimeters[1]. The length of the calorimeter system is 12.20 m, and its outer radius is 4.25 m. In Figure 3.3, an overview of the calorimeter system is given, with the sub-calorimeters indicated.

3.2.1 The calorimeters

In the central part of the detector, at low $|\eta|$, the innermost calorimeter is the electromagnetic liquid argon calorimeter (LAr). It is subdivided into the barrel part (called LAr barrel or EMB for "electromagnetic barrel") at $|\eta| < 1.475$ and the end-cap (EMEC) at $1.375 < |\eta| < 3.2$, where all parts uses liquid argon as active material and lead as absorber. The principal layout of a LAr barrel module is shown in Figure 3.4. The electrodes are folded in an accordion shape, as shown in the figure, which is to ensure full ϕ coverage and enable a fast extraction of the signal. The first sampling layer in the LAr barrel consists of the strips, which are very fine-grained in η, with a

[1] These concepts are explained in Chapter 4

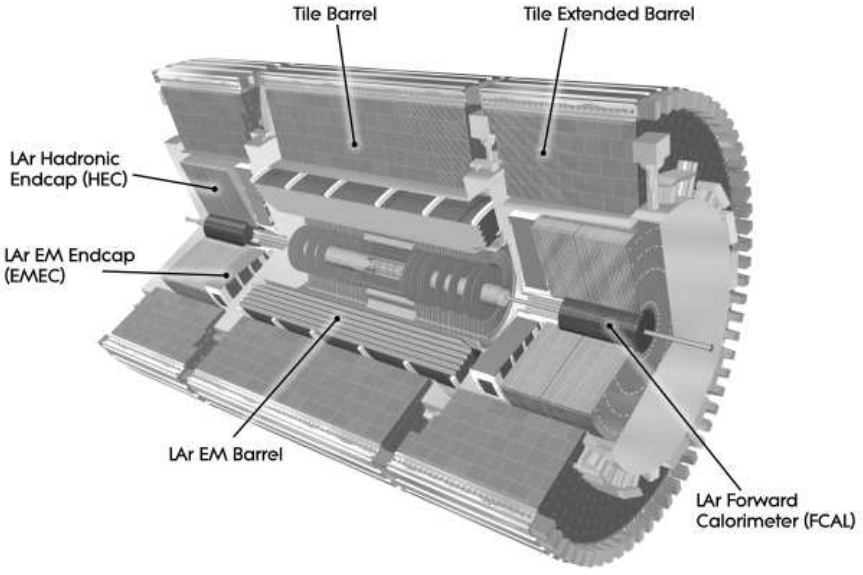

Figure 3.3: Overall layout of the calorimeter system of ATLAS (Figure from [36].) The outer radius of the calorimeter system is 4.25 m and its length is 12.20 m.

granularity of $\Delta\eta \times \Delta\phi \times \Delta r = 0.0031 \times 0.098 \times 4.3X_0$. One radiation length[2] X_0 in the alternating liquid argon and lead layers in the LAr barrel module is approximately 21 mm. The second sampling layer, the middle one, has the granularity $\Delta\eta \times \Delta\phi \times \Delta r = 0.025 \times 0.0245 \times 16X_0$, and the granularity of the third, back, sampling layer is $\Delta\eta \times \Delta\phi \times \Delta r = 0.05 \times 0.0245 \times 2X_0$.

To keep the liquid argon cold, the LAr barrel calorimeter is surrounded by a cryostat, with an inner radius of 1385 mm, and an outer radius of 2132 mm. Inside the cryostat close to the inner wall, the LAr pre-sampler is placed. Its purpose is to correct for energy losses before the calorimeters. In Chapter 7.6.4, the usage of the pre-sampler information to this purpose is described in detail.

At larger radii, between 2280 and 4230 mm, and outside the electromagnetic LAr calorimeter, the hadronic calorimeter system is placed. At $|\eta| < 1.7$, the calorimeter is made out of iron with plastic scintillator tiles as active material, which is the origin of the abbreviations Tile or TileCal for this part of the hadronic calorimeter system. The Tile barrel covers the $|\eta| < 1.0$ region, and the Tile extended barrel is placed at $0.8 < |\eta| < 1.7$. A Tile barrel module is divided into three longitudinal segments, or sampling layers, which from smaller to larger radii are the A-cells, the BC-cells and the D-cells. The

[2] A radiation length is the average distance in the material that a photon or electron travels before interacting. See also Section 4.1.2.

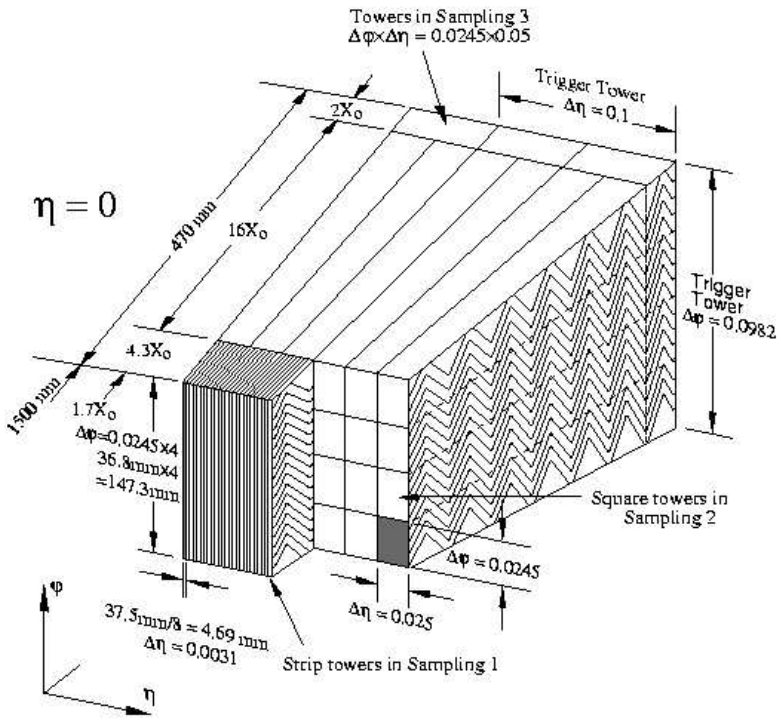

Figure 3.4: Layout of a LAr barrel module. See text for cell sizes and layer descriptions. (Figure from [37]).

$\Delta\eta \times \Delta\phi$ granularity of the A-cells and the BC-cells is 0.1×0.1, and for the D-cells the granularity is $\Delta\eta \times \Delta\phi = 0.2 \times 0.1$.

At high η and some distance from the interaction point, the hadronic end-cap (HEC) and the forward calorimeter (FCAL) are placed. Both calorimeters have liquid argon as active material, and are placed inside the same cryostat as the electromagnetic LAr end-cap calorimeter, EMEC. The relative placement of the calorimeters within the cryostat is shown in Figure 3.6.

The hadronic end-cap is subdivided into two wheels with outer radii 2.03 m. Each wheel is constructed from 32 equal modules. The absorber material of HEC is copper.

The forward calorimeter will be most exposed to radiation from the collisions, and to absorb the radiation, a dense calorimeter is needed. The FCAL consists of three parts, where the first (closest to the interaction point) has copper as absorber, and the other two uses tungsten.

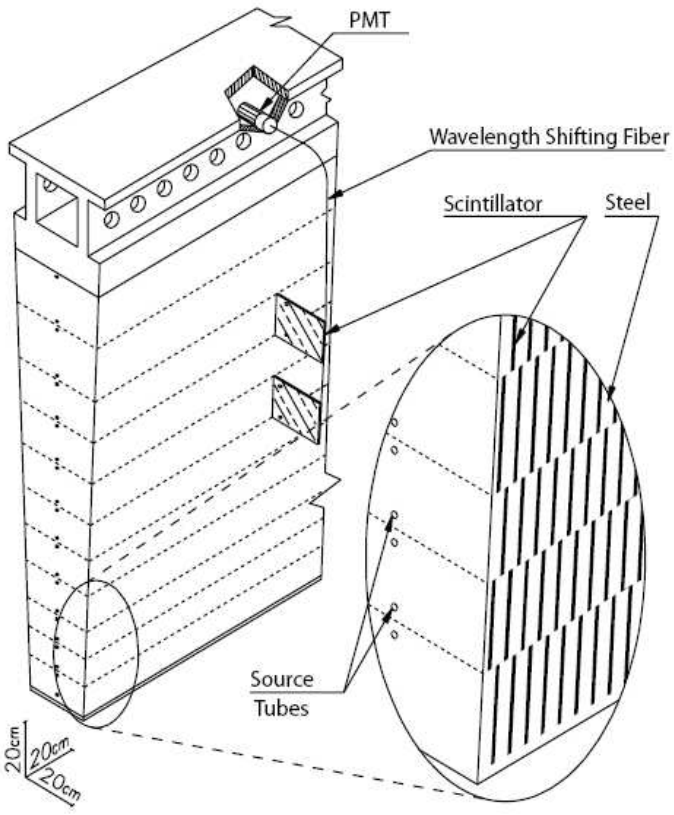

Figure 3.5: Layout of a Tile barrel module, with the placement of the plastic scintillator tiles indicated, as well as the signal read-out to the photo-multiplies tubes (PMT). The source tubes are used for calibration with ^{137}Cs, as described in Section 3.2.2. (Figure from [3]).

3.2.2 Calibration to the electromagnetic scale

The calorimeters must be calibrated on several levels before the output can be interpreted as physics signals. In this section, the calibration systems of the barrel calorimeters (LAr barrel and Tile) are given. After all the calibration steps described in this section, the calorimeters are calibrated to the *electromagnetic* scale. This does not mean that the energy response to hadrons is correct, an effect which is described in Section 4.1.3. A method for hadronic calibration of the barrel calorimeters is described in Chapter 7.

The calibration of the LAr barrel calorimeter is described in reference[38], and it consists of two steps: conversion from ADC counts (analogue to digital converter) to the injected current, and interpretation of the injected current in terms of deposited energy. The first step is obtained with the injection of a calibration pulse of known amplitude, similar to the ionisation pulses of the

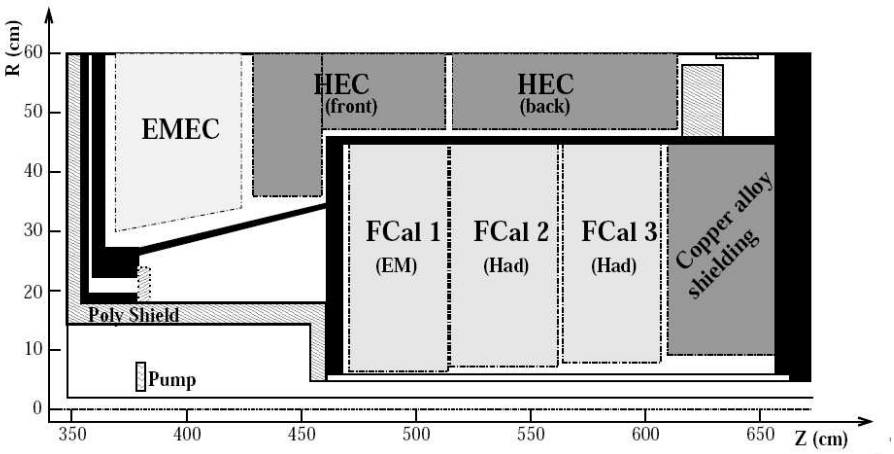

Figure 3.6: Layout of the electromagnetic end-cap (EMEC), the hadronic end-cap (HEC) and the forward calorimeter (FCAL). The figure is a cross section of the top half of the calorimeter system, along the beam line axis, and only the innermost parts of the HEC and the EMEC are shown. The particles are incident from the bottom left in the figure. (Figure from [3]).

particles, so that an ADC-to-μA factor can be determined. The conversion factor between current and energy can be determined from first principles, although a more precise value can be obtained from the comparison between simulations of electrons and test beam data.

In the Tile calorimeter, the charge injection system (CIS) also injects a known charge into the electronics through the discharges of capacitors. From this system, the factor to convert ADC counts to deposited charge, can be determined for each channel[39]. There are also additional systems for monitoring the calorimeter performance over time. With the laser system, short laser pulses are sent to the photo-multiplier tubes (PMTs), in order to monitor the PMT stability over time. With the cesium source system, a γ source (^{137}Cs) is brought through every scintillator in the calorimeter with the aid of a hydraulic system. Since the mean free path of the emitted photons is of the same order as the distance between the scintillator tiles, the response of each individual scintillator tile can be studied. The results of the cesium runs are used to ensure a uniform response from the Tile cells and monitor the calibration over time.

The final conversion factor needed to bring the energy to the electromagnetic scale, the conversion from charge to deposited energy, can be determined by exposing the Tile modules to electron beams of known energy.

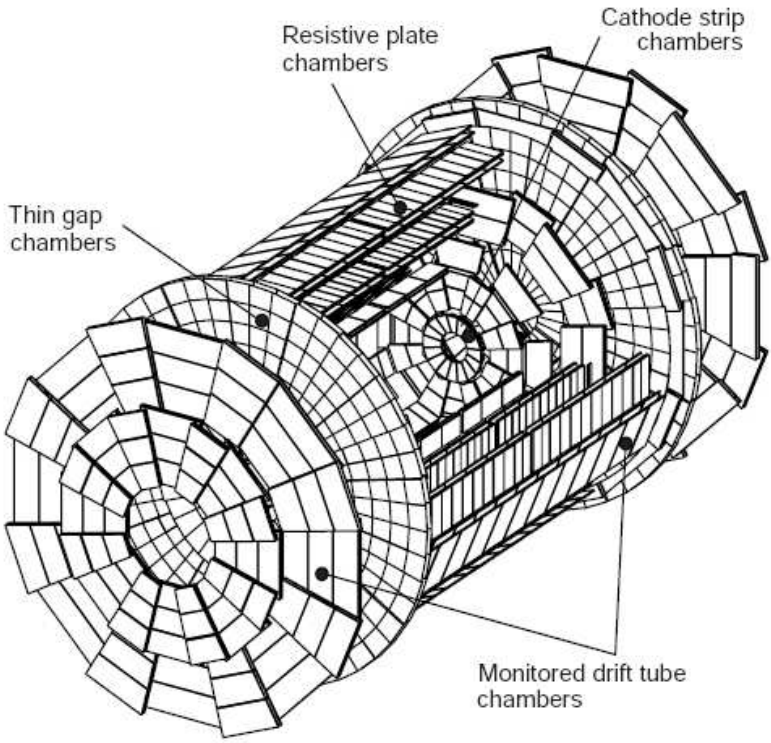

Figure 3.7: Layout of the muon chambers. The diameter of the muon system is 22 m and the length is 46 m. (Figure from [33]).

3.3 Muon system

The outer part of the ATLAS detector consists of the muon system, where the momentum of muons escaping the calorimeters are measured. An overview of the muon system layout is given in Figure 3.7. In the barrel region, at $|\eta| < 1.6$, the muon tracks are bent in a magnetic field, which is as orthogonal to the muon trajectories as possible, and the tracks are measured by chambers arranged in three cylindrical layers. For the end-cap regions, the muon chambers are installed vertically, as wheels in three layers. In the $|\eta| < 2.0$ range, Monitored Drift Tubes (MDTs) measure the track coordinates. At higher pseudorapidities, $2 < |\eta| < 2.7$, were the radiation and background levels are higher, Cathode Strip Chambers (CSCs) with higher granularity are used. For triggering purposes (see next section), resistive plate chambers (RPCs) and thin gap chambers (TGCs) are installed in the barrel and end-cap regions, respectively. The MDTs and the CSCs provide precision measurements of the η coordinate of the track, while the trigger chambers (the RPCs and TGCs) measure both the η and the ϕ coordinate. With the combination of the infor-

mation from the trigger chambers and the MDTs and CSCs, the ϕ coordinate of the track in the MDT or CSC can be reconstructed.

3.4 Read-out, data acquisition and the triggers

When LHC is operating at design luminosity, 10^{34} cm^{-2} s^{-1}, there will be 40 million collisions between proton bunches every second. Technical limitations and cost aspects demand that only about 200 events per second are permanently stored[3]. With a necessary rejection rate of $2 \cdot 10^5$, it is absolutely crucial to have a sophisticated system that quickly selects the interesting physics from all the background collisions. This task is performed by the *triggers*. The trigger system consist of the first level trigger[40], the second level trigger and the event filter. At each level, events are rejected or kept, depending on the information in the event and the decisions on the previous level.

The decisions of the first level trigger are based on reduced information from the calorimeters and the muon system, where especially events with large missing transversal energy, muons with high transversal momentum, electrons, photons and jets are kept. After the rejection in the first level trigger, the event rate is about 75 kHz.

From the first level trigger, information about the possible interesting physics is passed on to the second level trigger, where the interesting regions in the detector are analysed more carefully, when information from all sub-detectors is considered. After the second level trigger rejections, the event rate is about 3.5 kHz. In the final step, the event filtering, the events kept are reduced to the required 200 per second.

Part II:
ATLAS calorimetry

4. Basic concepts of calorimetry

calorie
*from classical Latin calor (gen. caloris) "heat," from Proto-Indo-European *kle-os-, suffixed form of base *kele- "warm" (cf. classical Latin calidus "warm," calere "be hot;" Sanskrit carad- "harvest," literally "hot time;" Lithuanian silti "become warm," silus "August;" Old Norse hlær, Old English hleow "warm").*
– Online Etymology Dictionary, 2001 (Douglas Harper)

In the previous chapters, the ATLAS detector has been described, and the potential of finding new physics at the LHC has been outlined. As mentioned, a good understanding of the calorimeters is necessary for the discovery of many interesting new physics phenomena.

In this chapter, some basic concepts of calorimetry are presented, which are necessary for the understanding of the challenges of hadronic calibration. In Chapter 3, some techniques for calibrating calorimeters to the electromagnetic scale were outlined. In this chapter, the need for additional calibration in order to correctly describe the hadronic energy is explained, and in Chapter 7 a method for hadronic calibration is described in detail.

In calorimeters, the energy of particles are measured through total absorption, when the incident particle reacts in the calorimeter material. Calorimeters are especially important as energy measuring devices in high-energy particle physics experiments, since the energy *resolution*, σ/E, (where E is the mean energy and σ the width of the energy distribution) improves with increasing energy, as opposed to the energy resolution in, for example, spectrometers[7]. Calorimeters can also measure the energy of certain neutral particles, such as neutrons. As will be shown, the minimal size of the calorimeter necessary to completely absorb the energy of a particle, scales approximately with the logarithm of the energy measured, which makes it possible to construct calorimeters of manageable size and material cost even for high-energy physics experiments.

When evaluating the performance of a calorimeter, the *response* is often discussed, which is defined as the ratio between the energy detected by the calorimeter and the true energy of the incident particle. The response as a function of the incident particle energy is called the *linearity* and a calorimeter with an energy-independent response is *linear*.

There are many ways to build a calorimeter, and the detecting material can be any of a large selection of substances, such as scintillating plastic, inorganic crystals, a liquid or a gas mixture. The detecting material is often called the *active* material. The calorimeter can be *homogeneous*, when it is made out of active material only, or a *sampling* calorimeter, when the active material is placed in layers between dense absorber material, such as lead or iron.

In this chapter an introduction to calorimetry is given and different calorimeters are described. The important physics processes when high-energy particles enter the calorimeter material are outlined. In Chapter 7, some examples of how to calibrate calorimeters to the hadronic scale are given.

4.1 Energy measurements using calorimeters

As mentioned above, the calorimeter measures particle energies through the total absorption of the particles and subsequent detection of the energy released in the detector medium. Different particles react in different ways in the calorimeter material, which has important consequences for calorimetry. In this section, the behaviour of muons in matter is discussed, as well as the difference between electrons and hadrons when reacting in the detector material. At the end of the section, a discussion on how to separate particles using the calorimeter signal is given.

4.1.1 Ionisation losses

All charged particles ionise atoms when passing through a material. For most high-energy particles, other energy-loss processes dominate over the ionisation, but for muons in most energy regions considered in high-energy experiments, this is the most important reaction. The rate of energy loss is described by the Bethe-Bloch formula [9],

$$-\frac{\mathrm{d}E}{\mathrm{d}x} = C_1 \cdot \frac{z^2}{\beta^2} \cdot \left(\frac{1}{2} \cdot \ln \left[\frac{C_2 \cdot \beta^4 \gamma^4}{1 + 2\gamma m_e/M + (m_e/M)^2} \right] - \beta^2 - \delta/2 \right) \qquad (4.1)$$

where C_1 and C_2 are constants dependent on the medium only, z is the charge of the incoming particle (in fractions of the proton charge), m_e/M is the mass ratio between an electron and the incident particle, β is the kinematic variable $\beta = v/c$ and $\gamma = (1-\beta^2)^{-\frac{1}{2}}$. δ is a density effect correction, which is important only at very high energies. The values of the formula, for muon momenta between 0.01 and 1000 GeV/c and various materials, can be found in Figure 4.1.

The Bethe-Bloch formula has its minimum around muon momentum $p_\mu = 0.3$ GeV/c and muons in this momentum region are called minimum ionising particles (MIPs). Technically, only particles in the momentum region

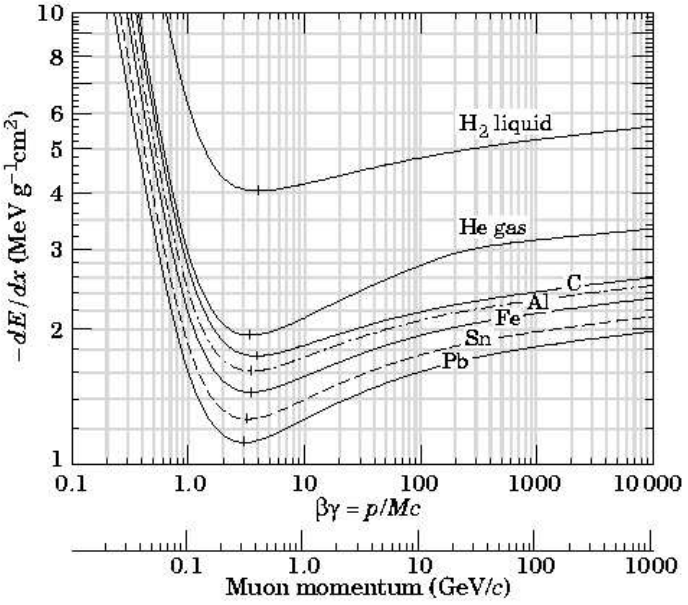

Figure 4.1: Ionisation energy loss per centimeter divided by the absorber density for various absorbers, according to the Bethe-Bloch formula. (Figure from [9]).

around the minimum of the Bethe-Bloch formula are MIPs, but the mean rate of energy loss rises only slowly with particle momentum after that, which means that even muons of energies of several hundred GeV are approximately minimum ionising particles.

The distribution from the muon energy losses have a slightly asymmetric shape, which is described by a Gauss-Landau convolution function[41]. The tail of the distribution comes from the occasional δ electrons ("knock-on electrons") that are emitted from the atoms in the material due to the passage of a muon, leading to a greater energy loss than the ionisation process alone, as shown in Figure 4.2.

The ionisation losses are small per unit length traversed, which means that muons can penetrate thick layers of material.

4.1.2 Electromagnetic showers

When the particle energy exceeds about 100 MeV, the most important mode of energy loss for electrons and positrons is radiation energy loss ("bremsstrahlung")[6]. The incoming particle interacts with the electric field of the nucleus, emitting photons. The rate of energy loss is proportional to the inverse of the particle mass squared,

$$-\frac{\mathrm{d}E}{\mathrm{d}x} \propto \frac{1}{m^2} \tag{4.2}$$

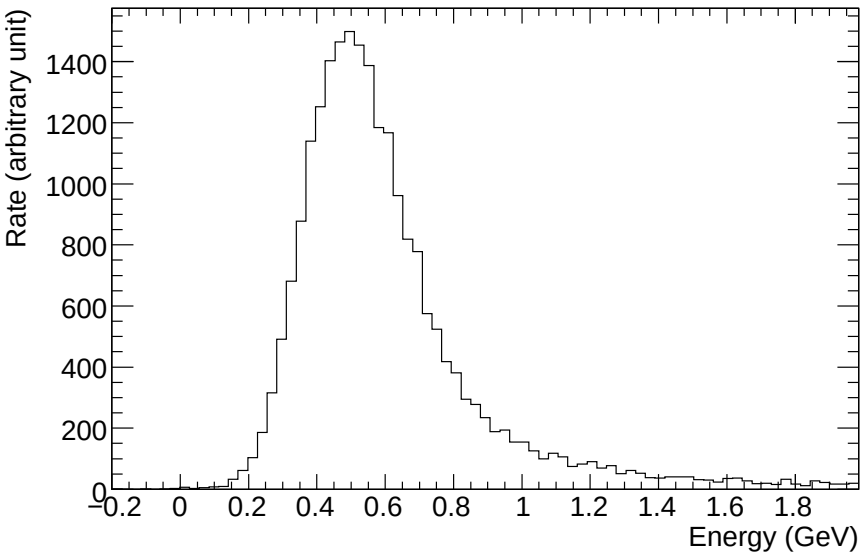

Figure 4.2: Muon energy loss in a TileCal cell. Data from the 2003 stand-alone test beam of the ATLAS hadronic calorimeter[42].

The proportionality constant is dependent on the absorbing material only. The mass dependence of the energy loss explains why bremsstrahlung is not so important for muons: since the muon mass is about 200 times that of an electron, the bremsstrahlung energy loss is suppressed by a factor of $40,000$.

In a simple model of the bremsstrahlung process, the electron travels about one radiation length in the absorbing material. Then it interacts and half its energy is emitted as a bremsstrahlung photon. The photon travels about one radiation length and is then absorbed via pair production, in which an electron and a positron are produced. The secondary particles react in the same way, as long as their energies are above the critical energy, E_C, which is defined as the energy at which the energy loss rates from ionisation and bremsstrahlung are equal for electrons[9]. After each interaction length, the number of particles in the shower is approximately doubled, and the energy of each particle is halved[1]. The interactions quickly give rise to an electromagnetic cascade, a "shower". The energy of the shower is finally deposited in the calorimeter through ionisation (if the particles are electrons or positrons) or Compton scattering and the photoelectric effect (photons). Figure 4.3 shows the principle of an electromagnetic shower development.

[1] In reality, many of the radiated photons will be very low-energetic[6], but then many of them will be emitted in the bremsstrahlung process instead, so the simple model described above still gives us a good idea of the shower development initiated by electrons.

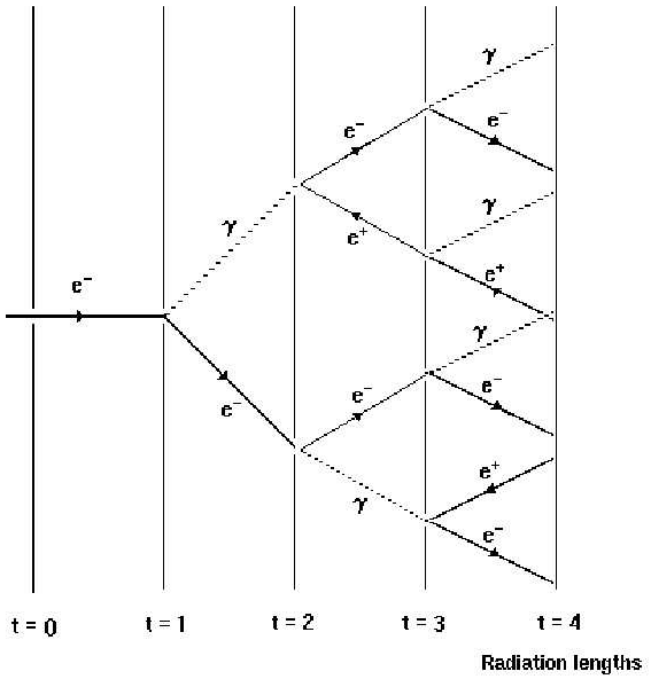

Figure 4.3: Simple model of the development of an electromagnetic shower when an electron enters an absorbing material. After t radiation lengths, the number of particles will be approximately 2^t, and the energy of each particle $E_0/2^t$ where E_0 is the energy of the initial electron.

After t interaction lengths, the number of particles in the shower in this simple model will be 2^t, and the energy of each particle $E_0/2^t$ where E_0 is the energy of the initial electron. When the particle energy is as low as E_C, ionisation losses begin to dominate and the process stops. The total number of interaction lengths in which the shower is contained is thus[7]

$$t_{\max} = \ln(E_0/E_C)/\ln 2 \tag{4.3}$$

For solid and liquid elements, the critical energy can be computed approximately from the formula $E_C = 610\,\mathrm{MeV}/(Z+1.24)$[9]. The radiation length is of the order of centimetres for metals, 1.76 cm for iron and 0.56 cm for lead[9]. Using Eqn. 4.3 and these numbers, we find that a 10 GeV electron targeted at iron will produce an electromagnetic shower of about 15 cm depth. Since the number of radiation lengths grows logarithmically with initial energy, a 1000 GeV electron produce only a 27 cm long shower in iron. This example illustrates that the necessary size of the calorimeter scales approximately with the logarithm of the energy measured, which is a prerequisite for constructing calorimeters of manageable size for physics experiments in the TeV region.

4.1.3 Hadronic showers and invisible energy

In hadronic interactions with matter, the strong force plays an important role, when the incoming hadron interacts strongly with the nuclei of the calorimeter material. This makes hadronic showers more complicated than electromagnetic ones. The strong interactions might include nuclear excitations or nuclear break-ups. Normally, the energy needed to release protons and neutrons from the atomic nuclei is not detected by the calorimeter. Consequently, for most types of calorimeters, the energy response of a hadron will be smaller than the energy response from an electron of the same nominal energy. This effect, which for obvious reasons causes problems in the calibration, can be circumvented by inserting layers of high-Z material, such as uranium (^{238}U), into the calorimeter, making it *compensating*[6]. Combined with, for example, scintillator plastic as active material, a calorimeter with uranium layers can have the same response to electrons as to hadrons. A part of the compensation is an effect of fission processes in the uranium induced by the invisible parts of the hadronic showers. However, a more important process is the reduction of the response to the electromagnetic showers in the high-Z material, which is caused by the absorption of soft photons from the electromagnetic shower in the absorber material[43, 44]. The response to the hadronic showers can instead be increased with the usage of active materials containing hydrogen (such as organic gas mixtures or plastic) since the evaporation neutrons of the hadronic shower lose energy in the active material through elastic scattering, a process much more efficient if the struck nucleus is light[44, 45]. The undetected energy of hadronic showers is called *invisible energy*, as opposed to the *visible energy* that can be detected. Some particles, mostly neutrinos, leave the detector completely undetected, and the energy loss they represent is called *escaped energy*.

The overall scale of the hadronic shower is determined by the nuclear interaction length, λ_{int}, similarly to the radiation length of the electromagnetic showers. The interaction length of protons is 16.8 cm in iron and 17.0 cm in lead. This is roughly one order of magnitude larger than the corresponding radiation lengths, which indicates that hadronic showers are more wide-spread than electromagnetic ones[9].

The calorimeters of ATLAS are non-compensating, and in the following discussion, non-compensating calorimeters are implied.

Energy dependence of the hadronic response

The fraction of the hadron energy that can be detected by a non-compensating calorimeter depends on the initial energy of the hadron, where larger initial energy means a higher response in the calorimeter. This effect can be understood by considering the development of a hadronic shower in the calorimeter. A charged hadron can ionise the calorimeter material, just like a muon would, but at some point it will interact strongly with an atomic nucleus. In this in-

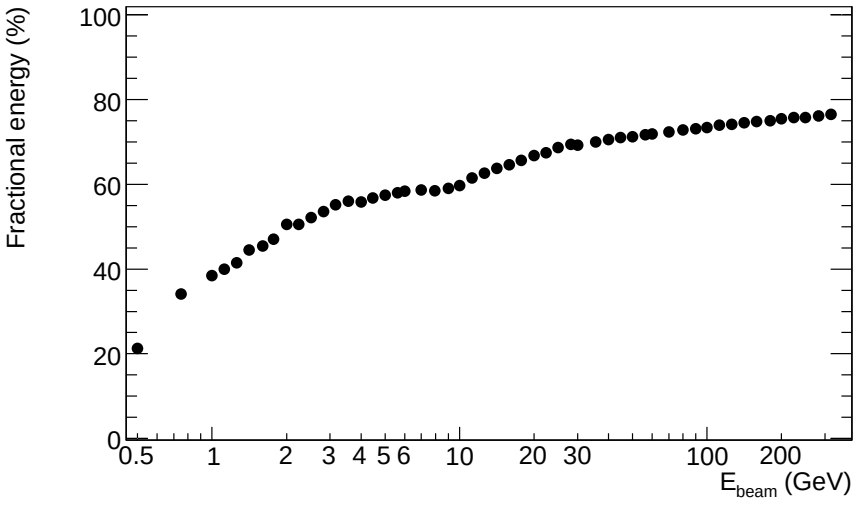

Figure 4.4: The response of the ATLAS barrel calorimeter, when exposed to pion beams of various energies. The response is the fraction of the pion energy that is detected by the calorimeter system. The values are the mean of Gaussians fitted to simulated energy distributions, divided by the beam energy.

teraction, several new hadrons might be produced, that will propagate through the calorimeter, ionising or interacting strongly with new nuclei, and for each interaction new hadrons will be formed, until the energy of the secondary hadrons is too low for new strong interactions. Many of the hadrons formed in interactions like these will be pions, and approximately one third of the pions will be neutral. Neutral pions rapidly decay into two photons, which deposit their energy electromagnetically in the calorimeter. Once a π^0 is formed, it no longer gives rise to secondary hadrons, and all its energy is deposited electromagnetically. So for each strong hadron-nucleus interaction, a certain fraction of the energy is deposited electromagnetically. If the incoming hadron has large energy, there will be more strong interactions and thus a larger fraction of the total energy will be deposited electromagnetically[6].

In Figure 4.4, the combined response of the ATLAS barrel calorimeter system (a liquid argon/lead electromagnetic calorimeter followed by a hadronic scintillator plastic/iron calorimeter), when exposed to pion beams of various energies, is shown. The values come from a simulation of the combined ATLAS test beam of 2004 (see Chapter 7). In this figure, the increased hadronic response when the initial particle energy rises is evident. For pion energies of about 1 GeV, the average response is about 40%, while the average response to 300 GeV pions is almost 80%.

Due to the production of neutral pions in the hadronic showers, the visible energy fraction fluctuates heavily from event to event, which results in a worse energy resolution for hadrons compared to electrons.

The response to different hadrons

So far, the discussion has been about hadrons in general. However, different hadrons shower in different ways. A hadronic shower induced by a proton contains fewer neutral pions than a pion-induced shower of the same nominal energy[6], due to conservation of the baryon number, which leads to a lower electromagnetic energy fraction in the proton showers, and thus a lower calorimeter response. The smaller number of neutral pions also lead to smaller event-by-event fluctuations and a better energy resolution in a proton-induced shower than in a pion one. It is possible that hadrons containing strange quarks (such as kaons) show a similar behaviour due to strangeness conservation[6].

The properties of single hadrons (such as pions, protons. . .) are important to consider and lots can be learnt from test beams in which calorimeter modules are exposed to hadron beams (see Section 5). However, in a high-energy collider experiment, single hadrons will not be the most important hadronic object. Instead, high-energy quarks and gluons produced in the collisions hadronise, and in the process give rise to a high-energetic, collimated spray of particles, known as a *jet*[35]. Generally, the number of particles in a jet will be larger than in a single hadron-induced shower. The properties of the jet will depend on the constituent particles. Like the hadron-induced showers, the visible energy content of the jet will fluctuate with the production of neutral pions. Many of the jet particles will be charged pions, so important things about the calorimeter response to jets can still be learnt from the study of pions. See also Chapter 7.

4.1.4 Particle separation in the calorimeters

Starting from the different behaviours of the particles discussed, several strategies for discriminating between the particles using the calorimeter signals can be formulated. As described in the previous sections, electromagnetic showers are shorter and denser than hadronic ones as a consequence of the different processes involved. An electron will deposit most of its energy in the first layers of a calorimeter, while a hadronic shower can penetrate deeper. For this reason, calorimeters are often divided into (at least) two parts: the electromagnetic calorimeter, closest to the impact point, and the hadronic calorimeter.

Muons, on the other hand, normally deposit a small, but approximately constant, amount of energy per unit length of material passed. Unless the muon energy is very low, it will leave the calorimeter, and additional detectors, like spectrometers, are necessary to measure the muon momentum.

In Figure 4.5, the total energy deposition measured in three Tile A-cells (75 centimetres iron with scintillator plastic) when exposed to an electron/ pion/

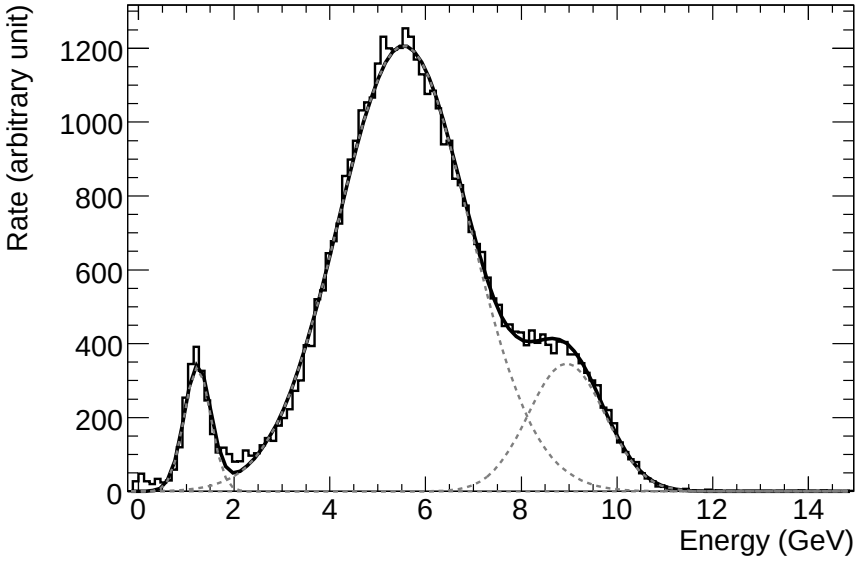

Figure 4.5: Total energy deposition from a 9 GeV pion/electron/muon beam in three Tile A-cells (75 centimetres iron/scintillator plastic). The three most abundant particles are clearly visible: muons at $\sim$ 1.3 GeV, pions at $\sim$ 5.5 GeV and electrons at $\sim$ 9 GeV. The distribution has been fitted with a sum of a Gauss-Landau convolution and two Gaussians. The plot has been made using the data from the Tile test beam of 2003, see Chapter 6.

muon beam at a nominal energy of 9 GeV is shown. The data was recorded in the Tile stand-alone test beam, as described in Section 5.1. This example clearly illustrates what we have learned about the behaviour of electrons, pions and muons in matter. The peak at lowest energy, $\sim$ 1.3 GeV, contains the muons, since they only lose a small amount of energy per unit length passed. The peak is slightly asymmetric due to the δ electrons. The largest peak, at $\sim$ 5.5 GeV, contains the pions. This peak is not at beam energy because the calorimeter has been calibrated to the electromagnetic scale, it is non-compensating and, to a smaller degree, because the pion showers are not fully contained within 75 centimetres of iron. At the beam energy, $\sim$ 9 GeV, the electron peak can be found. After 75 centimeters in iron, most of the electron energy has been deposited, and all of the energy can be reconstructed by the calorimeter.

4.1.5 Transverse energy

Calorimeters measure the energy deposited by the particles, and energy is a scalar physical quantity. However, in a high-energy collider experiment most

of the particle energy is kinetic energy and all particles are originally created in the initial collision (or are decay products of these particles). In this context it is convenient to think that the energy deposited has a direction, which in practise is the direction of the calorimeter cell with respect to the collision point. Just as momentum, this "vectorised" energy can be projected in different planes. Interesting physical processes in high-energy collisions often give rise to energy deposits in the plane perpendicular to the beam line. This projection of the energy is called the *transverse energy* E_{T} and is computed as

$$E_{\mathrm{T}} = \sin(\theta) \cdot E \tag{4.4}$$

where θ is the polar angle of the calorimeter cell, and E the deposited energy. It should be noted that $0 < \sin(\theta) \leq 1$ in the interval $0 < \theta < \pi$.

For many purposes, the transverse energy is more interesting than the energy itself. In particular, for a particle that leaves the detector volume without interacting, such as a neutrino, the only way to retrieve the information about the particle is to look at the transverse energy. Since energy and momentum of the particle collision is conserved, the vectorial sum of the E_{T} will not be 0 if a non-interacting particle was present in the reaction. This "hole" in the transverse energy is called the *missing transverse energy*, $E_{\mathrm{T}}^{\mathrm{miss}}$.

4.2 Calorimeter performance

In the previous sections we have learned that the performance of a calorimeter varies with the detected particle and with the material used to build it. As mentioned before, two variables closely related to the performance of a calorimeter are (the linearity of) the response and the resolution. The linearity of the hadronic energy response is governed by the level of non-compensation of the calorimeter. The resolution can be expressed as a sum,

$$\frac{\sigma}{E} = \frac{C_{fluct}}{\sqrt{E}} \oplus \frac{C_{instr}}{E} \oplus C_{const} \tag{4.5}$$

where $\oplus$ indicates addition in quadrature. The three terms arise from different processes in the calorimeter[35]. The first term, $C_{fluct}/\sqrt{E}$, comes from statistical fluctuations in the shower energy content, and, for sampling calorimeters, from fluctuations in the fraction of energy measured. This is the most important term, that dominates the resolution for most energies. Typical values of $C_{fluct}/\sqrt{E}$ are about ten percent (for electromagnetic showers) and about 50% for hadronic showers. The second term, C_{instr}/E, comes from instrumental noise effects. This term is very small for large energies, but limits the resolution for low energies. The constant term, C_{const} is determined by the performance of the read-out devices, such as PM tubes, ADC's, etc, as well as uncertanties in the calibration.

Generally, a homogeneous calorimeter achieve a better resolution for electromagnetic showers than a sampling calorimeter, because the sampling fluctuations are eliminated. However, a homogeneous calorimeter can never be compensating, and the response to hadronic showers is thus very non-linear. A sampling calorimeter, on the other hand, can be compensating or near compensating, thus giving a good hadronic linearity, at the cost of higher sampling fluctuations and a worse resolution. The sampling fluctuations can be reduced by increasing the sampling fraction (by increasing the amount of active material and thus the fraction of the energy deposited in the active layers) or by increasing the sampling frequency (by making the layers of absorber and active material thinner, but keeping the overall ratio)[6].

When designing a calorimeter system, the aspects of resolution and linearity must be considered and balanced. If the calorimeter system is divided into an electromagnetic and a hadronic part, the electromagnetic calorimeter is generally homogeneous or sampling with a high sampling fraction, to give a good resolution, while the hadronic calorimeter is a compensating or near-compensating calorimeter with a low sampling fraction. Such an approach might lead to undesired side effects, however. The resolution of hadronic showers that start in the highly non-compensating electromagnetic calorimeter will suffer from the fluctuations in the visible energy content. Even if the hadronic calorimeter is compensating, and provides a good resolution, it cannot recover from the losses in the electromagnetic calorimeter. For this reason, hadronic calorimeters are generally built of fairly cheap and robust material, because their performance is limited by the requirements on the performance of the electromagnetic calorimeter, and not as much by their own construction[6].

5. Test beams

Beam me up, Scotty.
– Captain James T. Kirk, in Star Trek: The Animated Series.

As described in the previous chapters, the ATLAS detector consists of several sub-detectors, each with its own purpose and design. Before assembling a giant detector like ATLAS, it is important to ensure that all sub-detectors work as intended. One way to test the calorimeters is to expose them to particle beams of well-known energy and study the read-out, as well as compare it to simulations. These particle beams are called *test beams*, an expression that often includes the entire beam testing process. The calorimeters of ATLAS have been studied with the aid of test beams several times, starting with calorimeter prototypes in the 1990's, to the last test of a slice of the entire barrel section of ATLAS in the autumn of 2004.

The barrel calorimeters have been tested in CERN's H8 beam line, in the North Area[8, 46]. The beams are created with the Super Proton Synchrotron accelerator (SPS) that provides protons with a momentum of up to 400 GeV/c. A diversity of particles with various energies are created after the proton beam is collided with a primary target (beryllium) and a secondary target. The material of the secondary target varies with the desired particle: for electrons the target is a combination of lead and air, for pions the beam is collided with a polyethylene and lead target[8]. Muon beams are created from pion beams, since the pions decay in flight to muons, and any remaining pions can be filtered with absorbers, such as concrete blocks that are thick enough to stop the pions.

Before impact, the beam passes a selection magnet, so that only particles with the desired momentum are chosen.

After the secondary target, the energies of the particles in the beam ranges from about 10 to 300 GeV. Particles with even lower energy, 1-9 GeV, can be produced after collision with a tertiary target.

No matter which targets are used, there will always be a contamination of pions, electrons and muons in the beams. If the particles chosen are positive, an additional contamination of protons might occur. In the case of the very low energy beams, 1-9 GeV, a contamination of high energy muons is present. Other particles can be filtered, but the muons penetrate vast amounts of material, and are not easily stopped (see Chapter 4). In order to clean the beam as much as possible and provide all necessary particle information, the beam line is also equipped with several wire chambers, scintillators, Čerenkov

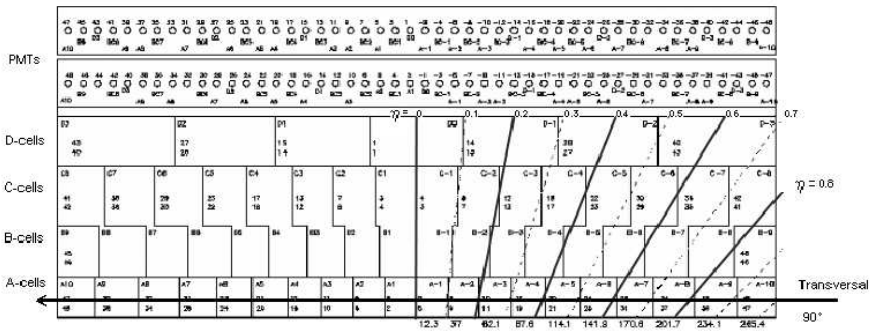

Figure 5.1: Schematic view of a Tile calorimeter barrel module. Some η directions are indicated, as well as the direction of transversal beams through the A-cells. (Figure from [47])

detectors etc., to measure and control the particles in the beam; all to ensure that a well-known particle with a well-known energy hits the detector.

In this section, two test beam set-ups are described: the stand-alone Tile test beam of 2003 and the combined ATLAS test beam of 2004. In this case, "stand-alone" means that the Tile modules were tested by themselves, without any other ATLAS sub-detectors present. In the "combined" test beam, a slice of the barrel part of ATLAS was tested, with a piece of the inner detector, the electromagnetic calorimeter, the hadronic calorimeter and the muon chambers present[1].

5.1 The Tile stand-alone test beam 2003

The Tile modules have been studied in stand-alone test beams several times, last time in 2003. The test beam activities are summarised in reference [42].

In the stand-alone test beam of 2003, the Tile modules were placed on a table that could be rotated with respect to the incident beam. This enabled beam impact in different η directions, as indicated in Figure 5.1. During normal data taking with the LHC collisions, the jets and particles will go in some η direction. In the Tile stand-alone test beam, however, some runs were taken with the beam targeted transversal to the Tile modules, providing a very long calorimeter for the shower development. In addition, with this set-up, the incident particles were perpendicular to the scintillator tiles in the calorimeter.

In Chapter 6, a study of very low energy muons (3-9 GeV) in beams targeted transversally at the Tile A-cells is described.

[1] In other words, "combined" does not refer to the beam (which we wish to be pure) but the combination of several sub-detectors.

5.2 The 2004 combined ATLAS barrel test beam

In the autumn of 2004, a slice of the barrel section of the ATLAS detector was tested in a combined sub-detector test beam, thus testing parts of the inner detector, the pre-sampler, the LAr barrel, the Tile barrel and the muon chambers together[8]. In Figure 5.2, a schematic view of the combined test beam set-up is shown.

The combination of a slice of all sub-detectors in the barrel part of ATLAS enables the possibility of studies of combined calorimetry, that is, how the electromagnetic and hadronic calorimeter work together. In Chapter 7, a method for hadronic calibration of single pions in the calorimeter system is described.

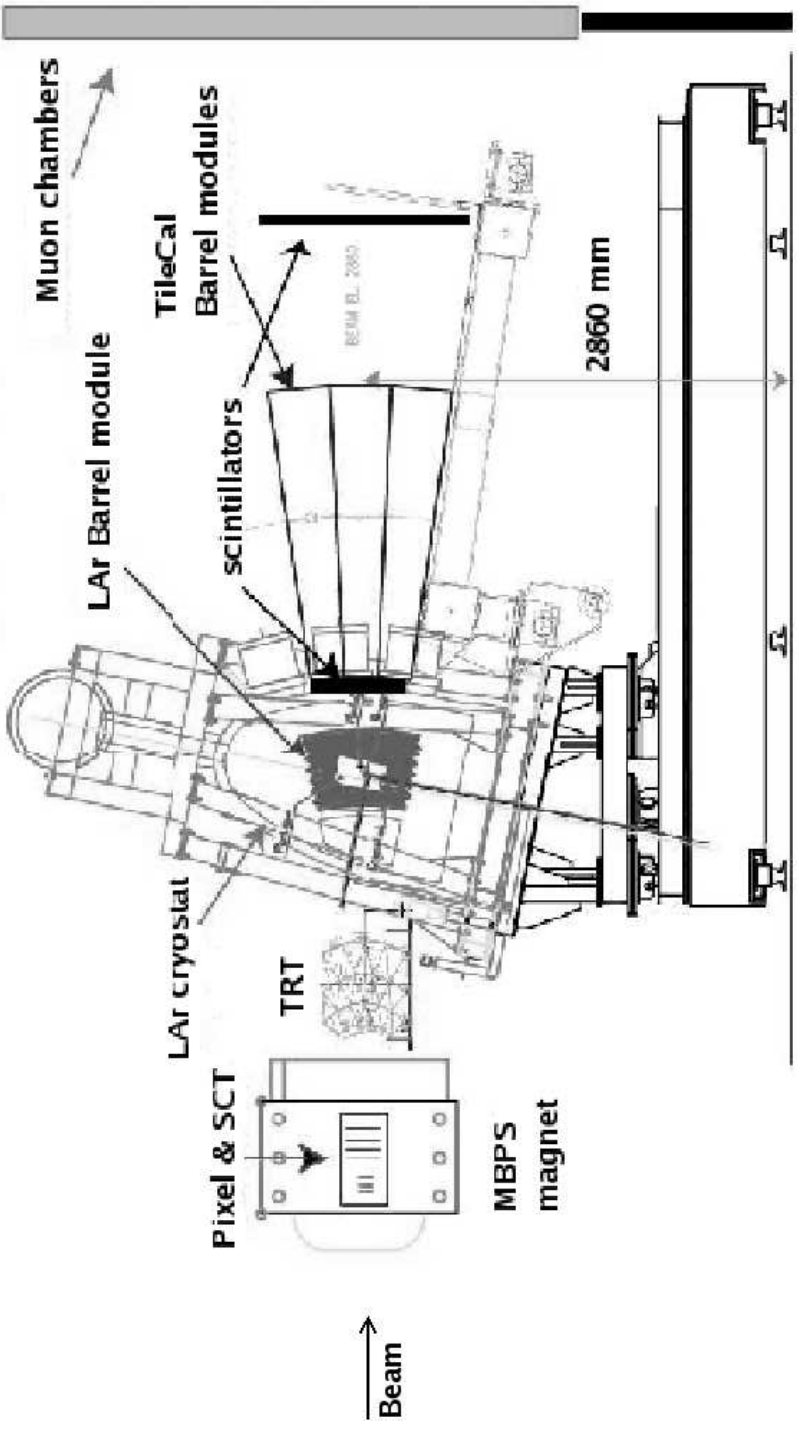

Figure 5.2: Set-up of the 2004 combined test beam. (Figure from [8]).

6. Very low-energy muons in the hadronic calorimeter

Before the installation in the ATLAS cavern at the LHC, the hadronic barrel calorimeter of ATLAS, TileCal, was subject to tests with real particle beams from the SPS accelerator at CERN. In this chapter, an analysis of the behaviour of very low-energy muons in TileCal is described. "Very low-energy" in this context means energies between 3 and 9 GeV.

In the stand-alone test beam, the different TileCal modules were tested separately. For the best resolution possible, this analysis contains only data from transversal ($\theta = 90^\circ$) test beam with impact on TileRow 2, which means that the beam goes through the smallest cells in the module, the A-cells. Three different runs were used, with nominal particle energy 9, 5 and 3 GeV. See Appendix A for ATLAS-specific details, such as run numbers.

The main focus of this analysis is to compute the range of the low-energy muons in the calorimeter material. As described in Chapter 4.1.1, high-energy muons are approximately minimum ionising particles, MIPs, that can penetrate wast amounts of material without stopping. Muons with energies as low as 1 GeV are also MIPs; however, when the muon energy becomes even lower, the energy loss per unit length passed rapidly increases, as shown in Figure 4.1 in Chapter 4, and the muon stops. Approximate calculations can be used to estimate the expected muon range. The Tile module is 5.64 metres long [48]. The active material is polystyrene plastic ($C_6H_5CH = CH_2$), but most of the module is steel[1]. Assuming that all of the module is steel, the mean energy loss for one muon passing the entire module should be about 7.9 GeV[9]. We can conclude that we expect most of the 9 GeV muons to pass, while a muon with lower energy should stop somewhere in the module. GEANT4 simulations[49] (see Section 6.3) confirm these approximations.

Throughout this chapter, measured energies are given in the unit pC, which is not a unit of energy but of charge. As mentioned in Chapter 3.2.2, the charge deposited by the particles of the shower is proportional to the energy of the shower. The charge stated is thus directly proportional to the energy on the electromagnetic scale. A conversion factor from pC to GeV (which is approximately 0.8) can be obtained from electron beams of known energy. However,

[1] In one so-called period, an 18 mm slice of calorimeter material from which all the cells are built, there is 14 mm steel and 3.1 mm scintillator plastic. The remaining $\sim$ 1 mm consists of glue and air[42].

for this analysis, the comparison of different energy depositions is enough, and an absolute energy scale is not needed.

6.1 Muon selection

As outlined in Chapter 5, the beams analysed contain mainly three different kinds of particles: pions, electrons and muons. In this analysis, pions are the most abundant for most energies.

Since a muon in the energy range between 3 and 9 GeV is approximately a minimum ionising particle (MIP), it will deposit the same amount of energy per unit length in every TileCal cell it passes, until it has no energy left. A pion in the same energy range does not behave like this, and the typical pion signature is a MIP signal in the first few cells, followed by an energetic shower. An electron showers even earlier, and typically deposits most of its energy in the first few cells. Since the Tile calorimeter is non-compensating, more energy will be detected from an electron than from a hadron (i.e. a pion) of the same energy.

In Figures 6.1(a)-6.1(c), histograms of the sum of the energy of the first cells, for the three different beam energies are shown. The function fitted to the histograms is a sum of a Gauss-Landau convolution[41] for the muons, and two Gaussians for pions and electrons. As shown in the figures, the fit is very good, and we can distinguish the three different kinds of particles we expected to find in the beam: muons, pions and electrons. Especially for the $E = 3$ GeV beam, it looks like there are many muons. However, there are not as many muons as the figure might suggest, since the muon peak also hides some late-showering pions. Also, the muon peak does not tell us anything about the energy of the muons it contains. Since muons of energies as large as several hundred GeV can also be considered as MIPs, they will lose the same amount of energy per cell as a muon of much lower energy.

The analysis should be done on low-energy muons only, so we have to cut all the other particles away. That is, electrons and pions should be removed from data, as well as the noise in data and any high-energy muons that might have slipped through the momentum selection. The variables used for selection are given in Table 6.1.

Name	Meaning
`Trig == 1`	particle present in the beam-line
`Beamextra`	removes a handful high-energy muons
`Ximp, Yimp`	to get a straight beam
Energy distribution	muon selection

Table 6.1: Muon selection cuts. See the text for details.

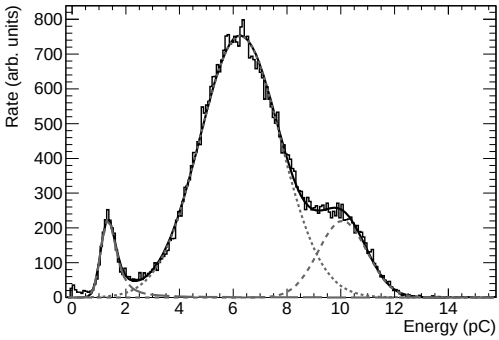

(a) Energy sum, first three cells, $E_{beam} = 9$ GeV.

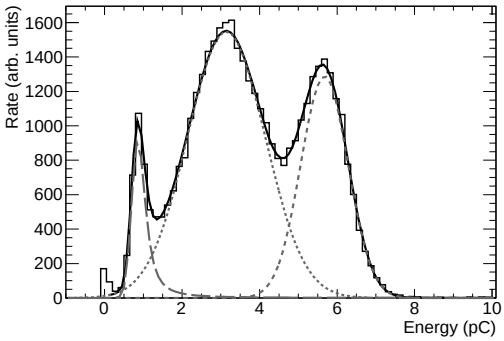

(b) Energy sum, first two cells, $E_{beam} = 5$ GeV.

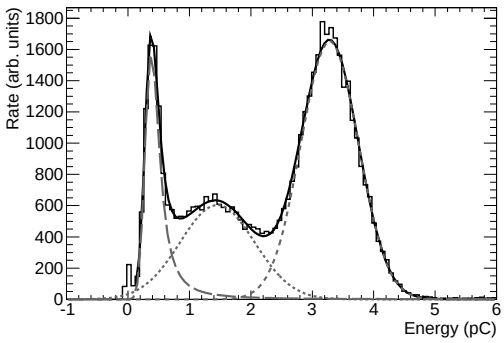

(c) Energy sum, first cell, $E_{beam} = 3$ GeV.

Figure 6.1: Sum of energy in the first few cells, for the different beam energies. Sums of two Gaussians and a Gauss-Landau convolution are fitted to the different histograms. The three different kinds of particles in the beam are clearly distinguishable, with muons in the leftmost peak, pions in the middle and electrons at the highest energy.

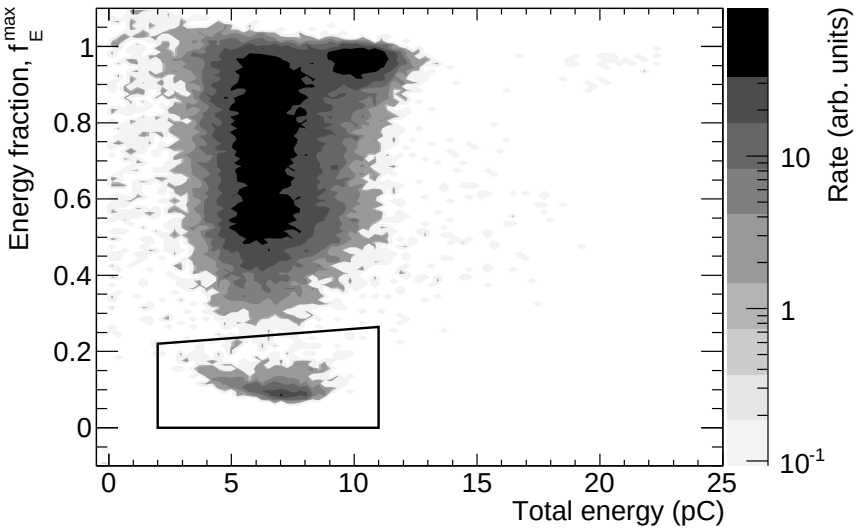

Figure 6.2: Fraction of energy in the cell with maximum energy, versus total energy in all cells. Nominal beam energy 9 GeV. The frame is placed around the muon cluster and indicates the limits of the cut applied. It should be noted that the z-scale is logarithmic.

The trigger system of the test beam set-up is a simple coincidence of the signals in three scintillators in the beam-line[42]. If `Trig==1`, there is a particle in the beam-line, and not an empty run. The `Beamextra` variable contains data from a scintillator that should give a signal if the muon is high-energetic. However, this does not work perfectly and an admixture of high-energy muons can be observed in the last Tile cells of the 5 and 3 GeV runs, which should be empty. These signals can be treated as background and subtracted. It should be noted that such a removal can not be done in the 9 GeV beam, which thus might contain high-energy muons.

The variables `Ximp` and `Yimp` give the impact coordinates where the beam hits the TileCal cell, as deduced from wire chambers in the beam-line. A proper choice of impact removes particles with inclined impact.

The "Energy distribution" cut is illustrated in Figures 6.2 – 6.4, which show the energy distribution for the different energies.

On the x-axis we have the total energy deposited in all the A-cells for each particle. On the y-axis we have, for each event, the fractional energy in the cell with maximum energy detected. The muons, being MIPs, deposit about the same amount of energy in several cells and can thus be seen as a cluster near the bottom left corner of the plots. The pions deposit most of their energy in a few cells, and form the long ridge in the upper left corner of the plots. The electrons deposit most of their energy in a single cell, and the total

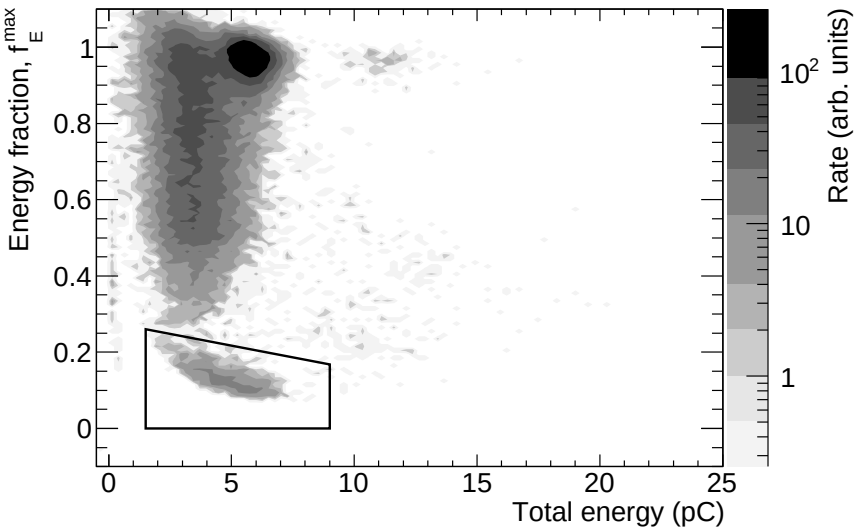

Figure 6.3: Fraction of energy in the cell with maximum energy, versus total energy in all cells. Nominal beam energy 5 GeV. The frame is placed around the muon cluster and indicates the limits of the cut applied. It should be noted that the z-scale is logarithmic.

visible energy deposited is larger than for the pions, since TileCal is a non-compensating calorimeter. The electrons form the peak in the top of the plots.

The cuts indicated in Figures 6.2 – 6.4 select the events that contain muons. The number of muons in each cell is deduced by looking at energy deposits above the noise level for each cell.

From Figures 6.2 – 6.4 it is evident that the separation between pions and muons is very good for the 9 GeV beam. For the 3 GeV beam, the separation is not as clear, and the data become very sensitive to the placement of the cut. But separation is still possible, as will be shown.

6.2 Pion decay in the beam

As demonstrated in Figure 6.1, the beam contains pions and electrons, as well as muons. For each energy, there is about 50,000 events and more than half of them are pions. The number of muons selected with the cuts described in Section 6.1 is only about 1000. Between the momentum selection magnets and impact of the particles on TileCal module, the particles travel about 17 metres.[2] Since the lifetime of a pion is $2.6 \cdot 10^{-8}$ s, a few percent of the

[2]See Section 6.5 for a more thorough discussion on pion decay and the test beam layout.

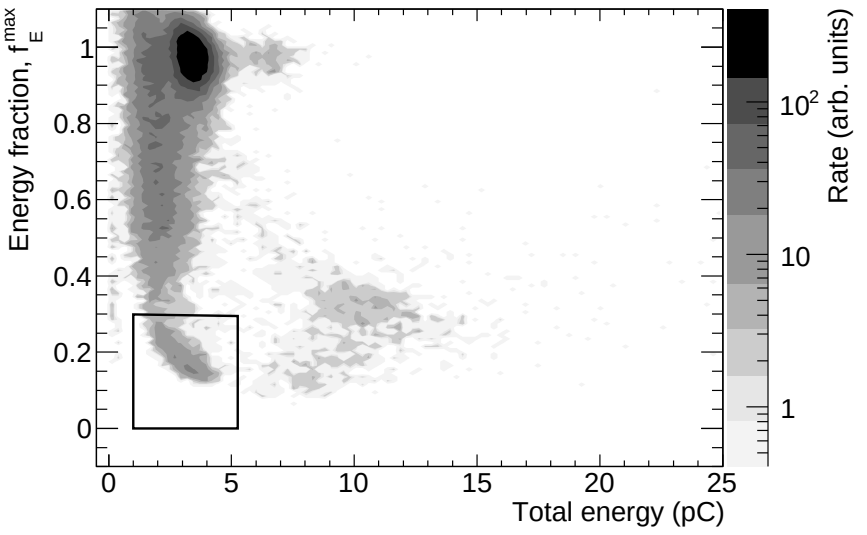

Figure 6.4: Fraction of energy in the cell with maximum energy, versus total energy in all cells. Nominal beam energy 3 GeV. The frame is placed around the muon cluster and indicates the limits of the cut applied. It should be noted that the z-scale is logarithmic.

pions decay into muons during flight, which means that we have around 1000 muons that are decay products, and therefore not necessarily of the same energy as the pions. Since the number of muons observed is about 1000, we can conclude that pion decay *is not* negligible.

Decay muons have lower energies than the original pions. The momentum $p_{\mu,\mathrm{CMS}}$ of a decay muon in the pion's centre-of-mass system (CMS) is

$$p_{\mu,\mathrm{CMS}} \cdot c = \frac{m_\pi^2 c^4 - m_\mu^2 c^4}{2 m_\pi c^2} \tag{6.1}$$

where m denotes the particle rest masses and c is the speed of light.

We are interested in the muon energy in the laboratory system, where we make our measurements. A Lorentz transformation of the energy to the laboratory frame, $E_{\mu,\mathrm{lab}}$, gives us

$$E_{\mu,\mathrm{lab}} = \gamma\left(\sqrt{m_\mu^2 \cdot c^4 + p_{\mu,\mathrm{CMS}}^2 \cdot c^2} + c \cdot p_{\mu,\mathrm{CMS}} \cdot \cos\theta\right) \tag{6.2}$$

where the pion speed $|\overline{v}|$ is approximated as c, and we have used the scalar product relation $\overline{v} \cdot \overline{p}_{\mu,\mathrm{CMS}} = v \cdot p_{\mu,\mathrm{CMS}} \cdot \cos\theta$, where θ is the CMS angle of the decay muon with respect to the beam direction.

The expressions for maximum and minimum muon energy in the laboratory frame are obtained by taking the extreme values of $\cos\theta$ in Eq. 6.2, that is ± 1. The numeric results from these equations can be found in Table 6.2.

E_π (GeV)	$E_{\mu,max}$ (GeV)	$E_{\mu,min}$ (GeV)
3	3.0	1.7
5	5.0	2.9
9	9.0	5.2

Table 6.2: Minimum and maximum energies of decay muons, for different pion energies.

From the values of Table 6.2, it is clear that the pion decay muons have energies that vary between a value about 57% of the pion energy and all of the pion energy. The energy spectrum is flat, since muon decay recoil is equally probable in every direction in CMS, and the solid angle element $\mathrm{d}\Omega = \sin\theta\,\mathrm{d}\theta\,\mathrm{d}\varphi$ also can be written as $\mathrm{d}\Omega = \mathrm{d}(\cos\theta)\,\mathrm{d}\varphi$.

6.3 Comparison with simulations

In the previous section it was demonstrated that the low-energy muons found in the beam are of two different kinds: either muons from pion decays or muons with nominal beam energy. In order to compare data with simulations, we must reproduce both the nominal energy muons and the continuous energy spectrum of the decay muons.

Nominal energy muons are easily reproduced, since those only require ordinary mono-energetic muon simulations. The decay muon energy spectrum is continuous, so the most correct simulation would of course be a continuous one. However, this is not as straight-forward as mono-energetic simulations. Another approach is to take appropriate amounts of mono-energetic samples of simulations with different energies in the correct range. This should not lead to any significant errors, as long as the energies of the samples chosen are sufficiently close.

As mentioned in Section 6.2, the decay muon energy spectrum is flat. However, the energy spectrum of the decay muons that are actually observed in TileCal is not. This can be understood by thinking about what determines the energy of the decay muon. If a decay muon in the pion rest system is emitted perpendicular to the beam direction, thus getting approximately the medium energy, it also deviates more from the beam than if it is emitted straight forwards or backwards which results in maximum or minimum energy. Since the acceptance in TileCal is energy dependent, we must compensate for this when comparing data with simulations.

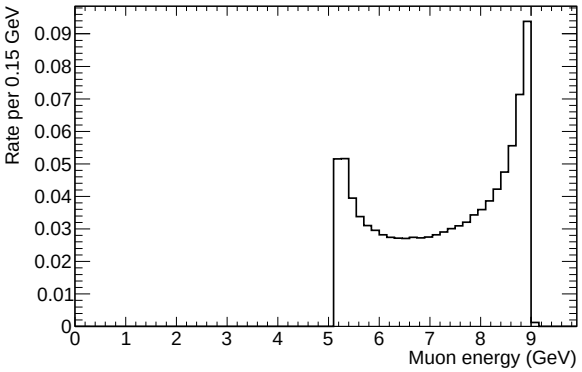

(a) Beam energy 9 GeV.

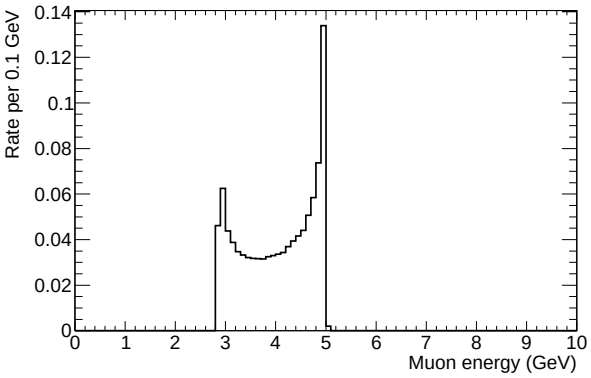

(b) Beam energy 5 GeV.

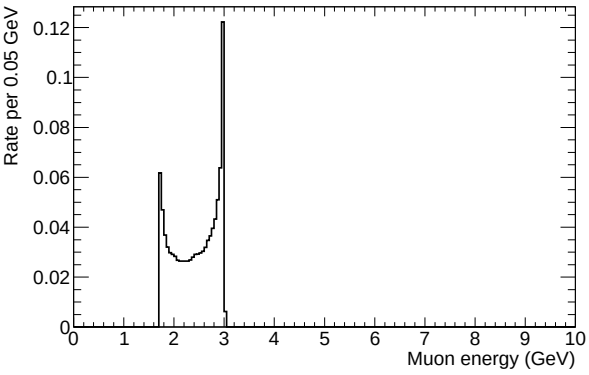

(c) Beam energy 3 GeV.

Figure 6.5: Energy spectra for muons accepted in TileCal, for various beam energies.

One way of estimating the acceptance energy dependence is to make a simple simulation, in which pions are allowed to decay during flight.

To simulate the beam-divergence, the x- and y-impact coordinates of mother particles were taken from the pions recorded in the respective runs. We distinguish two cases: for muons from pion decays before the the second of the two beam-chambers used to define the impact points on the calorimeter, the impact coordinates were computed using the small angle approximation by just adding the Δx and Δy obtained from the angle of the muon track with respect to the original pion direction. The acceptances for these muons were then obtained by applying the same impact parameter cut as used for data. There is thus no explicit requirement that the muon hits the trigger scintillator for this type of decay-muons. This is motivated by the fact that in the data sample there is a small admixture of events which, if relying on computed beam trajectory, should have missed the trigger scintillator. The presence of this type of events in data is not understood, but by applying the method above we try to include this type of events also in the acceptance correction. For muons originating from pion decays after the second of the two beam-chambers used to define the impact points on the calorimeter, the situation is different since the impact coordinates will be recorded as those of the mother pion. For this class of decays we therefore cut on the impact parameter of the mother particle, and in addition we require that the decay-muon does hit the trigger scintillator.

Figure 6.5 shows the energy spectra for accepted decay muons from pions of energies 9, 5 and 3 GeV. The overall acceptances are 38.0% for 9 GeV pion decay muons, 24.9% for 5 GeV and 15.8% for 3 GeV decay muons.

In order to create the simulation of the decay muons from the 9 GeV-energy pions, we have taken a sum of simulation samples with energies 5, 5.5, 6 etc up to 9 GeV. The terms in the sum are weighted according to the histogram of Figure 6.5(a). The 5 GeV beam decay muon simulation is a sum of samples from 3 GeV to 5 GeV with 0.5 GeV intervals, and the different energies are weighted according to the distribution in Figure 6.5(b). For the 3 GeV beam simulation, the sum ranges from 1.75 GeV to 3 GeV, but the intervals are 0.25 GeV, and the acceptance distribution is given in Figure 6.5(c). The same cuts are applied to the simulations as to data.

If our cuts are efficient, all the muons we observe in TileCal are either nominal energy muons or pion decay muons. To determine the relative amount of each type of muon, we can define the mixing hypothesis $N^{\mu}_{hyp,i}$ as

$$N^{\mu}_{hyp,\,i} = a \cdot N^{\mu}_{nom,\,i} + (1-a) \cdot N^{\mu}_{decay,\,i} \tag{6.3}$$

where a, the global fit parameter, is a real number between 0 and 1, i is an index that runs over the cells, $N^{\mu}_{nom,\,i}$ is the number of nominal beam energy muons in cell i and $N^{\mu}_{decay,\,i}$ is the number of muons from pion decays. The simulated number of muons have been normalised so that the number of muons in the first cell is equal for each of the simulations as for data. The χ^2

Beam energy	Mixing parameter a	$\tilde{\chi}^2$	$d.o.f.$
9 GeV	0.35 ± 0.05	0.43	18
5 GeV	0.38 ± 0.03	0.31	18
3 GeV	$0.29 \pm 0.03^*$	0.44	9

* The value of a for the beam energy 3 GeV is very sensitive to the placement of the cut, which adds another error of 0.07 to the statistical one, as described below.

Table 6.3: Values of the mixing parameter a, as obtained from the fit of simulations to data. See the text for details.

of the hypothesis is defined as

$$\chi^2 = \sum_{i=0}^{N_{cells}} \left(\frac{N_i^\mu - N_{hyp,\,i}^\mu}{\delta N_i^\mu} \right) \tag{6.4}$$

where N_i^μ is the observed number of muons in cell i, and δN_i^μ is the uncertainty of this number. For the 9 GeV beam, $\delta N_i^\mu = \sqrt{N_i^\mu}$, and for the 5 and 3 GeV beams, an additional uncertainty in the removal of the high-energy muons is added.

By letting a be a free parameter of the fit, the optimal mixing between the different muon samples is obtained by minimising the χ^2 of the fit. The best values of a determined in this way can be found in Table 6.3, as well as the χ^2 values for these fits.

The results of the comparisons of data with simulations can be seen in Figures 6.6 – 6.8, which show the muon flux as a function of penetrated depth into the calorimeter material. Data are marked with grey dots, and the simulated flux is represented by histograms. The mono-energetic muon simulations and the decay muon simulations are marked as dashed histograms above and below data. The bin widths of the histograms reflect the size of the individual Tile cells. For each muon flux plot, the reduced χ^2 of the fit of simulations to data is shown. The reduced χ^2 is defined as $\tilde{\chi}^2 = \chi^2/d.o.f.$, where $d.o.f.$ is the number of degrees of freedom of the fit.

Data are in good agreement with simulations, except for a small systematic effect when the muons begin to stop in the module. We see that for all three energies the data points are slightly lower than the optimal simulation in this particular region. Most likely this effect comes from pion contamination. Even though the cuts described in Section 6.1 separates the muons from the pions quite efficiently, extremely late-showering pions can pass the cuts. Such pions would of course stop quicker than muons in the calorimeter material, and could explain why it looks like the muons stop quicker than expected.

The value of a for the 3 GeV data is very sensitive to the placement of the upper cut limit in the energy distribution plot (Figure 6.4 in Section 6.1).

The cut is placed in the minimum between the particle clusters, where the maximum number of muons is included while the pion contamination is low, see Figure 6.9.

By moving this cut within sensible limits (that is, moving it up until we have almost all the muons but many pions as well, at approximately $f_E^{max} = 0.33$, or moving it down until we have almost no pions but also lose some muons, at $f_E^{max} = 0.27$) we can estimate the cut uncertainty. As shown in Figure 6.10, a varies linearly with the cut placement. When the cut in Figure 6.4 is placed high, we include almost all muons but also many pions. a then drops, because we expect a quicker fall-off among the particles if we have pions. When the cut is placed low, we exclude most pions but also lose some muons, mainly the low-energetic ones, since those are more likely to lose all of their energy in just a few cells, thus ending up in the upper parts of the muon cluster.

The uncertainty of a due to the cut placement can be determined from Figure 6.10. Since the cut is varied within reasonable limits in the figure, the cut uncertainty in a is estimated as the spread in a values in Figure 6.10. The final value of the mixing parameter a for 3 GeV data is
$a = 0.29 \pm 0.03(stat) \pm 0.07(cut\ uncertainty)$

The cut dependency check also shows that for large pion contamination, data tend to lie lower than the optimal simulation when the muons begin to fall

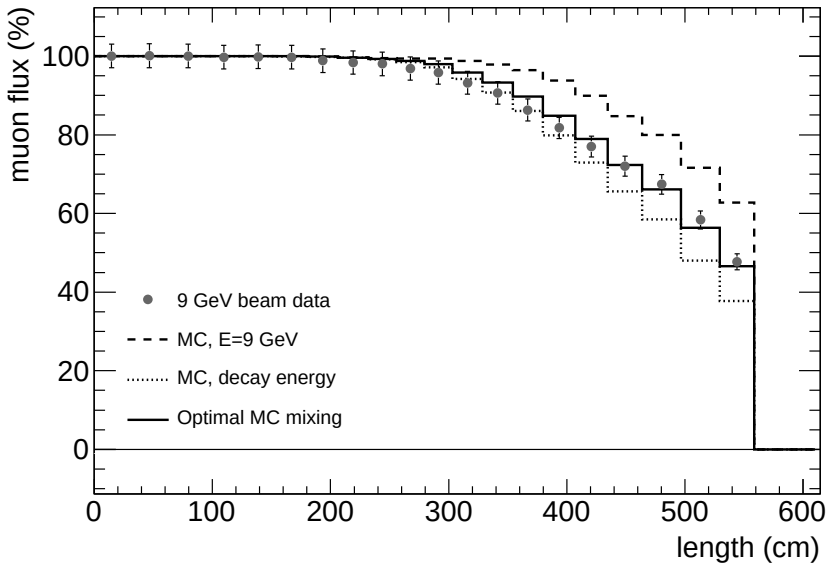

Figure 6.6: Muon flux as a function of calorimeter depth. Data and GEANT4 Monte Carlo simulations (MC) for nominal beam energy 9 GeV are shown. A value of $\tilde{\chi}^2 = 0.43$, $18 d.o.f.$ is obtained for the fit.

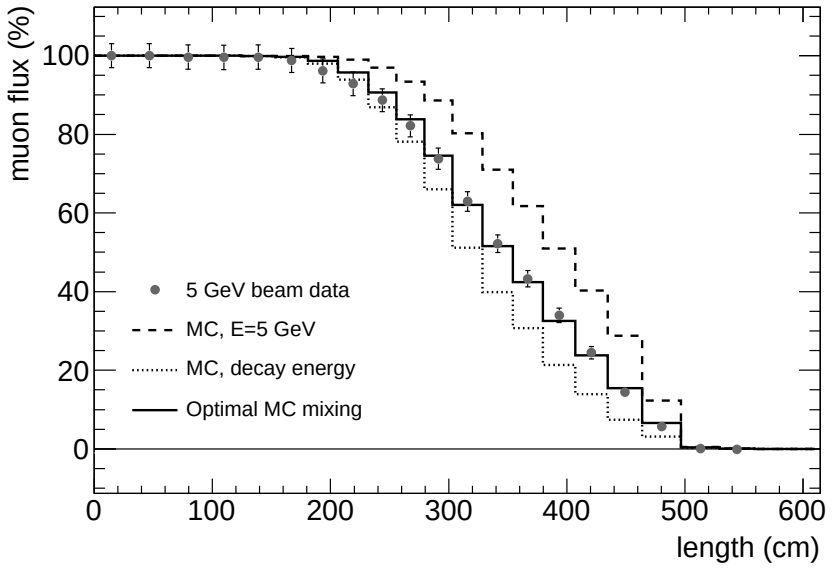

Figure 6.7: Muon flux as a function of calorimeter depth. Data and GEANT4 Monte Carlo simulations (MC) for nominal beam energy 5 GeV are shown. A value of $\tilde{\chi}^2 = 0.31,\ 18 d.o.f.$ is obtained for the fit.

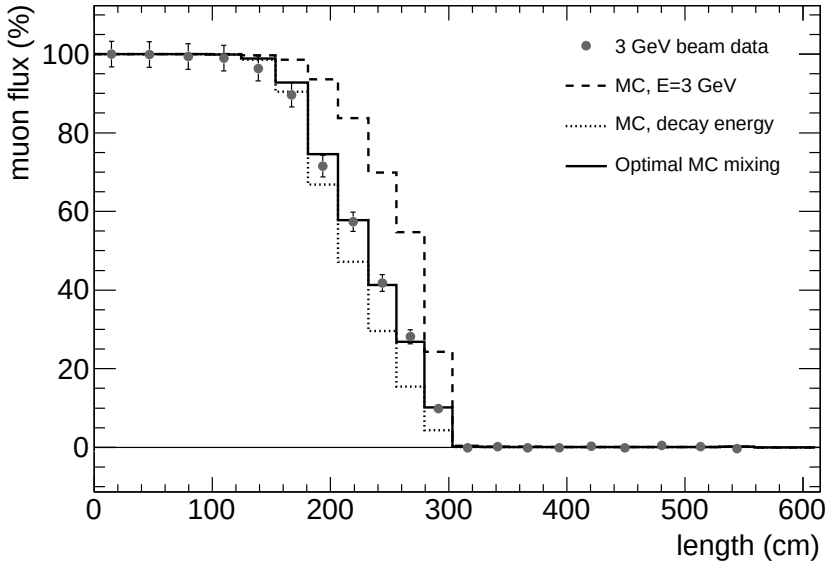

Figure 6.8: Muon flux as a function of calorimeter depth. Data and GEANT4 Monte Carlo simulations (MC) for nominal beam energy 3 GeV are shown. A value of $\tilde{\chi}^2 = 0.44,\ 9 d.o.f.$ is obtained for the fit.

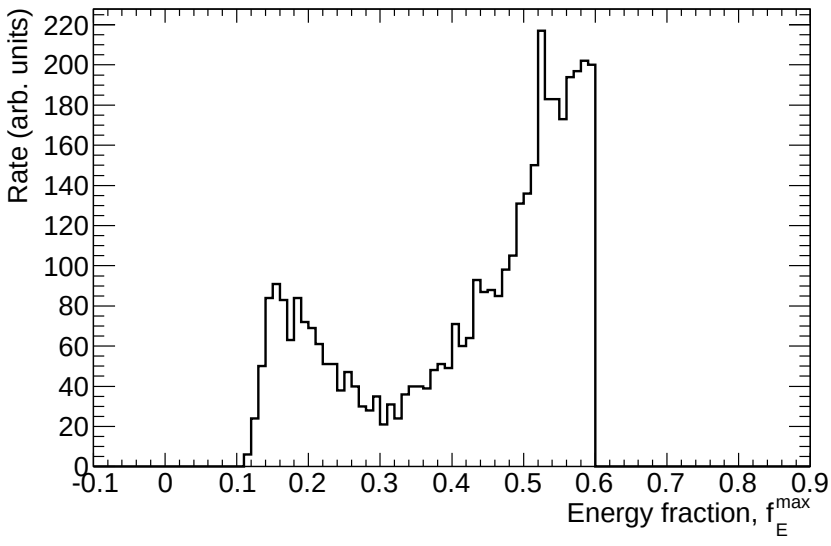

Figure 6.9: Projection on the y-axis of a strip of the energy distribution plot in Figure 6.4 (beam energy 3 GeV). The strip projected has the same width in total energy as the cut, and stretches up to $f_E^{max} = 0.60$. The left peak contains the muons, the right peak the pions. The pions and the muons are not completely separated, but we can see that the best placement of the cut is at $f_E^{max} = 0.30$.

off. This observation further strengthens the hypothesis that the systematical effect observed for all the energies comes from pion contamination.

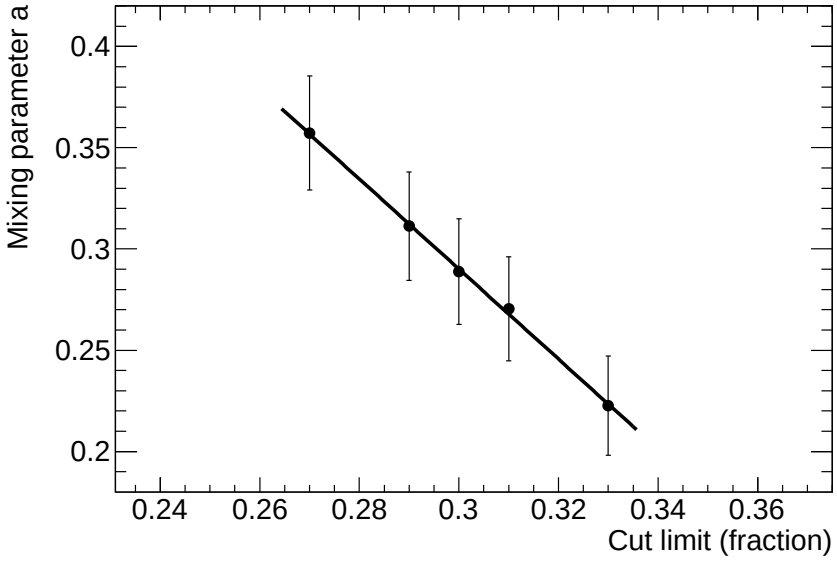

Figure 6.10: Cut dependency of the mixing parameter *a* from the 3 GeV data. By moving the upper limit of the cut in Figure 6.4 within sensible limits, the cut uncertainty can be determined.

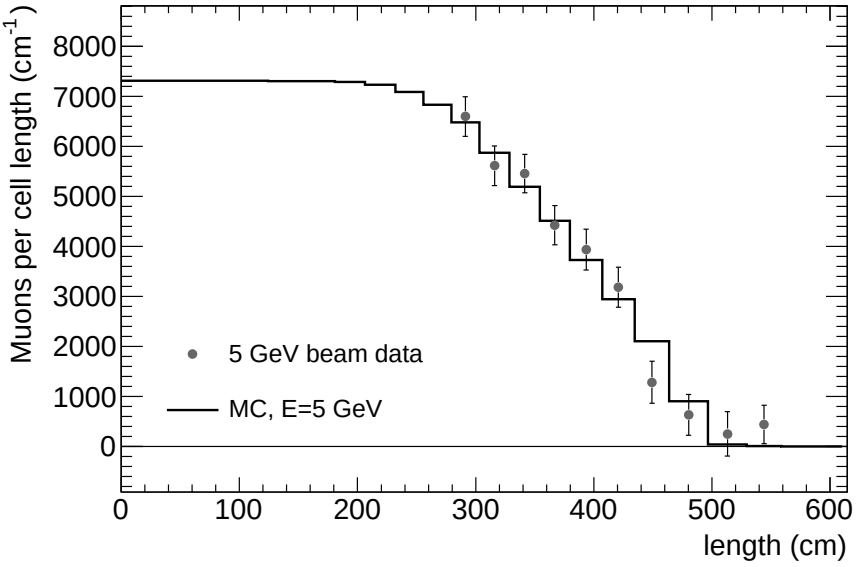

Figure 6.11: Data from a pure muon beam with energy 5 GeV. Only the last ten cells were equipped during data taking. A comparison with a 5 GeV mono-energetic muon Monte Carlo simulation (MC) is shown. The value of $\tilde{\chi}^2$ is 0.81 for the fit of simulation to data, with 9 degrees of freedom.

6.4 Comparison with a pure muon beam

In order to check the hypothesis of pion decay muons, we can take a look at a pure low-energy muon beam. During the test beam period of 1999, one such run was recorded, with 5 GeV muons. Data from that run and a comparison with 5 GeV mono-energetic simulated muons can be found in Figure 6.11. The ATLAS-specific details of the run can be found in Appendix A.

The normalisation of simulation to data was the free parameter of the fit in Figure 6.11, and the $\tilde{\chi}^2$ value obtained is 0.81, for 9 degrees of freedom of the fit. The agreement between data and simulation is thus very good, and most importantly, we can clearly see that there are no pion decay muons, since those would lie lower than the mono-energetic simulation.

6.5 Cross-check of pion decay

In addition to the fit of data to simulations, there is another way to determine the expected number of decay muons. From the number of pions observed in TileCal, $\tilde{N}^{\pi}$, it is possible to estimate the number of pions in the beam immediately after momentum selection, N_0^{π}. This number can be used to calculate

the expected number of pion decays during the flight to TileCal, and thus the expected number of decay muons in the detector, $\tilde{N}^{\mu}_{decay}$.

Immediately after the momentum selection, we have pions and muons in the beam (and electrons, but we can ignore them in this case), all with the nominal beam energy. Let us denote these numbers N^{π}_0 and N^{μ}_0. In TileCal, we observe certain numbers of pions and muons, $\tilde{N}^{\pi}$ and $\tilde{N}^{\mu}$. The observed muons are both nominal energy muons (the muons present after momentum selection) and decay muons from pion decays, $\tilde{N}^{\mu} = \tilde{N}^{\mu}_{nom} + \tilde{N}^{\mu}_{decay}$. But the particles observed in TileCal are not all the particles there are, since e.g. the cuts used and inclined flight-paths reduce the number of particles actually observed. The efficiency of the muon cuts, f^{μ}_{cut}, as described in Section 6.1 can be estimated from comparisons with simulations, and the acceptance efficiency of pions in TileCal (f^{π}_{acc}) can be determined by comparing the total number of events in the beams with the number of events that pass the technical cuts. Since most of the particles in the beam are pions, this ratio should be a good approximation of the pion efficiency. The acceptance efficiency of decay muons (f^{μ}_{acc}) has been discussed in Section 6.3.

If N^{π}_0 pions leave the momentum selection magnet, the number of pions that have not decayed after a time t is

$$N^{\pi} = e^{-t/\gamma\tau} \cdot N^{\pi}_0 \tag{6.5}$$

and the number of pions that have decayed into muons is

$$N^{\mu}_{decay} = (1 - e^{-t/\gamma\tau}) \cdot N^{\pi}_0 \tag{6.6}$$

so the total number of decay muons after a time t, expressed in terms of the pions remaining, is

$$N^{\mu}_{decay} = \frac{1 - e^{-t/\gamma\tau}}{e^{-t/\gamma\tau}} \cdot N^{\pi} \tag{6.7}$$

where τ is the pion life-time. The time-of-flight t is determined from the distance between momentum selection and the calorimeter. This distance, between the middle of the selection magnet and the front end of TileCal in position $\theta = 90^{\circ}$ is 16.55 m [50].

But the observed pions and muons in TileCal are not all the particles there are, because of cut inefficiency and path deviations as discussed above. We have the relations

$$\begin{aligned} \tilde{N}^{\mu}_{decay} &= f^{\mu}_{cut} \cdot f^{\mu}_{acc} \cdot N^{\mu}_{decay} \\ \tilde{N}^{\pi} &= f^{\pi}_{acc} \cdot N^{\pi} \end{aligned} \tag{6.8}$$

where $\sim$ denotes observed numbers.

The number of decay muons is related to all the muons in TileCal. Using the notation of Section 6.3, we have

$$N^{\mu}_{decay} = (1 - a) \cdot N^{\mu} \tag{6.9}$$

E_{beam} (GeV)	$\tilde{N}^{\mu}$	$\tilde{N}^{\pi}$	f^{μ}_{acc} (%)	f^{μ}_{cut} (%)	f^{π}_{acc} (%)	Mixing parameter a
9	1107 ± 33	35700 ± 600	38.0	98.5	92.0	0.56 ± 0.12
5	1087 ± 34	26700 ± 600	24.9	98.8	92.1	0.61 ± 0.18
3	1122 ± 34	13800 ± 400	15.8	97.6	88.4	0.77 ± 0.16

Table 6.4: Values of the mixing parameter a determined by pion calculation. The errors stated are the statistical ones. The values $\tilde{N}^{\pi}$ are estimations from the size of the pion peaks in Figure 6.1 with corrections for unreacted pions, and the values $\tilde{N}^{\mu}$ are the first cell values of Figures 6.6–6.8.

so we finally obtain the expression

$$\tilde{N}^{\mu}_{decay} = \Big(1-a\Big) \cdot \tilde{N}^{\mu} = f^{\mu}_{acc} \cdot f^{\mu}_{cut} \cdot \frac{1-e^{-t/\gamma\tau}}{e^{-t/\gamma\tau}} \cdot \frac{\tilde{N}^{\pi}}{f^{\pi}_{acc}} \tag{6.10}$$

from which a cross-check value of the mixing parameter a can be calculated. In Eq. 6.10 we assume that the amount of pions interpreted as muons (due to cut inefficiency) is negligible and that the trigger efficiency is the same for pions and muons. The a values obtained from Eq. 6.10, the number of muons and pions observed, and the acceptance and cut correction factors can be found in Table 6.4.

The a values obtained this way are about a factor two larger than those from the data-to-simulation fit. There are however considerable systematical errors in these calculated numbers. First of all, the distance from momentum selection to TileCal is measured from the middle of the selection magnet. In reality one can expect that the acceptance for some of the muons produced in decays between this point and the field-free region is low, which means that we underestimate a in this calculation. On the other hand: since the distance between the last and second to last dipole is considerable even a relatively small acceptance for muons from π-decays in this region would lead to an overestimation of a. Without a detailed simulation of the beamline transfer function it is difficult to evaluate the direction and magnitude of these effects.

This cross-check is not completely independent from the data-to-simulation fit, since the muon acceptance factor was used in both calculations.

6.6 Conclusions

In the analysis described in this chapter, it has been demonstrated that it is possible to separate muons from pions in TileCal for energies as low as 3 GeV, for beams transversal to the module.

In the low-energy pion beams studied, the muons found are of two different kinds: nominal energy muons and muons that come from pion decays. The latter particles have energies from a continuous spectrum between 57 and 100% of the beam energy.

Allowing for mixture between these two kinds of muons, the GEANT4 simulations describe 9, 5 and 3 GeV data within the experimental limits of this analysis. The parameter a, the ratio of nominal energy muons to all muons in TileCal, which gives the best agreement between experimental and simulated data can be compared to expectations based on the number of observed pions in TileCal. Although these values do not agree completely, they are still of the same order of magnitude. The value a estimated from pion decay may also have large systematical errors.

7. Hadronic calibration of a non-compensating calorimeter

The only man I know who behaves sensibly is my tailor; he takes my measurements anew each time he sees me. The rest go on with their old measurements and expect me to fit them.
– George Bernard Shaw, "Man and Superman", 1903.

All calorimeters of ATLAS are sampling non-compensating calorimeters. In this chapter, a scheme for hadronic calibration of them is described, but first some general remarks on hadronic calibration are given, and a few calibration methods are described.

Calibration of a non-compensating calorimeter is necessary to compensate for the invisible energy loss in the hadronic showers, and enable a linear response to the hadrons. When a non-compensating calorimeter is calibrated on the electromagnetic scale, the electromagnetic showers are correctly calibrated, while the invisible energy is still unaccounted for. Calibration to the electromagnetic scale, although very important, is not discussed in this section[1].

After a correct hadronic calibration, the invisible energy lost in the hadronic showers is retrieved and the calorimeter response to the hadrons is linear. However, the linear response in itself is not a sufficient goal. Because of the event-by-event fluctuations in the π^0 contents of a hadronic shower, the visible energy will also fluctuate. Ultimately, this will cause a worsening in the resolution for hadronic showers, compared to electromagnetic ones. Figures 7.1-7.2 illustrate the fluctuation problems. In the figures, four different simulated 100 GeV pion events from the combined ATLAS test beam of 2004 are shown, and the different kinds of energy deposited in the sampling layers (in the direction of the beam called "LAr0", "LAr1", "LAr2", "LAr3", "TileA", "TileBC" and "TileD"). In the figure, "electromagnetic energy" refers to energy deposited from electrons and photons, while "non-EM energy" is the visible energy deposited by hadrons and muons. "Invisible energy" is the invisible energy lost in the hadronic showers, and "escaped energy" represents the energy lost by particles that leave the detector volume undetected (mostly neutrinos). The "reconstructed" energy is the energy read out, with overlaid noise,

[1]The general principle for electromagnetic calibration is to study the calorimeter signal when exposing it to electron beams of well-known energy. See Section 3.2.2 for examples of electromagnetic scale calibration of the ATLAS barrel calorimeters.

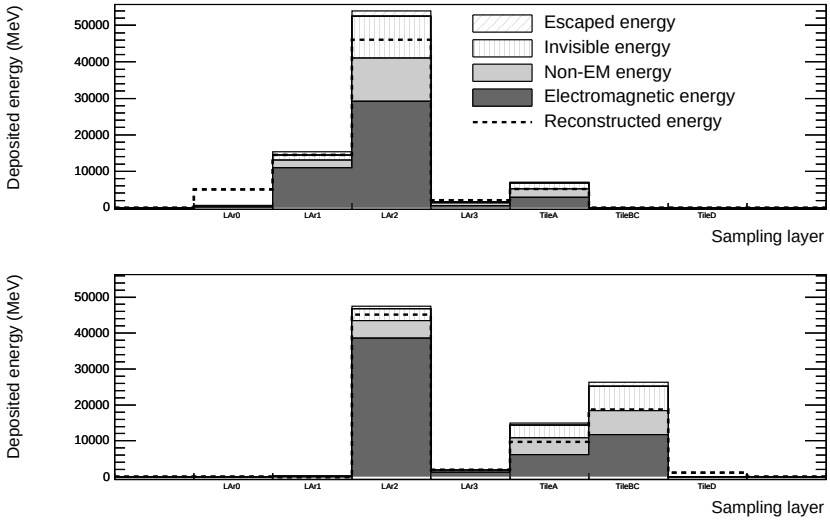

Figure 7.1: Shower development of two different pion events in a calorimeter system. In the top plot, the pion deposits most energy in the first layers, in the bottom plot, the depositions are more evenly distributed. Further explanation is given in the text.

which most of the time coincides with the visible energy (i.e. the sum of the electromagnetic and non-EM energy). It should be noted that although all four pions have the same nominal energy, 100 GeV, their shower developments are quite different. Some pions deposit all their energy in either the electromagnetic or the hadronic calorimeter (the first four or last three sampling layers, respectively) while others deposit their energy quite evenly over the layers. The invisible energy content also varies from event to event. These examples clearly show that hadronic calibration also should compensate for the event-by-event fluctuations.

To summarise our requirements, we can state that hadronic calibration should

– compensate for the invisible energy loss and make the calorimeter response to hadrons linear

– compensate for the event-by-event fluctuations in the hadronic shower (i.e. improve the hadronic energy resolution)

– not disturb the calibration of the electromagnetic showers.

The examples of hadronic calibration discussed in the next section try to different degrees to handle the mentioned challenges. They do not by any means constitute a complete list of hadronic calibration techniques, but serve to show some principles.

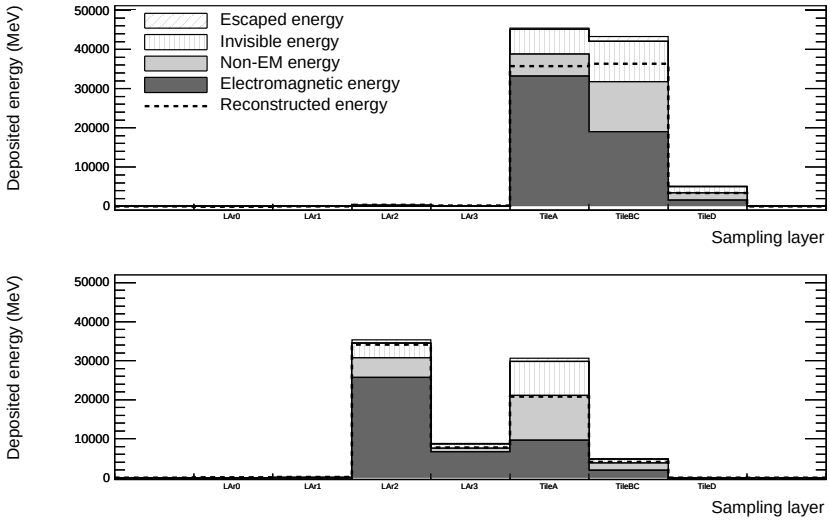

Figure 7.2: Shower development of two different pion events in a calorimeter system. In the top plot, the pion deposits most energy in the hadronic calorimeter, in the bottom plot, the depositions are more evenly distributed. Further explanation is given in the text.

7.1 Simple calibration schemes

First, we will consider two very simple calibration methods that both exploit the difference in shower development for electrons and hadrons.

Electrons start to shower earlier in the calorimeter, and their showers are shorter than hadronic ones. If a piece of absorber material is inserted before the calorimeter, more of the electromagnetic shower is absorbed, which, if the absorber thickness is chosen appropriately, leads to an equal hadronic and electromagnetic response. The advantage of this method is that it is very easy, since it can be designed and built in to the calorimeter. However, there are also several severe disadvantages with such an approach[6]. The most important objection is that the starting point of the shower is energy dependent, so the absorber thickness would need to change with energy for the calibration to be correct for all incoming particle energies. The method would also increase the non-linearity of the hadronic response, since high-energy hadronic showers penetrate deeper in the calorimeter and have a larger visible energy fraction at the same time.

A second, slightly more sophisticated method, assigns one calibration constant, C_{EM} to the first part of the calorimeter, the electromagnetic calorimeter, and another to the hadronic calorimeter, C_{had}. If the calorimeters have been calibrated on the electromagnetic level, $C_{EM} \approx 1$. All energy recorded in the electromagnetic calorimeter is weighted with the first constant, and all energy in the hadronic calorimeter is weighted with the second one. The weight-

ing reflects that most of the electron energy is deposited in the electromagnetic calorimeter, and need not be weighted, while the energy deposited in the hadronic calorimeter must be weighted in order to compensate for the invisible energy loss. If the constants C_{EM} and C_{had} are determined as functions of the electromagnetic scale energy in the calorimeters, it is possible to correctly reconstruct the average energy of both electrons and hadrons.

The problem with this method is that the hadronic energy is only reconstructed *on average*. If several neutral pions are formed in the hadronic calorimeter, their energy is overestimated. If the hadron showers early in the electromagnetic calorimeter, its energy is underestimated. Such a calibration approach obviously fails to handle the fluctuating nature of the hadronic showers, and cannot achieve the desired improvement in resolution.

7.2 Event-by-event calibration: Introduction to local hadronic calibration

The simple calibration methods described above both failed to compensate for the event-by-event fluctuations of the visible energy content in the hadronic shower. In order to achieve both hadronic compensation and follow the fluctuations in the showers, the corrections must be determined on an event basis. This can be done by considering the energy density of the calorimeter cells[51]. This technique was first developed in the H1 experiment[52] at DESY.

The neutral pions in the hadronic showers will cause small electromagnetic showers with a high energy density within the hadronic shower. The energy density, in combination with a global energy estimation of the total energy of the shower, can determine the factor needed to compensate for the invisible energy content of that specific calorimeter cell. The compensation factors are derived from simulations of the calorimeter response to single pions, and are stored as two-dimensional lookup tables[53, 54]. Because such an approach considers only calorimeter signals and calibrates parts of the calorimeter at the time, calibration schemes like these are called *local* calibration.

Local calibration meets our requirements of a hadronic calibration scheme: it compensates for invisible hadronic energy, it preserves the electromagnetic scale calibration of electromagnetic objects, it takes the event-by-event fluctuations into account, and it considers the energy dependence of the visible energy content of a hadronic shower. A detailed study of the computation of the weighting factors and the application of the local hadronic calibration on combined test beam pions and simulated jets in the full ATLAS environment is described in this chapter.

The study was performed in the environment of the combined ATLAS barrel test beam of 2004, using simulations and data of pions at various energies. The simulations have been done with the GEANT4[49] simulation engine within

ATHENA[55, 56], an object-oriented framework for data analysis developed by the ATLAS collaboration. An additional, introductory, study of simulated jets in ATLAS is also presented in Section 7.8, as well as a comparison with the current default jet calibration method. The main part of the study was performed in a test beam environment because of the opportunity to study the performance of the method on real data, instead of doing a simulation analysis only.

It should be noted that calibration of a calorimeter only serves to reconstruct the energy deposited inside the calorimeter. Before retrieving the true energy of a particle in a real detector, several additional corrections must be applied, such as corrections for energy lost in material outside the calorimeters, so called *dead* material. A method for jet corrections, which corrects for the invisible energy loss and other effects at the same time is currently the default calibration method of jets in the ATLAS experiment[57]. Since this method first determines what kind of object to calibrate (a jet, an electron. . .) and then corrects for detector and physics effects in one step, this method is called the *global* calibration scheme, and it is described in detail in Section 7.8.2. The possible advantages and disadvantages of compensating for different effects at the same time are discussed at the end of this chapter.

7.3 Hadronic Calibration of Single Pion Data

As mentioned in the previous section, the current default method for calibrating hadronic jets in ATLAS is a global method, the so-called global H1 scheme, where the reconstructed energy of a jet is optimised with respect to the full energy deposited, as obtained from simulation[53, 57]. This method compensates for detector and physics effects in one step, making the scheme dependent on the jet algorithm and the physics sample used.

In contrast, the local hadronic calibration schemes aim to apply weights not to large objects like jets, but instead calibrate topological clusters[2] in the calorimeter before constructing physics objects like jets. The advantage of such an approach is that the corrections can be modular, i.e. the correction for hadronic invisible energy loss is made independently of correction for energy losses in dead regions of the detector, or leakage. The local corrections are also totally independent of jet algorithms, but corrections for biases introduced by the physics reconstruction algorithms must be applied separately. The local calibration is, as all methods used for calibrating non-compensating calorimeters, based on simulations only, and a good understanding of the precision with which the Monte Carlo simulations can describe real data is needed. Thus it is crucial to test the local hadronic calibration schemes on real data whenever possible.

[2]Topological clusters are formed from energy depositions in the calorimeter cells, based on their energy content and closeness to neighbours. See section 7.5 and references [58, 59].

This chapter describes a method for local hadronic calibration of single pions in the ATLAS calorimeter system using a non-iterative software compensation technique, by weighting the energy on cell level. This method has been successfully applied to the liquid argon calorimeters of the H1 detector at HERA[51, 60].

To obtain the weights, we have simulated the response to single pions in a test beam environment. The development of the weights is described in Section 7.5, where we also demonstrate the performance of the weights on an independent simulated sample.

In Section 7.6 we present the results of applying these weights on real data from the combined test beam runs at the H8 beam line in 2004. The opportunity to try the method on real data from single pions of known energy in a controlled environment is the main reason for doing the simulation study in the test beam environment, rather than in a simulation of the full ATLAS set-up.

To check the stability of the method, we have deliberately altered and distorted the weights in various ways and the results of these studies can be found in Section 7.7. In that section, we also compare our results with other methods for hadronic calibration, in particular the current default version of local calibration, where the global energy scale is the energy of a single cluster[54].

The samples used for the derivation of the weights have been simulated using the simulation toolkit GEANT4[49] within the ATHENA framework[61], version 11.0.42. See Section 7.4 for details.

7.4 Simulation and data samples

For the study described in Sections 7.5-7.7, simulations and results from the combined test-beam of 2004 have been analysed. Only runs with beams targeted at the region of the calorimeter that will correspond to $\eta = 0.45$ in the final detector have been considered. This part is in the barrel region, and thus only read-out from the LAr and Tile barrel calorimeters will be used.

The simulated samples used to make the hadronic compensation factors consist of $10,000$ events from 53 different energies in the range 0.5-316.23 GeV. The energies are chosen to be logarithmically equidistant. In addition to these events, $10,000$ extra events of the same energies, independent of the first sample, were also produced for systematic studies. $20,000$ events of the beam energies 1.5, 3, 15, 150 and 300 GeV were also produced.

The simulations, digitizing and reconstructions were done using ATHENA version 11.0.42, which employs the GEANT4 simulation engine[3].

From the real data of the combined test beam of 2004, seven runs have been used in this chapter, two high-energetic negative pion runs at 180 and

[3]The full version number for the GEANT4 release used by default in ATHENA version 11.0.4 is geant4.7.1.p01.clhep1.9.2.1, see [56].

250 GeV respectively, three positive pion runs at 20, 50 and 100 GeV, one positron run at 180 GeV, and one low-energetic negative run at 9 GeV with a mixture of electrons and pions. From each of the runs, 10,000 events have been reconstructed using ATHENA version 11.0.41[4]. See Section 7.6 for a full description of the runs used and the cuts implemented to clean the data.

The 100 GeV π^+ real data run, run 2102355, is the run on which the simulations are based, i.e. all beam line scintillators, beam chambers etc. in simulation are placed as for run 2102355.

7.5 Development of the weights

As described in the previous section, the calorimeters of ATLAS are non-compensating, i.e. some of the energy deposited by hadronic showers is undetectable by the calorimeters.

In this analysis, we start from topological clusters[62, 58], (often referred to as "topo clusters") which are formed by selecting calorimeter cells with an energy signal larger than 4σ over the noise level. The cluster is then expanded in three dimensions by including all neighbouring cells with an energy signal larger than 2σ over noise. When no more neighbouring cells that fulfill the selection criterion can be found, all cells on the cluster perimeter, regardless of energy, are added to the cluster. Finally, if the topo cluster contains more than one cell with energy deposition larger than all its immediate neighbours, the cluster is split to separate the local energy maxima within the cluster, so that each final cluster only contains one energy maximum. The splitting only occurs if the local energy maxima is larger than 500 MeV.

The topo clusters have been calibrated on the electromagnetic scale[32, 48], so that the energy from electrons and photons is given correctly, while the hadronic energy is too low. We achieve compensation for the invisible hadronic energy loss by applying a weight to the electromagnetic scale cell energy. The weights have been determined from simulated samples, as the mean of the ratio $E_{cell}^{truth}/E_{cell}^{0}$,

$$w_{cell} = \langle E_{cell}^{truth}/E_{cell}^{0} \rangle, \tag{7.1}$$

where E_{cell}^{truth} is the energy truly deposited in the cell, as given from the simulation, and E_{cell}^{0} is the reconstructed energy on the electromagnetic scale.

In this section, we discuss the choice of weight parametrisation, take a closer look at the parameters chosen, give a brief overview of noise estimations and finally determine the weight tables given in Section 7.5.5. In Section 7.5.6, the performance of the weights when applied to independent simulated samples is shown.

[4]The only difference between version 11.0.41 and 42 lies in the simulation stage, since .42 contains a GEANT bug fix. This means that reconstructions with 11.0.41 and .42 are equivalent.

7.5.1 Weight parametrisation

As mentioned in Chapter 4, the fraction of the hadron energy that can be detected by the calorimeters depends on the initial energy of the hadron, where larger initial hadron energy means that a larger percentage of the total energy can be detected by the calorimeter.

In order to compensate for the invisible hadronic energy loss we face two problems: we must find a way to select the hadrons, since we do not want to disturb the energy deposited by electrons and photons, and we must find a way to estimate the total energy of the incoming hadron.

From Chapter 4 we know that the shower from a photon or an electron is more dense than the shower from a hadron. Thus the energy density in a cell within an electromagnetic shower is, on average, larger than the energy density in a cell within a hadronic shower. This relation can be used to separate hadrons from electrons or photons. The total energy of the incoming hadron can be estimated as the reconstructed electromagnetic energy in the topo clusters that fall within a cone around the most-energetic cluster of the event, see Section 7.5.3.

In order to separate hadrons from photons/electrons and also keep track of the initial hadron energy, the weights have been parametrised with the cell energy density and the cone energy.

7.5.2 Energy density

The cell energy density, $\rho_E = E^0_{cell}/V_{cell}$, where E^0_{cell} is the energy recorded in the cell which is calibrated on the electromagnetic scale and V_{cell} the cell volume, can be used to distinguish electromagnetic showers from hadronic ones, as described in the previous section. In Figures 7.3(a) and 7.3(b), the cell energy densities for the various layers of the calorimeters, as given by a pion beam of initial energy 10 GeV, are shown. All cells that fall within a topo cluster have been included. For comparison, the cell energy densities from a 100 GeV beam are shown in Figures 7.4(a)-7.4(b).

From Figures 7.3 and 7.4 we can see some general trends in the cell energy density distributions. In the 10 GeV beam case, the highest densities are found in layer 1 of the electromagnetic calorimeter (the strips). These cells are closest to the impact point. Then the maximal energy densities found are smaller the farther away from the impact point we get. For the 100 GeV beam, this pattern is changed. The maximal energy densities are recorded in layer 2 of the electromagnetic calorimeter, although they are only slightly larger than the energy densities found in layer 1. This reflects the development of the shower in the calorimeter, where the shower penetrates deeper in the calorimeter the more energetic the initial particle is. We also see that the maximal cell energy density in the electromagnetic calorimeter is approximately 0.02 MeV/mm^3 for the 10 GeV beam, and about 0.08 MeV/mm^3 in the 100 GeV case. For Tile, these values are $4.5 \cdot 10^{-4}$ MeV/mm^3 (10 GeV events) and

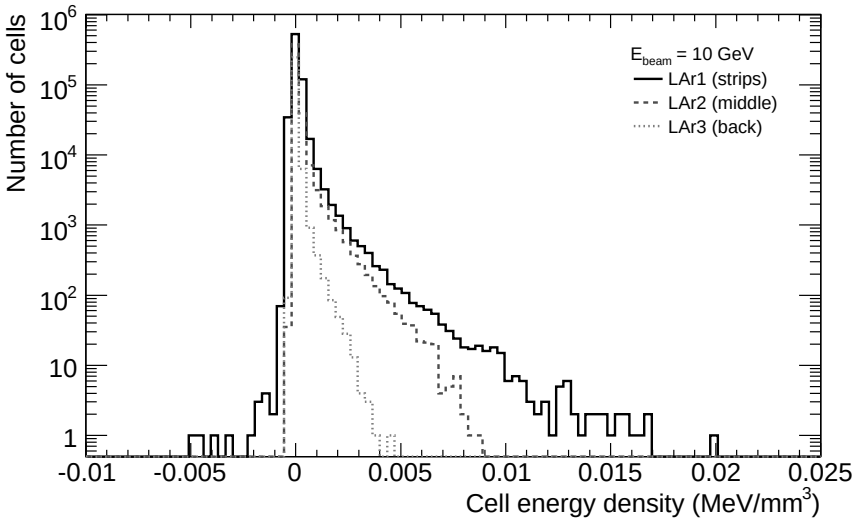

(a) Cell energy density distribution in the LAr sampling layers

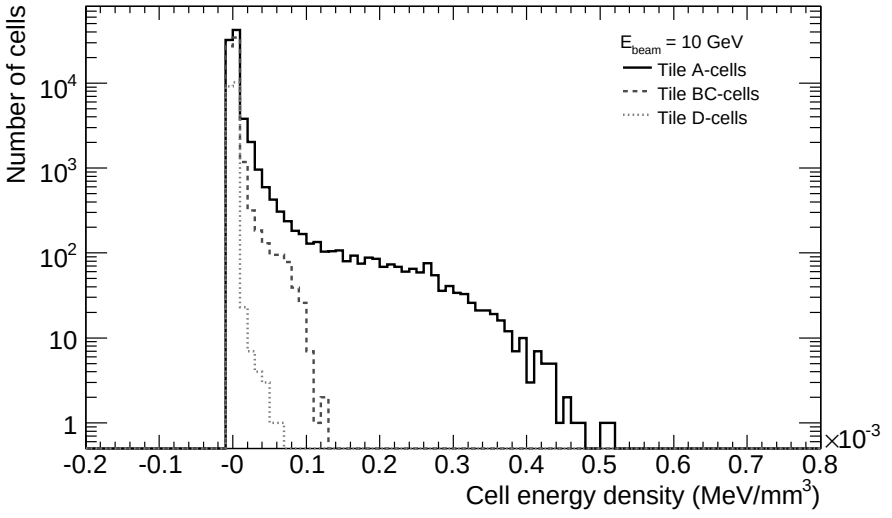

(b) Cell energy density distribution in the Tile sampling layers

Figure 7.3: Cell energy density distribution in the various sampling layers, for a 10 GeV pion beam.

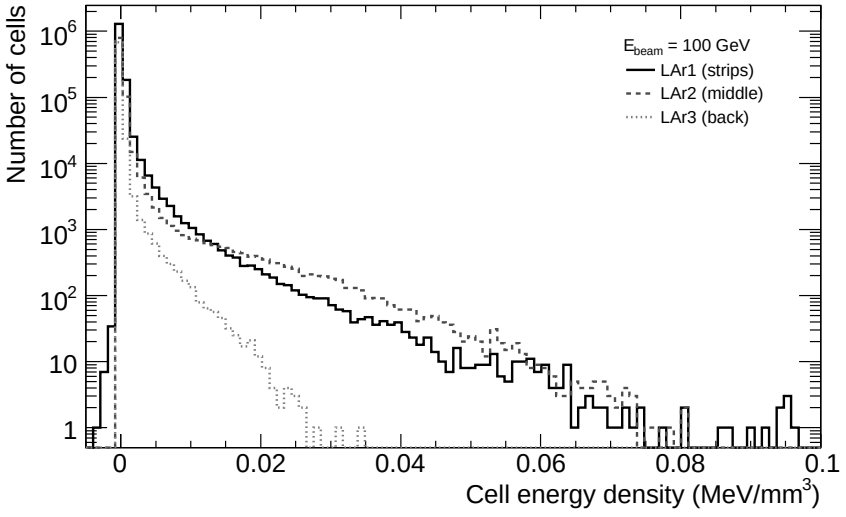

(a) Cell energy density distribution in the LAr sampling layers

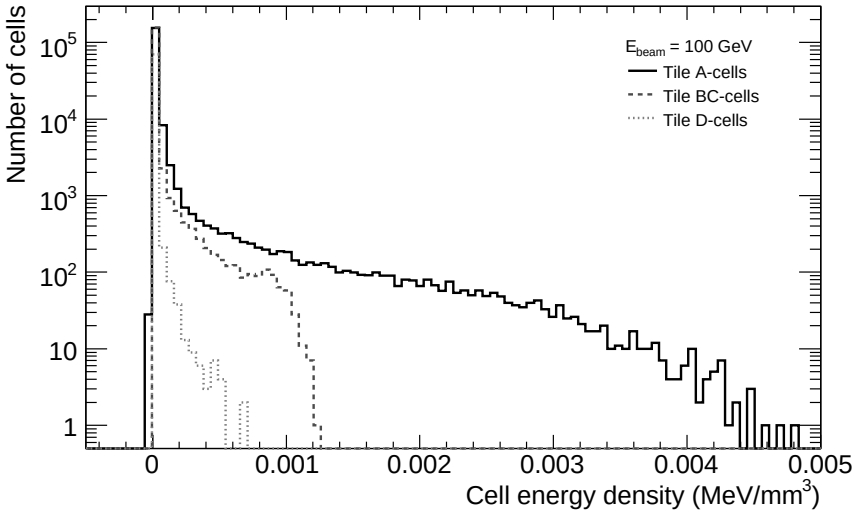

(b) Cell energy density distribution in the Tile sampling layers

Figure 7.4: Cell energy density distribution in the various sampling layers, for a 100 GeV pion beam.

$4.5 \cdot 10^{-3}$ MeV/mm^3 (100 GeV events). The difference in energy density values recorded in the various calorimeters is mainly an effect of the difference in cell volumes, since the cells of the Tile calorimeter are about two orders of magnitude larger than the cells of the LAr calorimeter, see Chapter 3.

A comparison between the energy density from 10 and 100 GeV beams is given in Figures 7.5-7.6. These histograms are not normalised, but reflect the differences at the various beam energies. In the 100 GeV beam, the maximum energy density deposited in any cell is significantly larger than in the 10 GeV beam, and the number of cells involved in the hadronic shower is larger.

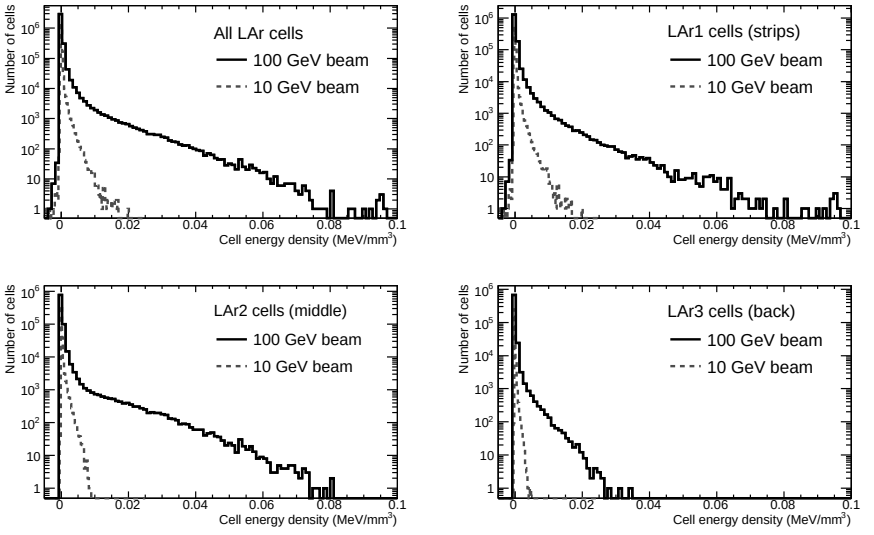

Figure 7.5: Cell energy density distribution in the various LAr sampling layers. Comparison between the energy densities in a 10 GeV and a 100 GeV pion beam.

7.5.3 Cone energy

The energy of all clusters that fall within a cone is the second parameter of the weights. The cone energy is determined in the following way:

- Find the topo cluster with the highest energy in the calorimeter.
- Draw a cone axis through the most energetic cluster and the primary vertex.
- Make a cone with an opening angle (i.e. angle between axis and cone surface) of 11 degrees around the axis. Include all topo clusters whose energy center-of-mass falls within the cone and sum their energies.

If some of the clusters of the event fall outside the most energetic cone, these steps are repeated to make secondary cones, including only clusters that belong to no other cone.

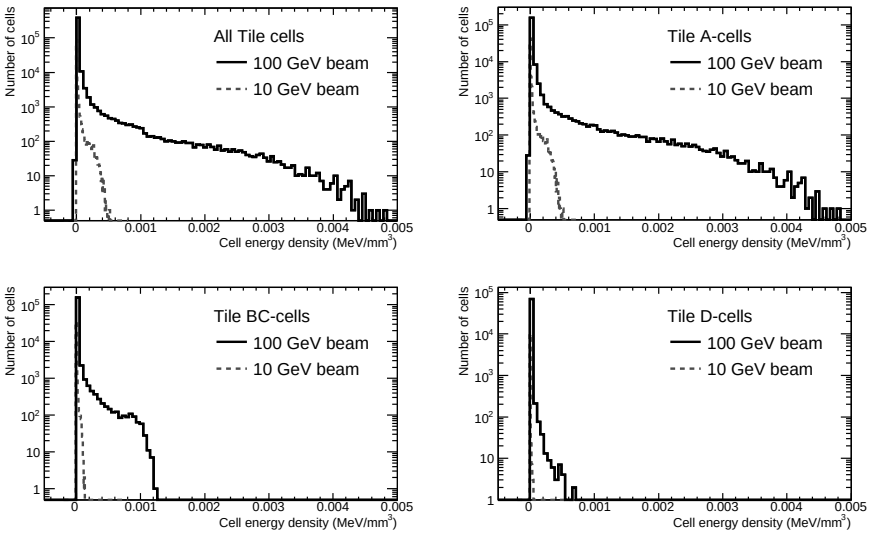

Figure 7.6: Cell energy density distribution in the various Tile sampling layers. Comparison between the energy densities in a 10 GeV and a 100 GeV pion beam.

When computing the weights, only the primary, most energetic, cone is considered. Since the most energetic cone generally contains all or almost all of the single pion energy of the event, this is a fair estimation of the beam energy. If secondary cones are present, they occur in the outskirts of the shower. The physical processes there are different from the ones in the core, and the fluctuations there are larger, generally giving a lower hadronic energy content. If included, weights derived from low-energy secondary cones from high-energy events could distort the weight tables for the low-energy regions.

Distributions of cone energies for a 10 GeV beam and a 100 GeV beam are shown in Figures 7.7-7.8.

The energy of the primary cone divided by the beam energy is given as a function of the beam energy in Figure 7.9, as well as a comparison with the fraction of the beam energy that is reconstructed on the electromagnetic scale. The majority of the electromagnetic scale energy of each event fall within the primary cone, as demonstrated.

7.5.4 Noise considerations

Both when computing and applying the weights, noise considerations play an important role. Quite naturally, it does not make sense to apply hadronic weights to a cell dominated by noise. There are also good reasons to take care not to use noisy cells for derivation of the compensation factors. The Monte Carlo samples used to determine the weights have simulated noise included in

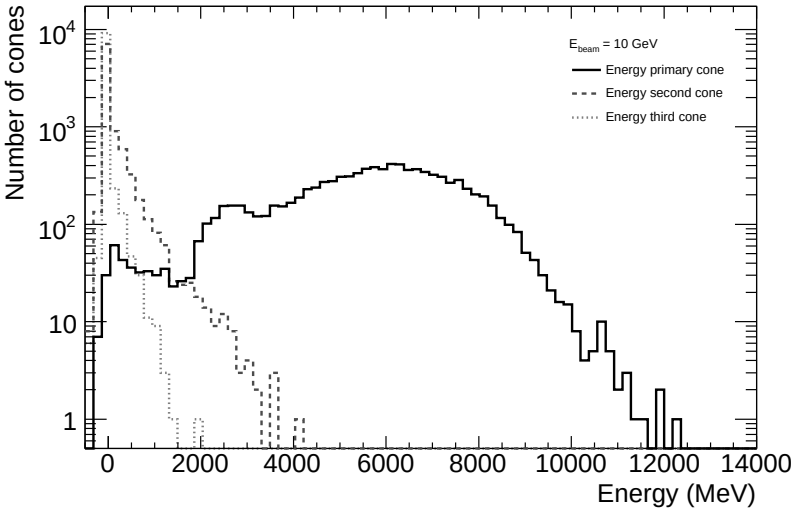

Figure 7.7: Cone energy distribution in a 10 GeV beam. The energy distributions of the first three cones are displayed.

the reconstructed (data-like) energy. This is necessary to get a clustering of the cells as similar to the one in data as possible. However, when the weights are computed as the mean of the ratio between the energy truly deposited and the energy reconstructed on the electromagnetic level, $w_{cell} = \langle E_{cell}^{truth}/E_{cell}^{0} \rangle$, inclusion of noisy cells will give a lowering of the weights, which comes from the cells with a signal just above the noise cut threshold. Let us consider a cell with a small electromagnetic energy deposition slightly above the noise cut. The ideal weight of this cell would be $w_{cell} = 1$, but due to the Gaussian smearing of the signal, E_{cell}^{0} can be both slightly larger and slightly smaller than E_{cell}^{truth}. However, since the signal is just above the noise threshold, the occasions when $E_{cell}^{truth} > E_{cell}^{0}$ will be removed, leaving a bias towards high E_{cell}^{0} values. This gives a general lowering of the ratio $E_{cell}^{truth}/E_{cell}^{0}$. This happens even when the noise cuts are symmetric, since the cut is applied to the sum of noise and signal.

In this section, two ways of removing noisy cells will be considered: a cut on the energy density, and a restriction on the range of the energy ratios filled in the weight tables.

Whenever the energy signal is negative, we know for sure that it is dominated by noise. By looking at the negative part of an energy density distribution, we can get an estimation of the noise level. In Figures 7.10 and 7.11 the energy density distributions for a 10 GeV pion beam in the various LAr and Tile layers are given, together with the Gaussian fits to the negative part of the distributions. When looking at each sampling layer separately, the Gaussian

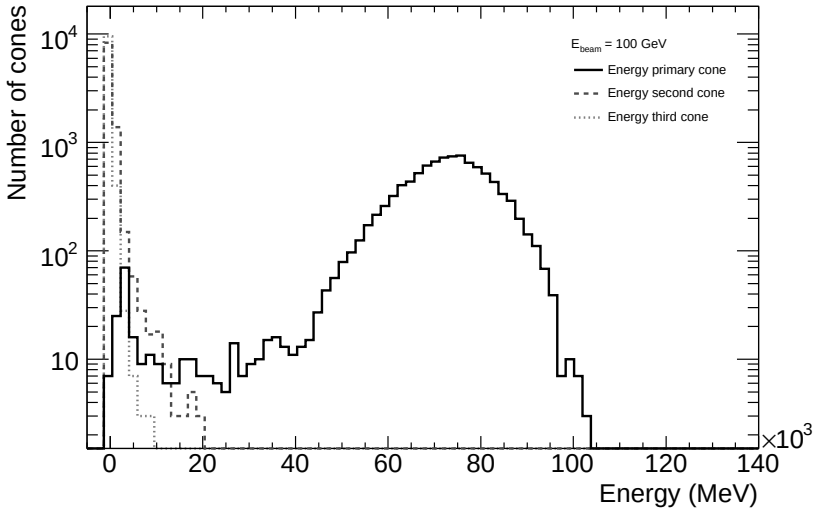

Figure 7.8: Cone energy distribution in a 100 GeV beam. The energy distributions of the first three cones are displayed.

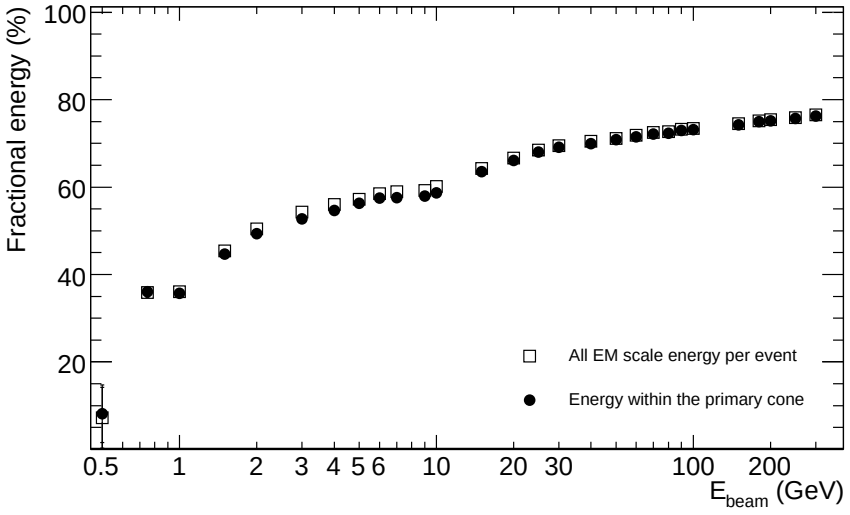

Figure 7.9: Fractional energy of the primary (most energetic) cone, E_{cone}/E_{beam}, as a function of beam energy. The fraction of all energy per event, as reconstructed on the electromagnetic scale, E_0/E_{beam}, is shown for comparison.

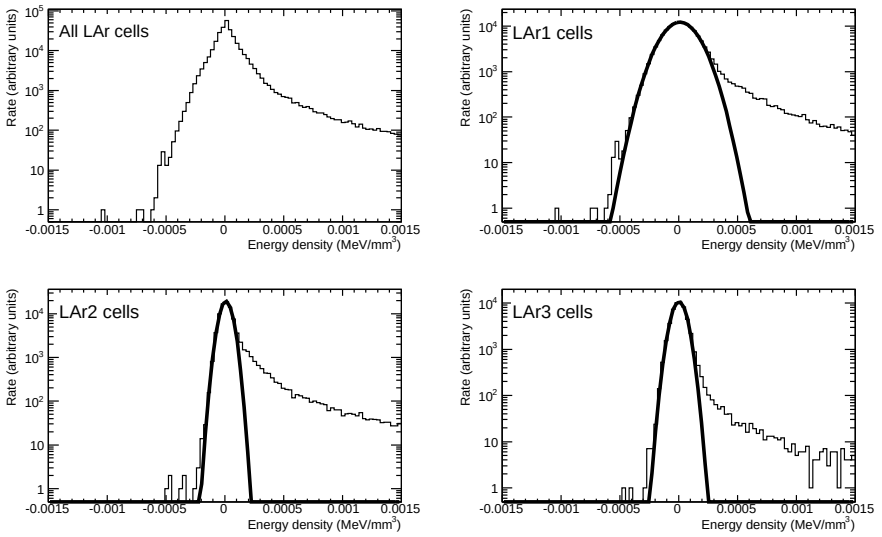

Figure 7.10: Cell energy density in LAr cells, expanded around 0 and fitted with Gaussians. The beam energy is 10 GeV. The Gaussians have been fitted to the negative part of the histogram and plotted for the full range. The top left plot show the energy density in all LAr cells, and the other plots show the cell energy density for the various sampling layers. It should be noted that the pre-sampler (LAr0) has cell volume 0 in the simulation, so no energy densities can be computed.

correctly reproduces the shape of the distribution, but when considering the energy density distribution of all cells in all LAr layers or all Tile layers, the distributions are clearly not Gaussian. This indicates that the noise can be estimated from the energy density, if we consider each sampling layer separately. The noise estimations found this way are in agreement with other methods for handling the noise, see Section 7.6.3.

In Figures 7.12-7.13, the estimated energy density noise level for the various sampling layers of LAr and Tile are given for a selection of beam energies. The noise levels are independent of beam energy to the first order, as demonstrated in the figures.

For the remainder of the chapter, unless something else is explicitly stated, only cells that fulfil $|\rho_E| > \rho_{E,noise}$ have been weighted. The energy density noise estimates are given in Table 7.1.

Another way to reduce noise when making the weight is to implement a restriction on the energy ratios filled in the weight tables. As described earlier, the noise cuts in the topo cluster formation will give a weight that is too low. When correcting for invisible hadronic energy, there is in theory never need for a weight lower than 1. However, just cutting out all energy ratios below 1 would give a bias towards higher weights, due to the Gaussian smearing of the reconstructed E^0_{cell} values. For the computation of the weights in the

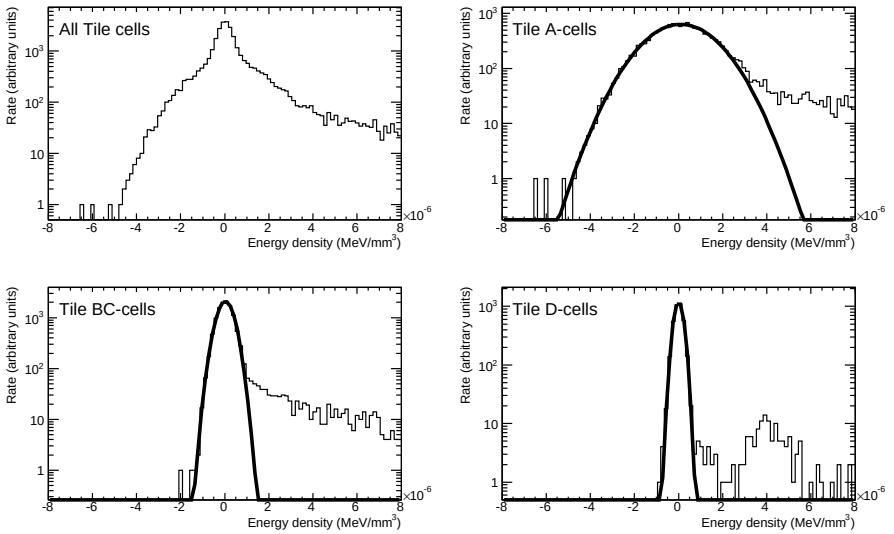

Figure 7.11: Cell energy density in Tile cells, expanded around 0 and fitted with Gaussians. The beam energy is 10 GeV. The Gaussians have been fitted to the negative part of the histogram and plotted for the full range. The top left plot shows the energy density in all Tile cells, and the other plots show the cell energy density for the various sampling layers.

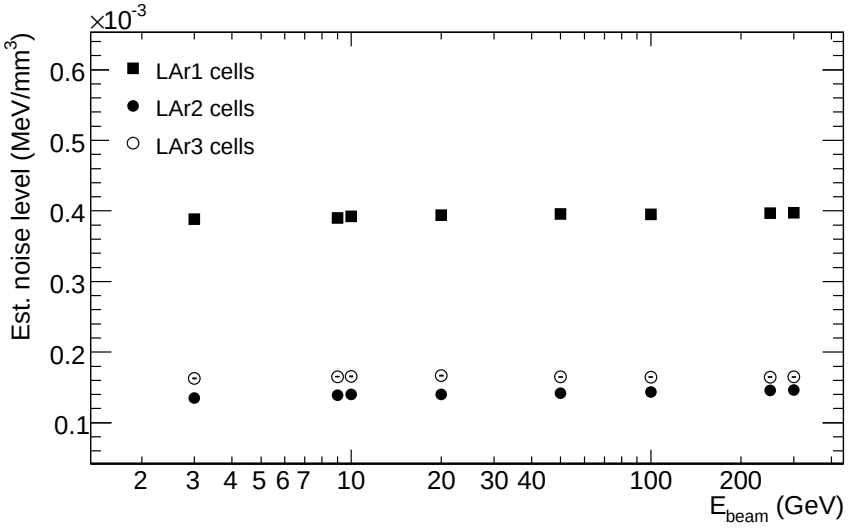

Figure 7.12: Estimate of the cell noise level in the various LAr layers, for a selection of beam energies. The estimated noise level has been computed from $3 \cdot \sigma$ of a Gaussian fit to the negative part of the energy density distribution (compare Figure 7.10).

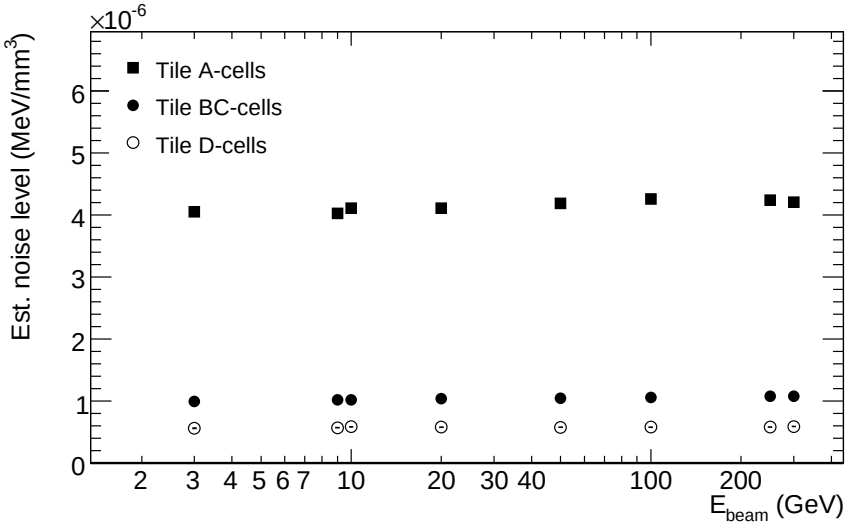

Figure 7.13: Estimate of the cell noise level in the various Tile layers, for a selection of beam energies. The estimated noise level has been computed from $3 \cdot \sigma$ of a Gaussian fit to the negative part of the energy density distribution.

Sampling layer	$\rho_{E,noise}$ (MeV/mm^3)
LAr1	$(3.9495 \pm 0.0034) \cdot 10^{-4}$
LAr2	$(1.4244 \pm 0.0015) \cdot 10^{-4}$
LAr3	$(1.6490 \pm 0.0021) \cdot 10^{-4}$
Tile A-cells	$(4.1623 \pm 0.0013) \cdot 10^{-6}$
Tile BC-cells	$(1.0483 \pm 0.0023) \cdot 10^{-6}$
Tile D-cells	$(5.7918 \pm 0.0017) \cdot 10^{-6}$

Table 7.1: Energy density noise estimates. The values and the uncertainties are given by the Gaussian fits to the energy density distributions.

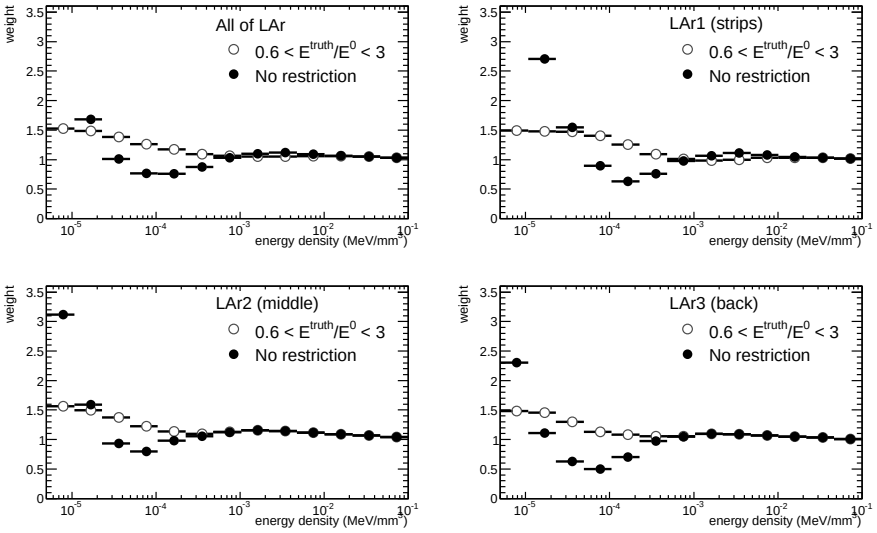

Figure 7.14: Weights for the LAr cells as a function of energy density, with and without the energy ratio restriction cut, $0.6 < E^{truth}_{cell}/E^{0}_{cell} < 3$. The weights have been averaged over all cone energies. The top left plot shows the mean weights in all LAr cells, and the others show the weights in the various sampling layers. The approximate energy density noise level in LAr is $2 \cdot 10^{-4}$ MeV/mm^3 (see Table 7.1 for more precise values).

test beam environment in this chapter, we have applied the restriction $0.6 < E^{truth}_{cell}/E^{0}_{cell} < 3$ on the energy ratios filled in the weight tables. The lower limit is intended to remove the low-weight bias from noise, as described above. The upper limit removes weights from cells with a very low reconstructed signal compared to the true energy deposition. The effects of the weight restriction in the LAr and Tile calorimeters are shown in Figures 7.14 and 7.15.

In both the calorimeters, the energy ratio restriction cut clearly has the greatest impact about and below the energy density noise cut, which is approximately $2 \cdot 10^{-4}$ MeV/mm^3 for LAr cells and 10^{-6} MeV/mm^3 for Tile cells, (see Table 7.1), while the cut has very little effect on weights for cells with high energy density. After the weight restriction cut, the weights in LAr show the expected behaviour: at low energy densities, the weights are high, but they shrink as the energy density increases, stabilising at 1 for high densities. In Tile, the weights without the restriction cut are very high at low energy densities, and after the restriction, the weights show an overall decreasing behaviour as the energy density increases, from $w_{cell} \approx 1.5$ at the very lowest energy densities, to $w_{cell} \approx 1.2$ at the highest energy densities.

Figures 7.17-7.18 in Section 7.5.6, show the effects of the combination of the energy density and weight restriction cuts on the linearity and resolution of weighted energy. A restriction on the energy ratios filled in the weight tables

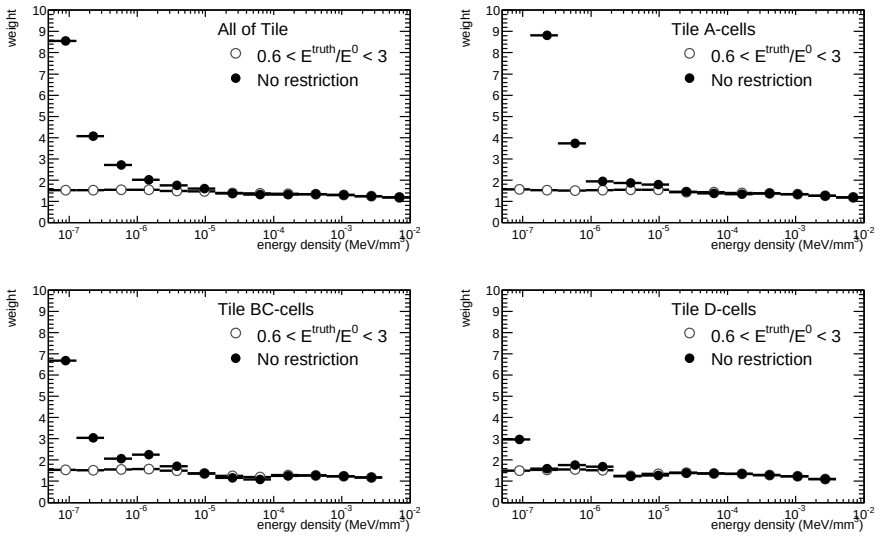

Figure 7.15: Weights for the Tile cells as a function of energy density, with and without the energy ratio restriction cut, $0.6 < E^{truth}_{cell}/E^{0}_{cell} < 3$. The weights have been averaged over all cone energies. The top left plot show the mean weights in all Tile cells, and the other show the weights in the various sampling layers. The approximate energy density noise level in Tile is 10^{-6} MeV/mm^3 (see Table 7.1 for more precise values).

is necessary to eliminate noise effects, that are not removed by the noise cut on the energy density, such as the general lowering of the weight values when the signal is close to the noise cut. As demonstrated in Figure 7.17, especially the linearity is sensitive to the noise bias in the weights, and the noise cut on energy density alone is not enough to reduce the noise-induced lowering of the weights. However, there are problems in implementing a restriction on the energy ratios themselves, since a cut on the ratio is a cut on simulation level, which is irreproducible on reconstruction level, where we do not have access to the true value of the deposited energy.

The systematic effects from the choice of restriction limits on the performance of the weights have not been studied. Lowering any of the weight limits will lead to a lowering of the weights, and raising any of the limits will lead to a similar raise in the weights. In that sense, the cut values are chosen somewhat arbitrarily, and for the local calibration weight tables implemented in ATHENA, the values are slightly different (see Section 7.8). The currently used schemes for local hadronic calibration employ a restriction on the weights themselves, but for future applications, it is necessary to investigate other cuts for reducing noise-induced weight biases, based on variables accessible at the reconstruction level, since weight restriction might lead to a bias in the hadronic scale energy.

7.5.5 The weights

The weights are computed from simulated single pions in the combined test beam set-up, using 10,000 events from each of the 53 different logarithmically equidistant beam energies in the range $0.5 - 316.23$ GeV, as described in Section 7.4. The variables mentioned above, the cell energy density and the energy cone, are used to parametrise the weights. The weights are computed as

$$w_{cell} = \langle E_{cell}^{truth} / E_{cell}^{0} \rangle \tag{7.2}$$

where E_{cell}^{truth} is the true energy of the cell as given in the simulation, and E_{cell}^{0} is the cell energy reconstructed on the electromagnetic scale, i.e. the data-like uncalibrated energy. The weights are filled into two-dimensional tables, according to cell energy density and the energy of the cone in which the cell falls. One weight table for each sampling layer of the calorimeters is made, giving 3 weight tables for the LAr calorimeter and 3 for the Tile calorimeter. The LAr pre-sampler cells cannot be calibrated using the method described here, because the passive material belonging to the pre-sampler cells (essentially the inner detector and the dead material in front of the pre-sampler) is heterogeneous and cannot be characterised by a single volume value. The pre-sampler energy is by default calibrated for electrons, and must be re-calibrated to the different properties of pions. This is done together with the dead material corrections, see Section 7.6.4.

All beam energies are used to fill each weight table, making the weights as unbiased by the initial beam energy as possible. When applying the weights, the only information used to extract the corresponding weight for a cell in a given sampling layer is the energy of the cone in which the cell falls and the energy density of the cell.

Weights are computed from all cells in all topo clusters of the most energetic cone of each event. When filling the weight tables, only ratios that fulfill $0.6 < E_{cell}^{truth} / E_{cell}^{0} < 3$ are entered into the tables. The weight used is the mean value of the weights filled into the bin in question[5]. When applying the weights, all cells within any topo cluster that have energy density above the estimated noise level, as given in Table 7.1, are weighted.

The numerical values of the weights can be found in Appendix B. In the next section, the performance of the weights when applied to an independent Monte Carlo sample is shown.

7.5.6 Linearity and resolution of weighted energy

In order to study the performance of the weights, they have been applied to the energy of independently simulated pions at different energies in the range 0.5 - 300 GeV. In Figure 7.16, the energy distributions of the unweighted topo

[5]The technical solution we have used is to fill the weights from each cell into the ROOT histogram type `TProfile2D`, where the averaging over each bin is done automatically[63].

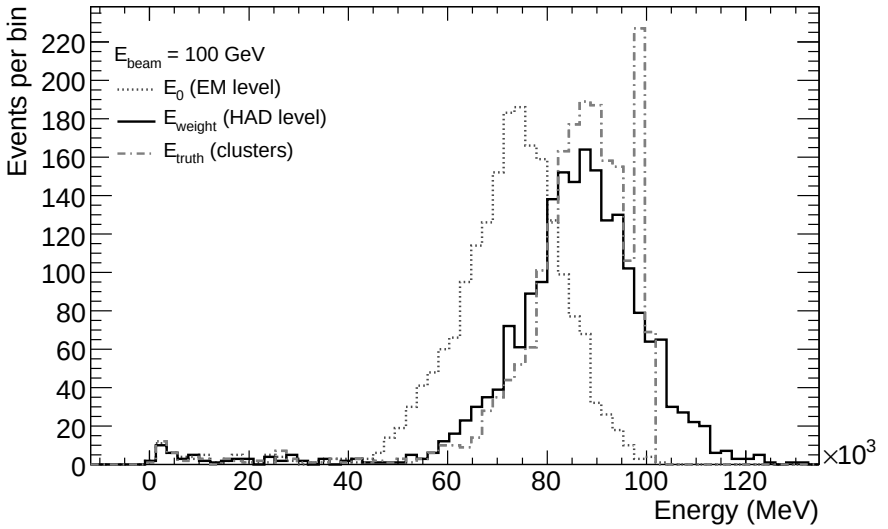

Figure 7.16: Unweighted (E_0), weighted ($E_{weighted}$) and Monte Carlo truth energy (E_{truth}) distributions for a 100 GeV pion beam. All energies considered are the energies within topo clusters.

cluster energy on the electromagnetic scale is compared with the energy after weighting and the simulation truth energy.

Two things should be noted in Figure 7.16: the Monte Carlo truth energy does not peak (solely) at the beam energy, and the distribution is not Gaussian. Both these observations can be explained with losses in "dead" material (see also Section 7.6.4). Some of the pions start to shower in LAr, and lose part of their energy in the cryostat between LAr and Tile. These events form the broad peak at 90 GeV. Some pions do not shower until they reach Tile, where they lose the majority of their energy. These events form the narrow peak at the beam energy. The width of the 90 GeV peak of the E_{truth} distribution is an effect of the energy losses in the cryostat.

Ideally, the weighting procedure will reproduce the Monte Carlo truth distribution, which means that we do not expect the distribution of the weighted energy to be Gaussian.

When comparing results of weighting schemes, normally a Gaussian is fitted to the energy distribution, and the quantities E_{mean}/E_{beam} as a function of the energy (the *linearity*) and σ/E_{mean} (the *resolution*) are computed. However, when the weighted energy distribution is not expected to be Gaussian, these quantities do not make sense. Instead we are interested in the weighted energy in relation to the Monte Carlo truth, rather than the beam energy. The

ratio

$$\frac{E}{E_{truth}}, \tag{7.3}$$

where E is the weighted or unweighted energy and E_{truth} is the Monte Carlo truth energy deposited within the topo clusters can be used to measure the performance of the weighting. The distribution of this ratio is expected to be Gaussian with a mean value close to 1, and parameters of a Gaussian fit[6] can be used to estimate the resolution as

$$r = \frac{\sigma}{mean}. \tag{7.4}$$

The linearity is taken to be $mean - 1$ of the E/E_{truth} distribution.

In Figure 7.17, the linearity of the energy on the electromagnetic scale is shown, as well as the linearity of the weighted energy, with and without noise restriction on the energy ratios filled into the weight tables, as described in the previous section.

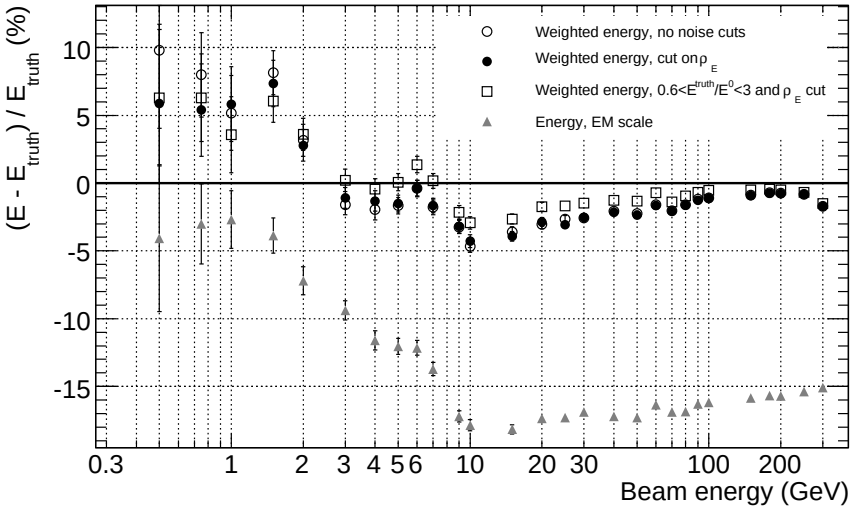

Figure 7.17: Linearity of weighted and unweighted energy, from Monte Carlo simulations. Comparison between the unweighted energy on the electromagnetic scale, (grey triangles), energy which has been weighted with weight tables with energy density noise cuts (filled circles), weight tables with energy density noise cuts and ratio restriction (squares) and without noise reduction (open circles). All errors are statistical errors from the Gaussian fits.

As shown in Figure 7.17, the weighting improves the linearity for all energies above 2 GeV. If the weight tables that are filled with the restriction

[6] In order to make the fit as stable and independent of non-Gaussian tails as possible, the fit is first made to the full distribution, and then redone in the region $mean \pm 2\sigma$. Unless something else is explicitly stated, this is how all Gaussian fits throughout this chapter are made.

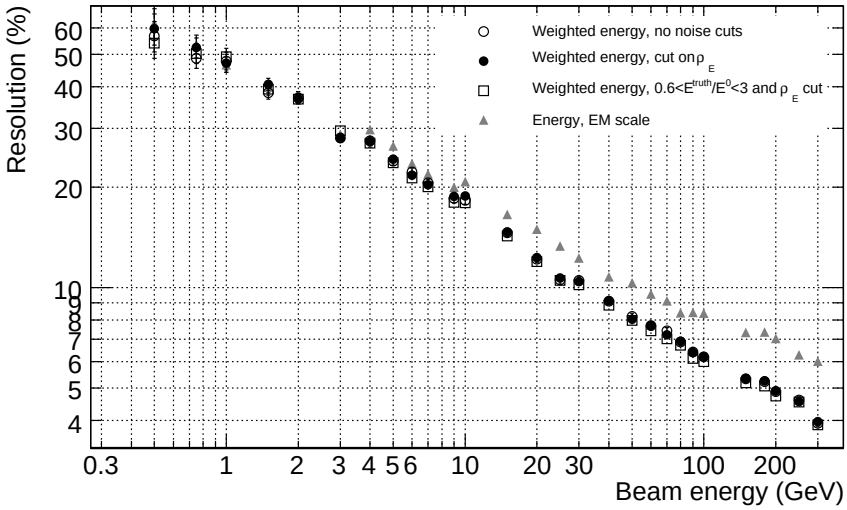

Figure 7.18: Resolution of weighted and unweighted energy from Monte Carlo as a function of beam energy. Comparison between the unweighted energy on the electromagnetic scale, (grey triangles), energy which has been weighted with weight tables with energy density noise cuts (filled circles), weight tables with energy density noise cuts and ratio restriction (squares) and without noise reduction (open circles). All errors are statistical errors from the Gaussian fits.

$0.6 < E_{cell}^{truth}/E_{cell}^{0} < 3$ are used in combination with the energy density cut, which gives the best performance, the linearity is within 3% of the expected value for all energies above 2.5 GeV.

The unexpected rise in linearity at beam energies lower than 10 GeV is an effect of the noise in the calorimeters, which is discussed further in Section 7.7.5. The drop in linearity for the weighted energy at the highest beam energies is discussed in Section 7.7.4.

In Figure 7.18, the resolution, as defined in Equation 7.4, of the weighted and unweighted energy is shown as a function of beam energy, and in Figure 7.19 the difference of resolutions, $r_0 - r_{weight}$ is given.

As shown in Figures 7.18 - 7.19, the weighting procedure improves the resolution of the energy, compared to the unweighted electromagnetic scale energy, for all beam energies above 3 GeV. The impact of the noise cuts is not as visible in the resolution as in the linearity, but it seems like the combination of energy density cuts and weight restriction gives a systematically slightly better resolution, although the fluctuations are within the statistical errors for most beam energies.

It should be noted that although the beam energies 1.5, 3, 15, 150 and 300 GeV were not used to fill the weight tables, the properties of the weighted

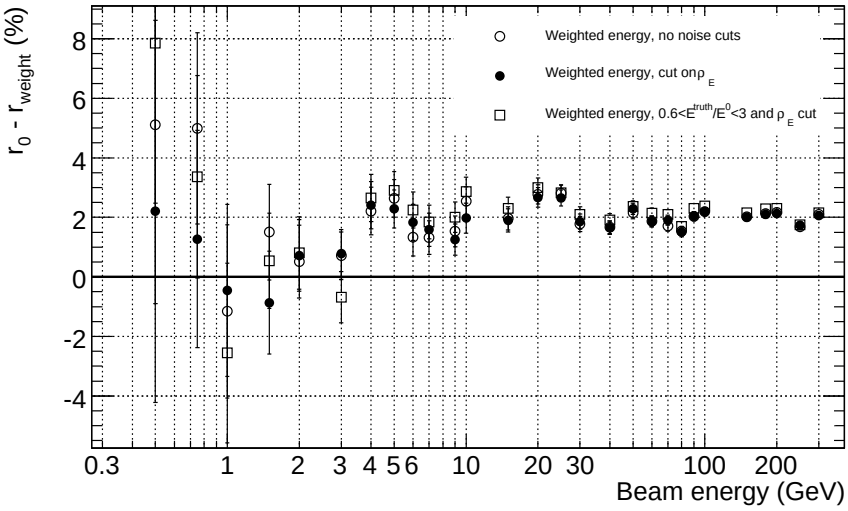

Figure 7.19: Difference of resolutions, $r_0 - r_{weighted}$ as a function of beam energy. A positive value in this plot means that the weighting procedure improved the resolution. Comparison between the unweighted energy on the electromagnetic scale, (grey triangles), energy which has been weighted with weight tables with energy density noise cuts (filled circles), weight tables with energy density noise cuts and ratio restriction (squares) and without noise reduction (open circles). All errors are statistical errors from the Gaussian fits.

energy from these beam energies are as expected from the behaviour of the neighbouring beam energies.

7.6 Application to data from the combined testbeam of 2004

In the previous section, the performance of the weighting factors on an independent Monte Carlo sample was studied. However, the performance of the weights on real data is of greater interest. For studies of the weighting scheme, seven runs of real data from the combined test beam of 2004 have been used. In this section, the conditions of the data runs are described, as well as the cuts needed to get a pure pion sample. A comparison between data and simulation of certain variables is shown, and finally the weights are applied to the real data.

7.6.1 Runs used

Of the seven real data runs used, two are high-energetic negative pion runs, 2101257 and 2101335 (beam energies 180 and 250 GeV), three are positive pion runs, 2102347, 2102355 and 2102396 (beam energies 50, 100 and 20 GeV), one is a positron run at 180 GeV, run 2102182, and one is a low-energetic negative run at 9 GeV, run 2102095. This latter run is nominally an "electron" run, but for very low energies, the particles in the beam are always a mixture of pions, muons and electrons. The 180 GeV e^+ run is only used for comparing the cuts and is not included in the linearity or resolution plots shown in Section 7.6.5.

In all beams, regardless of label, a contamination of muons, electrons and pions is present. See Table 7.2 for a list of the runs used[64].

run	*type*	E (GeV)	E_{true} (GeV)	η
2101257	π^-	180	180.92 ± 0.52	0.450
2101335	π^-	250	251.22 ± 0.51	0.440
2102095	e^-	9	9.009 ± 0.090	0.45
2102182	e^+	180	179.68 ± 0.52	0.45
2102347	π^+	50	–	0.45
2102355	π^+	100	100.45 ± 0.56	0.45
2102396	π^+	20	–	0.45

Table 7.2: A list of the data runs used in the analysis[64]. E_{true} refers to the real energy of the particles in the beam, determined from the currents of the selection magnets. From each of the runs, 10,000 events have been reconstructed.

The run energies given in the logbook are not the exact energies of the particles on impact, only an approximation. A more accurate value can be obtained using information from the currents of the selection magnets. For some reconstructions, the true beam energy, as computed from the selection magnets, is given in the reconstructed data files [7] .

From each of the seven runs, 10,000 events have been reconstructed using ATHENA11.0.41.

7.6.2 Cuts on data

The particle types listed in Table 7.2 only give an indication of which particle was most abundant in the beam, since the conditions of beam production always give a contamination of pions, electrons and muons. The contamination rate varies greatly from run to run, from a few percent to more than half the events. For the positive pion beams, we also have a contamination of protons, which consist about half the particles in the beam[65]. The weights were developed from and tested on pion beams, so we want the real data runs to be purely pions as far as possible. To achieve this, we have implemented certain cuts on data, which are summarised in Table 7.3. In that table, the number of events surviving the various cuts is also given. The cuts follow the standard procedure for cleaning data, with the exception of the electron cut and the "energy OK" cut. The protons, however, cannot be removed with any cut. The effect of the proton contamination will be discussed later in this section.

The number of events out of the original 10,000 surviving the cuts varies greatly, from more than 8000 events for the 50 GeV π^+ run to only about 2400 for the 180 GeV π^- run.

For a few of the events, the energy is abnormally high in Tile, giving a total reconstructed energy of about 400 GeV. This is most likely caused by a misreconstruction in Tile. Since these energies are clearly wrong, the events are removed with the $|E_0| < E_{beam} + 100$ GeV cut. After this cut, a very small tail between 250 and 350 GeV remains in the 250 GeV run. The origin of these few high-energy events is unknown. However, since the tail only contains one event in a thousand, the effect is negligible.

The `sADC_S1` cut is a cut on a beam-line scintillator, placed upstream of the ATLAS detector parts in the test beam set-up[8]. The $N_{cluster} > 0$ cut requires that at least one topo cluster was formed per event used. This cut is a built-in feature of how we define our signal: only energy depositions within topo clusters are considered as signal. Muons are removed from the runs with a cut on the `sADC_muTag` scintillator, which is placed downstream of the muon chambers, behind the beam dump[8]. The `Clock` cut was only applied to the high-energetic π^- runs, 180 and 250 GeV, due to timing problems in

[7] For example, the official reconstruction with version 12.0.5 contains a variable "Energy", which is the true beam energy.

E_{beam} (GeV)	Trigger $= 1$	Energy OK	sADC_S1	$N_{cluster} > 0$	No μ	No e	Clock	All cuts
250	9620	9798	8885	9962	9907	9850	7307	6119
180	9177	9610	8847	9816	4420	9357	7330	2418
100	9304	9709	9028	9898	8430	9649	10000	7187
50	9263	9684	9050	9869	9409	9619	10000	8048
20	9718	10000	9502	9856	9632	6158	10000	5406
9	9628	9944	9238	9732	9998	5837	10000	5271
180, e	9595	9903	9143	9918	6103	7985	10000	3810

Cut	Code	Meaning of cut
Trigger	Trigger$= 1$	only physics events chosen
"Energy OK"	$\lvert E^0_{event}\rvert < E_{beam} + 100$ GeV	Remove abnormally high energies
sADC_S1	$150 <$ sADC_S1 < 1400	Beam line scintillator cut
$N_{cluster}$	$N_{cluster} > 0$	At least one cluster formed in the event (noise reduction)
No μ	sADC_muTag< 450	removes muons by cutting on muon scintillator signal
No e	$E_{Tile} > 0.01 \cdot E_{beam}$	removes electrons by requiring a signal in Tile
Clock	Clock > 18 ns	Compensate for timing problem (180 and 250 π^- runs only)

Table 7.3: Cuts on data, and the number of events surviving the various cuts. The top table shows the number of events surviving the various cuts. For all runs, 10000 events were reconstructed. The rightmost column gives the number of events passing all the cuts. It should be noted that some cuts are overlapping, and that the Clock cut was only applied to the high-energetic π^- runs, 180 and 250 GeV. The bottom table gives a summary of the cuts used and their meanings, which are elaborated in the text.

these runs[64]. The cut Trigger=1 picks out the "physics" events, which means that events with at least one particle in the beam line were chosen.

The most significant cut for the low-energetic runs and the electron run is the electron removal cut. In Figure 7.20(a), the effect of the muon cut when applied to the 100 GeV positive pion beam is clearly visible, since the muon peak at ≈ 2 GeV almost completely vanishes after that cut. The effects of the electron cut on a positron beam at 180 GeV are shown in Figure 7.20(b), where the positron peak at beam energy is much affected by the cut.

The standard procedure for removing electrons is to look at information from the inner detector. However, for some of the runs used, the inner detector read-out was unstable, making cuts on inner detector variables impossible. Since it is important to treat all runs as equally as possible, the properties of electron showers have been used instead. By requiring that at least 1% of the beam energy is reconstructed in the Tile calorimeter, particles that are fully

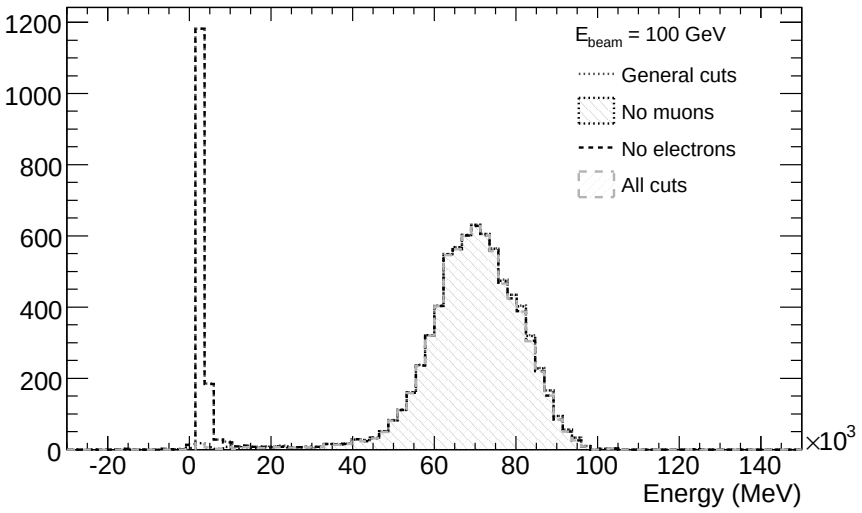

(a) 100 GeV positive pion beam.

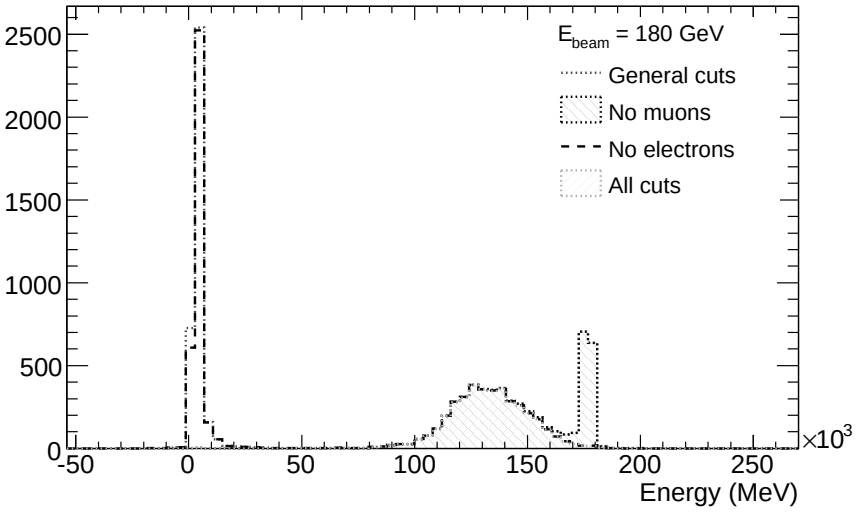

(b) 180 GeV positron beam.

Figure 7.20: Effect of the cuts on the 100 GeV positive pion beam (top) and on a 180 GeV positron beam (bottom). "General cuts" summarises the "energy OK" cut, the $N_{cluster} > 0$ cut, the `Trigger` cut and the `sADC_S1` cut. The effect of the muon and electron cuts is shown. The significance of the muon cut is visible in both runs, since the muon peak at ≈ 2 GeV almost completely vanishes after that cut. The electron cut can be seen as a small decrease of the distribution at the highest energies in the pion run. The positron peak at beam energy is much affected by the electron cut.

contained in LAr are discarded. This action removes the vast majority of the electrons.

However, the electron cut will affect the pions as well, especially at low energies, when not all pions necessarily reach the Tile calorimeter. In Figures 7.21-7.22, linearity and resolution of the simulated pions, with and without the electron cut have been plotted. As shown in these figures, the linear-

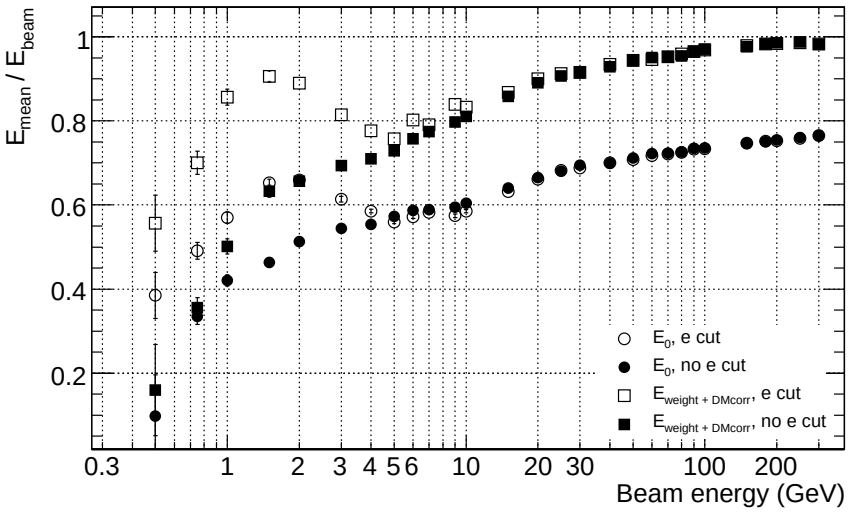

Figure 7.21: Effect of the electron cut on the linearity. Conclusions in text.

ity and the resolution are little affected by the electron cut for beam energies above ≈ 20 GeV. At very low beam energies, some odd effects can be observed: the linearity is much larger than expected, with a peak at 2 GeV. The resolution is improved in an unexpected way for beam energies below ≈ 5 GeV, most likely as a result of the increased linearity. This low-energy effect could be caused by the electron cut selecting events with unusually high energy in Tile, in an energy region where most pions are fully contained in LAr. However, the effects of the electron cut are only interesting for beam energies where we have data runs, which is 9 GeV and higher. The small effects from the electron cut will be considered as systematic uncertainties. Details of the computation of the systematic effects are given in Appendix C.

Whenever data and simulated distributions are compared, the electron cut have been applied to the simulated sample, as well as the $N_{cluster} > 0$ cut. The other cuts cannot be applied to the simulated samples, since the necessary scintillators and clocks were not simulated.

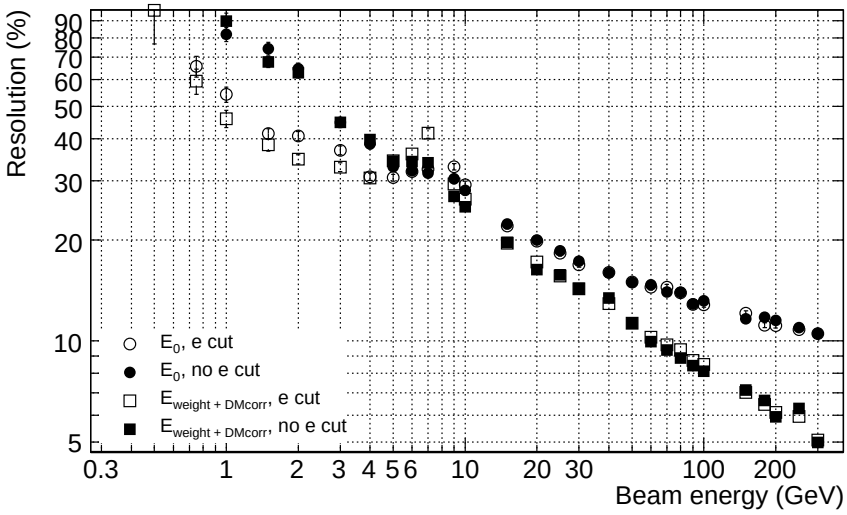

Figure 7.22: Effect of the electron cut on the resolution. Conclusions in text.

7.6.3 Comparison between data and Monte Carlo simulations

Simulated samples are used to compute the weights that we use for the hadronic weighting of the energy. Thus it is of great importance that the simulation correctly reproduces the data, since the results otherwise will contain errors inherited from the simulations.

In this section we take a closer look at the parameters of the weights, namely the cell energy density distributions (Figures 7.23 - 7.26) and the cone energy distributions (Figures 7.28 and 7.27). In addition, the shower development description is studied in Figures 7.29 and 7.30.

In the distributions of the LAr cell energy densities, Figure 7.23, the data distributions have larger negative tails than the corresponding simulated distributions. This is an effect of non-Gaussian tails in the data distributions. If the negative part of the data distributions are fitted with Gaussians, as in Section 7.5.4, the values agree within 10% with those obtained from the simulated distributions, see Table 7.4.

The package `CaloNoiseTool`, available in ATHENA, can be used to extract the estimated noise for each cell. The expected energy density of the noise, as obtained from this package, is also given in Table 7.4. These values are of the same order as the estimations obtained using the energy density.

All positive data beams used contain a large proton contamination of as much as 50%[65]. Proton showers contain fewer neutral pions than a pion shower of the same nominal energy[6], due to conservation of the baryon number, which leads to a lower electromagnetic fraction in proton-induced

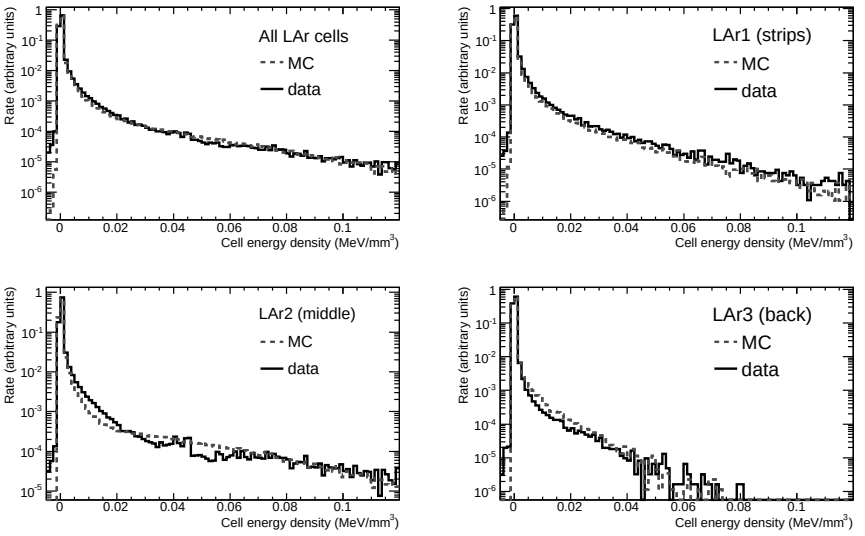

Figure 7.23: Cell energy density distribution in the various LAr sampling layers, for a 250 GeV beam. Comparison between data (negative pions) and a simulated pion sample (MC). The histograms have been normalised to 1.

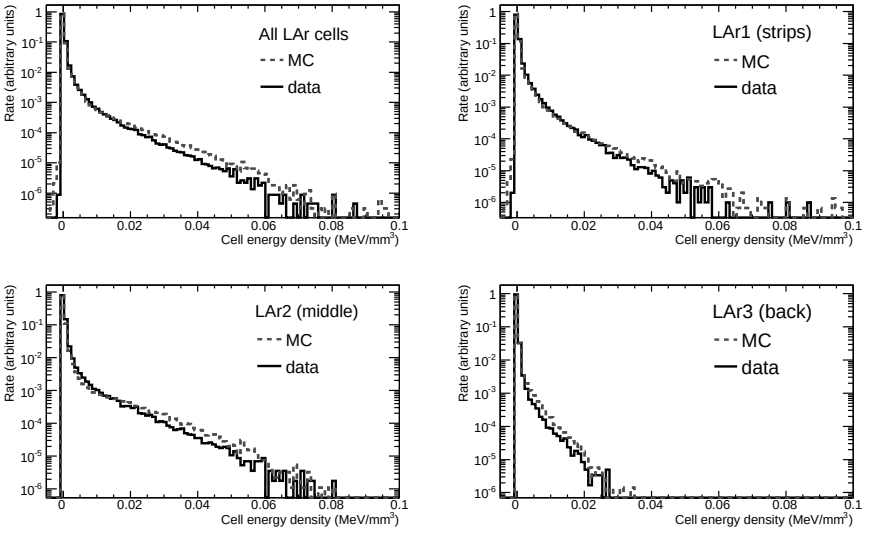

Figure 7.24: Cell energy density distribution in the various LAr sampling layers, for a 100 GeV beam. Comparison between data (positive pions) and a simulated pion sample (MC). The histograms have been normalised to 1.

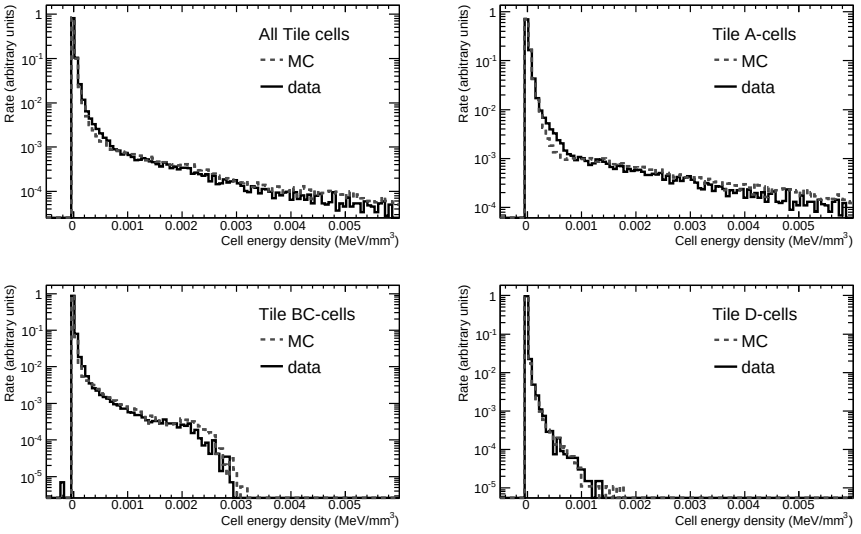

Figure 7.25: Cell energy density distribution in the various Tile sampling layers, for a 250 GeV beam. Comparison between data (negative pions) and a simulated pion sample (MC). The histograms have been normalised to 1.

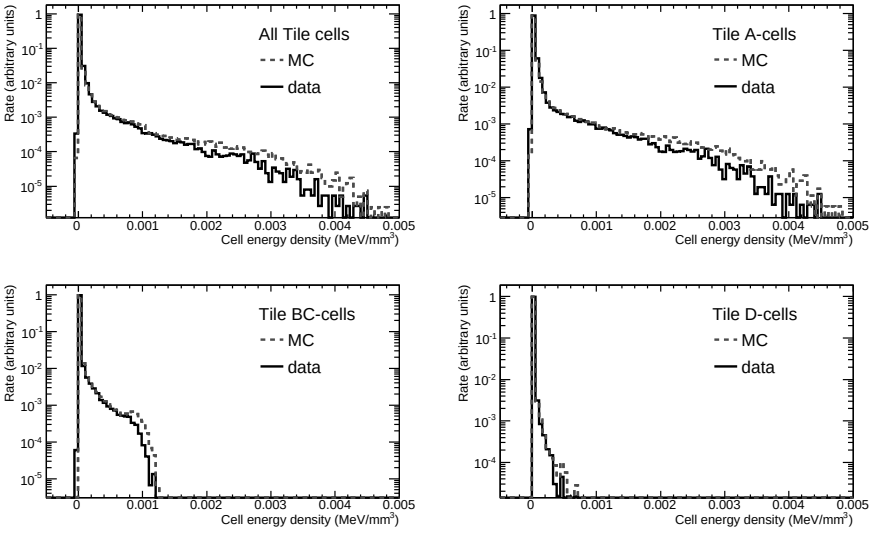

Figure 7.26: Cell energy density distribution in the various Tile sampling layers, for a 100 GeV beam. Comparison between data (positive pions) and a simulated pion sample (MC). The histograms have been normalised to 1.

	Data		*Simulation*
Sampling layer	`CaloNoiseTool` (MeV/mm^3)	$\rho_{E,noise}$ (MeV/mm^3)	$\rho_{E,noise}$ (MeV/mm^3)
LAr1	$(4.57 \pm 0.07) \cdot 10^{-4}$	$(4.034 \pm 0.002) \cdot 10^{-4}$	$(3.950 \pm 0.003) \cdot 10^{-4}$
LAr2	$(1.59 \pm 0.05) \cdot 10^{-4}$	$(1.493 \pm 0.001) \cdot 10^{-4}$	$(1.424 \pm 0.002) \cdot 10^{-4}$
LAr3	$(2.0 \pm 0.2) \cdot 10^{-4}$	$(1.633 \pm 0.001) \cdot 10^{-4}$	$(1.649 \pm 0.002) \cdot 10^{-4}$
Tile A-cells	$(4.0 \pm 0.1) \cdot 10^{-6}$	$(4.611 \pm 0.007) \cdot 10^{-6}$	$(4.162 \pm 0.001) \cdot 10^{-6}$
Tile BC-cells	$(9.8 \pm 1.3) \cdot 10^{-7}$	$(1.143 \pm 0.001) \cdot 10^{-6}$	$(1.048 \pm 0.002) \cdot 10^{-6}$
Tile D-cells	$(5.6 \pm 0.4) \cdot 10^{-7}$	$(6.173 \pm 0.008) \cdot 10^{-7}$	$(5.792 \pm 0.002) \cdot 10^{-6}$

Table 7.4: Energy density noise estimates for data and simulated samples. The values and the uncertainties of $\rho_{E,noise}$ are given by the Gaussian fits to the energy density distributions (compare with Table 7.1). The `CaloNoiseTool` values are the estimated noise energy density, obtained from the package `CaloNoiseTool`.

showers than in pion showers and thus a lower reconstructed energy. The resolution of the energy in the pure proton beams is better, because the event-by-event fluctuations in the production of neutral pions is lower. Proton showers tend to be broader than pion-induced ones, while the latter generally reach deeper into the calorimeter[66], because of the higher total cross section of a proton-nucleus reaction than such a reaction involving a pion[9].

The effect of the proton contamination on the energy level is seen in the distribution of the cone energy of the positive 100 GeV beam (Figure 7.28), where the energy distribution from real data seems shifted towards lower values compared to the simulated energy distribution. In the energy density distributions for the positive beam (Figures 7.24 and 7.26), the proton contamination can be seen as a generally lower level of energy density in data than in the simulation. These effects are not seen in the energy density distributions of the negative 250 GeV beam (Figures 7.23 and 7.25), nor in the distribution of the 250 GeV π^- cone energy distribution in Figure 7.27.

The effects of proton contamination on the linearity are straight-forward: the lower response to the proton energy will lead to a general worsening of the linearity, at least for the electromagnetic scale energy. Since the weights have been developed for pions, and the physics of proton shower development is different than the development of a pion shower, the worsening in linearity might persist after weighting too, due to differences in the visible energy content and the longitudinal spread of the shower. The expected effects of the proton contamination on the resolution are difficult to predict, since the resolution of pure proton energy is better than the pion energy resolution. The energy distribution from the combination of pions and protons is two Gaussian distributions on top of each other, with slightly different mean values. Under such circumstances it is reasonable to expect a worsening in the resolution.

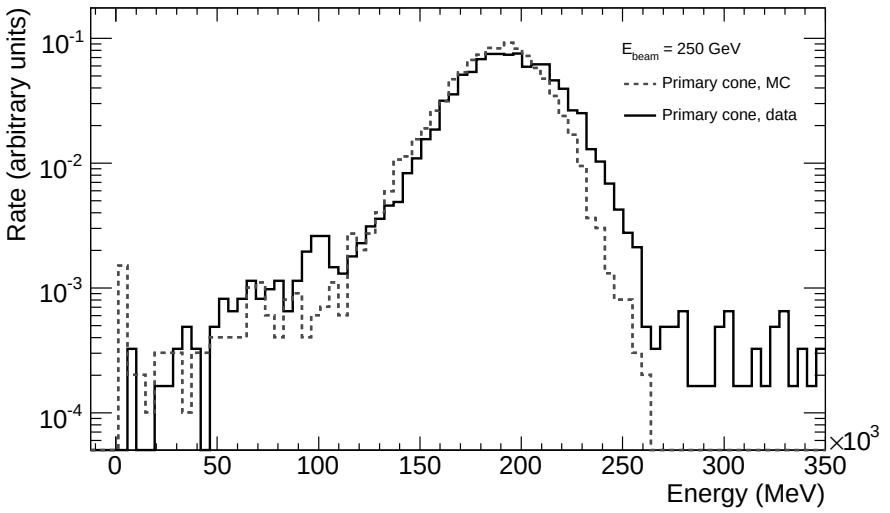

Figure 7.27: Cone energy distribution for a 250 GeV beam. Comparison between data (negative pions) and Monte Carlo simulation (MC).

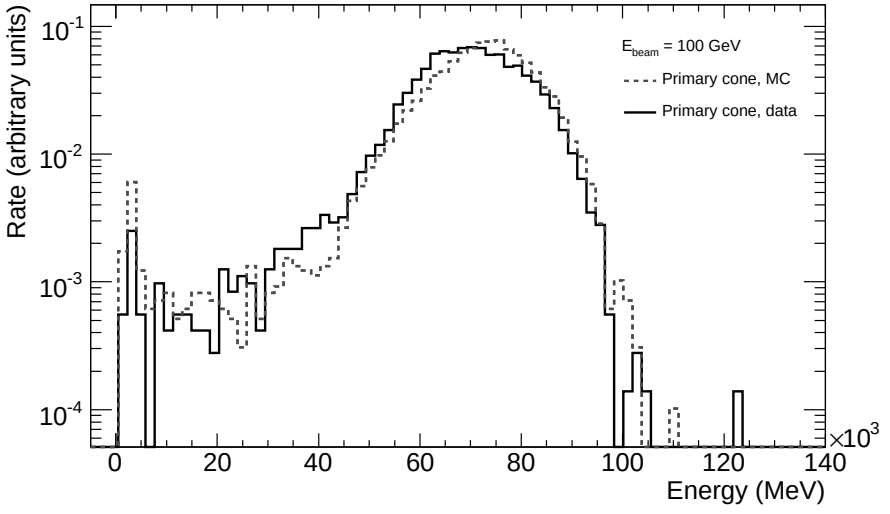

Figure 7.28: Cone energy distribution for a 100 GeV beam. Comparison between data (positive pions) and Monte Carlo simulation (MC). The proton contamination in real data can be seen as a shift towards lower values, compared to the distribution on the simulated energy.

Unfortunately, we have not been able to make a comparison of the resolutions of π^- and π^+/p data beams of the same energy.

When comparing the energy density and the cone energy distributions, the agreement between data and simulations seems adequate. However, the simulation does not correctly describe the shower development in data, but underestimates the energy deposition in Tile and overestimates the deposition in LAr. In Figures 7.29 and 7.30, the energy distribution in LAr and Tile, for simulations and data, is given for the beam energies 100 and 250 GeV. The

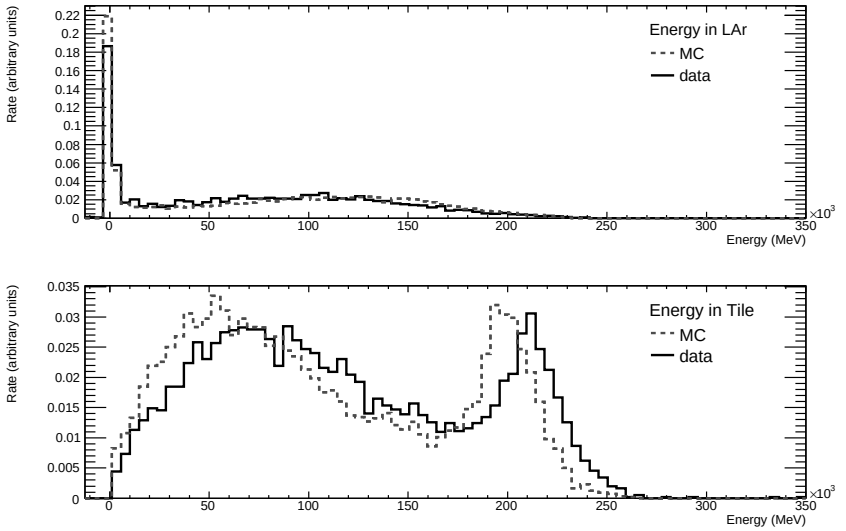

Figure 7.29: The energy distributions in the LAr and Tile calorimeters for 250 GeV beams. Comparison between Monte Carlo simulation (MC) and test beam data of a negative pion beam.

shower development mis-description in the simulation will affect the weights and the energy after weighting to a high degree, which is demonstrated in Section 7.6.5.

7.6.4 Correction for losses in dead material

In ATLAS, some regions are referred to as "dead", since energy lost in these regions is not recorded in any calorimeter system. In this sense, the inner detector is also "dead" from a calorimetry point of view. Another more significant dead region is the cryostat between the LAr and the Tile calorimeters. The energy lost in these dead regions must be accounted for in some way, in order to reconstruct the true energy of a particle. The methods for dead material corrections used in this chapter are, with a few exceptions, based on the schemes described in reference [67].

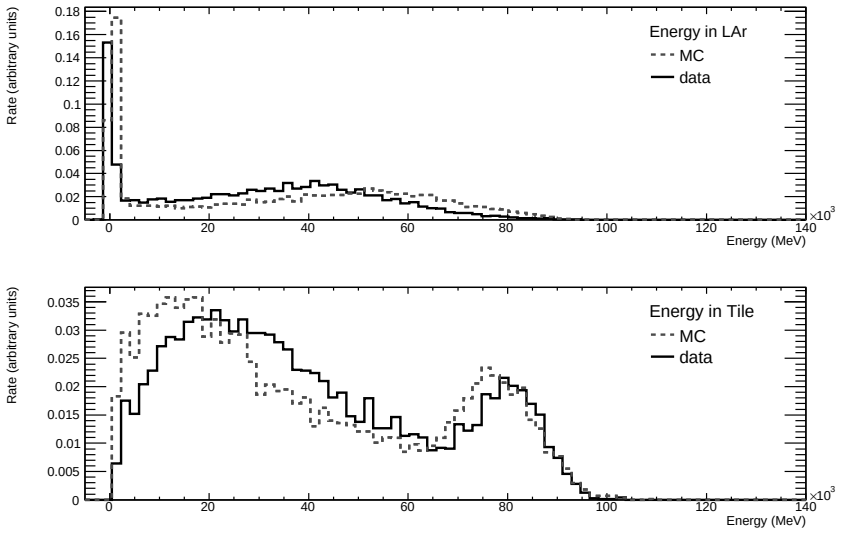

Figure 7.30: The energy distributions in the LAr and Tile calorimeters for 100 GeV beams. Comparison between Monte Carlo simulation (MC) and test beam data of a positive pion beam.

For the barrel region, there are four major dead regions to consider: the upstream region of material before the LAr pre-sampler, the material between the pre-sampler and the first LAr barrel sampling layer, the region between LAr and Tile, and any energy lost due to leakage beyond Tile, to either side of the calorimeters or in any other internal dead regions. The correction is made using information on the energy deposited in the calorimeter layers close to the dead region, or in some cases all of the deposited energy in the calorimeters. The correction constants are determined using the Monte Carlo truth information from the simulated pions. A schematic view of the dead regions is given in Figure 7.31. The sample used to derive the weight is also used to compute the dead material correction constants.

The dead region correction constants are computed by plotting the true energy lost in the dead region of interest as a function of the uncalibrated energy in relevant parts of the calorimeter. A straight line though the origin is then fitted to the distribution. The slope of the fitted line, multiplied with the uncalibrated energy returns the energy in the dead region, if the correlation between the energy lost in the dead region and the energy deposited in the calorimeter layers in question was sufficiently strong. In Figure 7.32, examples of fits to energy lost in dead regions for simuated 100 GeV pions are given.

The upstream correction also calibrates the pre-sampler energy, which cannot be calibrated using the hadronic weighting scheme described in this chapter, as described in Section 7.5.5. The correction is given by the slope of a line

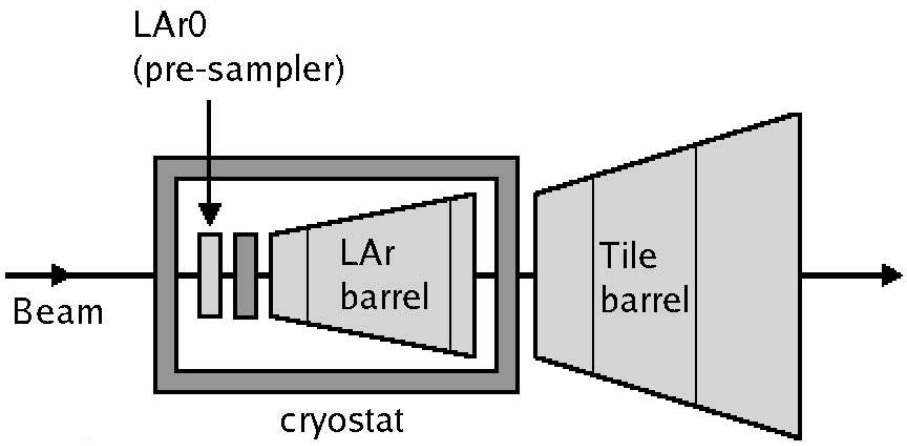

Figure 7.31: Schematic view of the dead regions in the test beam barrel set-up. The dead regions are drawn in dark grey, the active regions in a brighter shade. The upstream region consists of the cryostat before the pre-sampler. The dead material between the pre-sampler and the first layer of the LAr barrel is indicated as a bar. The largest energy losses occur in the part of the cryostat that is placed between the LAr barrel and the first Tile layer. The fourth category of dead material losses is leakages beyond Tile and laterally (not indicated in the figure).

fitted to the sum of the energy lost in the cryostat before the LAr pre-sampler ($E^{truth}_{upstream}$) and the true energy deposited in the pre-sampler, as given from the simulation ($E^{truth}_{presamp}$), as a function of the data-like uncalibrated reconstructed energy in the pre-sampler ($E^{0}_{presamp}$). The constant obtained, $C_{upstream}$, is used to estimate the energy lost before the pre-sampler ($E^{est.}_{upstream}$), and to calibrate the pre-sampler energy ($E^{est.}_{presamp}$), as

$$E^{est.}_{upstream} + E^{est.}_{presamp} = C_{upstream} \cdot E^{0}_{presamp} \tag{7.5}$$

The correction constant for the region between the pre-sampler and the first layer of the LAr barrel is given by the linear fit to the true energy deposited in the cryostat before the LAr barrel ($E^{truth}_{presamp/LAr}$) as a function of the geometric mean of the data-like energy in the pre-sampler ($E^{0}_{presamp}$) and the first sampling layer of the LAr barrel, LAr1 (E^{0}_{LAr1}). The estimated energy lost in the cryostat before LAr barrel, $E^{est.}_{presamp/LAr}$, is given as

$$E^{est.}_{presamp/LAr} = C_{presamp/LAr} \cdot \sqrt{E^{0}_{presamp} \cdot E^{0}_{LAr1}} \tag{7.6}$$

where $C_{presamp/LAr}$ is the slope of the fitted line.

The largest energy depositions in dead regions occur in the cryostat between LAr and Tile. The correction constant for this region, $C_{LAr/Tile}$, is obtained in

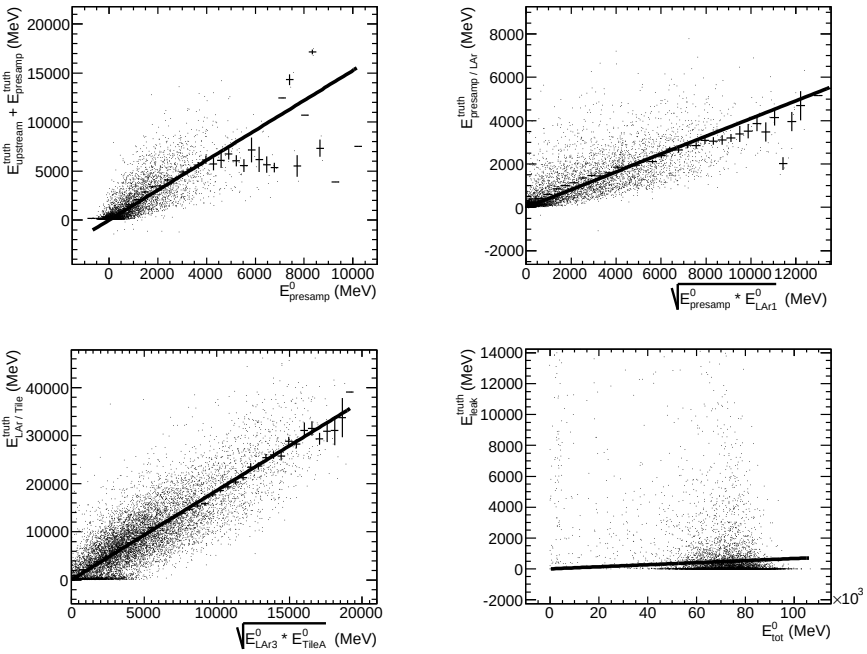

Figure 7.32: Example of energy depositions in dead region as a function of deposited energy in calorimeter layers. The labels and the choice of fits are described in the text.

the same fashion as for the region between the pre-sampler and the LAr barrel, and the energy used is the energy deposited in the last LAr sampling layer, LAr3 (E^0_{LAr3}) and the first Tile sampling layer, TileA (E^0_{TileA}). The estimated energy lost in the cryostat between LAr and Tile, $E^{est.}_{LAr/Tile}$, is thus given as

$$E^{est.}_{LAr/Tile} = C_{LAr/Tile} \cdot \sqrt{E^0_{LAr3} \cdot E^0_{TileA}} \tag{7.7}$$

For leakage beyond Tile, no correlation between energy deposited in any calorimeter layer can be seen. However, on average the leakage is dependent on the beam energy. As a first approximation, the estimated leakage, $E^{est.}_{leak}$, can be computed as a constant, C_{leak}, multiplied with the total reconstructed unweighted energy of all calorimeter layers (E^0_{tot}),

$$E^{est.}_{leak} = C_{leak} \cdot E^0_{tot} \tag{7.8}$$

The corrections for dead material are made on event basis and, except in the case of the pre-sampler energy, independent of the hadronic calibration. The total energy of an event after weighting and correction for losses in dead material, is computed as

$$\begin{aligned} E_{DMcorr} &= E_{weighted} + (E^{est.}_{upstream} + E^{est.}_{presamp}) + \\ &\quad + E^{est.}_{presamp/LAr} + E^{est.}_{LAr/Tile} E^{est.}_{leak} - E^0_{presamp} \end{aligned} \tag{7.9}$$

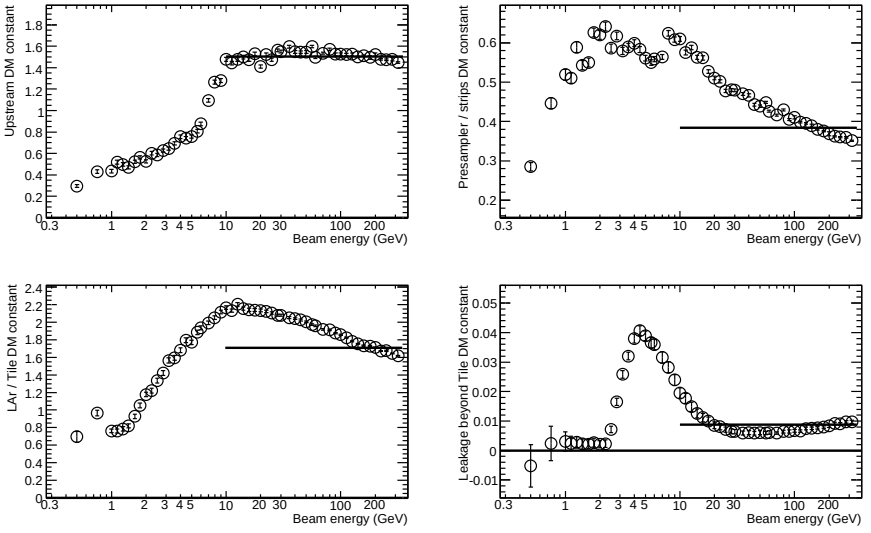

Figure 7.33: Dead material correction constants as a function of beam energy. The top left plot shows the correction constants for the upstream energy losses, before the LAr pre-sampler. The top right plot show the correction constants for the region between the pre-sampler and the LAr barrel. The bottom left plot show the dead material correction constants for the region between LAr and Tile, and the bottom right plot show the correction constants for leakage. The horizontal lines indicate the constant value when computed for all beam energies above and including 10 GeV. The values are given in Table 7.5. Conclusions on the behaviour of the correction constants as a function of beam energy are given in the text.

The reconstructed unweighted pre-sampler energy is subtracted, in order not to count the pre-sampler energy twice.

Dead material constants for the various regions as a function of beam energy are given in Figure 7.33. As shown in this figure, the correction constants for dead material are not constant with respect to the beam energies. All corrections behave strangely for beam energies below ≈ 10 GeV, reflecting the fact that correction for dead material energy losses is hard at low energies. The peak in the distribution of correction constants for the leakage beyond Tile (bottom right plot in Figure 7.33) seems unexpected at first, but when considering that this constant must be multiplied with the total uncalibrated energy of the event to retrieve the leakage, the peak translates into an approximately constant leakage of about 100 MeV for beam energies between 4 and 30 GeV. For high beam energies, the leakage correction factors are roughly linear, as are the upstream corrections. The corrections obtained when using all beam energies above and including 10 GeV are indicated with horizontal lines in the plots.

For the corrections of losses in the regions before and after LAr barrel, the values do not flatten at energies above 10 GeV, but rather show a decreasing linear behaviour. This is most likely a manifestation of the increasing energy fraction of the true pion energy recorded by the calorimeters. The dead material compensation energy is in some sense calibrated on the hadronic scale, while the energies $\sqrt{E^0_{presamp} \cdot E^0_{LAr1}}$ and $\sqrt{E^0_{LAr3} \cdot E^0_{TileA}}$ are not. When multiplying the correction constants with the unweighted energy, the correction constants must decrease to follow the increase in visible energy in the calorimeters.

Constant	value (dimensionless)
$C_{upstream}$	1.5023 ± 0.0022
$C_{presamp/LAr}$	0.38399 ± 0.00049
$C_{LAr/Tile}$	1.7014 ± 0.0011
C_{leak}	$(8.729 \pm 0.085) \cdot 10^{-3}$

Table 7.5: Values of the dead material correction constants, for the four different regions considered.

The dead material losses correction constants not being constant over the beam energies will affect the value of the corrected energy. Ideally, a correction based on the beam energy would be used. In test beam data, the beam energy is well-known. However, this is not the case for pions or jets in ATLAS during real data taking, which is the reason for using one correction constant per dead region, rather than making the recourse to beam energy dependent corrections. In Figure 7.34, the linearity of the weighted energy with dead material correction is shown, both with and without the beam energy dependence in the correction constants. In Figure 7.35, the difference of the linearities in dead material corrected energy is shown, and in Figure 7.36, the difference in resolution is given.

As demonstrated in Figure 7.35, the beam energy independent dead material corrections will give a systematically too low reconstructed weighted energy for most of the beam energies considered. The worst underestimations of the energy will occur for beam energies around 10 GeV, where the shift is as much as 4%. The resolution, on the other hand, is not affected in a significant way when the dead material corrections constants are beam energy independent, as shown in Figure 7.36.

For the remainder of this chapter, whenever an energy is said to have been corrected for dead material losses, the correction of Equation 7.10 has been applied, using one correction constant for each dead region, same constant for all beam energies. Unless something else is stated, the constants have been obtained from all beam energies above and including 10 GeV, as described in this section. The values of the corrections are given in Table 7.5. The devia-

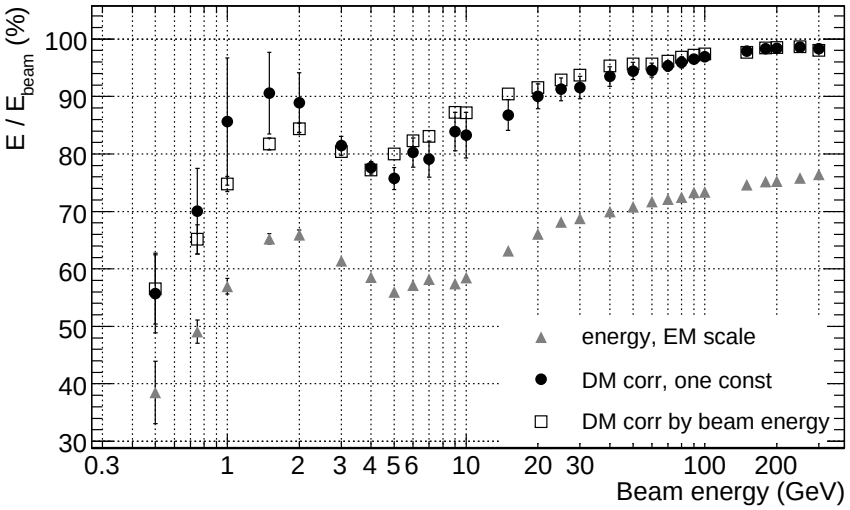

Figure 7.34: E_{mean}/E_{beam}, where E_{mean} comes from a Gaussian fit to the energy distribution, as a function of the beam energy. The unweighted energy on the electromagnetic scale is marked by grey triangles. The black circles mark the weighted and dead material corrected energy using one constant per region, same for all beam energies. The squares mark weighted and dead material corrected energy using beam energy dependent DM correction constants. The error bars at the black circles are computed from the errors of the Gaussian fit and the distance to the beam energy corrected points (systematic uncertainties). The error bars on the other markers are from Gaussian fits only.

tions from the values obtained using the beam energy dependent corrections are treated as systematic uncertainties. The values are given in Appendix C.

The dead material correction constants computed here are valid only for pseudorapidities close to $\eta = 0.45$, since the dead regions are different at other η, and only in the test beam set-up, because the cryostat in the full ATLAS set-up is slightly different. Moreover, these constants are only valid for pions, since the shower development of electrons in the calorimeters is different from the shower development of pions. For instance, the energy leakage of electrons is smaller and electrons seldom reach the Tile calorimeter.

7.6.5 Linearity and resolution of pions from real data and simulations

In Section 7.5.6, the weighted energy was compared to the Monte Carlo truth energy obtained from the simulation. For the test beam data, the only "truth" we have is the beam energy. Moreover, after correction for energy losses in dead material, we expect the energy distribution to be Gaussian. Hence we

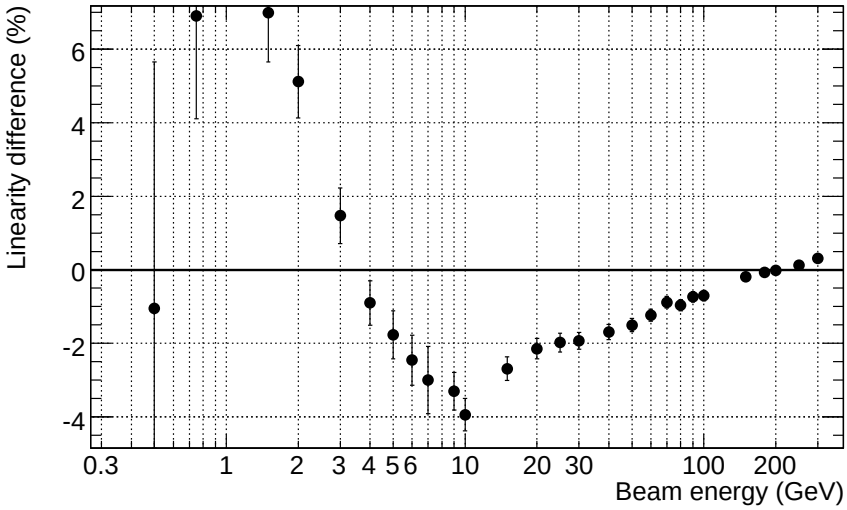

Figure 7.35: Difference of linearities, linearity from one correction constant per region minus linearity using beam energy dependent corrections. The uncertainties indicated are the errors from the Gaussian fit of the linearity from the dead material correction with one constant per dead region.

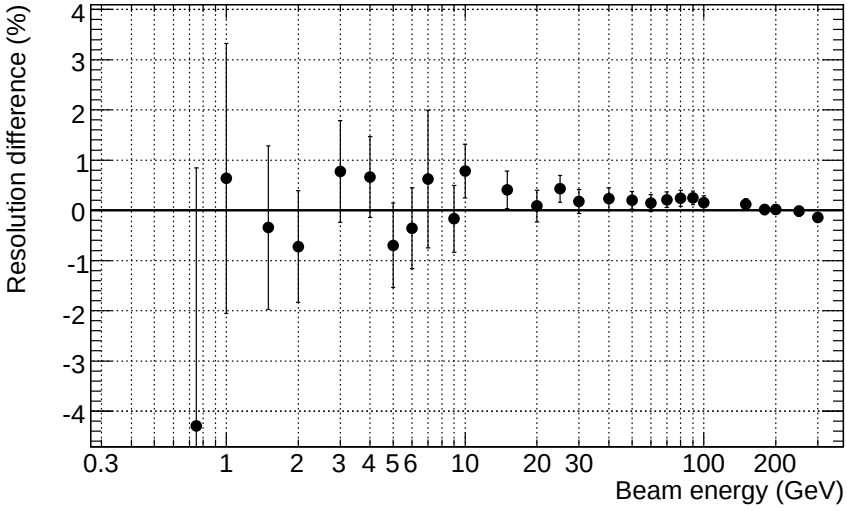

Figure 7.36: Difference of resolutions, resolution from one correction constant per region minus resolution using beam energy dependent corrections. The error bars indicate the errors of the resolution from the dead material correction with one constant per dead region.

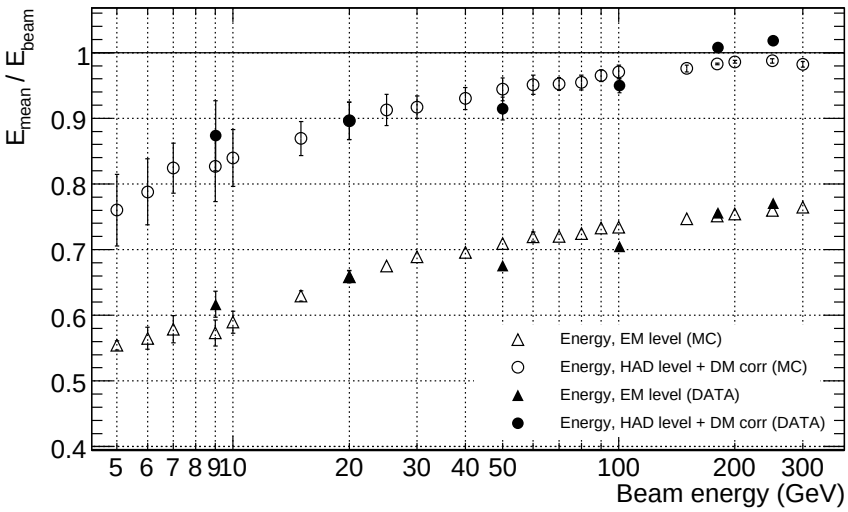

Figure 7.37: Linearity, E_{mean}/E_{beam}, of weighted and unweighted energy (Monte Carlo simulation, MC, and data) as a function of beam energy. Comparison between the unweighted energy on the electromagnetic scale (triangles), and weighted and dead material corrected energy (circles). Data points are marked with filled symbols, simulation with open symbols. It should be noted that data runs of beam energy 250, 180 and 9 GeV are negative runs, while beam energies 100, 50 and 20 GeV are positive runs with proton contamination.

can make a sensible Gaussian fit to the distribution, use the ratio E_{mean}/E_{beam} for the linearity, and compute the resolution as σ/E_{mean}. In Figure 7.37 a comparison of the data and Monte Carlo linearity of weighted and unweighted energy is shown.

The most striking feature of the linearity in Figure 7.37, is that even after weighting it is a bit short of unity for most of the beam energies, especially the lower ones. This is partly an effect of energy falling outside the topo clusters[54], but in the test beam case, lateral leakage in the ϕ direction can also occur, which does not happen in the full ATLAS set-up. Corrections for the out-of-cluster energy should be done to retrieve the full energy of an event. This is not done for singe pions within this chapter, but only for jets in the full ATLAS environment, as described in Section 7.8. Since the treatment of the energy lost due to clustering differs between the test beam and the full ATLAS set-ups, and we only strive to make a study of the hadronic weighting scheme when applied to test beam data, which can be done after weighting and subsequent corrections for losses in dead material, the corrections for energy depositions outside the clusters are omitted.

The overestimation of data energy in the highest energy points can be explained by the shower development mis-description in the simulation, which

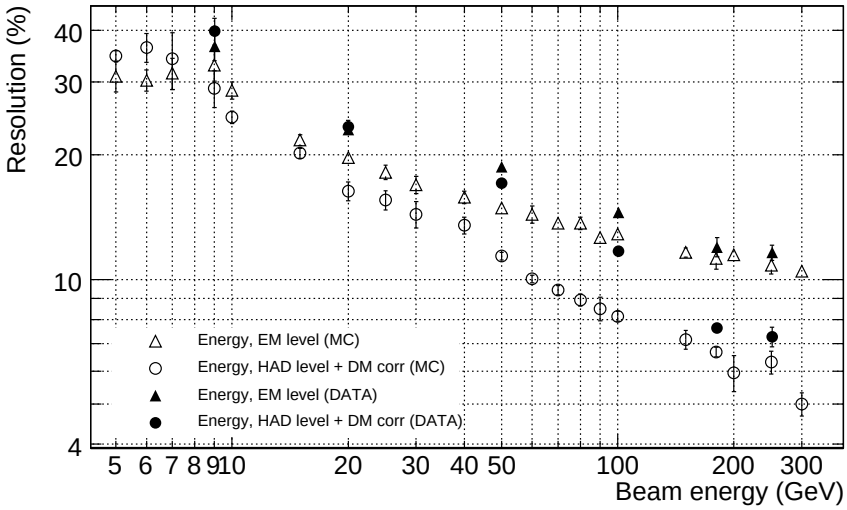

Figure 7.38: Resolution of weighted energy (simulation and data) as a function of beam energy. Comparison between the unweighted energy on the electromagnetic scale (triangles), and weighted and dead material corrected energy (circles). Data points are marked with filled symbols, Monte Carlo simulation with open symbols. It should be noted that data runs of beam energy 250, 180 and 9 GeV are negative runs, while beam energies 100, 50 and 20 GeV are positive runs with proton contamination.

was shown in Section 7.6.3. The imbalance between the energy depositions in LAr and Tile will lead to an imbalance in the weights. Since the simulation underestimates the energy depositions in Tile, the Tile weights will be higher than they should be. In the same way, the LAr weights will be lower. Since the LAr weights are closer to unity than the Tile ones, the raising effect of the Tile weights can be expected to dominate. When the weights are applied to data, the overestimation observed for the negative pion beams is the result.

When the above mentioned effects are accounted for, the data and simulation linearities in Figure 7.37 are in acceptable agreement.

In Figure 7.38, the resolution of the weighted and unweighted energy is given as a function of the beam energy, and in Figure 7.39, the difference of the resolution is shown.

For the resolution, there are quite large differences between data and simulation. For all beam energies, the resolution of data energy is worse than the resolution of the simulated energy signal, which most likely reflects the generally more difficult conditions in real data taking, such as noise unaccounted for and scattering in the beam line. Since the general worsening in resolution in data compared to the simulation is present in the electromagnetic scale energy, this is not an effect of the weighting scheme. For comparison, it is in-

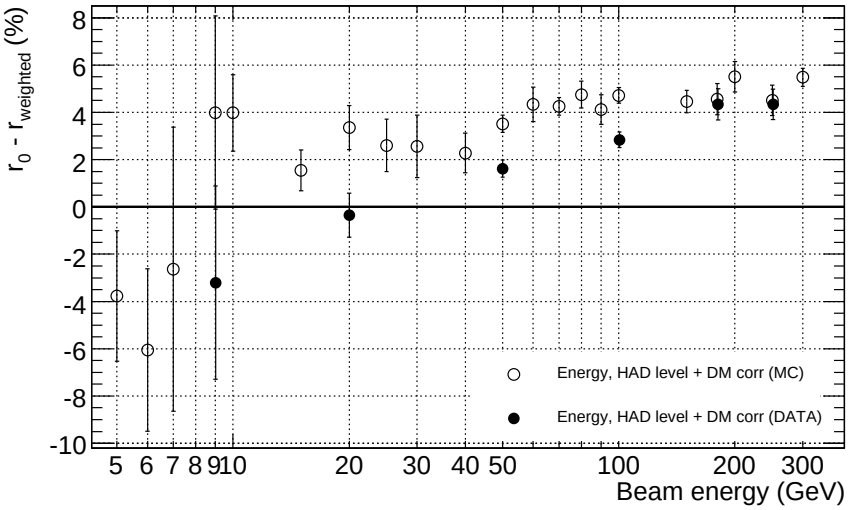

Figure 7.39: Difference of resolutions, $r_0 - r_{weighted+dead\ material\ corrected}$ as a function of beam energy. A positive value in this plot means that the weighting and dead material correction procedure improves the resolution. Comparison between Monte Carlo simulation (open circles) and data (filled circles). It should be noted that data runs of beam energy 250, 180 and 9 GeV are negative runs, while beam energies 100, 50 and 20 GeV are positive runs with proton contamination.

teresting to compute the difference between the resolution of the unweighted energy and the resolution after weighting, which is shown in Figure 7.39. Even though the resolution of data energy is much worse than for the simulated energy signal, the weighting and dead material correction improve the resolution for energies above 20 GeV. For the simulated energy signal, the resolution improvement is achieved for beam energies above 8 GeV.

In Figure 7.40 the resolution is plotted as a function of $1/\sqrt{E_{beam}}$, and the simulated energy resolution has been fitted with the function $r = a/\sqrt{E_{beam}} \oplus b$. The values of the parameters are given in Table 7.6.

Unweighted energy			Weighted + DM corr energy		
$a(\% \cdot \text{GeV}^{1/2})$	$b(\%)$	χ^2/NDF	$a(\% \cdot \text{GeV}^{1/2})$	$b(\%)$	χ^2/NDF
78.4 ± 1.4	9.80 ± 0.16	$15.00/17$	76.2 ± 1.1	3.12 ± 0.32	$15.59/17$

Table 7.6: Parameters of fit to the resolution of the simulated energy signal, $r = a/\sqrt{E_{beam}} \oplus b$, as drawn in Figure 7.40.

No fit is made to the data energy resolution, because of the possible disturbances of the resolution as a result of the proton contamination in the positive runs.

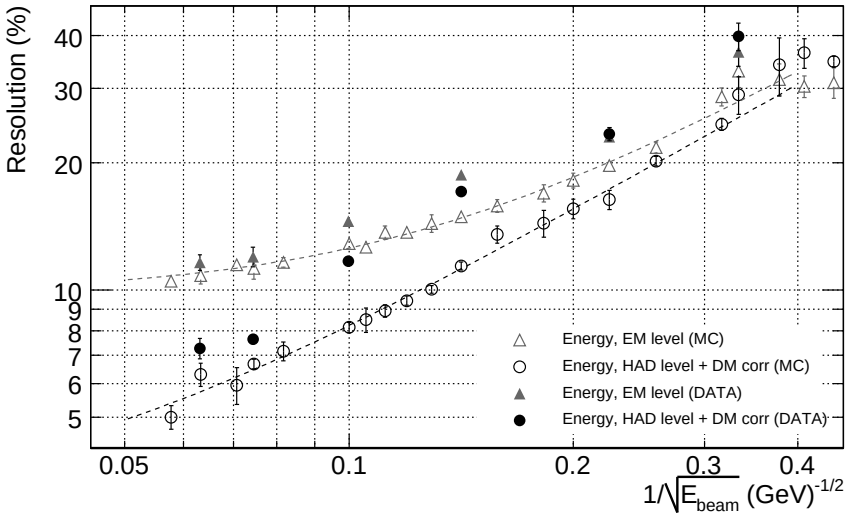

Figure 7.40: Resolutions of weighted and unweighted energy (Monte Carlo simulation and data) as a function of $1/\sqrt{E_{beam}}$, with fits to the function $r = a/\sqrt{E_{beam}} \oplus b$. The values of the parameters are given in Table 7.6. It should be noted that data runs of beam energy 250, 180 and 9 GeV are negative runs, while beam energies 100, 50 and 20 GeV are positive runs, with proton contamination.

7.7 Stability checks and comparisons with other methods

In the previous sections of this chapter, the weighting scheme has been described and the performance of the weighting when applied to simulations and real data from the combined test beam has been demonstrated. In this section, we show the performance of the weighting scheme under slightly different conditions, such as various changes in the global energy scale.

7.7.1 Energy of a single cluster as the global energy

The default local calibration method for jets currently in use in the ATHENA framework does not use the energy of a cone of topo clusters as the global energy scale, but rather the energy of a single topo cluster (the "cluster" method)[54]. For the understanding of the method and the underlying mechanisms of local hadronic calibration, it is important to investigate both these schemes, to see if they perform differently.

In this section, the performance of the cluster method when applied to simulations and data is compared to the results from our standard approach (the "cone" method), as presented in Section 7.6.5.

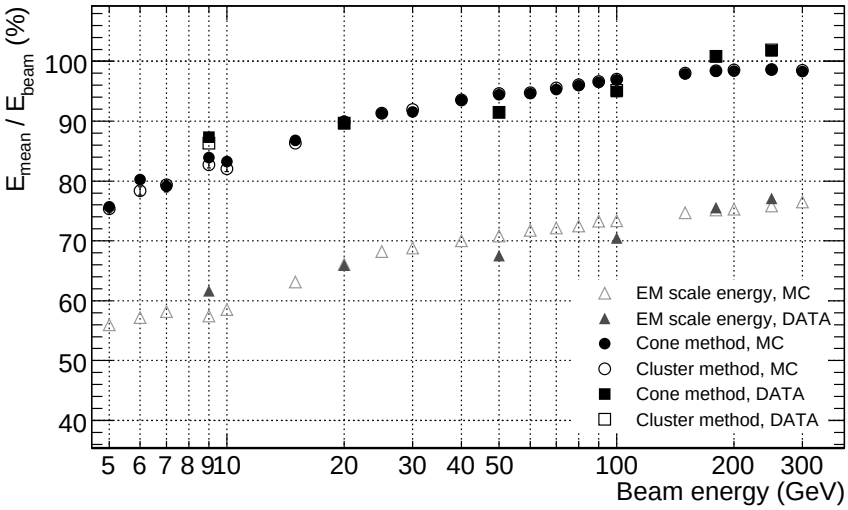

Figure 7.41: Linearity of weighted and dead material corrected energy (Monte Carlo and data) as a function of beam energy. Comparison between our standard approach (the cone method) and the cluster method, as described in the text. The uncertainties given are the statistical uncertainties from the Gaussian fits.

The weighting factors for the cluster method is derived in the same way as the cone method weights (see Section 7.5), with the same weight restrictions. The only difference is that when the cone method only uses the most energetic cone of each event for the weight computation, the cluster method uses all topo clusters of each event to fill the weight tables. The cluster method weights are parametrised with the cell energy density and the topo cluster energy, and one weight table for each sampling layer is made. When applying the weights, only cells with an absolute energy density larger than the estimated noise level are weighted, as described in Section 7.5.4.

In Figure 7.41, the linearity of the energy after weighting and correction for dead material losses is shown, for both methods. The linearity is computed as the mean of a Gaussian fitted to the energy distribution divide by the beam energy, E_{mean}/E_{beam}, and plotted as a function of the beam energy. In Figure 7.42, the difference between the resolution of the unweighted energy and the energy after weighting and dead material correction is shown. The absolute values of the resolution of the energy after weighting with the cone method is shown in Figure 7.38 in Section 7.6.5.

The performances of the cone and cluster methods are very similar, as shown in Figures 7.41-7.42, both when applied to data and Monte Carlo simulations. A very small systematic shift towards slightly higher linearity for the

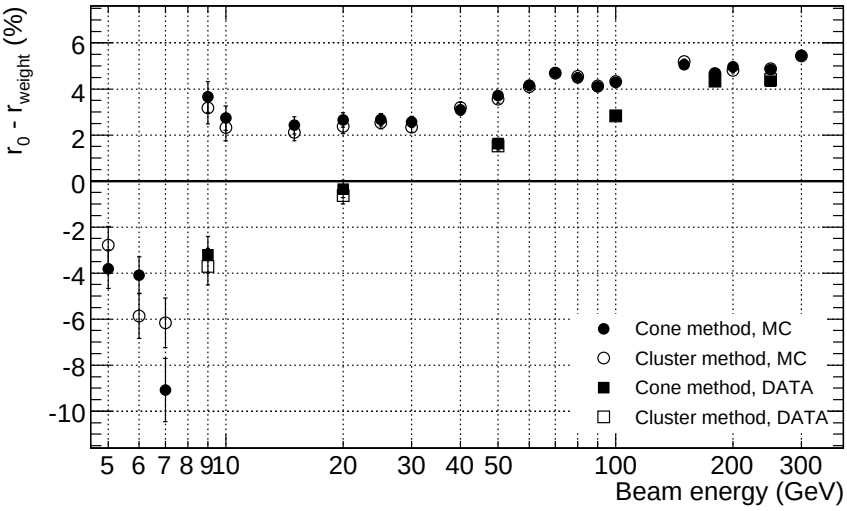

Figure 7.42: Difference between the resolution of the unweighted energy on the electromagnetic scale, r_0, and the weighted and dead material corrected energy r_{weight} as a function of beam energy. Comparison between our standard approach (the cone method) and the cluster method, as described in the text. The uncertainties given are the statistical uncertainties from the Gaussian fits.

cone method in the beam energy region between 5 and 20 GeV might be seen, but this shift is within the statistical errors.

The similarity between the methods indicate that weighting procedures like these are stable and not sensitive to minor changes in the global energy scale or cluster size. In the rest of this section, the stability of the method is shown in other ways.

7.7.2 Distortion of the cone energy

The test-beam environment is very "clean" compared to what we can expect from data taking in ATLAS. In the high-energy proton-proton collisions, we will face problems with pile-up noise, underlying event and low-energy debris from the collisions in the detector. In the previous section, we showed that the weighting scheme works well when the global energy scale is the energy of a single cluster. However, for the cluster method, the weights were derived specially, with the intention of using them in combination with the cluster energy as the global energy. If the underlying event distorts the cone energy by introducing additional energy preferentially in the inner calorimeter cells, then the weighting of the outer cells might be affected.

In order to make a very simple check of the performance under slightly more complicated conditions, we have deliberately distorted the cone when

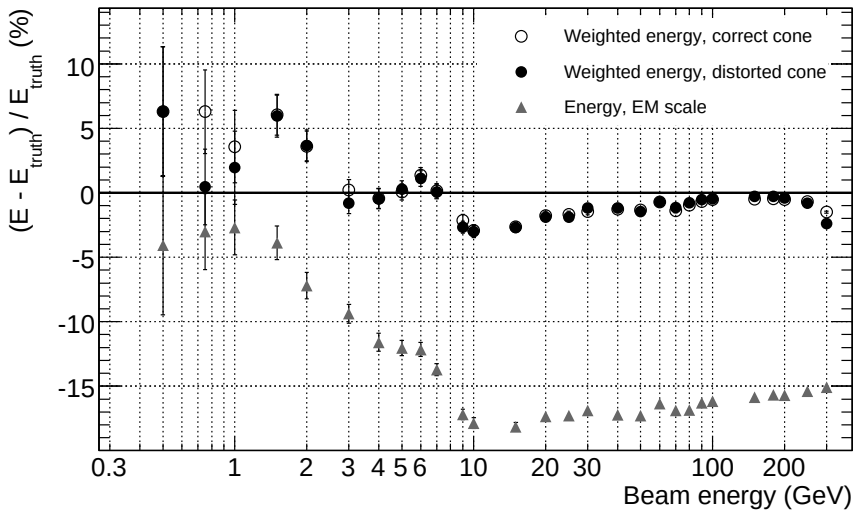

Figure 7.43: Linearity of weighted energy (simulation) using a deliberately distorted cone.

choosing the weights. The weight tables used are the same as before, but when picking the weights, we use the weights belonging to a cone of 10% higher energy. This way, a first-order test assessing whether the underlying event distortion to the cone would disturb the outer cells can be made.

In Figure 7.43, mean values of Gaussians fitted to the distribution $(E - E_{truth})/E_{truth}$ for the weighted energy is shown, both when using the correct cone energy, and in comparison to the distorted cone energy. As before, E is the weighted or unweighted energy and E_{truth} is the truly deposited energy as given from the Monte Carlo simulation. In Figure 7.44, the difference between the resolution of the unweighted energy and the weighted energy is plotted as a function of the beam energy. The resolution is estimated as $\sigma/mean$ of a Gaussian fitted to the distribution E/E_{truth}.

As shown in Figures 7.43-7.44, the cone method is stable against small changes in the cone energy scale. The only point where the cone distortion has a significant effect is for beam energy 300 GeV, where the linearity is worsened after the cone distortion. This is most likely a weight table border effect, see Section 7.7.4.

7.7.3 Variation of the cone size

In all previous applications of the cone-based weighting in this chapter, the cone opening angle has been 11°, which is the cone opening angle used when this method was applied in the H1 experiment[51]. Changes of the cone open-

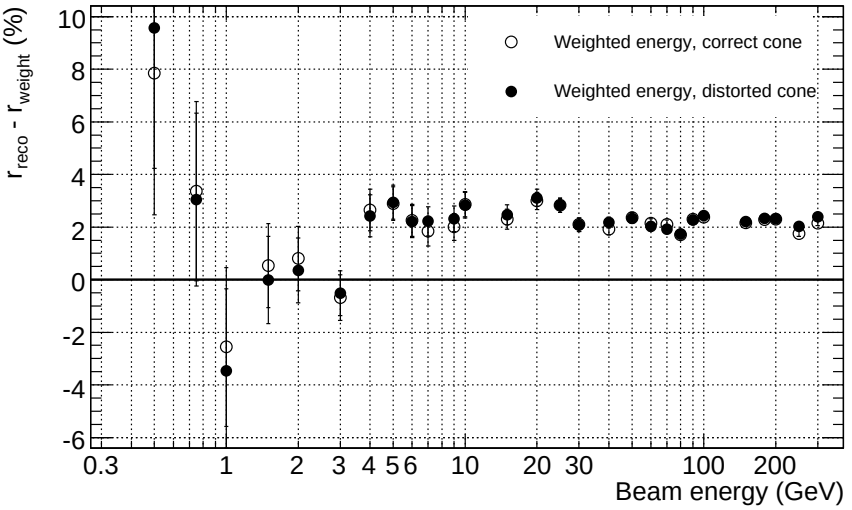

Figure 7.44: Difference of resolutions of weighted and unweighted energy (Monte Carlo) using a deliberately distorted cone.

ing angle might affect the performance of the weighting, and should be studied.

In order to study the properties of the weighted energy when the cone opening angle is changed, a set of new weight tables were produced, using the energy from cones with the opening angles 2, 8, 14, 20 and 26° as the global energy. These weight tables were applied to simulated energy signals, similar to the procedure described in Section 7.5. From a Gaussian fitted to the weighted and dead material corrected energy distribution, the linearity can be computed as E_{mean}/E_{beam} and the resolution as σ/E_{mean}. In Figure 7.45, the difference between the linearity obtained for the normal weighting procedure (opening angle 11°) and the linearity after applying weights from other cone sizes are shown. In Figure 7.46, the differences in resolution is shown. These plots should be compared with Figures 7.37-7.38 in Section 7.6.5, where the absolute values of the linearity and the resolution is shown.

The changes in linearity when varying the cone size are very small, as shown in Figure 7.45, but a clear pattern can be seen in the grouping of the linearity. A smaller cone opening angle (2 or 8°) leads to a lower E_{mean}/E_{beam} ratio than in the 11° case, whereas a larger opening angle (14, 20 or 26°) leads to a larger E_{mean}/E_{beam} ratio. The shifts are within the statistical errors for beam energies lower than about 100 GeV, and for the higher beam energies the effect is less than 0.9%. The resolution is not affected by the cone size changes in any systematic way, as shown in Figure 7.46.

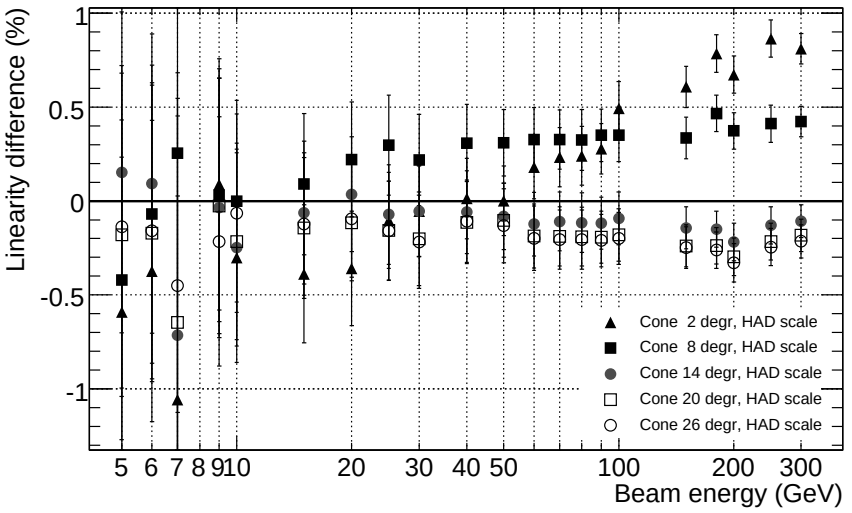

Figure 7.45: Difference between E_{mean}/E_{beam} of the weighted energy when using weight tables for a cone with opening angle 11° and other opening angles. The uncertainties indicated come from the statistical uncertainties of the Gaussian fits.

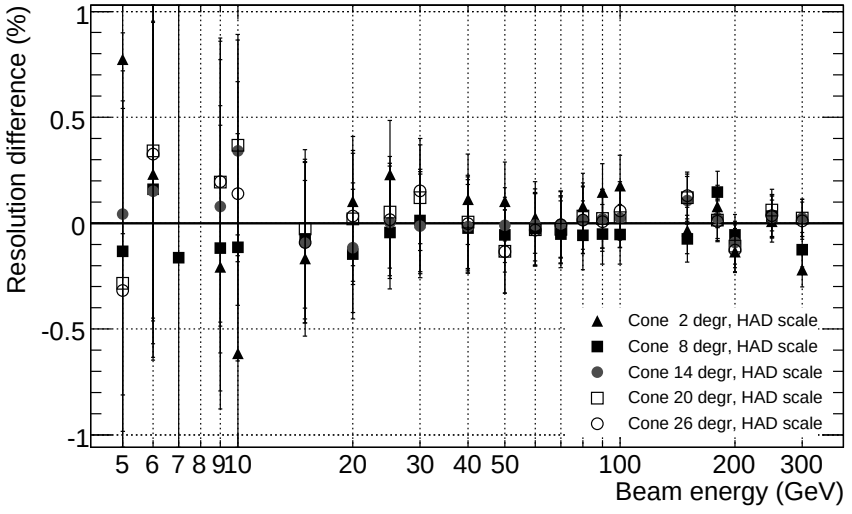

Figure 7.46: Difference between σ/E_{mean} of the weighted energy when using weight tables for a cone with opening angle 11° and other opening angles. The uncertainties indicated come from the statistical uncertainties of the Gaussian fits.

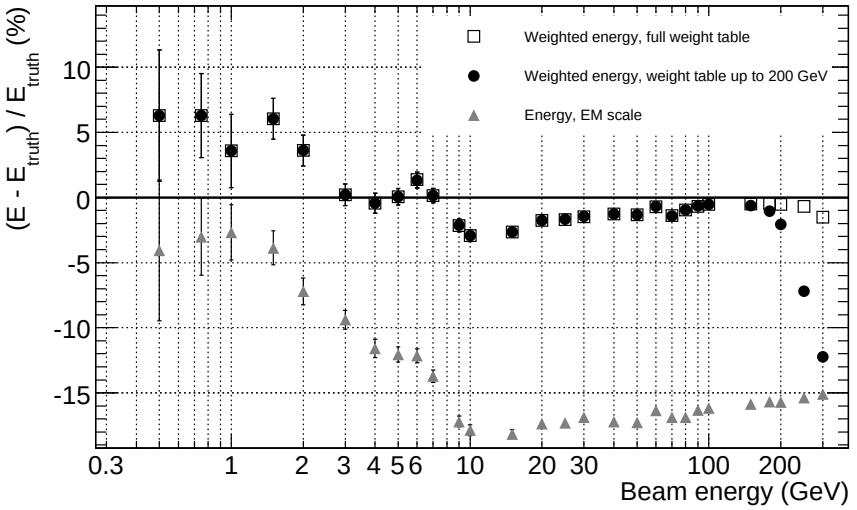

Figure 7.47: Linearity of weighted simulated energy using a shortened weight table (where the weights have been computed using beam energies up to 200 GeV only), and the linearity of the energy which has been weighted with the default weight tables (beam energies up to 316 GeV).

7.7.4 Discussion on the validity of the weights

In Section 7.5.6, an unexpected drop in the linearity at the highest beam energies investigated was observed. A similar but more pronounced effect was also seen when the cone energy was deliberately distorted in Section 7.7.2. The drop in linearity is an effect of some of the cone energies being close to the border of the weight table, which can be demonstrated with a shortened weight table, where only simulated samples of beam energies up to 200 GeV have been used to compute the weights. In Figure 7.47, the mean value of the distribution $(E - E_{truth})/E_{truth}$ is plotted as a function of the beam energy, where E is either the energy after weighting with our usual weight tables, or with the weight tables derived for beam energies up to 200 GeV only.

The effect on the linearity when using the shortened weight tables, as shown in Figure 7.47, clearly demonstrates the border effect: when applying weights to cells from an event with a beam energy close to the maximal beam energy used to compute the weights, the linearity drops, and this drop does not only affect the largest beam energy used for making the weights, but beams at lower energies too. In the example shown here, with weights computed from beam energies up to 200 GeV, the unexpected drop in linearity begins at beam energies around 150 GeV.

From this demonstration, a very important feature of the weighting can be seen: when applying the weights, it is important to make sure that a variety of

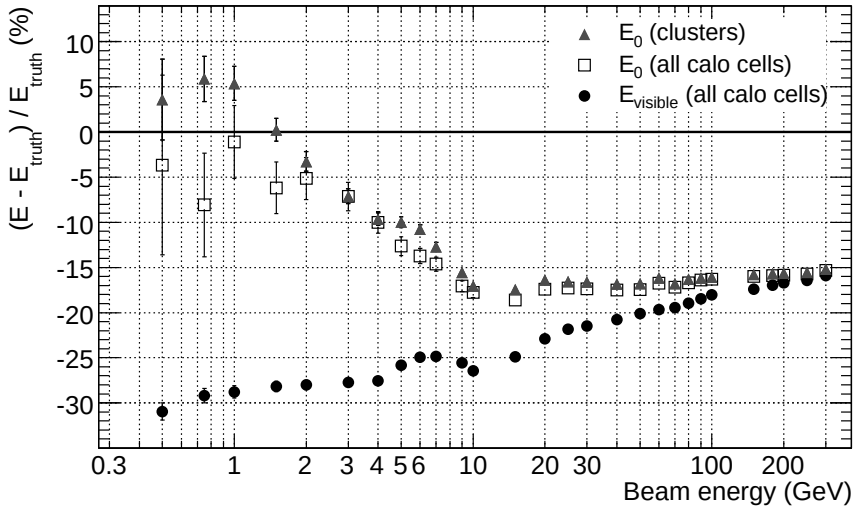

Figure 7.48: Properties of the electromagnetic scale energy in relation to the Monte Carlo truth energy. The ratio $(E - E_{truth})/E_{truth}$ plotted as a function of beam energy, where E is the electromagnetic scale energy within topo clusters, the electromagnetic scale energy within all calorimeter cells, or the true visible energy deposited in the cells, $E_{visible}$, as given from the simulation.

beam energies, both larger and smaller than the energy of the sample which is to be weighted, were used in the computation of the weights.

7.7.5 Properties of the electromagnetic scale energy

In all comparisons between weighted or unweighted energy and the true energy depositions as given from the simulation, an unexpected rise in the $(E - E_{truth})/E_{truth}$ ratio has been observed for beam energies lower than about 10 GeV. In Figure 7.48, properties of the electromagnetic scale energy are investigated. By looking at the electromagnetic scale energy within topo clusters, $E_{0,\,clusters}$ in relation to the electromagnetic scale energy in all calorimeter cells, $E_{0,\,all\ calo\ cells}$, and in relation to the visible energy truly deposited in the calorimeter cells, $E_{visible}$, we can disentangle the effects of noise in cells (which is not present in $E_{visible}$) and the topo clustering (which is only used in $E_{0,\,clusters}$). In Figure 7.48, it is clearly demonstrated that the unexpected rise in the $(E - E_{truth})/E_{truth}$ ratio at low beam energies is an effect of the overlaid noise in the cells, since this effects disappears when we consider the visible energy only.

It should be noted that the unexpected rise in linearity is only visible when comparing energy event-by-event with the Monte Carlo truth energy. If the

electromagnetic scale energy is compared to the beam energy, as in Figure 7.9 in Section 7.5.3, the linearity behaves as expected.

7.8 Application to jets in ATLAS set-up

In the previous part of this chapter, the performance of the local hadronic calibration when applied to single pions within the framework of the test beam set-up, with a slice of the calorimeters, has been demonstrated. During data taking with ATLAS, the calibration of jets is the primary aim of the hadronic calibration. In this section the performance of the local hadronic calibration when applied to jets in the full ATLAS set-up is demonstrated and compared with the performance of the global jet calibration, which is the current default calibration for jets in ATLAS.

The jet calibration presented in this section is a summary of the initial local jet calibration studies that were made in 2007, with a comparison with the global calibration. These results were originally published in paper III. Since then, the method has been developed further. See e.g. [68] for a detailed update.

7.8.1 Jet algorithms

The interactions between coloured particles can be described by Quantum Chromodynamics (QCD), and in this picture, the proton collisions at the LHC can lead to a hard scattering of the partons. The partonic final state of the collision may consist of the outgoing hard partons and additional initial and final state radiation of gluons (ISR and FSR). Due to colour confinement, the partons can never be observed freely but fragment into hadrons, hadronise, a process that can be modelled by phenomenological approaches[69]. The scattered parton gives rise to a spray of collimated hadrons, a *jet*. The particles within a jet carry the information about the original parton and the measurements of jets are therefore important tools when understanding the underlying physics processes at a hadron collider. The performance of the calibration, the ability of the jet algorithm to find all the jet constituents (and nothing but jet constituents) and the presence of initial and final state radiation put a limit on the jet information accuracy[70, 71]. It should be pointed out that a jet is what the jet algorithm defines it to be; sometimes it is desirable to try to reconstruct the parton as well as possible, but as the parton is not a well-defined physical entity (since it immediately hadronises), there can be reasons to define other criteria for the jet algorithm.

General requirements for a good jet algorithm is that it should be reasonably quick in terms of CPU time, and it should also be infrared-safe and collinear-safe[70]. Infrared-safety means that the jet algorithm is insensitive to soft parton emissions, i.e. if there are two partons from the hard scattering, that are

combined into two jets by an algorithm, the same algorithm should still find two jets, even if one of the partons radiate a soft gluon. A collinear-safe algorithm finds the same jet, even if the original parton is split into two collinear fragments. It is also insensitive to the E_{T} ordering of the particles, such that if the leading particle of the jet is split into two particles, the algorithm finds the same jet.

Three different jet algorithms have been widely used by the ATLAS collaboration: the cone algorithm[68], the $k_{\perp}$ algorithm[72] and the anti-$k_{\perp}$ algorithm[73], which are described below. For the work of this section, the cone algorithm has been used.

The cone algorithm

As the name suggests, the cone algorithm essentially clusters the jet constituents in a simple cone. As a starting seed, each calorimeter energy deposition greater than 2 GeV is considered. The 4-vector energy-momentum depositions within a cone of radius $\Delta R = \sqrt{(\eta_i - \eta_{seed})^2 - (\phi_i - \phi_{seed})^2} = 0.7$ are summed, forming a proto-jet. If the jet direction fail to coincide with the seed cell, a reiteration takes place with the seed cell replaced by the current jet axis, until a stable system of jets is obtained. To remove overlap between jets, the proto-jets are either merged or split in the last step, with the merging occurring if two jets share more than 50% of the energy of the jet with the lowest energy. Only jets with a minimum energy of 10 GeV are kept.

As the cone algorithm is seeded, it is not collinear-safe. Neither is it infrared-safe, but the split-and-merge procedure partly remedies this[68]. It is, on the other hand, very straight-forward, easy to understand, fast and can be useful for initial studies and comparisons.

The $k_{\perp}$ algorithm

There exist several sequential recombination jet algorithms, of which the $k_{\perp}$ algorithm is one. The $k_{\perp}$ algorithm starts with a set of jet constituents i, for example topological clusters. For each component i, the quantity $d_i = k_{T,i}^2$ is defined, where $k_{T,i}$ is the transverse momentum of the cluster i, with respect to the beam axis. For each pair of clusters (i, j), we have

$$d_{ij} = \frac{\min(k_{T,i}^2, k_{T,j}^2)\Delta R_{ij}^2}{D^2} \tag{7.10}$$

where ΔR_{ij} is the distance between the clusters and D is a distance parameter characteristic for the algorithm. If the minimum of the set of all d_i and d_{ij} is a d_{ij}, the clusters i and j are merged to a new cluster n. If instead the minimum is a d_i the cluster i is a jet, and it is removed from the cluster list. This procedure continues until all the clusters have been formed into jets.

It should be noted that the last jet to be formed with this scheme is the one with the largest p_{T}, and that the jets can have very irregular shapes. The $k_{\perp}$ algorithm is both collinear- and infrared-safe[72].

The anti-$k_\perp$ algorithm

The $k_\perp$ algorithm fulfils the theoretical requirements on a jet algorithm, while the cone algorithm is simple but not as theoretically well-founded. The anti-$k_\perp$ algorithm[73] combines the best features of these two algorithms.

The recombination scheme follows the same steps as the $k_\perp$ algorithm, with the replacement of Eq. 7.10 with

$$d_{ij} = \frac{\min\left(\frac{1}{k_{T,i}^2}, \frac{1}{k_{T,j}^2}\right) \cdot \Delta R_{ij}^2}{D^2} \tag{7.11}$$

that is, the minimum is not taken of the transverse momenta of the clusters, $k_{T,i}^2$, but of the inverse, $1/k_{T,i}^2$. The recombination scheme creates jets in the logical order, starting with the high-p_{T} ones, which makes the algorithm faster. It is both collinear- and infrared-safe and the jets formed are roughly conical in shape.

7.8.2 Weight extraction and implementation of the cone method in the full ATLAS set-up

The cone version of the local hadronic calibration method is implemented in the ATHENA package[55]. Weights for the jet calibration in the full ATLAS set-up has been extracted from fully simulated single pion events, with energies logarithmically equidistant between 1 and 1000 GeV. ATHENA version 12.0.31 was used for generation and simulation.

The weights were derived using the same approach as outlined in Section 7.5, using the energy of a cone with an opening angle of 11 degrees as the global energy scale and extracting weights from the leading cone only. The weights were parametrised with the cell energy density and the cone energy and separate weight look-up tables were made for the various sampling layers of each calorimeter system and for different η values in intervals of 0.2.

The hadronic corrections for jets in ATLAS are applied in several steps. First the energy is formed into topological clusters, which are classified as hadronic or electromagnetic, based on their energy density and shower depth. Then the weights are applied to the hadronic clusters only. Finally corrections are made for energy falling outside the clusters (*out-of-cluster corrections*) and for energy deposited in non-calorimeter material (*dead material corrections*).

After the application of all the local hadronic calibration factors, the particles in the jets are correctly calibrated. However, this does not necessarily correspond to the "true" jet energy, due to inefficiencies in the jet algorithm, such as missed clusters, or mis-classification of clusters. Additional jet corrections are needed to fully recover the jet energy, as demonstrated below. The out-of-jet corrections are energy-dependent, since high-energy jets deposit a larger fraction of their energy in a cone of a fixed size about the jet axis compared to jets of lower energies, an effect which is caused by the boost of the initial parton[74].

Jet samples

The calibration methods were applied to a dijet sample consisting of about 1 million events, that were simulated using the PYTHIA[75] event generator. All quark flavours except top were considered, and the p_{T} of the leading parton was in the range $10-2280$ GeV/c. The jets were reconstructed with the cone algorithm, using $\Delta R = 0.7$ as the size cut-off parameter. For the locally calibrated jets, the input to the jet algorithm was locally calibrated topological clusters. The global calibration of the jets was performed on jets formed from calorimeter towers that had been calibrated to the electromagnetic scale.

Global calibration

The local hadronic calibration that has been described in this chapter corrects for one effect at the time, disentangling detector and physics effects. The global calibration, on the other hand, aims to calibrate directly to the "true" energy of the jet[68].

In the global scheme, first a global physics object is found (e.g. a jet) and the weights are derived from a matching "truth" object, which is found by requiring that the spatial separation $\Delta R = \sqrt{\Delta\phi^2 + \Delta\eta^2}$ is less than 0.2. The weights are parametrised with the cell energy density and the sampling layer, and the numerical values are found by minimising the χ^2 function

$$\chi^2 = \sum_{i \in \mathrm{jet}} \left(\left(\frac{w_i \cdot E_i}{E_i^{\mathrm{truth}}} \right) - 1 \right)^2 \tag{7.12}$$

where the index i runs over all the cells in the jet, w_i is the cell weight, E_i is the cell energy on the electromagnetic scale and E^{truth} is the energy of the matching truth jet. The weights are given as $w_i = p_1 + p_2 E_{sum} + p_3 E_{sum}^2$ where E_{sum} is the total energy of all the calorimeter cells in the jet and p_n are the coefficients in the minimisation. Only weights in the range $1 < w < 2$ are used, and the jets are required to fulfil $E_{\mathrm{T}}^{\mathrm{jet}} > 20$ GeV[76, 77].

7.8.3 Estimation of performance: linearity and resolution of jet samples

As in the case of the single pion calibration, the quantities to study in order to compare the performance of the various calibration methods are the linearity and the resolution. In this context, the linearity is measured as the response as a function of the jet energy, and it reflects the requirement that the energy of the reconstructed jet should be equal to the incident energy of the "true" jet, as given by the simulation, for all jet energies. The response is given by the mean μ of the distribution of the reconstructed (calibrated) jet energy divided by the true jet energy, $E_{\mathrm{reco}}^{\mathrm{jet}} / E_{\mathrm{truth}}^{\mathrm{jet}}$. The mean is obtained from a Gaussian fit, which is constrained to the core of the signal, the $\mu \pm 2\sigma$ region of an initial Gaussian fit, as described in Section 7.5.6. The resolution is computed as σ/μ from the same restricted Gaussian fit.

The energy dependence of the resolution can be expressed as

$$\frac{\sigma(E)}{E} = \sqrt{\frac{a^2}{E} + b^2} = \frac{a}{\sqrt{E}} \oplus b \tag{7.13}$$

where the a^2/E term stems from sampling and statistical fluctuations and the b term originates from for example sampling fluctuations[6]. The latter limits the performance at very high energies. At ATLAS, the ultimate goal is to achieve a flat linearity with a deviation of at most 2% up to an energy of 4 TeV and a resolution of $\frac{\sigma(E)}{E} = \frac{50\%}{\sqrt{E}} \oplus 3\%$ for $|\eta| < 3$[32].

Linearity

In Figure 7.49, the behaviour of the response E_{rec}/E_{truth} as a function of the true jet energy is shown for different intervals of η corresponding to different sub-detector regions, where $0.4 < \eta < 0.5$ is the central barrel region, $2.45 < \eta < 2.55$ is the endcap region and $3.5 < \eta < 3.95$ is the forward region.

The linearity is shown for jets on the electromagnetic scale, jets after global calibration and locally calibrated jets, using the cone and the cluster methods. Two versions of the cone method has been used. The first uses the angular distance in θ when forming the cone (labelled "angle") and the second uses the distance ΔR in η-ϕ space. The first method, which is the one used for the single pion calibration of this chapter, was used for the extraction of the weights. The second is shown for comparison and only a small sub-set of all the dijet samples were used for that type of calibration.

From Figure 7.49 it is evident that the global calibration method performs best for all the sub-detectors. However, it should be noted that the local methods lack out-of-jet corrections, which cause the deviations from responses of 100%. These deviations are especially pronounced for jets of low energies, which is expected since high-energy jets are more collimated[74].

In the forward region, where the jets are most energetic, it is expected that the local methods perform better, but as shown in Figure 7.49(c), the linearity of the locally calibrated jets is only about 90%. Upon closer examination of the samples, it was shown that for this particular simulation there was a problem with the energy scale in the forward calorimeter, which caused the electromagnetic energy to be $\sim$12% too low. Hence the local calibration fails to reach the full jet energy, as the electromagnetic scale, from which the calibration starts, is wrong.

Resolution

The jet energy resolution as a function of $1/\sqrt{E_{true}}$ is shown in Figure 7.50 for different intervals of pseudorapidity corresponding to the different sub-detector regions. The jets have been calibrated to the electromagnetic scale, or with the global method or one of the local methods (cone or cluster). The fitted functions follow Eq. 7.13 and the parameter values of the fits are summarised in Table 7.7.

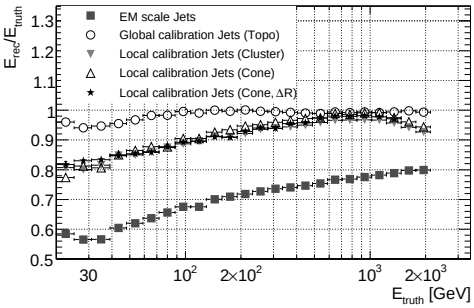

(a) $\frac{E_{rec}}{E_{truth}}$ as a function of true jets energy in the central barrel region, $0.4 < \eta < 0.5$

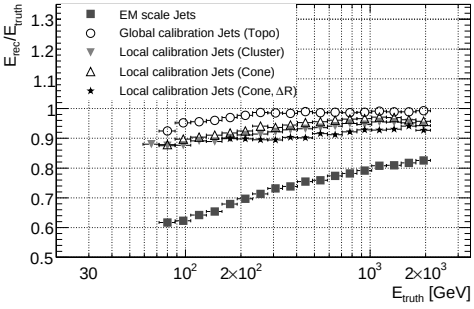

(b) $\frac{E_{rec}}{E_{truth}}$ as a function of true jets energy in the endcap region, $2.45 < \eta < 2.55$

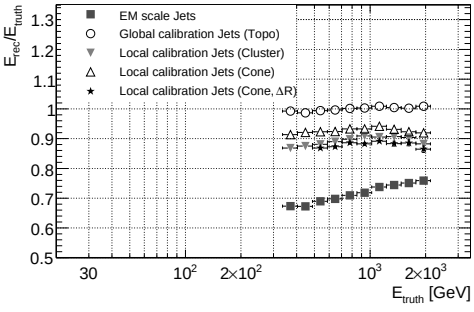

(c) $\frac{E_{rec}}{E_{truth}}$ as a function of true jets energy in the forward region, $3.5 < \eta < 3.95$

Figure 7.49: Response as a function of true jets energy in different η-regions of the detector. Results are shown for jets calibrated on the electromagnetic scale, and for global and local (cone and cluster) calibration methods for cone jets with $\Delta R = 0.7$. Figures by K. Lohwasser, originally published in Paper III.

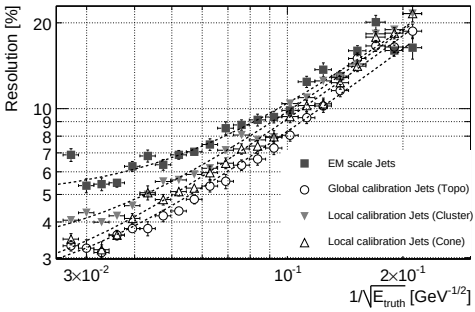

(a) Resolution as a function of $\frac{1}{\sqrt{E_{true}}}$ in the central barrel region, $0.4 < \eta < 0.5$

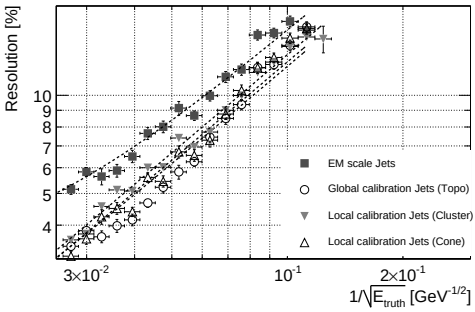

(b) Resolution as a function of $\frac{1}{\sqrt{E_{true}}}$ in the endcap region, $2.45 < \eta < 2.55$

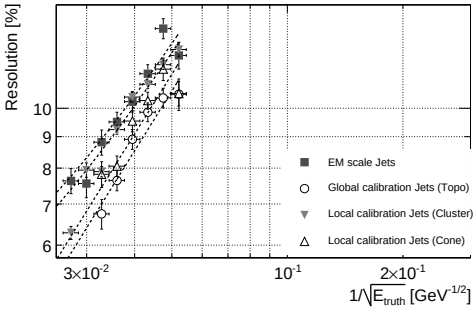

(c) Resolution as a function of $\frac{1}{\sqrt{E_{true}}}$ in the forward region, $3.5 < \eta < 3.95$

Figure 7.50: Jet resolution in different η-regions of the detector. Results are shown for jets calibrated on the electromagnetic scale, and for global and local (cone and cluster) calibration methods for cone jets with $\Delta R = 0.7$. Figures by K. Lohwasser, originally published in Paper III.

Calibration approach	a (% GeV$^{1/2}$)	b (%)	χ^2 / NDF
$0.4 < \eta < 0.5$			
EM scale jets	92.4 ± 2.3	4.9 ± 0.1	48.2 / 22
Global Method	80.3 ± 1.7	2.2 ± 0.1	37.7 / 22
Local method (cluster)	92.8 ± 1.5	3.1 ± 0.1	69.3 / 23
Local method (cone, angle)	89.5 ± 1.9	2.2 ± 0.2	62.5 / 22
$2.45 < \eta < 2.55$			
EM scale jets	132.7 ± 5.1	3.9 ± 0.3	19.3 / 15
Global Method	117.6 ± 4.1	2.1 ± 0.3	23.5 / 15
Local method (cluster)	134.9 ± 3.1	1.3 ± 0.3	25.8 / 15
Local method (cone)	129.6 ± 2.7	0.0 ± 0.4	38.8 / 15
$3.5 < \eta < 3.95$			
EM scale jets	241.2 ± 11.5	4.1 ± 0.7	9.8 / 9
Global Method	213.4 ± 4.3	0.0 ± 1.7	14.1 / 9
Local method (cluster)	235.1 ± 8.2	3.7 ± 0.5	49.7 / 9
Local method (cone)	227.2 ± 4.6	0.0 ± 2.7	17.3 / 9

Table 7.7: Resolution as function of $1/\sqrt{E_{true}}$ with fits of the form $r = a/\sqrt{E_{true}} \oplus b$ for different regions of η. $\Delta R = 0.7$ jets. The numbers have been computed by K. Lohwasser and were originally published in paper III.

As expected, the jets that have been calibrated to the electromagnetic scale only exhibit the worst resolution for all energies and η regions. The global calibration performs best at the higher energies, while the difference between the different calibration methods shrinks at low energies. In the forward region, the difference between the two local methods is largest, with a marginally better performance by the cone version. However, the differences are within the statistical uncertainty, and this similarity further underlines the stability of the local calibration.

7.9 Summary and Discussion

In this chapter, the local hadronic calibration scheme has been applied to real data from a combined test beam and the performance of the scheme on simulated jets in full ATLAS set-up has also been demonstrated. The studies presented here were originally published in paper III and were the first application of local hadronic calibration to real data from test beams.

It has been shown that calibration by applying tabulated weighting factors to individual calorimeter cell signals provide a stable method for calorimeter

compensation, and that the two versions of the local calibration, the "cone" and the "cluster" methods, give very similar results. The local method achieves calorimeter compensation within 3% for beam energies above ~ 2 GeV, as demonstrated in Section 7.5.6. In addition, the linearity after weighting and corrections for energy losses in dead material is compatible for combined test beam data and simulation, as shown in Figure 7.37, Section 7.6.5. Hadronic scale linearity in the calorimeter within 3% is slightly larger than what is specified in the technical proposal[28], but as mentioned previously, the method has room for improvement, especially in the noise reduction.

Of the two noise reduction techniques described in Section 7.5.4, the weight restriction $0.6 < w_{cell} < 3$ implemented when filling the weight tables might lead to a bias in the hadronic scale energy, as the cut affects the weights on a level not reproducible on data. The weight restriction cut was shown to be necessary in order to eliminate noise effects, such as the lowering of the weights when the signal is close to the noise threshold. Clearly, a plain noise cut alone does not serve to fully reduce the problems that overlaid noise cause. Ideally, we would like to find a set of variables on reconstruction level (i.e. values that are accessible in data) that would provide us with a possibility to perform an additional noise reducing cut. Such studies are important to perform to ensure a bias-free hadronic weighting.

In this chapter, the main focus has been the hadronic compensation of the calorimeters. However, to demonstrate the performance of the weighting on the combined test beam pion data, a set of cuts and corrections have been applied, as described in Sections 7.6.2 and 7.6.4, among them the electron removal cut and the corrections for losses in dead material. These corrections have room for improvement. Normally, the inner detector would be used to discriminate between electrons and pions. For jets in ATLAS, the electromagnetic clusters are excluded from weighting using cluster moments as described in Section 7.8.2 and Ref. [54]. The exclusion of electromagnetic clusters when applying the weights is necessary in order to let the hadronic calibration follow the event-by-event fluctuations in the electromagnetic fraction of the shower energy, and thus improve the resolution of the energy. The corrections of dead material energy losses has been further studied since these results were obtained (see for example Ref. [68] and [54]).

In Section 7.6.5, the differences between data and simulation seen in the weight performance was explained by the inability of the simulation to correctly describe the shower development of the data. As all hadronic compensation schemes rely on simulations, the example given here clearly demonstrates the need for a good understanding of the simulations in relation to data. A lot of work is being done in this area, see, for example, References [65] and [78].

The application of the local hadron calibration to jet samples was studied and compared with the global calibration method, which calibrates to the level of particle truth jets. As the local method calibrates only to detector level,

without applying final and genuine jet corrections, it fails to reach the high level of linearity and resolution that the global calibration method is able to achieve over a large kinematic region. However, the strength of the local calibration method is still evident. As it does not calibrate inclusively, but in a modular approach, it is able to reveal problems with the electromagnetic scale calibration in the forward calorimeter, where the global calibration proved to be insensitive. For a better and fairer comparison between the global and the local calibration approaches, jet corrections should be included. See for example Ref. [68].

The modular approach of the local calibration might prove to be an important aid when calibrating ATLAS with the first collision data, a period during which any imperfections in the simulation will be exposed. Since detector and physics effects are disentangled in the calibration procedure, the local calibration method provides an easier way of finding possible problems in the simulation description of the detector. The systematic uncertainties of the jet energy scale are also easier to evaluate with a modular calibration.

It should be noted that after local hadronic calibration, the energy distribution within a jet is correctly described, as each particle in the jet regains its proper energy. This is of particular importance when the jet sub-structure is studied. In the following chapters, a proposed search for heavy particles that decay into top quark pairs is described. When lots of energy is available in the centre-of-mass system, the top decays are boosted and the decay products from the top quark can be merged in the detector. In such a case, the probing of the underlying structure of the jets is of great relevance.

Part III:
Heavy top quark resonances

8. Top quarks and new physics

> *In the history of physics, every time we've looked beyond the scales and energies we were familiar with, we've found things that we wouldn't have thought were there. You look inside the atom and eventually you discover quarks. Who would have thought that? It's hubris to think that the way we see things is everything there is.*
> – Lisa Randall, interviewed in Discover magazine, July 2006.

The top quark is the heaviest known elementary particle, and its large mass has prompted speculation on the nature of the third generation of quarks[79, 80]. By exploring the top quark properties, new physics at the electroweak symmetry breaking scale could be discovered. Even in the absence of $t\bar{t}$ resonances, the $t\bar{t}$ mass spectrum is well worth exploring.

In this chapter, a few theoretical models that give rise to $t\bar{t}$ resonances are briefly outlined, and the result from previous searches for $t\bar{t}$ resonances is given. In the following chapters, the experimental challenges for reconstructing high-energy top quarks is described, and an analysis for measuring the cross section of Z' resonances is outlined.

8.1 Theoretical motivation for $t\bar{t}$ resonances

Several proposed extensions to the Standard Model exists, in which one or more new heavy particles that decay into top quarks emerges. A review of different scenarios of $t\bar{t}$ resonances can be found in Ref. [79]. The proposed top resonances can be subdivided into two categories: coloured resonances (colour octets) and uncoloured resonances (colour singlets).

8.1.1 Un-coloured resonances (colour singlets)

An example of a colour singlet resonance is the Z', a spin 1, Standard Model Z-like heavy particle. The Feynman diagram of leading order Z' production and decay is shown in Figure 8.1. It should be noted that a Z', being uncoloured, does not couple to gluons at tree level.

One of the models in which a Z' resonance occurs is the "little Higgs model"[81], which is an extension to the Standard Model with several Higgs fields that acquire mass through a symmetry breaking at the electroweak scale. At the same time, the Higgs fields are associated with a global symmetry

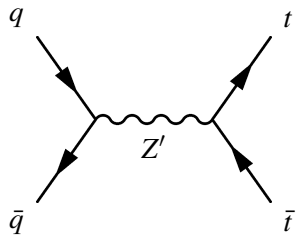

Figure 8.1: Leading order Z' production. See also Standard Model $t\bar{t}$ production (Figure 2.1 in Section 2.2).

which is broken at a higher energy scale Λ_S. In this model there exists a set of heavy gauge bosons with the same quantum numbers as the Standard Model gauge bosons. In particular, the model contains a new heavy Z-like boson. The extra gauge bosons postpone the problem of the fine-tuning of the Higgs mass until the larger energy scale Λ_S.

For a particular choice of benchmark parameters, the mass width ratio is $\Gamma/M = 3.4\%$ and the production cross section at LHC ($\sqrt{s} = 14$ TeV) is 19 pb for a $M = 1$ TeV/c^2 resonance and 0.9 pb for 2 TeV/c^2. The Z' resonance is expected to couple to all the Standard Model fermions, and in particular the branching ratio to $t\bar{t}$ pairs is $1/8$ (12.5%)[82].

The little Higgs Z' decays with equal probability to all the elementary fermions, if the colour factors are taken into account. A model in which a heavy neutral gauge boson exists, which couples primarily to top quarks, is the topcolor model[83, 80]. The motivation for the topcolor model is to give a natural explanation to the very large mass of the top quark. In the topcolor model, the QCD gauge group $SU(3)_C$ is part of a larger symmetry structure, and in the breaking of that symmetry, massive coloured bosons emerge. The observed top quark mass is assured when topcolor is combined with for example the Higgs mechanism, or additional strong dynamics (technicolour[80]). However, in order to keep the b quark light in comparison to the top quark, an additional neutral gauge boson is needed. This massive gauge boson, generally called Z'_t, couples strongly to the third generation quarks, and weakly to the other quarks, which enhances the branching ratio for decay of Z'_t into $t\bar{t}$ pairs.

Other examples on uncoloured resonances are spin-2 graviton-like bosons, which could be created in for example Kaluza-Klein excitations of gravitons (see also Section 8.1.2).

8.1.2 Coloured resonances (colour octets)

A general model for a colour octet "coloron" which couples to top quarks through new strong dynamics is described in Ref. [79]. In this model, the new coloron can easily be implemented in the quark production by making a

substitution of the gluon propagator:

$$\frac{g_3^2}{s} \rightarrow \frac{g_3^2}{s} + \frac{g_3^2 z_1 z_2}{(s - M_B^2) + i\Gamma_B} \tag{8.1}$$

where g_3^2 is the QCD coupling constant, z_1 and z_2 are scaling factors of the coupling due to the coloron, s is the energy scale ($\sqrt{s} = 10$ TeV in the analysis presented in the next chapters), M_B is the mass of the coloron and Γ_B is its width. From Eq. 8.1, we can deduce that the coloron will interfere with the $t\bar{t}$ spectrum, and the level of interference is governed by the factor $z_1 z_2$. For an experimentalist, this offers the interesting possibility of separating coloured and uncoloured resonances by examining the shape of the mass spectrum.

Kaluza-Klein gluons in warped extra dimensions

A more specific coloured resonance could be the Kaluza-Klein excitation of the gluon. Kaluza-Klein[1] modes occur in many extra dimensions scenarios. The general motivation for proposing extra dimensions is the hierarchy problem, that is the great discrepancy in scale between the strength of the electroweak force and gravity. Differently formulated, this problem boils down to the mass discrepancy between the Planck mass $M_P \sim 10^{19}$ GeV/c^2 and the expected Higgs mass $M_H \sim 10^2$ GeV/c^2. In certain extra dimensions scenarios, the apparent weakness of gravity is generally explained by the presence of extra dimension(s) in which gravity can propagate, while the Standard Model fields are contained in our normal four-dimensional spacetime.

In the Randall-Sundrum scenario[25] one single extra dimension is proposed, which is warped (curled up with a finite radius). In an extension to the theory, all the Standard Model fields are free to propagate in the extra dimension. The hierarchy problem is solved geometrically through an exponential warp factor. The metric of the warped space can be written as[84, 85, 86]

$$ds^2 = e^{-k|y|}\eta_{\mu\nu}dx^\mu dx^\nu - dy^2 \tag{8.2}$$

where y is the extra dimension and $e^{-k|y|}$ is the warp factor. The extra dimension has a periodic geometry, such that $y = 0 = 2n\pi r_c$ where r_c is the radius of the warped dimension. At either end of the warped dimension, there is a brane. The one at $y = 0$ is called the "Planck" or "UV" brane, and the one at $y = \pm\pi r_c$ is the "TeV" or "IR" brane. For appropriate values of kr_c, the ratio

$$\frac{e^{-k|y(UV)|}}{e^{-k|y(IR)|}} = e^{k\pi r_c} \tag{8.3}$$

can take any value. In particular, we can choose $kr_c \approx 11$, which gives us $M_{Planck}/M_{EW} \approx 10^{15}$, i.e. a solution to the hierarchy problem in the geometry.

[1] Named after two of the pioneers of the theory of extra dimensions, the German mathematician Theodor Kaluza (1885–1954) and the Swedish theoretical physicist Oskar Klein (1894–1977).

When a Standard Model particle is excited into the extra dimension, it acquires an effective mass in the 4-dimensional space-time. The mass is proportional to n/r_c, where the integer n is the excitation number.

Of particular interest as a $t\bar{t}$ resonance is the Kaluza-Klein excitation of the gluon, g_{KK}. In the Randall-Sundrum scenario, g_{KK} is expected to have a large branching ratio to $t\bar{t}$ (92.5%[84]), and the expected production cross section at $\sqrt{s} = 14$ TeV is 30 pb for a 1 TeV/c^2 resonance, and 2 pb for a 2 TeV/c^2 resonance[84].

8.2 Previous searches at the Tevatron

The CDF and D0 experiments at the Tevatron accelerator at Fermilab in the U.S. have made searches for coloured and uncoloured $t\bar{t}$ resonances. At the Tevatron protons and anti-protons are collided at a centre-of-mass energy of $\sqrt{s} = 1.96$ TeV. The general result from the Tevatron is that no deviations from the Standard Model has been reported, and resonance masses up to approximately 800 GeV/c^2 have been considered.

The D0 experiment has excluded a narrow uncoloured resonance $M_{Z'} <$ 820 GeV/c^2 at 95% CL for $\Gamma_{Z'} = 1.2\% M_{Z'}$[87].

The CDF experiment reports on searches for a leptophobic Z' in a specific topcolor-assisted technicolor production model with a width of $\Gamma_{Z'} = 0.012 \cdot M_{Z'}$. For this model, masses below 725 GeV/c^2 are excluded at the 95% confidence level[88]. Another analysis[89] reports that a topcolor leptophobic Z' with mass below 720 GeV/c^2 is excluded, and they found that $\sigma < 0.64$ pb at 95% C.L. for a narrow Z'-like resonance that decays into $t\bar{t}$ with $700 < M_{Z'} < 900$ GeV/c^2.

The CDF experiment has also searched for a massive gluon and report no deviations from the Standard Model in the $t\bar{t}$ mass spectrum below 800 GeV/c^2[90]. An updated, more recent search confirms this result[91].

9. Analysis strategy

> *If it looks like a duck, and quacks like a duck, we have at least to consider the possibility that we have a small aquatic bird of the family Anatidae on our hands.*
> – Douglas Adams: "Dirk Gently's Holistic Detective Agency", 1987.

When searching for a $t\bar{t}$ resonance, the reconstructed top pair mass spectrum is the fundamental observable needed to infer the signal. In the absence of a resonance, the invariant mass spectrum of the top and anti-top quarks created in the proton-proton collisions will fall off exponentially, due to the kinematic effects and dynamics of the system. If a particle that decays into top anti-top quark pairs exist however, the $t\bar{t}$ mass spectrum will be changed. If the particle does not interfere with the top quarks, the result can be a peak in the mass spectrum. In the case of interference, the spectrum will be modified in other ways. Reconstructing the invariant mass spectrum is thus the key to finding a resonance.

As outlined in Chapter 2.2, top quarks decay promptly to a b quark and a W boson. The b quark is reconstructed as a jet. The W decays either to a charged lepton and a neutrino or a quark anti-quark pair. The final state of the top pair decay is thus either of the form $t\bar{t} \to \ell^+\ell^-\nu\bar{\nu}b\bar{b}$ (di-leptonic), $t\bar{t} \to \ell\nu b\bar{b}q\bar{q}$ (semi-leptonic) or $t\bar{t} \to bq\bar{q}\bar{b}q\bar{q}$ (all-hadronic).

The semi-leptonic decay channel has a reasonably large branching ratio (about 38% of the $t\bar{t}$ decays, counting only e and μ final states). This is a smaller branching ratio than the all-hadronic decay channel (56%), but in a hadron collider, all-hadronic top decays are much harder to distinguish from the light jets background than a semi-leptonic decay, which is characterised by its high-energetic charged lepton.

The resonances we are looking for are massive, with masses between 1 and 2 TeV[1]. When such large energies are present in the system, the decay products are likely to be boosted, and in that case the decay products can be merged. The standard procedure for reconstruction jets in ATLAS relies on the reconstruction of each of the top decay products, i.e. the reconstruction of four jets, one charged lepton and $E_{\mathrm{T}}^{\mathrm{miss}}$ in the case of semi-leptonic top decay[92]. This situation is referred to as the *resolved case*, when all the top

[1] In this and the following chapter, the scientific shorthand is used where the energy is given in units of eV, in a unit base where $c = 1$. In this case, c can be omitted when giving the unit for mass (formally eV/c^2) and momentum (eV/c).

decay products are well separated. This is in contrast to the more energetic case, where the top decay products start to merge (the *transition region*). When all the top decay products from each top quark are merged, we have the fully merged *mono-jet* situation.

The following analysis assumes that the products of each top decay are merged into one single jet (mono-jet), with three sub-jets (in the case of the hadronic top decay) or one jet containing the b jet and the charged lepton, in the case of leptonic top decay.

The objects needed to reconstruct the $t\bar{t}$ pair are thus two energetic jets, of which one contains a charged lepton, and missing transverse energy from the neutrino. These three objects (the hadronic top jet, the leptonic top jet and the $E_{\mathrm{T}}^{\mathrm{miss}}$) combined give us the invariant mass of the system. In the absence of a $t\bar{t}$ resonance, the invariant mass spectrum is expected to be exponentially declining with mass. If a resonance is present, a peak will be seen, provided the production cross section is large enough.

For the analysis presented in this and the following chapter, an integrated luminosity of 200 pb^{-1} and a collision centre-of-mass energy $\sqrt{s} = 10$ TeV has been assumed, which roughly corresponds to the expectations of one year of early data-taking with the LHC.

9.1 Signals and backgrounds

The signal searched for is a heavy particle in the mass range $1-2$ TeV, that decays into $t\bar{t}$ pairs. With an optimal selection, Standard Model $t\bar{t}$ and resonances will dominate our signal.

The simulated samples used belong to a centrally produced collection[2] that the ATLAS collaboration made in 2008, known as MC08, with $\sqrt{s} = 10$ TeV[93, 94]. The cross sections used for the Standard Model processes have been normalised to the accepted theoretical values of each process. The numbers listed in the tables are the cross sections used for each sample, which include cut efficiencies and NLO corrections. The samples have either been "fully" simulated, where the full ATLAS detector is simulated, or "fast" simulated using the ATLFASTII package[95], in which the inner detector and the muon system are fully simulated, while the calorimeter response is parametrised. At present, ATLFASTII does not contain a simulation of the high-level trigger.

In the remainder of this section, the datasets used for signal and background simulation are described. For each sample, a 6 digit sample number is given. This is a unique sample identifier in the ATLAS production, stated here for the sake of reproducibility within the ATLAS collaboration. Non-ATLAS readers can ignore the sample number without loss of information about the analysis.

9.1.1 Signal: top and top resonances

The resonance signal used in this analysis is a Z', a heavy Standard Model Z-like colour singlet spin 1 particle, as outlined in Section 8.1. It is a narrow resonance in terms of its mass, $\Gamma/M = 3.4\%$[82]. The advantage of using an uncoloured resonance in an analysis like this, is that it has no interference with the $t\bar{t}$, and the combination of the resonance and the $t\bar{t}$ spectrum is simply the addition of the samples. For a coloured resonance, such as a Kaluza-Klein gluons, there is an interference with the $t\bar{t}$ spectrum, and for the simulation of each mass point, the entire $t\bar{t}$ spectrum must be generated to correctly account for this effect.

The Z' signals that have been fully simulated using the PYTHIA generator[96, 97, 75, 98], using the couplings described in Ref. [82], are listed in Table 9.1(a). In full simulation, the masses 1 and 2 TeV are available. In order to investigate the behaviour of the resonances in the intermediate mass region, an additional set of Z' resonances with masses of 1.0, 1.1,... 2.0 TeV was also simulated using ATLFASTII. These samples are listed in Table 9.1(b).

The standard model $t\bar{t}$ sample has been generated with MCATNLO[99, 100] using HERWIG/JIMMY parton showering[101, 102, 103, 104]. Another sam-

[2]For the samples used, the dataset tags are `e368` (event generation), `s462` (GEANT simulation), `r635` (digitisation and reconstruction) and `t53`.

Particle	Sample	Events	Mass (GeV)	σ (pb)
$Z' \to t\bar{t}$	105600	14898	1000	14.8
$Z' \to t\bar{t}$	105609	14976	2000	0.987

(a) Signal Z'samples, full simulation with PYTHIA. The production cross section given is the one used for plots, but it has no other consequence for the analysis.

M (TeV)	1.0	1.1	1.2	1.3	1.4	1.5	1.6	1.7	1.8	1.9	2.0
Events	15k	30k	30k	30k	29.8k	30k	30k	30k	30k	30k	30k

(b) Signal Z', PYTHIA/ATLFASTII simulation. The number of events is given in multiples of a thousand (k).

Table 9.1: Signal Z' samples, full simulation and fast simulation with ATLFASTII, $Z' \to t\bar{t} \to$ all decay channels. The event generator is PYTHIA, using the couplings described in Ref. [82].

Process	Sample	σ (pb)	Generator	Filter	Events
$t\bar{t} \to \ell + X$	105200	294.472	MCATNLO	–	1930444
$t\bar{t} \to$ all decays	Private	66.1272	PYTHIA	$p_{\mathrm{T}}^{top} > 200$ GeV	294499

Table 9.2: Simulated $t\bar{t}$ samples, full simulation with MCATNLO (using HERWIG/JIMMY parton showering) and fast simulation with PYTHIA interfaced with ATLFASTII. The settings of the fast simulation are identical to the settings used for the samples in Table 9.1(b).

ple, using PYTHIA/ATLFASTII with the same configuration as the Z' samples has also been produced. For this sample, a cut on the generated top quark of $p_{\mathrm{T}} > 200$ GeV has been applied, to keep only events in the high-energy region, which are of greater interest to us. The information about the $t\bar{t}$ samples is summarised in Table 9.2.

The leading jet p_{T} for the fully simulated Z' samples are drawn in Figure 9.1 and a comparison between the full simulation and the ATLFASTII sample for the mass $M = 1$ TeV is shown in Figure 9.2.

A comparison between the different $t\bar{t}$ samples is given in Figure 9.3.

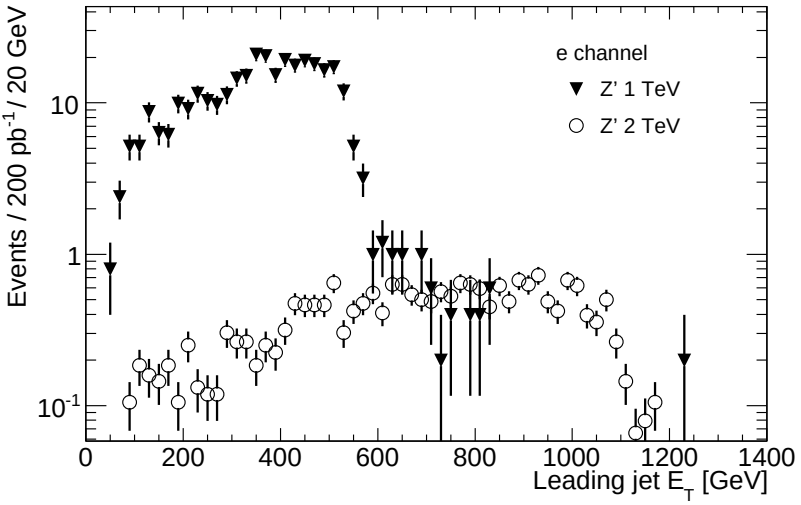

(a) Transverse energy of the leading jet in the electron channel

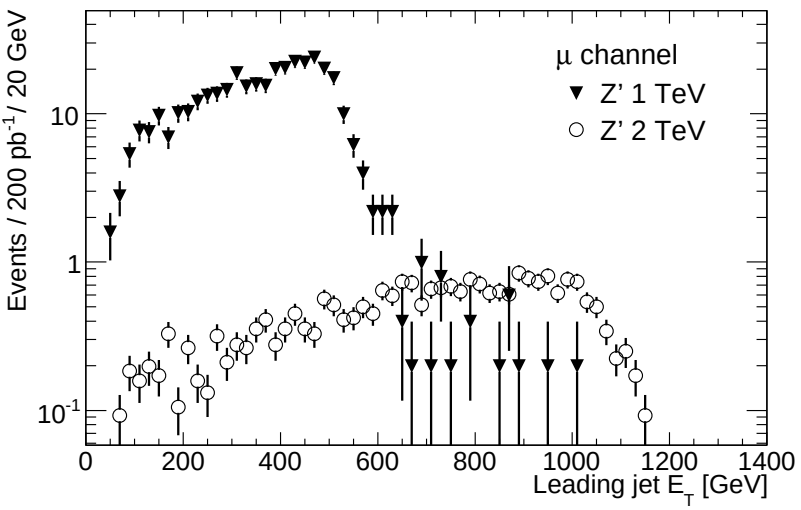

(b) Transverse energy of the leading jet in the muon channel

Figure 9.1: Z' sample comparison, for Z'_1 ($M = 1$ TeV) and Z'_2 ($M = 2$ TeV). The transverse energy of the leading jet after a $E_{\mathrm{T}}^{\mathrm{miss}} > 20$ GeV cut is shown. In this plot, the cross sections $\sigma \cdot BR(\rightarrow t\bar{t}) = 14.8$ pb for the 1 TeV resonance and 0.987 pb for the 2 TeV one have been assumed.

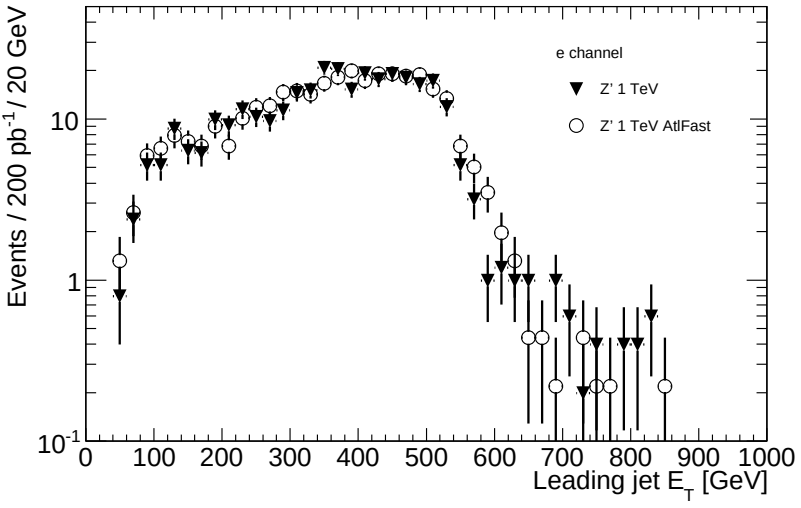

(a) Transverse energy of the leading jet in the electron channel

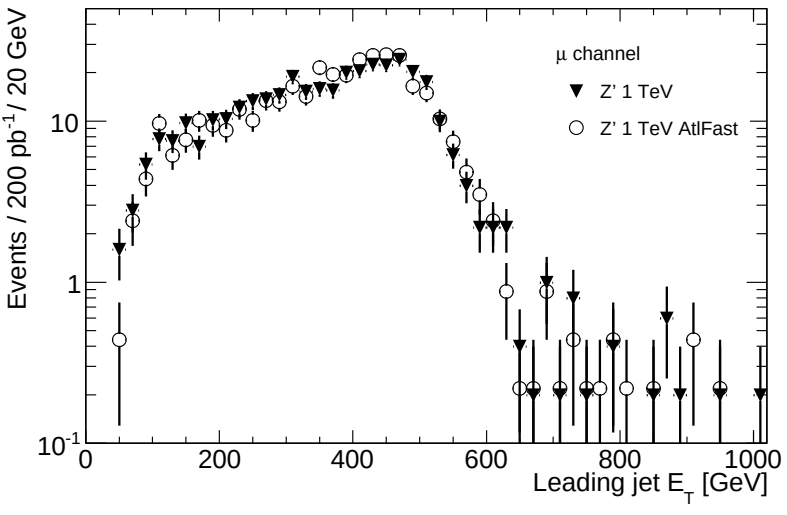

(b) Transverse energy of the leading jet in the muon channel

Figure 9.2: Z' sample comparison, for the ATLFASTII and the fully simulated Z' ($M =$ 1 TeV) samples. The transverse energy of the leading jet after a $E_{\mathrm{T}}^{\mathrm{miss}} > 20$ GeV cut is shown. In this plot, the cross sections $\sigma \cdot BR(\rightarrow t\bar{t}) = 14.8$ pb for the 1 TeV resonance and 0.987 pb for the 2 TeV one have been assumed.

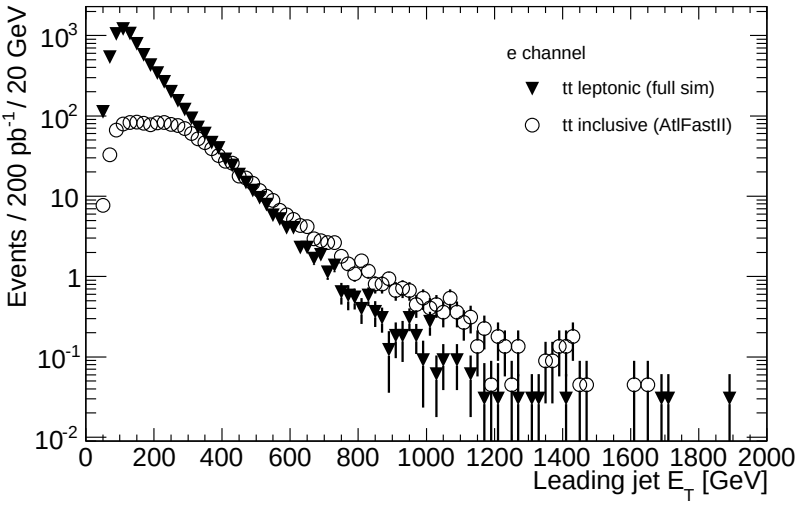

(a) Transverse energy of the leading jet in the electron channel

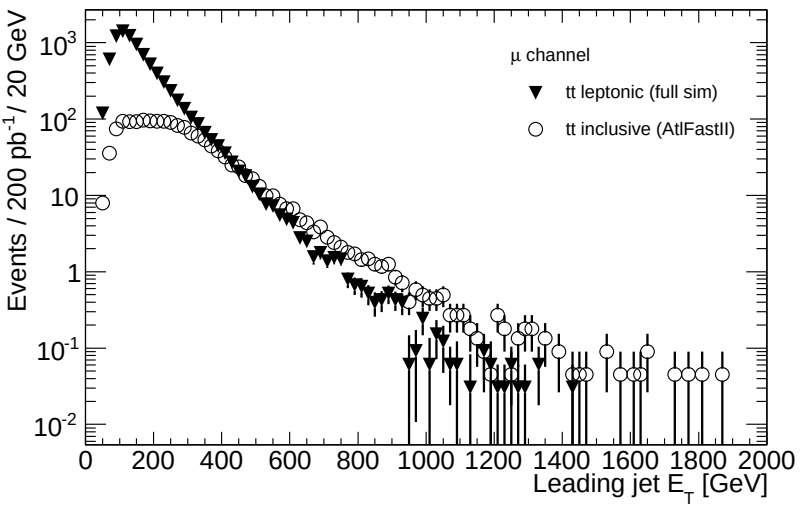

(b) Transverse energy of the leading jet in the muon channel

Figure 9.3: $t\bar{t}$ sample comparison, for the ATLFASTII and the fully simulated samples (MCATNLO). The transverse energy of the leading jet after a $E_{\mathrm{T}}^{\mathrm{miss}} > 20$ GeV cut is shown. The impact of the filter cut of $p_{\mathrm{T}}^{top} > 200$ GeV in the ATLFASTII sample has a clear impact in the reconstructed energy of the leading jet, even for energies significantly larger than 200 GeV.

9.1.2 Background samples

The signature we are looking for contains at least two massive jets, a charged lepton and $E_{\mathrm{T}}^{\mathrm{miss}}$. Besides the $t\bar{t}$ pair production process, this signal could also be created by any signal producing a charged lepton and a neutrino, such as $W+$jets. Other backgrounds that must be considered are multijet events (two or more partons from the collision) which have a very large production cross section at a hadron collider. Also single top and all-hadronic top decays must be considered.

W + jets

For the $W+$jets process, two different generators have been used: ALPGEN[105] and PYTHIA. Information about the samples are listed in Tables 9.3 and 9.4.

E_{T} of the leading jet in the ALPGEN and PYTHIA W samples are plotted for comparison in Figure 9.4. The ALPGEN sample has a higher rate at high

Particle	Sample	σ (pb)	Reconstructed events
$W(\to e+\nu)+0$ partons	107680	12425.3	1142471
$W(\to e+\nu)+1$ parton	107681	2577.13	248174
$W(\to e+\nu)+2$ partons	107682	824.72	776283
$W(\to e+\nu)+3$ partons	107683	248.026	199374
$W(\to e+\nu)+4$ partons	107684	68.442	58872
$W(\to e+\nu)+5$ partons	107685	20.252	17492
$W(\to \mu+\nu)+0$ partons	107690	12353.4	1328626
$W(\to \mu+\nu)+1$ parton	107691	2629.71	227220
$W(\to \mu+\nu)+2$ partons	107692	832.406	729598
$W(\to \mu+\nu)+3$ partons	107693	246.44	223087
$W(\to \mu+\nu)+4$ partons	107694	67.71	58928
$W(\to \mu+\nu)+5$ partons	107695	19.886	17475
$W(\to \tau+\nu)+0$ partons	107700	12417.5	1326080
$W(\to \tau+\nu)+1$ parton	107701	2570.42	246827
$W(\to \tau+\nu)+2$ partons	107702	820.816	764468
$W(\to \tau+\nu)+3$ partons	107703	247.294	223162
$W(\to \tau+\nu)+4$ partons	107704	67.466	58729
$W(\to \tau+\nu)+5$ partons	107705	20.74	17413

Table 9.3: W + jets Monte Carlo samples, full detector simulation. The generator used is ALPGEN with HERWIG parton showering.

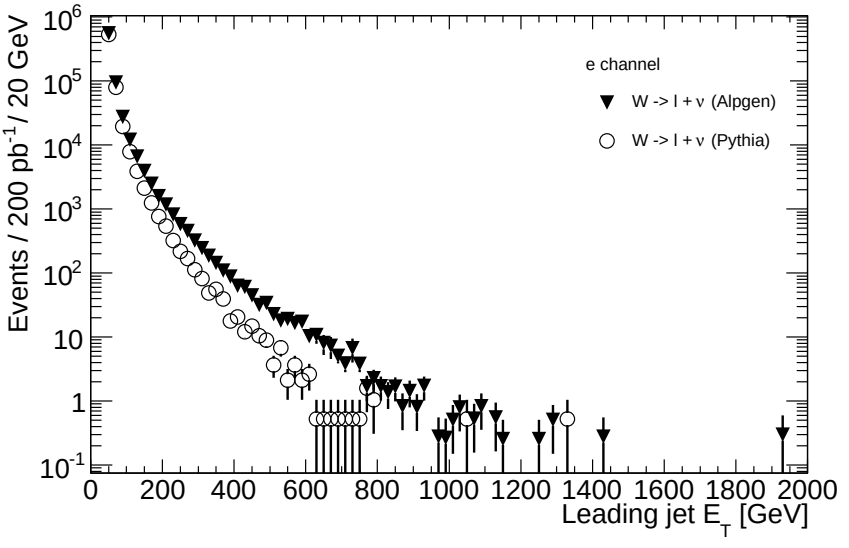

(a) Leading jet E_{T}, e channel

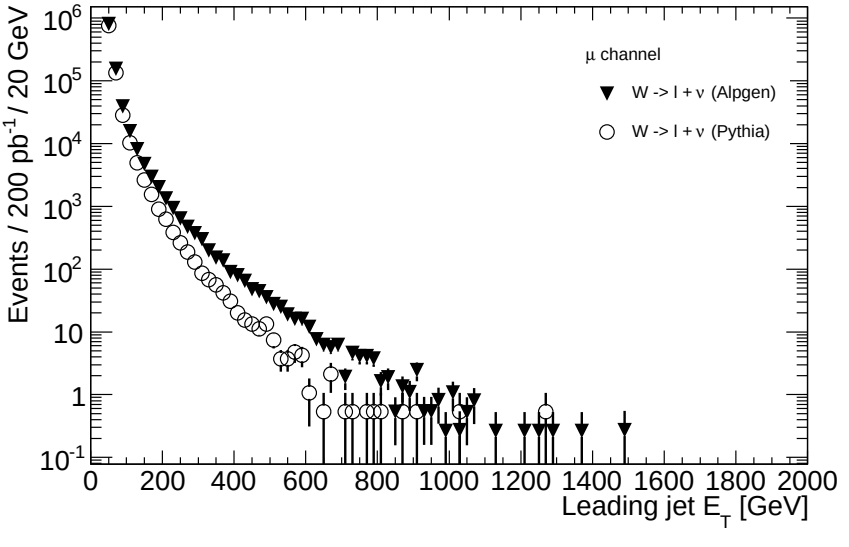

(b) Leading jet E_{T},μ channel

Figure 9.4: W generator comparison; E_{T} of the leading jet for PYTHIA and ALPGEN. For these events, one charged lepton (e or μ) is reconstructed and $E_{\mathrm{T}}^{\mathrm{miss}} > 20$ GeV.

Particle	Sample	σ (pb)	Reconstructed events
$W(\rightarrow e+\nu)$	106020	12630.7	4798140
$W(\rightarrow \mu+\nu)$	106021	12630.7	4760474

Table 9.4: W samples, full simulation. The generator used is PYTHIA.

energy, a trend that holds also for the invariant mass spectrum. The conservative approach is thus to use only the ALPGEN sample, which is done in the following analysis, unless something else is stated.

Multijets

At a hadron collider, a multijet event, when two or more high-energy partons emerge from the collision, is the most likely process to occur that result in high-p_{T} signals in the detector. In order for a multijet event to be reconstructed as a $t\bar{t}$ event, a charged lepton must be reconstructed. Since both muons and electrons can be produced in hadronic showers, this can happen. In addition, the algorithms may by mistake reconstruct an electromagnetic cluster in a jet as an electron, or jet punch-through fragments as a muon.

Particle	Sample	σ (pb)	p_{T} range (GeV/c)	Events
2 partons	105010	866800000.0	$17 < p_{\mathrm{T}} < 35$	398312
2 partons	105011	56010000.0	$35 < p_{\mathrm{T}} < 70$	979316
2 partons	105012	3280000.0	$70 < p_{\mathrm{T}} < 140$	1357129
2 partons	105013	151600.0	$140 < p_{\mathrm{T}} < 280$	529429
2 partons	105014	5122.0	$280 < p_{\mathrm{T}} < 560$	1390403
2 partons	105015	111.9	$560 < p_{\mathrm{T}} < 1120$	359293
2 partons	105016	1.075	$1120 < p_{\mathrm{T}} < 2240$	398022
2 partons	105017	0.001112	$p_{\mathrm{T}} > 2240$	398719

Table 9.5: Dijets samples, full simulation with the generator PYTHIA.

For the multijets, the generators PYTHIA (see Table 9.5) and ALPGEN (Table 9.6) have been used, as in the W case. In PYTHIA, only two partons are generated in the hard scattering, while the ALPGEN samples contain up to 6 partons. A comparison between the PYTHIA dijets and the ALPGEN multijets is given in Figure 9.5. In the electron channel, the agreement between the different generators is excellent for all energies. In the muon channel, the agreement is good for jet $E_{\mathrm{T}} > 250$ GeV. In the following analysis, the ALPGEN multijets sample has been used, unless otherwise stated.

Particle	Sample	σ (pb)	p_{T} range (GeV/c)	Events
2 partons	108352	30114200.0	$35 < p_{\mathrm{T}} < 70$	2732195
3 partons	108353	9835390.0	$35 < p_{\mathrm{T}} < 70$	977891
4 partons	108354	1494830.0	$35 < p_{\mathrm{T}} < 70$	98987
5 partons	108355	249185.0	$35 < p_{\mathrm{T}} < 70$	24845
2 partons	108357	1116550.0	$70 < p_{\mathrm{T}} < 140$	1097612
3 partons	108358	1486730.0	$70 < p_{\mathrm{T}} < 140$	1423116
4 partons	108359	552311.0	$70 < p_{\mathrm{T}} < 140$	551024
5 partons	108360	189793.0	$70 < p_{\mathrm{T}} < 140$	187775
2 partons	108362	31872.0	$140 < p_{\mathrm{T}} < 280$	317920
3 partons	108363	65508.9	$140 < p_{\mathrm{T}} < 280$	634156
4 partons	108364	49028.2	$140 < p_{\mathrm{T}} < 280$	489270
5 partons	108365	24249.3	$140 < p_{\mathrm{T}} < 280$	241596
6 partons	108366	11571.7	$140 < p_{\mathrm{T}} < 280$	115763
2 partons	108367	750.2	$p_{\mathrm{T}} > 280$	223992
3 partons	108368	1944.8	$p_{\mathrm{T}} > 280$	579039
4 partons	108369	2149.9	$p_{\mathrm{T}} > 280$	642301
5 partons	108370	1392.8	$p_{\mathrm{T}} > 280$	416906
6 partons	108371	972.6	$p_{\mathrm{T}} > 280$	278654

Table 9.6: Multijets samples in full simulation. The generator is ALPGEN.

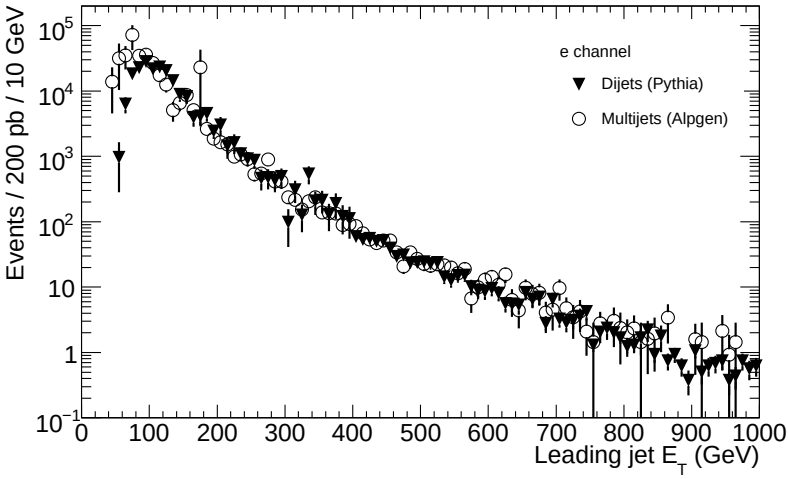

(a) Leading jet E_{T}, e channel

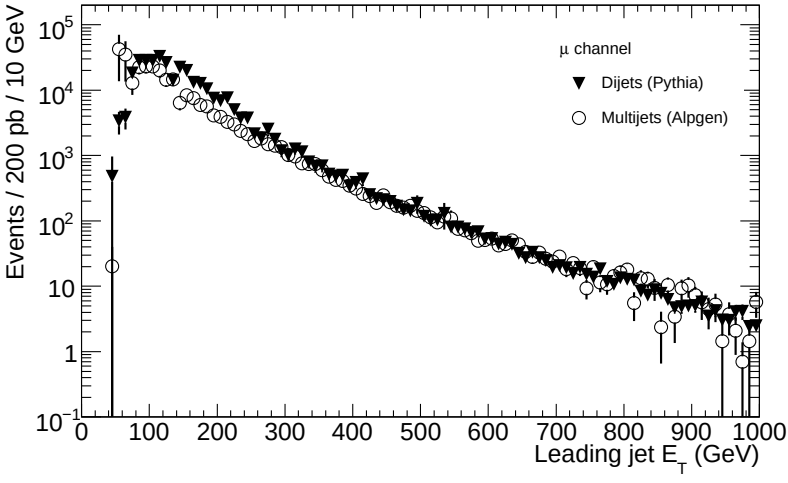

(b) Leading jet E_{T},μ channel

Figure 9.5: Multijet generator comparison; E_{T} of leading jet as given by the PYTHIA and ALPGEN generators. For these events, one lepton (e or μ) is reconstructed and $E_{\mathrm{T}}^{\mathrm{miss}} > 20$ GeV.

Particle	Sample	σ (pb)	Events
Single top, t-channel	105502	43.176	29961
Single top, associated W production	105500	14.266	9999
$t\bar{t} \rightarrow$ jets	105204	247.846	967920

Table 9.7: Secondary background samples; single top and all-hadronic top.

Secondary backgrounds

Since the signal we are looking for contains $t\bar{t}$ production, all backgrounds with top quarks must be considered. Samples of single top[17, 18] and all-hadronic top are listed in Table 9.7.

Due to the low production cross section (in the case of single top) and the low fake-rate of charged leptons, these backgrounds are less important than the $t\bar{t} \rightarrow \ell\nu + X$, W and the multijets backgrounds.

The s-channel single top production is negligible at the LHC compared to the other single top channels. See also Chapter 2.2.

9.2 Object reconstruction

For semi-leptonic decays of $t\bar{t}$ where the decay products are merged we want to reconstruct the charged lepton from the W decay, the neutrino (which we see only through the missing energy, $E_{\mathrm{T}}^{\mathrm{miss}}$), one jet from the b quark of the leptonic top decay and one jet containing the hadronic top decay. The object definitions largely follow the standard prescriptions[34].

For electrons we require $E_{\mathrm{T}} \geq 20$ GeV, $|\eta| < 2.47$ with the cryostat crack excluded ($1.37 < |\eta| < 1.52$), and no isolation requirement in the initial pre-selection[3].

For muons, we require $E_{\mathrm{T}} \geq 20$ GeV, $|\eta| < 2.4$ and no pre-selection isolation requirement.

The missing transverse energy used is the $E_{\mathrm{T}}^{miss\ RefFinal}$, which is described in detail in Ref. [68]. For the deduction of the missing energy, the transverse energy and momentum contributions of all reconstructed objects are considered, and the final $E_{\mathrm{T}}^{\mathrm{miss}}$ is the balance of these objects.

For the jets, the algorithm anti-$k_{\perp}$[73] is used, with radius parameter $R = \sqrt{\Delta\eta^2 + \Delta\phi^2} = 1.0$, and an E_{T} cut of $E_{\mathrm{T}} > 40$ GeV is applied. As input for the jet finder, locally calibrated topological clusters are used[68], with a calibration technique very similar to the method outlined in Chapter 7. In this cluster collection the muons are included. By deliberately adding the muon collection to the jet clusters, we are placing the muons and the electrons on an equal footing, as the electrons already are (potentially) included in the jet

[3] In ATLAS jargon, this corresponds to"`ElectronMediumNoIso`" (egammaPID 1982451)

clusters. No overlap removal between jets and charged leptons is performed in the pre-selection stage. Double-counting is instead avoided by matching the reconstructed charged leptons to the leading lepton inside a jet, using only the lepton in the jet for the analysis. For the leptonic top decay, we expect a b jet with a charged lepton in close proximity, which corresponds to the situation with a jet and a lepton overlapping.

For the hadronic top decay, we expect to find a single jet containing all the decay products from the top (a b quark and two light quarks from the W). In order to resolve the substructure of the jet, the FASTJET package[106] has been used to split the jets.

9.2.1 Pre-selection

For electroweak processes (such as $W \to \ell\nu$, and leptonic top decay), the selection is events with one truth lepton from a W decay (possibly via the decay of a τ) and one reconstructed lepton of the same kind (e or μ).

For quantum chromodynamical (QCD) processes (multijets, all-hadronic top decays), all events with at least one reconstructed lepton are considered.

We require at least one charged lepton reconstructed (electron or muon) that is also attached to a jet, and require $E_{\mathrm{T}}^{e} > 20$ GeV or $p_{\mathrm{T}}^{\mu} > 20$ GeV. In addition, $E_{\mathrm{T}}^{\mathrm{miss}} > 20$ GeV.

An E_{T} cut on the leading jet of $E_{\mathrm{T}} > 250$ GeV is made. In Figures 9.6 and 9.7, the E_{T} of the next-to-leading jet for Z' 1 TeV, Standard Model top pairs and $W \to \ell\nu$, after the $p_{\mathrm{T}} > 250$ GeV cut on the leading jet is shown, for the electron and muons channels, respectively. At this stage, before selection cuts, we are dominated by the multijets background, despite having required one reconstructed charged lepton, especially in the muon channel. The leading jet cut at 250 GeV affects the spectrum of the second jet in such a way that the turnover point for the spectrum occurs at $E_{\mathrm{T}} \approx 200$ GeV.

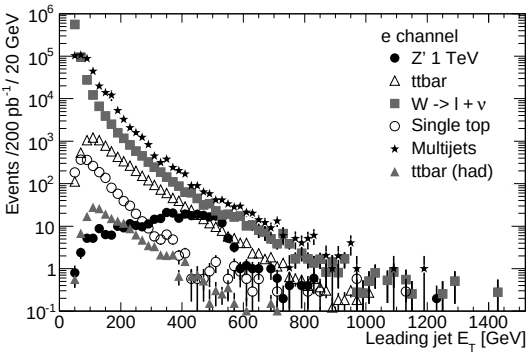

(a) Leading jet E_{T}

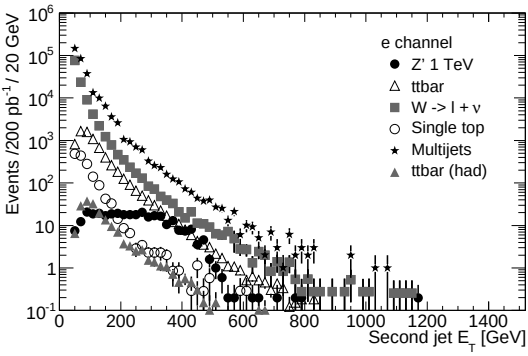

(b) Second jet E_{T}

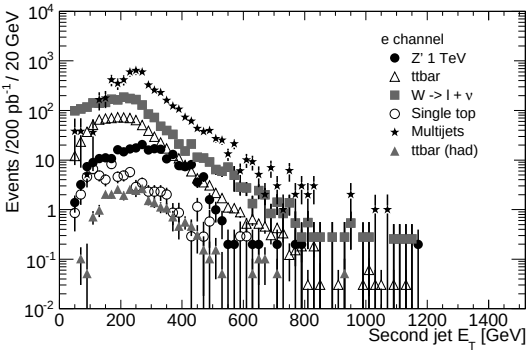

(c) Second jet E_{T}, $E_{\mathrm{T}}^{jet1} > 250$ GeV

Figure 9.6: Transverse energy (E_{T}) of the leading and next-to-leading jets in the electron channel for Z' 1 TeV, SM top pairs, $W \to \ell\nu$, multijets and single top. In the bottom plot, an E_{T} cut of 250 GeV has been applied to the leading jet.

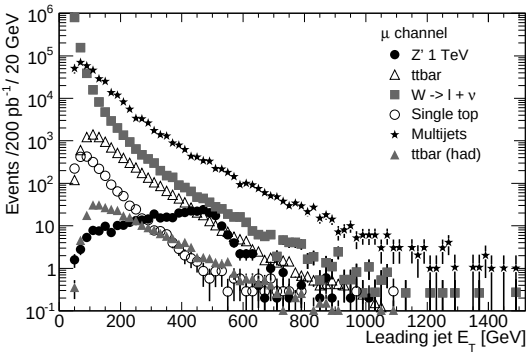

(a) Leading jet E_{T}

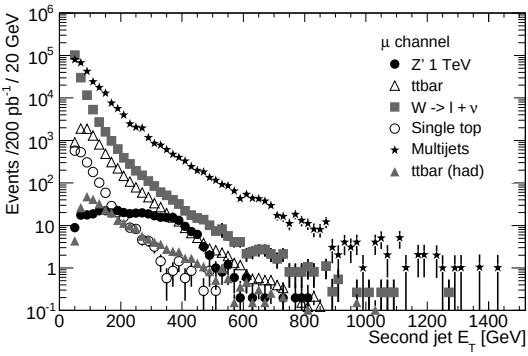

(b) Second jet E_{T}

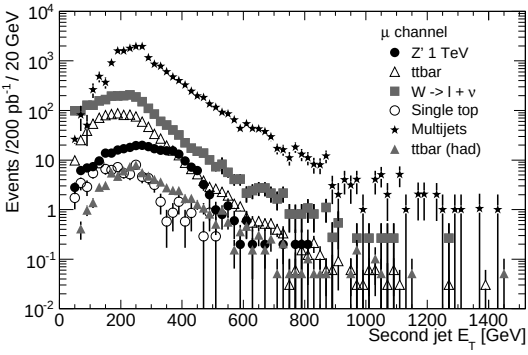

(c) Second jet E_{T}, $E_{\mathrm{T}}^{jet1} > 250$ GeV

Figure 9.7: Transverse energy (E_{T}) of the leading and next-to-leading jets in the muon channel for Z' 1 TeV, SM top pairs, $W \to \ell\nu$, multijets and single top. In the bottom plot, an E_{T} cut of 250 GeV has been applied to the leading jet.

9.3 Selection

In the top decay, we assume merged top decay products, and the challenge in the selection is to distinguish the jets from top decays from light jets. To this end, we perform a top-tagging[107], by using a set of variables that offer good discrimination against the background. The selection of top-tags is made using straight-forward variable cuts or multivariate techniques (TMVA)[108]. The variables are inspired by Thaler and Wang[109], and described in detail below.

9.3.1 Variables and pre-selection

The global requirement on the event is the pre-selection described in the previous section, i.e. $E_{\mathrm{T}}^{leading} > 250$ GeV (leading jet in the event), at least one charged lepton reconstructed (electron or muon) with $E_{\mathrm{T}}^{e} > 20$ GeV or $p_{\mathrm{T}}^{\mu} > 20$ GeV and $E_{\mathrm{T}}^{\mathrm{miss}} > 20$ GeV.

For all the plots in this section, the signal used is the combination of all the Z' ATLFASTII samples ($M_{Z'} = 1-2$ TeV) and the backgrounds used are the ALPGEN W and multijets samples.

Variables for leptonic top-tagging

The variables for leptonic top-tagging explore different aspects of the lepton/jet kinematics. A leptonic top jet candidate must have a reconstructed charged lepton associated with it (i.e. an electron or a muon is included among the jet clusters). We require that $E_{\mathrm{T}} > 40$ GeV for the jet, which is the normal jet cut.

The variables for leptonic top-tagging, x_{lep}, z_{lep}, *iso*, ΔR and Q_{vis} are described in detail below. They are also shown in Figures 9.8, 9.9, 9.10 and 9.11, and a summary of the definitions and pre-selection cuts is given in Table 9.8.

The variable Q_{vis} (see Figures 9.10(b) and 9.11(b)) is the invariant mass of the leptonic top jet candidate, which includes the lepton. Ideally, this should be close to the top mass for top events (allowing for lower mass due to the missing neutrino), while the multijet and W backgrounds should be lower. However, even jets that originate from a massless object do appear massive due to the hadronisation process, and the mass is roughly a function of the jet E_{T} and radius[110, 111]. The variable Q_{vis} is nonetheless a powerful discriminant against the W background.

The variable x_{lep} (Figures 9.8(a) and 9.9(a)) is defined as

$$x_{\mathrm{lep}} = \frac{p_{\mathrm{lep}}(p_{\mathrm{jet}} - p_{\mathrm{lep}})}{p_{\mathrm{jet}}^2} \tag{9.1}$$

where p_{lep} it the four-vector of the lepton (electron or muon) and p_{jet} is the four-vector of the leptonic top jet candidate. If the jet indeed comes from a leptonic top decay, it consists of a b quark jet and a lepton. In the $m_{\mathrm{lep}} \to 0$

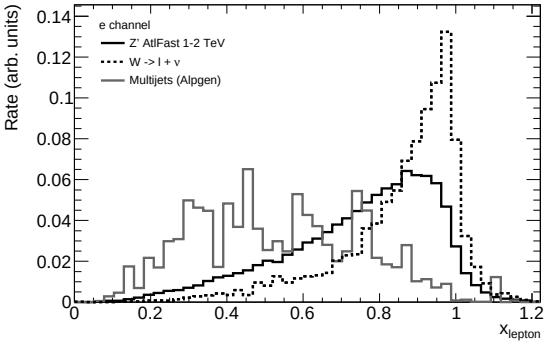

(a) Distribution of the variable x_{lep}.

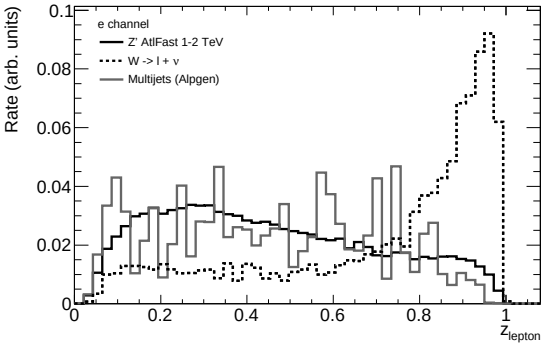

(b) Distribution of the variable z_{lep}.

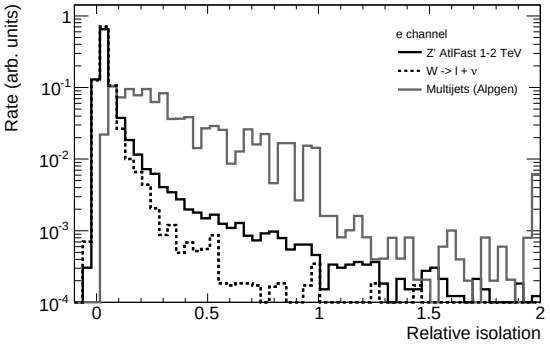

(c) Distribution of the electron isolation.

Figure 9.8: Variables for leptonic top-tagging: x_{lep}, z_{lep} and *iso* in the *e* channel. Comparison between signal (Z' ATLFASTII, $M_{Z'} = 1-2$ TeV) and background (ALPGEN W and multijets samples). All histograms have been normalised to unity.

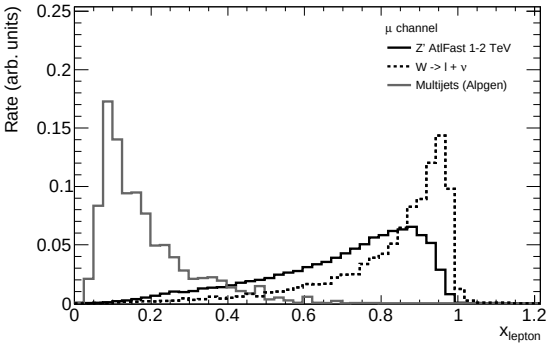

(a) Distribution of the variable x_{lep}.

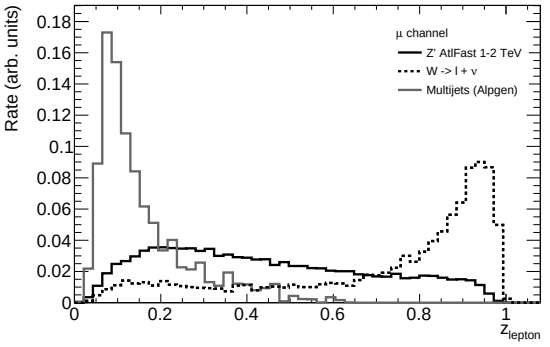

(b) Distribution of the variable z_{lep}.

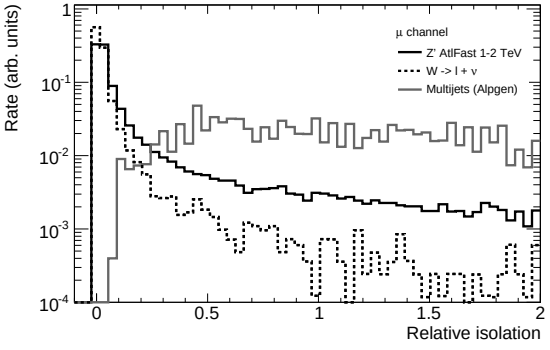

(c) Distribution of the muon isolation.

Figure 9.9: Variables for leptonic top-tagging: x_{lep}, z_{lep} and *iso* in the μ channel. Comparison between signal (Z' ATLFASTII, $M_{Z'} = 1-2$ TeV) and background (ALPGEN W and multijets samples). All histograms have been normalised to unity.

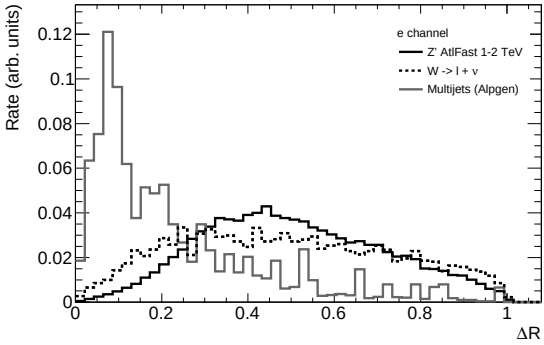

(a) Distribution of the variable ΔR.

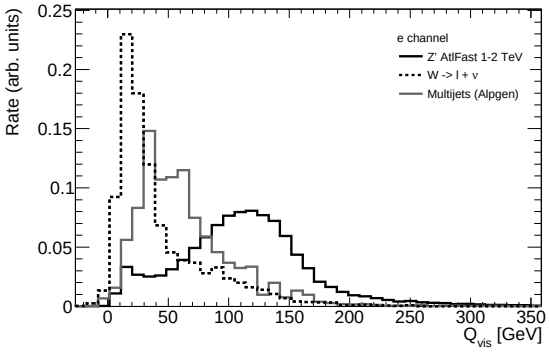

(b) Distribution of the variable Q_{vis}.

Figure 9.10: Variables for leptonic top-tagging: ΔR and Q_{vis} in the e channel. Comparison between signal (Z' ATLFASTII, $M_{Z'} = 1-2$ TeV) and background (ALPGEN W and multijets samples). All histograms have been normalised to unity.

limit (which is valid for both muons and electrons at these energies) it can be shown that

$$x_{\text{lep}} = \frac{Q_{\text{vis}}^2 - m_b^2}{Q_{\text{vis}}^2}, \tag{9.2}$$

where m_b is the mass of the b quark. x_{lep} is typically large for electroweak processes, such as the leptonic W decay, and small for QCD processes. As a pre-selection cut, $x_{\text{lep}} < 1.2$, which is a very loose cut, since for a perfectly calibrated top decay, this variable should never exceed 1.

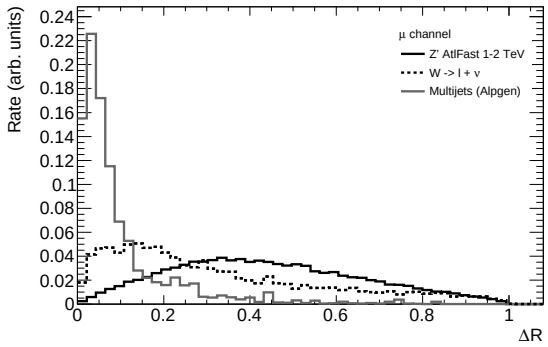

(a) Distribution of the variable ΔR.

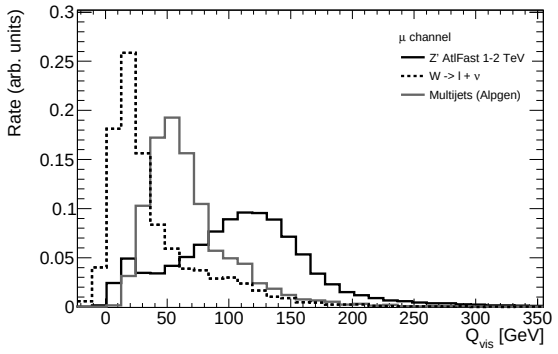

(b) Distribution of the variable Q_{vis}.

Figure 9.11: Variables for leptonic top-tagging: ΔR and Q_{vis} in the μ channel. Comparison between signal (Z' ATLFASTII, $M_{Z'} = 1-2$ TeV) and background (ALPGEN W and multijets samples). All histograms have been normalised to unity.

z_{lep} is computed as the ratio between the energy of the lepton and the energy of the leptonic top jet candidate,

$$z_{\text{lep}} = \frac{E_{\text{lep}}}{E_{\text{jet}}}. \tag{9.3}$$

Since the lepton is included in the jet, this ratio should always be less than 1, which is included as a pre-selection quality cut. z_{lep} can also be viewed as an isolation measure. The more traditional way of measuring the lepton isolation, *iso*, is to look at the energy deposited in a $R = 0.2$ cone around the lepton (not including the lepton itself). This variable is also included among the top-tagging variables, and it turns out that *iso* offers a better discrimination be-

tween signal and the multijets background, while z_{lep} is more efficient against the W background (compare Figures 9.8(b) – 9.9(b) with Figures 9.8(c) – 9.9(c)). No pre-selection cuts are made on the isolation.

The separation ΔR between the lepton and the jet with the lepton's four-momentum subtracted is also of interest. Although the lepton is required to be included in the jet, the actual separation angle still carry information on the internal structure of the jet, see Figures 9.10(a) and 9.11(a). As a quality pre-selection cut, $\Delta R < 1$.

Symbol	Definition	Pre-sel. cut
x_{lep}	$x_{\text{lep}} = (p_{\text{lep}}(p_{\text{jet}} - p_{\text{lep}}))/(p^2_{\text{jet}})$	$x_{\text{lep}} < 1.2$
z_{lep}	$z_{\text{lep}} = E_{\text{lep}}/E_{\text{jet}}$	$z_{\text{lep}} < 1.0$
iso	Relative isolation; energy in a 0.2 cone around the lepton in units of the lepton energy	–
ΔR	Lepton/jet separation angle, $\Delta R(p_{\text{lep}}, p_{\text{jet}} - p_{\text{lep}})$	$\Delta R < 1.0$
Q_{vis}	mass of the leptonic top jet candidate	–

Table 9.8: Variables for leptonic top-tagging. The subscript "lep" refers to the lepton (either electron or muon) and "jet" means the leptonic top jet candidate, which includes the lepton. See the text for more details.

Variables for hadronic top-tagging

The variables for hadronic top-tagging, Q_{jet}, Q_{W} and z_{cut} all relate to the properties of the mono-jet containing the hadronic top decay products. A summary of the variables and the pre-selection cuts are given in Table 9.9 and the variables are drawn in Figure 9.12. The hadronic top jet candidates are required to have $E_{\text{T}} > 100$ GeV, in addition to the global requirement that $E_{\text{T}} > 250$ GeV for the leading jet. In all the distributions shown, we have required that the event contains exactly one pre-selected leptonic top jet.

Q_{jet} is the mass of the hadronic top jet candidate, as drawn in Figure 9.12(a). Ideally this should be the top mass for a top event and less for a light quark-induced jet, however as previously described, even jets from massless objects appear massive.

Using the FASTJET package[106], the jet can be split into its constituents by running the $k_\perp$ algorithm[112] backwards. If the $k_\perp$ splitting level is d_{cut} when splitting the jet into two subjets A and B, a boost-invariant cut-level variable z_{cut} can be defined as

$$z_{\text{cut}} = d_{\text{cut}}/(d_{\text{cut}} + M(p_{\text{A}} + p_{\text{B}})), \tag{9.4}$$

where $M(p_{\text{A}} + p_{\text{B}})$ is the invariant mass of the two subjets A and B.

Assuming the splitting can continue and the algorithm finds three subjets, the invariant mass of each pair of these sub-jets can be computed. The mini-

Symbol	Definition	Pre-sel. cut
Q_{jet}	invariant mass of the hadronic top jet candidate	–
z_{cut}	$d_{\text{cut}}/(d_{\text{cut}} + M(p_{\text{A}} + p_{\text{B}}))$	–
Q_{W}	invariant mass of the subjet pair with lowest mass, out of three subjets	$Q_{\text{W}} > 0$

Table 9.9: Variables for hadronic top-tagging. d_{cut} is the $k_{\perp}$ splitting level into the subjets A and B. For the computation Q_{W}, the hadronic top jet candidate must be possible to split into three subjets. Additional pre-selection cuts are a requirement that the hadronic top jet candidate is not also leptonically tagged and that the ϕ angle between the hadronic top jet candidate and the leptonic jet candidate is larger than 2. See the text for more details.

mum of these pair-wise masses is called Q_{W}, and for a proper hadronic top decay, this should correspond to the W mass. However, as seen in Figure 9.12(b), this is not always the case for the Z' sample. The lower mass peak, which is more pronounced for the low mass samples ($M_{Z'} < 1.5$ TeV), is most likely an effect of either not the entire top decay being contained in the jet, or of an initial or final state radiation gluon being associated with the jet.

The only pre-selection cut applied to these variables is a requirement that the hadronic top jet candidate can be split into three subjets. This requirement can be formulated as $Q_{\text{W}} > 0$. Additional pre-selection cuts are a requirement that the hadronic top jet candidate is not also leptonically tagged and that the ϕ angle between the hadronic top jet candidate and the leptonic jet candidate is larger than 2.

It should be noted that the distributions of the backgrounds, W and multi-jets, are very similar for the hadronic top-tagging variables. This is expected, since we are looking at the hadronic side of the decay, in which these two backgrounds should be the same.

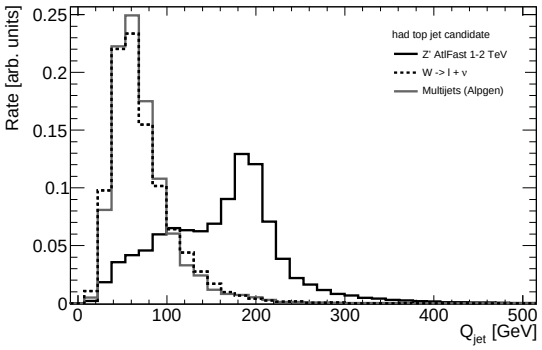

(a) Q_{jet} of the hadronic top jet candidate

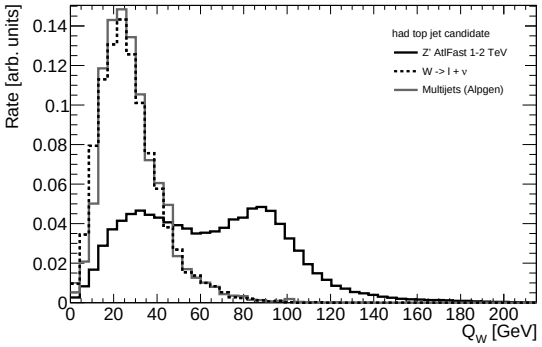

(b) Q_{W} of the hadronic top jet candidate

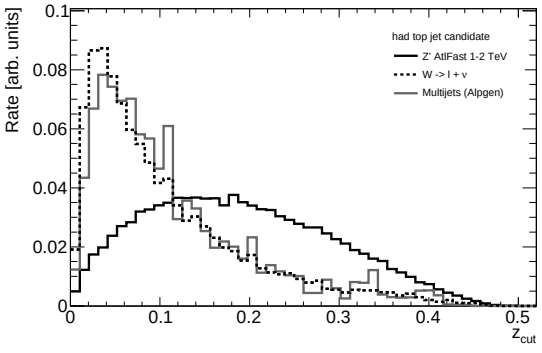

(c) z_{cut} of the hadronic top jet candidate

Figure 9.12: Variables for hadronic top-tagging: Q_{jet}, Q_{W} and z_{cut}. Comparison between signal (Z' ATLFASTII, $M_{Z'} = 1 - 2$ TeV) and background (ALPGEN W and multijets samples). All histograms have been normalised to unity.

Variable	Multijets suppression		W suppression	
	e channel	μ channel	e channel	μ channel
x_{lep}	$x_{\text{lep}} > 0.4$	$x_{\text{lep}} > 0.35$	–	–
z_{lep}	–	$z_{\text{lep}} > 0.15$	$z_{\text{lep}} < 0.8$	$z_{\text{lep}} < 0.8$
iso	$iso < 0.1$	$iso < 0.5$	–	–
ΔR	$\Delta R > 0.25$	$\Delta R > 0.15$	–	–
Q_{vis}	–	–	$Q_{\text{vis}} > 50$	$Q_{\text{vis}} > 53$

Table 9.10: Variable cuts for the leptonic top-tagging. See the text for a description of the variables.

9.3.2 Top-tagging using variable cuts

As seen in the previous section, the variables chosen for top-tagging purposes all behave distinctly different for signal and background. The most straightforward top-tagging procedure is thus to make simple cuts on the variables.

When choosing an appropriate cut value, two aspects must be considered: the signal efficiency after the cut must be reasonably high, and the background suppression should be as good as possible.

In the following plots the efficiency is displayed, when placing an upper or lower cut on the variable, together with the background suppression, computed as $S/\sqrt{S+B}$ where S is the integrated signal and B the integrated background. The signal used is the combination of all the Z' ATLFASTII samples (masses between 1 and 2 TeV) and the backgrounds have been combined into the ones containing electroweak (EWK) processes (dominated by $W+$ jets, but also including leptonic decays of single top) or the ones with quantum chromodynamical (QCD) processes, which is dominated by multijets but also contains the all-hadronic top decay. For the $S/\sqrt{S+B}$ computation, the sample production cross sections and efficiencies have been considered. A summary of the variable cuts for the leptonic top-tagging is given in Table 9.10, and for the hadronic top-tagging in Table 9.11.

The leptonic top-tag

For the variable x_{lep} the efficiency and the background suppression $S/\sqrt{S+B}$ is shown in Figure 9.13. The placement of the cut on x_{lep} is a compromise between having a reasonable signal efficiency and a good background rejection. Too sharp a cut on x_{lep} would only enhance the electroweak background. The cuts chosen are 0.4 for the electron channel and 0.35 for the muon channel.

In the electron channel, no lower cut can be placed on the variable z_{lep}, since the QCD background and the signal are too much alike, as demonstrated in Figure 9.14(a). In the muon channel, a QCD-reducing cut on z_{cut} has been

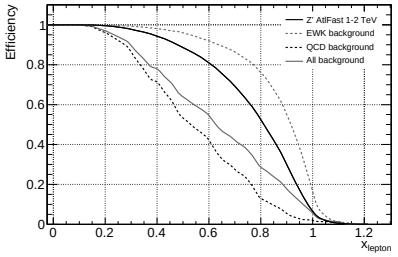

(a) Efficiency for the placement of the lower x_{lep} cut, e channel.

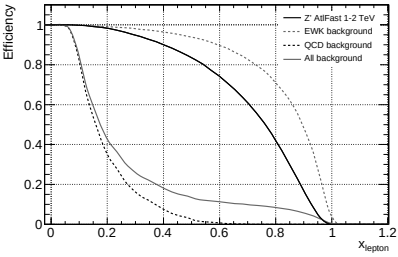

(b) Efficiency for the placement of the lower x_{lep} cut, μ channel.

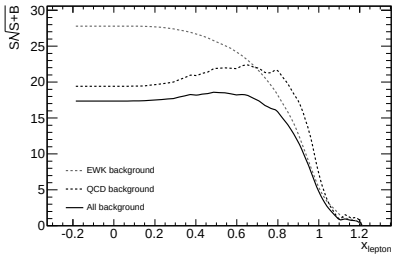

(c) $S/\sqrt{S+B}$ ratio for the placement of the lower x_{lep} cut, e channel.

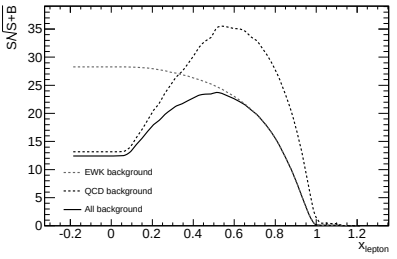

(d) $S/\sqrt{S+B}$ ratio for the placement of the lower x_{lep} cut, μ channel.

Figure 9.13: Efficiency and background suppression (signal compared to signal plus background, $S/\sqrt{S+B}$) when placing a lower cut on the x_{lep} variable. The cuts chosen are 0.4 (e channel) and 0.35 (μ channel).

placed at 0.15, which is close to the $S/\sqrt{S+B}$ peak for the combination of all the backgrounds (Figure 9.14(d)).

An upper cut on $z_{\text{lep}}$is placed at 0.8 for both the electron and the muon channel, where the signal efficiency is larger than 85%, as demonstrated in Figures 9.15(a) and 9.15(b), and the $S/\sqrt{S+B}$ is at a maximum (Figures 9.15(d) and 9.15(d)).

In Figures 9.16(a) and 9.16(c) we can see that placing the ΔR cut at $\Delta R > 0.25$ keeps 90% of the signal, while being close to the $S/\sqrt{S+B}$ peak. In the muon channel, the cut is placed at $\Delta R > 0.15$, which, although not at the $S/\sqrt{S+B}$ peak, still offers an excellent background suppression.

In the electron channel the signal efficiency in the isolation variable has a sharp kink at $iso \approx 0.1$ (Figure 9.17(a)). Placing the cut significantly higher than 0.1 would only enhance the background. Although the $S/\sqrt{S+B}$ in the muon channel (Figure 9.17(d)) also peaks at $iso \approx 0.1$, the signal efficiency is

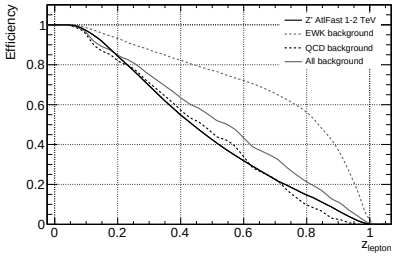

(a) Efficiency for the placement of the lower z_{lep} cut, e channel.

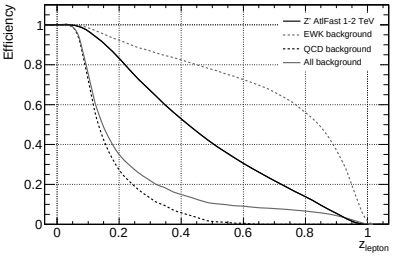

(b) Efficiency for the placement of the lower z_{lep} cut, μ channel.

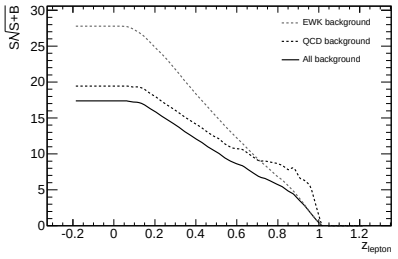

(c) $S/\sqrt{S+B}$ ratio for the placement of the lower z_{lep} cut, e channel.

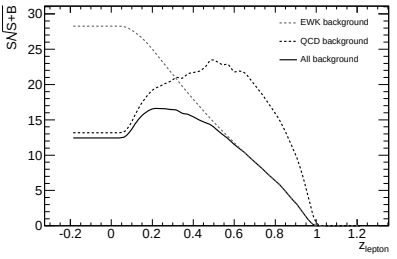

(d) $S/\sqrt{S+B}$ ratio for the placement of the lower z_{lep} cut, μ channel.

Figure 9.14: Efficiency and background suppression (signal compared to signal plus background, $S/\sqrt{S+B}$) when placing a lower cut on the z_{lep} variable. The cut value $z_{\text{lep}} > 0.15$ has been chosen for the μ channel. No upper cut on z_{lep} in the electron channel.

much lower than in the electron case, which is demonstrated in Figure 9.17(b). Instead the cut is placed at $iso = 0.5$, where the signal efficiency is about 90% and the background suppression still very good.

For the variable Q_{vis}, the $S/\sqrt{S+B}$ ratio for the electroweak background peaks at $Q_{\text{vis}} = 50$ GeV and $Q_{\text{vis}} = 53$ GeV for the electron and muon channels respectively, as seen in Figures 9.18(c) and 9.18(d). By placing the cuts at these values, a signal efficiency of about 80% is achieved in both channels (see Figures 9.18(a) and 9.18(b)).

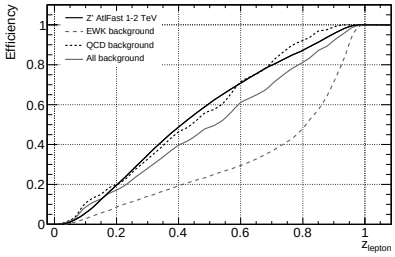

(a) Efficiency for the placement of the upper z_{lep} cut, e channel.

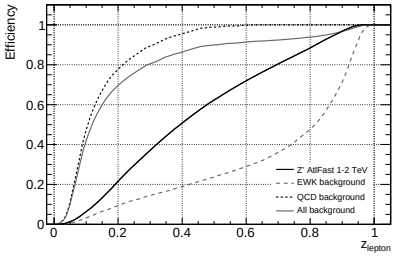

(b) Efficiency for the placement of the upper z_{lep} cut, μ channel.

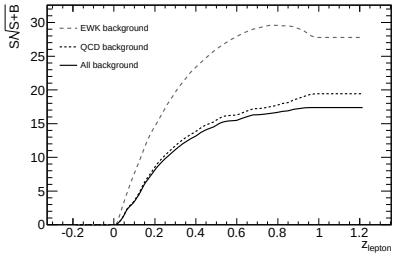

(c) $S/\sqrt{S+B}$ ratio for the placement of the upper z_{lep} cut, e channel.

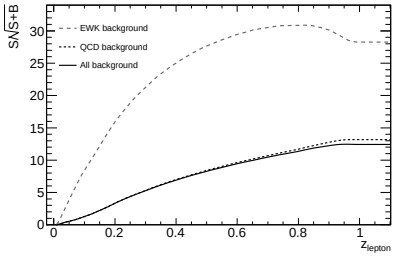

(d) $S/\sqrt{S+B}$ ratio for the placement of the upper z_{lep} cut μ channel.

Figure 9.15: Efficiency and background suppression (signal compared to signal plus background, $S/\sqrt{S+B}$) when placing an upper cut on the z_{lep} variable. The cut $z_{\text{lep}} < 0.8$ is chosen for both the electron and the muon channels.

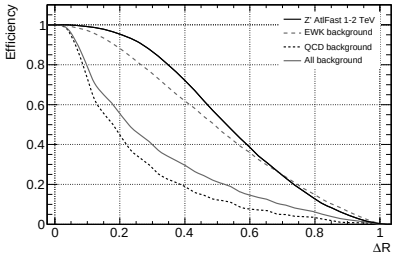

(a) Efficiency for the placement of the lower ΔR cut, e channel

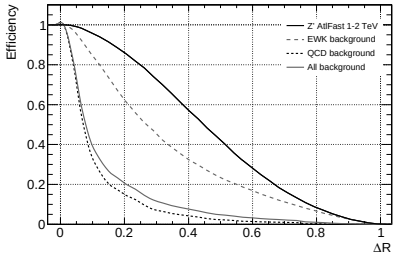

(b) Efficiency for the placement of the lower ΔR cut, μ channel

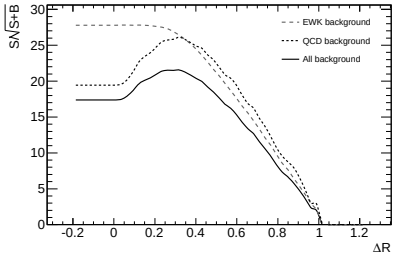

(c) $S/\sqrt{S+B}$ ratio for the placement of the lower ΔR cut, e channel

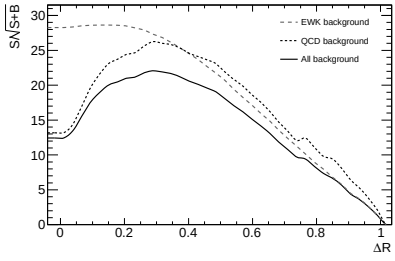

(d) $S/\sqrt{S+B}$ ratio for the placement of the lower ΔR cut, μ channel

Figure 9.16: Efficiency and background suppression (signal compared to signal plus background, $S/\sqrt{S+B}$) when placing a lower cut on the ΔR variable. The cuts chosen are $\Delta R > 0.25$ for the e channel and $\Delta R > 0.15$ for the μ channel.

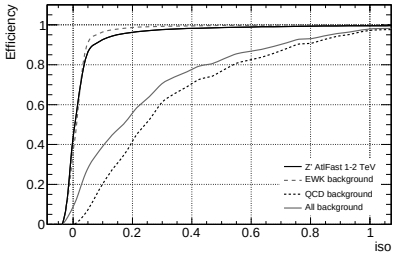

(a) Efficiency for the placement of the upper *iso* cut, *e* channel

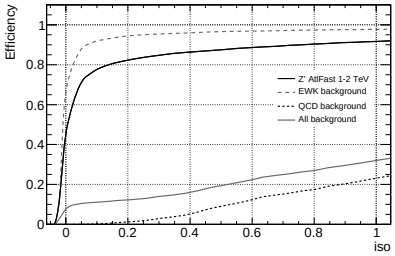

(b) Efficiency for the placement of the upper *iso* cut, μ channel

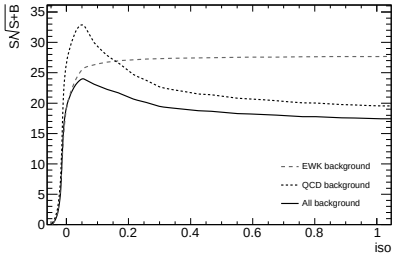

(c) $S/\sqrt{S+B}$ ratio for the placement of the upper *iso* cut, *e* channel

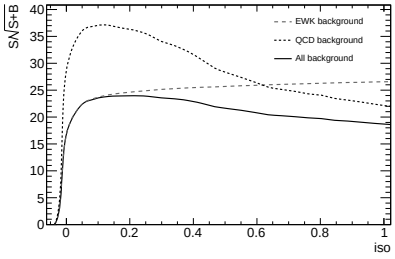

(d) $S/\sqrt{S+B}$ ratio for the placement of the upper *iso* cut, μ channel

Figure 9.17: Efficiency and background suppression (signal compared to signal plus background, $S/\sqrt{S+B}$) when placing an upper cut on the *iso* variable. The cut chosen is $iso < 0.1$ for the *e* channel and $iso < 0.5$ for the μ channel.

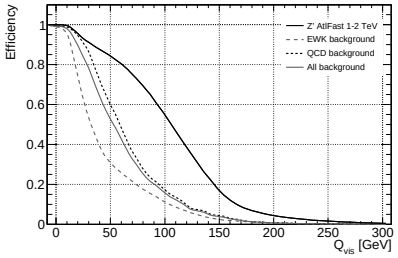

(a) Efficiency for the placement of the lower Q_{vis} cut, e channel

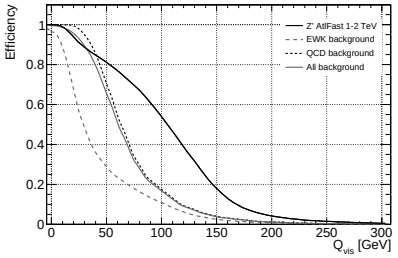

(b) Efficiency for the placement of the lower Q_{vis} cut, μ channel

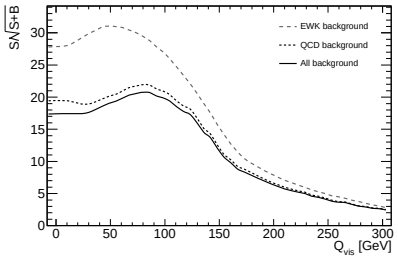

(c) $S/\sqrt{S+B}$ ratio for the placement of the lower Q_{vis} cut, e channel

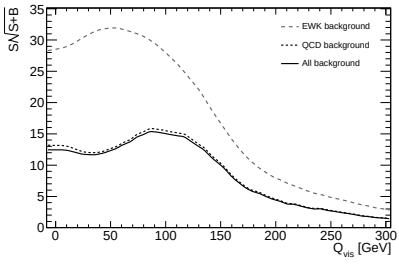

(d) $S/\sqrt{S+B}$ ratio for the placement of the lower Q_{vis} cut, μ channel

Figure 9.18: Efficiency and background suppression (signal compared to signal plus background, $S/\sqrt{S+B}$) when placing a lower cut on the Q_{vis} variable. The cuts chosen are $Qvis > 50$ GeV for the e channel and $Q_{\mathrm{vis}} > 53$ GeV for the μ channel.

Variable	cut
z_{cut}	$z_{\text{cut}} > 0.08$
Q_{W}	$Q_{\text{W}} > 30$
Q_{jet}	$Q_{\text{jet}} > 100$

Table 9.11: Top-tagging cuts, hadronic top decay.

The hadronic top-tag

For the variable Q_{jet}, the $S/\sqrt{S+B}$ ratio peaks at $Q_{\text{jet}} \approx 100$ GeV, as shown in Figure 9.19(b) and a cut at $Q_{\text{jet}} > 100$ GeV also offers a reasonable signal efficiency as demonstrated in Figure 9.19(a).

The peak of the $S/\sqrt{S+B}$ ratio of the Q_{W} variable is broad with an unclear peak at $Q_{\text{W}} \approx 30$ GeV as seen in Figure 9.20(b). A cut at $Q_{\text{W}} > 30$ GeV offers a reasonable balance between signal efficiency and background suppression.

For the z_{cut} variable, the $S/\sqrt{S+B}$ peak is also broad (Figure 9.21(b)). By placing the cut at $z_{\text{cut}} > 0.08$, we assure that the signal efficiency is larger than 85%.

In Section 9.3.6, a summary of the selection efficiencies for the leptonic top-tagging is given.

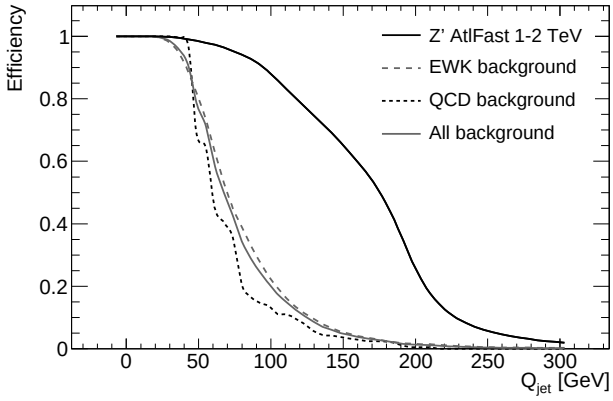

(a) Efficiency for the placement of the lower Q_{jet} cut

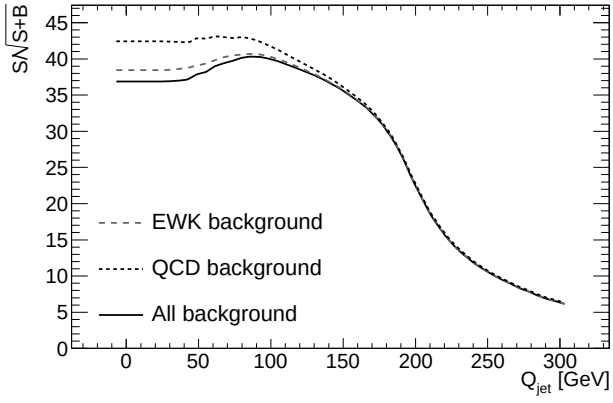

(b) $S/\sqrt{S+B}$ ratio for the placement of the lower Q_{jet} cut

Figure 9.19: Efficiency and background suppression (signal compared to signal plus background, $S/\sqrt{S+B}$) when placing a lower cut on the Q_{jet} variable. The cut chosen is $Q_{\text{jet}} > 100$ GeV.

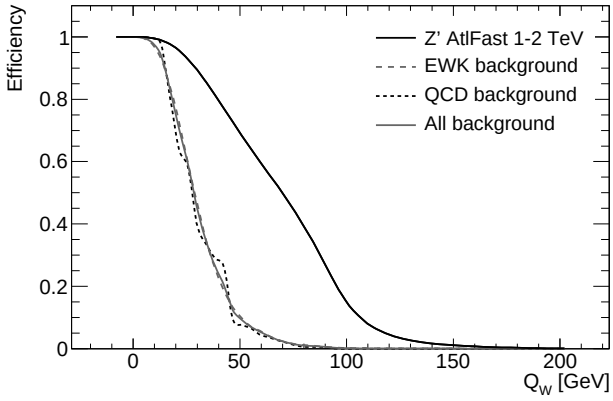

(a) Efficiency for the placement of the lower Q_{W} cut

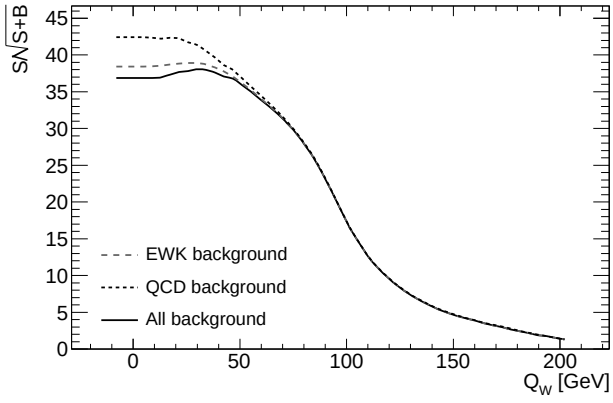

(b) $S/\sqrt{S+B}$ ratio for the placement of the lower Q_{W} cut

Figure 9.20: Efficiency and background suppression (signal compared to signal plus background, $S/\sqrt{S+B}$) when placing a lower cut on the Q_{W} variable. The cut chosen is $Q_{\mathrm{W}} > 30$ GeV.

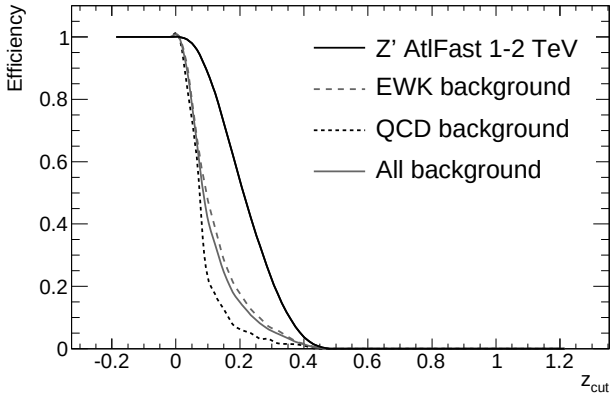

(a) Efficiency for the placement of the lower z_{cut} cut

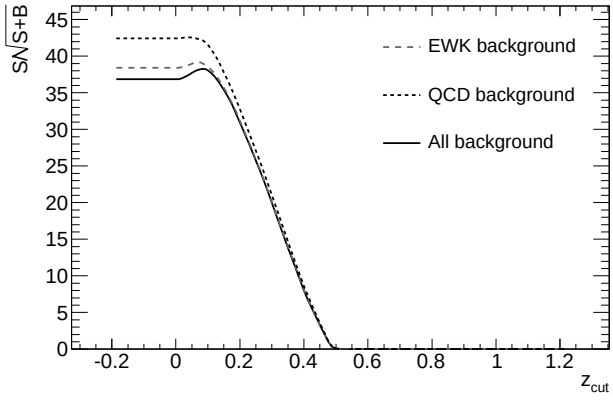

(b) $S/\sqrt{S+B}$ ratio for the placement of the lower z_{cut} cut

Figure 9.21: Efficiency and background suppression (signal compared to signal plus background, $S/\sqrt{S+B}$) when placing a lower cut on the z_{cut} variable. The cut chosen is $z_{\text{cut}} > 0.08$.

9.3.3 Top-tagging using multivariate analysis

In the previous section, the top-tagging was performed with straight-forward cuts on the input variables. A more sophisticated way of performing a selection based on many variables is to use a multivariate technique. In this section, top-tagging with the ROOT package TMVA (Tool for Multi-Variate Analysis)[108] is outlined.

The TMVA package offers a wide selection of multivariate techniques, such as different neural networks and boosted decision trees. We have chosen to use the linear discriminant analysis technique often called Fisher[113].

The Fisher method exploits the differences in sample mean between the signal and the background samples. The Fisher discriminant for event i, $F(i)$, is defined as[108]

$$F(i) = K_0 + \sum_{k=1}^{n_{var}} C_k x_k(i) \tag{9.5}$$

where the summation index k runs over all the n_{var} number of input variables x_k, K_0 is an offset that centres the mean of all signal and background discriminants F at 0 and C_k is the Fisher coefficient, which is given from

$$C_k = \frac{\sqrt{N_S N_B}}{N_S + N_B} \sum_{\ell=1}^{n_{var}} W_{k\ell}^{-1} (\bar{x}_{S,\ell} - \bar{x}_{B,\ell}). \tag{9.6}$$

In Eq. 9.6, N_S (N_B) is the number of signal (background) events and $\bar{x}_{S,\ell}$ ($\bar{x}_{B,\ell}$) is the mean of the variable x_ℓ in the signal (background) sample. The matrix elements $W_{k\ell}$ are given from

$$W_{k\ell} = \sum_{P=S,B} \langle x_{P,k} - \bar{x}_{P,k} \rangle \langle x_{P,\ell} - \bar{x}_{P,\ell} \rangle, \tag{9.7}$$

where $x_{S,k}$ ($x_{B,k}$) is the variable x_k in the signal (background sample) and bars over the variables indicate sample means as before.

The Fisher discriminants work best when the signal and background samples have distinctly different mean values, which is the case for our variables. The discriminants are constructed such that background events get a low F and signal events a high value. The average of all Fisher discriminants is 0, as given from Eq. 9.5, and the optimal cut on the discriminant is often approximately $F > 0$.

The signal consists of all the Z' ATLFASTII samples (masses $1.0 - 2.0$ TeV). The background is either the W ALPGEN samples or the ALPGEN multijets. The Fisher network is trained on a part of the sample which is then discarded in the following analysis. $1/10$ of the Z' ATLFASTII sample is used for training, $1/6$ of the multijets sample and $1/3$ of the W sample. The input samples have been weighted according to their respective cross sections, to ensure a correct treatment of the sub-samples.

Leptonic top-tagging

As for the cut-based top-tagging, the input variables for the leptonic top-tagging using Fisher discriminants are x_{lep}, z_{lep}, ΔR, Q_{vis} and the lepton isolation, for the e and μ channels.

Distributions of the Fisher discriminants, efficiencies for certain placement of the cuts and the signal-to-background efficiency ($S/\sqrt{S+B}$ ratio) are given in Figure 9.22 (electron channel) and Figure 9.23 (muon channel).

The Fisher discriminants clearly distinguish signal from background in the multijets case. For the W background however, there is a greater overlap, as can be seen from Figures 9.22(b) and 9.23(b). Especially in the muon case, there is a subset of events in the W background that form a small signal-like peak. However, the average separation is good. The cuts on the Fisher discriminants are placed in such a way that the signal efficiency is about 80% for the network trained with the multijets background and 90% signal efficiency with respect to the W background.

Hadronic top-tagging

The variables used for top-tagging are Q_{jet}, Q_{W} and z_{cut}, just as in the cut-based top-tagging.

Values of the Fisher discriminants, efficiencies for certain placement of the cuts and the signal-to-background efficiency ($S/\sqrt{S+B}$ ratio) are shown in Figure 9.24.

The Fisher discriminants are computed for the multijets background only. Since this is the hadronic side of the $t\bar{t}$ decay, we expect equal behaviour from the W background variables, as demonstrated in Section 9.3.1. In Figure 9.24(a), the distributions of the Fisher discriminants for the multijets background and the signal are shown. The spikes in the multijets distribution are an effect of the sample weighting. The low-momentum samples have a larger weight than the high-momentum samples, and a few events cause the spikes in the distribution.

The cuts on the Fisher discriminants are placed such that the average signal efficiency is about 80%. The total efficiencies for the top-tagging is listed in Table 9.14.

	Background	
Channel	Multijets	W
e channel	0.1	−0.22
μ channel	0.22	−0.27
hadronic side	−0.055	–

Table 9.12: Fisher discriminant cut values.

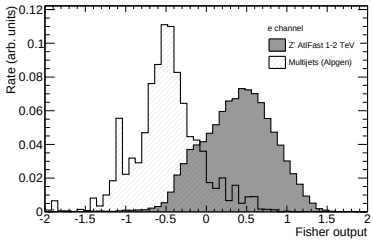

(a) Fisher discriminant F_e^{jets}, multijets background

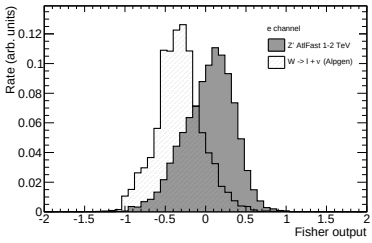

(b) Fisher discriminant F_e^W, W background

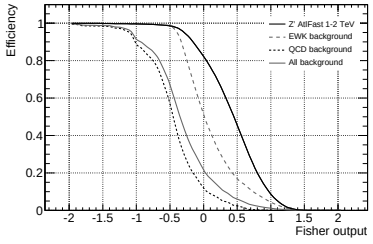

(c) Discriminant efficiency, multijets background

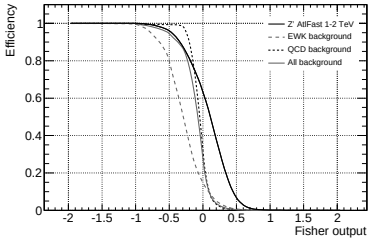

(d) Discriminant efficiency, W background

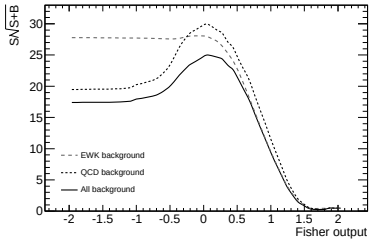

(e) $S/\sqrt{S+B}$, multijets background

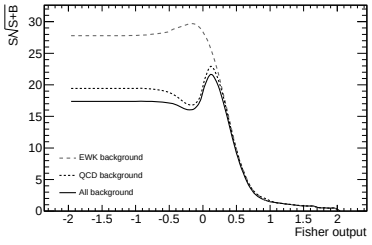

(f) $S/\sqrt{S+B}$, W background

Figure 9.22: Fisher discriminants F_e for leptonic top-tagging in the electron channel. The cuts chosen are $F_e^{\text{jets}} > 0.1$ (for the multijets background) and $F_e^W > -0.22$ (for the W background).

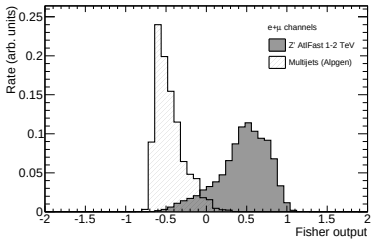

(a) Fisher discriminant F_μ^{jets}, multijets background

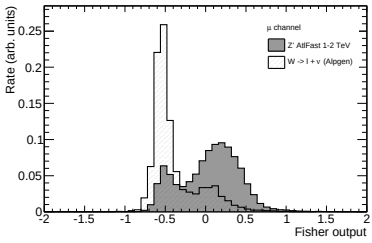

(b) Fisher discriminant F_μ^W, W background

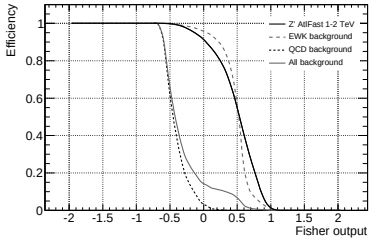

(c) Discriminant efficiency, multijets background

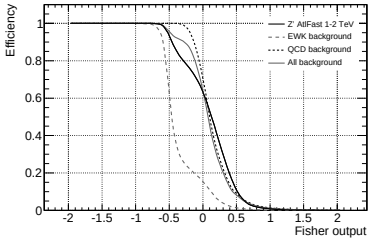

(d) Discriminant efficiency, W background

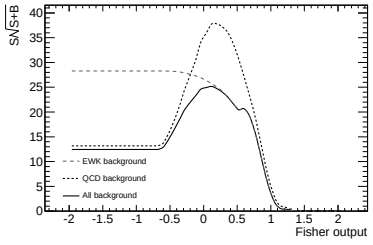

(e) $S/\sqrt{S+B}$, multijets background

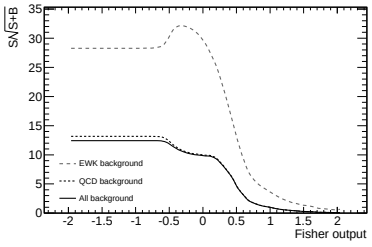

(f) $S/\sqrt{S+B}$, W background

Figure 9.23: Fisher discriminants F_μ for leptonic top-tagging in the muon channel. The cuts chosen are $F_\mu^{\text{jets}} > 0.22$ (for the multijets background) and $F_\mu^W > -0.27$ (for the W background).

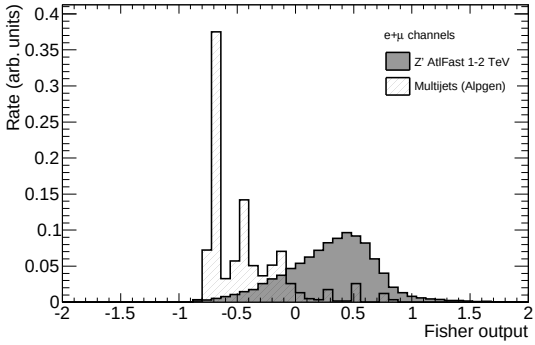

(a) Fisher discriminant F_{had}, multijets background

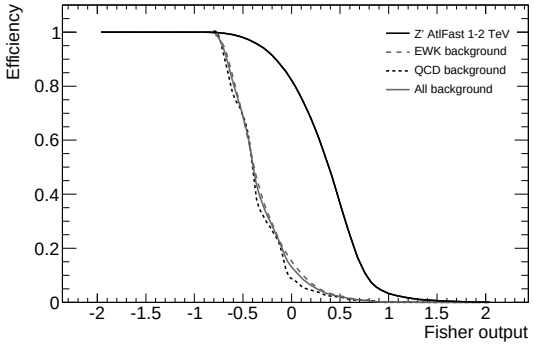

(b) Discriminant efficiency

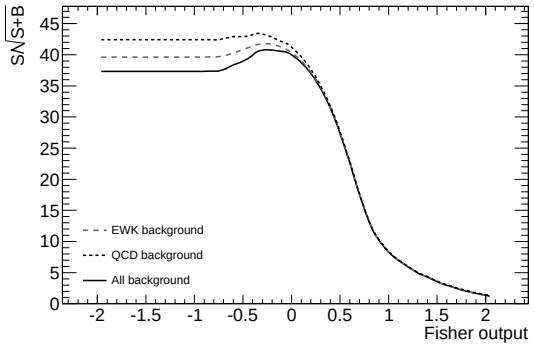

(c) $S/\sqrt{S+B}$

Figure 9.24: The Fisher discriminant F_{had} for hadronic top-tagging. The cut chosen is $F_{had} > -0.055$.

9.3.4 Tag efficiency

In Figure 9.25, the efficiency for the leptonic top-tag using the multivariate technique and the variable cuts are compared for the Z' signal, the fully simulated $t\bar{t}$ sample and the W background. The two top-tagging methods perform similarly for the backgrounds, but for the Z' signal, the MVA method shows a much more stable performance, as the efficiency is constant as a function of mass. This points to a weakness in the simple cutting procedure: as the leptonic top-tagging variables can be correlated with the invariant mass, simple cuts can introduce a mass-dependent bias. When combined in a linear discriminant, this effect is not as pronounced.

In Figure 9.26, the hadronic top-tag efficiency using the multivariate technique and the variable cuts are compared for the Z' signal, the fully simulated $t\bar{t}$ sample and the W background.

In comparing Figures 9.26(a) and 9.26(b), we can see that there is a clear difference in the hadronic top-tagging for the Z' sample and the $t\bar{t}$ sample. This effect is not (to first order) a generator problem, which is demonstrated in Figure 9.27, where the hadronic top-tagging efficiencies of the two different $t\bar{t}$ samples are compared. It should be noted that the settings of ATLFASTII is identical for the Z' and $t\bar{t}$ samples. It is more likely that the observed discrepancy is kinematic and topological difference. $t\bar{t}$ is produced both in the s-channel and the t-channel, whereas Z' only is produced through quark annihilation (s-channel process). Since Z' is an uncoloured resonance, the colour flow is also different.

In Figure 9.28, the truth match efficiency of the hadronic top jet is shown. A hadronic top jet is "truth-matched" if the true top quark from the simulation is found within a $\Delta R < 0.5$ radius from the hadronic top jet axis. As can be seen from the figure, the truth-matching is heavily deteriorated for high masses in the $t\bar{t}$ sample, which explains the lower top-tagging efficiency: at high masses, the hadronic top jet reconstructed from the $t\bar{t}$ sample is just as likely a light jet from ISR or FSR as a top jet. At higher masses, the t-channel production becomes more dominant[114], and the top-tagging techniques we have developed for the s-channel process of the Z' decay fails.

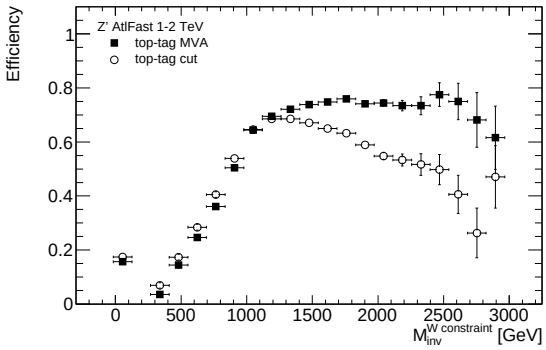

(a) Z' 1-2 TeV (PYTHIA/ATLFASTII)

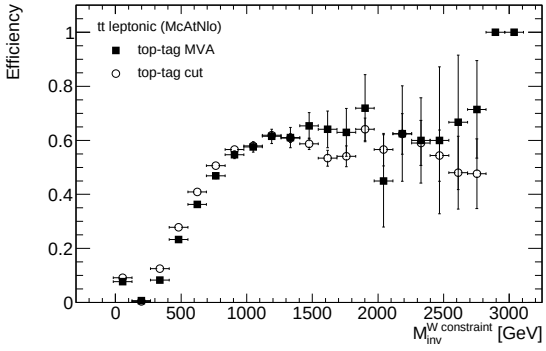

(b) $t\bar{t}$ (MCATNLO)

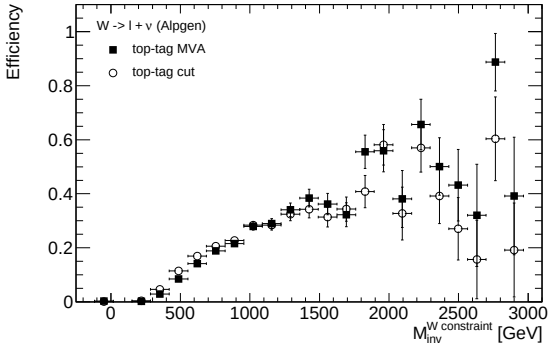

(c) W ALPGEN

Figure 9.25: Leptonic top-tag efficiency, for the Z' signal sample, the fully simulated $t\bar{t}$ sample and the W ALPGEN background. Comparison between the multivariate top-tagging technique (MVA) and the variable cut approach (cut). The combination of the leptonic channels, e and μ, is shown.

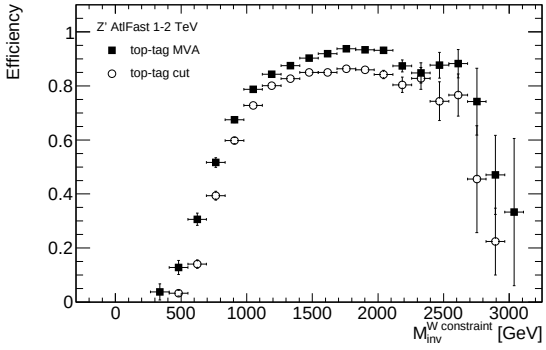

(a) Z' 1-2 TeV (PYTHIA/ATLFASTII)

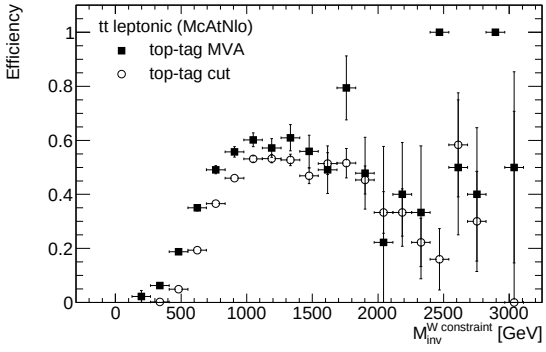

(b) $t\bar{t}$ (MCATNLO)

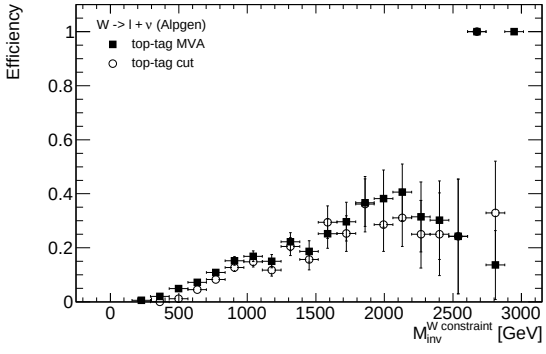

(c) W ALPGEN

Figure 9.26: Hadronic top-tag efficiency, for the Z' signal sample, the fully simulated $t\bar{t}$ sample and the W ALPGEN background. Comparison between the multivariate top-tagging technique (MVA) and the variable cut approach (cut).

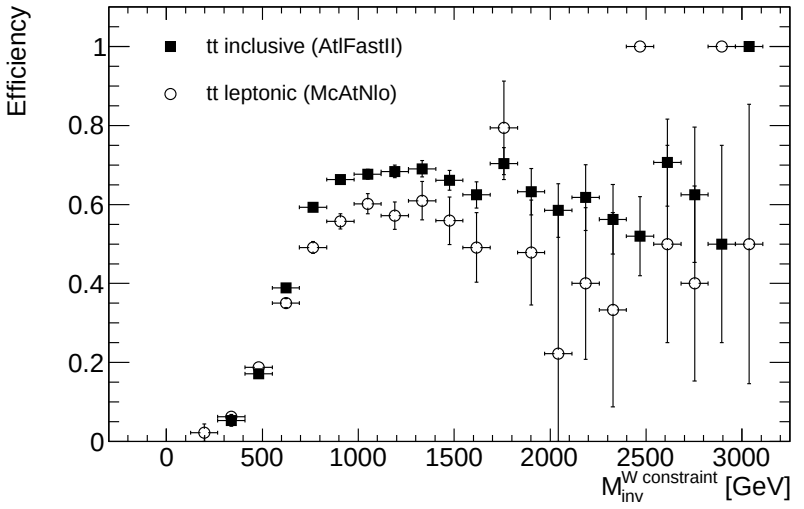

Figure 9.27: Hadronic top-tag efficiency using the multivariate technique. Comparison between different $t\bar{t}$ generators.

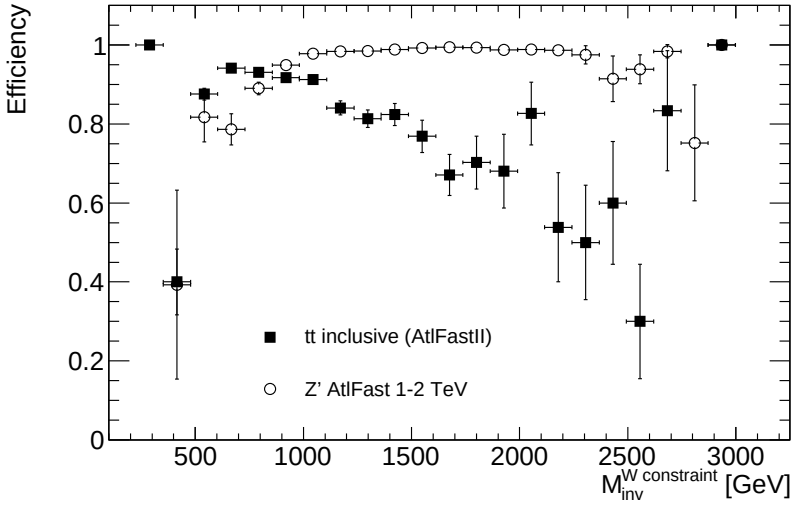

Figure 9.28: Efficiency of the hadronic top quark truth-match for the Z' and $t\bar{t}$ ATLFASTII samples. An event is truth-matched if the true top quark from the simulation is within a ΔR distance of 0.5 from the hadronic top jet. These events contain exactly one leptonic top-tag and exactly one hadronic top-tag.

9.3.5 Trigger efficiency for selected objects

In Figure 9.29 the trigger efficiency is shown as a function of the invariant mass.

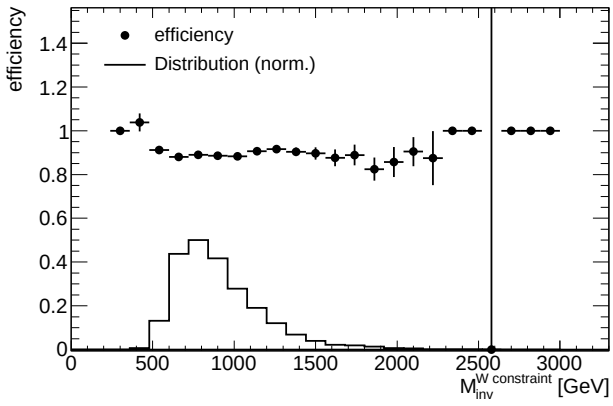

(a) Trigger efficiency for the $t\bar{t}$ sample, simulated with MCATNLO.

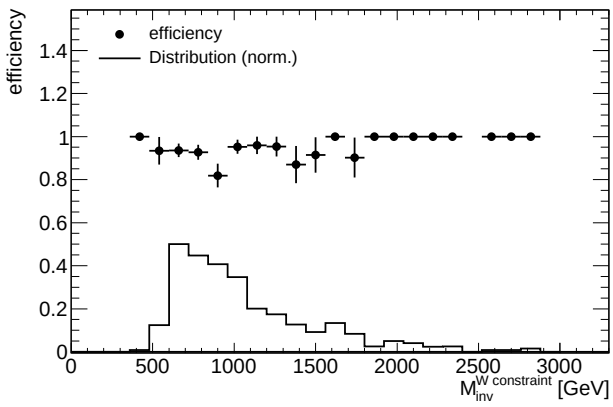

(b) Trigger efficiency for the W sample, simulated with ALPGEN.

Figure 9.29: Trigger efficiency as a function of invariant mass after the final selection, for the $t\bar{t}$ and the W samples.

The trigger efficiency is studied after all pre-selection and selection cuts have been applied, i.e. one lepton has been reconstructed, $E_{\mathrm{T}}^{\mathrm{miss}} > 20$ GeV, $E_{\mathrm{T}} > 250$ GeV for the leading jet of the event and the event contains exactly one lepton-tagged top jet, and exactly one hadron-tagged top jet. The efficiency shown corresponds to events that have passed all these cuts also are

required to pass the trigger cut, which means that either the `ele20_loose` or the `muo20` trigger has fired in the same region as the reconstructed lepton of the same kind.

The trigger efficiency is roughly flat as a function of invariant mass, which is desirable. The trigger was not simulated in the ATLFASTII samples, but since the trigger efficiency is flat in the invariant mass, no special trigger acceptance is needed in the following analysis, and to first order we can assume that the shape of the invariant mass spectrum is the same before and after the trigger selection.

9.3.6 All efficiencies – overview

We can now summarise all the efficiencies from the pre-selection, the top-tagging and the trigger in Tables 9.13 (for the cut-based top-tagging) and 9.14 (top-tagging with MVA).

ch.	LAcc	LRec	$E_{\mathrm{T}}^{\mathrm{miss}}$	E_{T}^{jet}	lqtag	lwtag	htag	trig	match	total	ev.
Z' 1 TeV											
e	81.5	73.6	94.1	77.7	76.9	71.4	71.4	100.0	100.0	17.2	489
μ	84.8	79.7	94.0	77.7	71.8	69.5	68.2	78.5	100.0	13.2	376
Z' 2 TeV											
e	87.5	70.0	97.1	93.7	68.8	85.2	80.9	99.5	100.0	26.3	730
μ	89.4	78.5	97.0	93.0	60.5	82.3	82.0	81.2	100.0	21.0	587
$t\bar{t}$ leptonic decays, MCATNLO											
e	74.0	72.9	89.6	11.4	69.1	58.6	41.0	99.8	99.9	0.91	6007
μ	79.0	79.5	90.4	11.1	68.7	55.3	39.6	78.9	99.8	0.75	5057
$t\bar{t}$ ATLFASTII											
e	76.4	75.1	91.7	45.6	70.3	62.2	49.0	–	99.9	5.15	2870
μ	81.6	79.6	92.2	45.2	71.4	58.2	47.3	–	100.0	5.31	2965
$t\bar{t}$ all-hadronic decays, MCATNLO											
e	–	1.2	40.2	15.1	4.8	68.0	47.1	100.0	–	$1\cdot10^{-3}$	8
μ	–	1.7	46.1	28.0	8.3	70.4	29.5	73.1	–	$3\cdot10^{-3}$	29
W ALPGEN											
e	44.8	77.2	89.7	0.2	55.4	28.8	13.0	100.0	99.4	$1\cdot10^{-3}$	162
μ	47.0	89.3	91.8	0.2	58.8	24.8	13.7	85.6	100.0	$1\cdot10^{-3}$	155
Multijets, ALPGEN											
e	–	0.1	5.7	1.2	6.5	28.3	12.9	91.8	–	$1\cdot10^{-7}$	11
μ	–	0.0	15.0	5.2	1.3	63.7	4.9	28.6	–	$2\cdot10^{-8}$	2

Table 9.13: Selection efficiency in percent for all cuts. Cut-based top-tagging selection. See the text for a description of the column titles.

In the tables, the efficiency for each cut is listed column-wise. The number given is the efficiency when going from the previous cuts to the current one. The only exception is the "total" column which shows the total efficiency. The "ev" column shows the number of events that have survived all the cuts.

ch.	LAcc	LRec	$E_{\mathrm{T}}^{\mathrm{miss}}$	E_{T}^{jet}	lqtag	lwtag	htag	trig	match	total	ev.
Z' 1 TeV											
e	81.5	73.6	94.1	77.7	61.2	80.3	76.5	100.0	99.6	16.4	468
μ	84.8	79.7	94.0	77.7	77.5	63.1	75.6	79.8	100.0	14.6	415
Z' 2 TeV											
e	87.5	70.0	97.1	93.7	71.2	93.8	88.7	97.1	99.8	32.0	888
μ	89.4	78.5	97.0	93.0	75.0	86.3	88.5	79.9	100.0	29.0	811
$t\bar{t}$ leptonic decays, MCATNLO											
e	74.4	72.9	89.6	11.2	52.3	71.5	50.4	99.2	100.1	1.02	1405
μ	79.0	79.4	90.5	11.0	75.8	49.2	48.7	78.9	99.9	0.90	1312
$t\bar{t}$ ATLFASTII											
e	76.4	75.1	91.7	45.6	52.9	75.0	58.8	–	99.7	5.59	3113
μ	81.6	79.6	92.2	45.2	76.9	53.5	58.3	–	100.0	6.49	3621
$t\bar{t}$ all-hadronic decays, MCATNLO											
e	–	1.2	40.2	15.1	25.6	77.4	44.7	93.5	–	$6 \cdot 10^{-3}$	63
μ	–	1.7	46.1	28.0	2.9	88.6	33.3	76.9	–	$1 \cdot 10^{-3}$	14
W ALPGEN											
e	44.8	77.2	89.7	0.2	27.9	51.1	14.9	100.0	99.4	$1 \cdot 10^{-3}$	167
μ	47.0	89.3	91.8	0.2	82.1	19.0	15.7	82.8	100.0	$1 \cdot 10^{-3}$	183
Multijets, ALPGEN											
e	–	0.1	5.7	1.2	7.6	79.4	8.9	74.0	–	$2 \cdot 10^{-7}$	20
μ	–	0.0	15.0	5.2	0.3	95.6	11.9	0.0	–	0	0

Table 9.14: Selection efficiency in percent for all cuts. Top-tagging with Fisher discriminants. See the text for a description of the column titles.

The term "ch." indicates the electron or the muon channel. We start with the set of all events that contain a truth lepton from a W decay (possibly via the decay of a τ), or, in the case of QCD processes, with all events. "LAcc" is the lepton acceptance, that is the fraction of truth leptons that fall within the fiducial region of the detector. This column is empty for QCD processes, that lack truth leptons. "LRec" indicates the rate of events that passes the lepton reconstruction criterion. "$E_{\mathrm{T}}^{\mathrm{miss}}$" and "$E_{\mathrm{T}}^{jet}$" are the cuts on the $E_{\mathrm{T}}^{\mathrm{miss}}$ and the E_{T} of the leading jet, respectively. "lqtag" and "lwtag" indicate the amount of events that survive the multijets and W-reducing leptonic top-tagging. The term "htag" is the hadronic top-tag, while "trig" is the trigger requirement, which is empty for the ATLFASTII samples. "match" indicate how many of the reconstructed leptons that are also associated with a truth lepton. This column is empty for QCD processes.

As seen from Tables 9.13 and 9.14, the two different methods for top-tagging perform surprisingly similar when looking at the overall efficiency for signal and background. However, there are hidden differences in the performance between the two techniques, which was demonstrated in Figure 9.25(a), where the efficiency in the leptonic top-tagging is shown to be mass-dependent for the Z' signal sample.

Although the multivariate analysis top-tag performs slightly better in terms of signal efficiency and background suppression, the cut-based version is much more transparent and less likely to contain unknown biases. It is thus preferable for applying to early collision data. In the next chapter, only the cut-based top-tags will be used. It should be kept in mind, though, that the multivariate top-tagging seems to perform better at high masses, and its stability should be investigated further.

9.3.7 The invariant mass spectrum

The invariant mass spectrum, for all the backgrounds and the Z' signal at masses 1 and 2 TeV is drawn in Figure 9.30. The invariant mass is computed from the leptonic top jet, the hadronic top jet and the $E_{\mathrm{T}}^{\mathrm{miss}}$. The neutrino z component is estimated using a W mass constraint, with the assumptions that the lepton and the neutrino originate from a W and that $E_{\mathrm{T}}^{\mathrm{miss}} = E_{\mathrm{T}}^{\nu}$ [115, 116, 117, 118, 119].

In Figure 9.31 the backgrounds have been summed and consistently fitted with an exponential function in the range $800 < M_{inv} < 2500$ GeV.

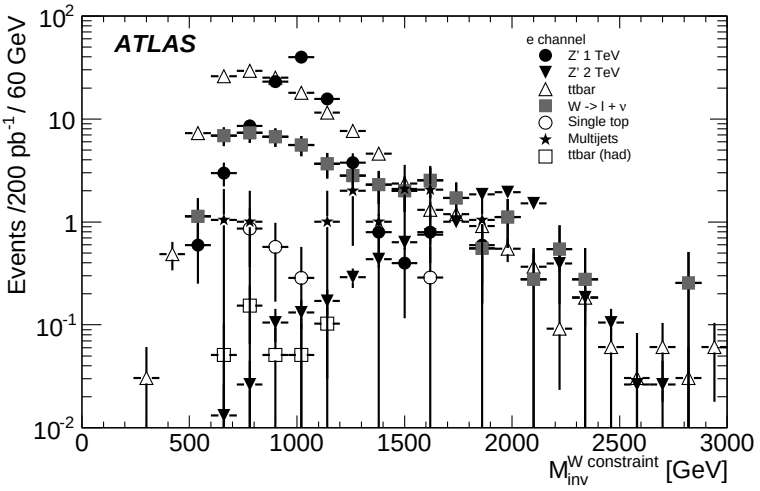

(a) Electron channel.

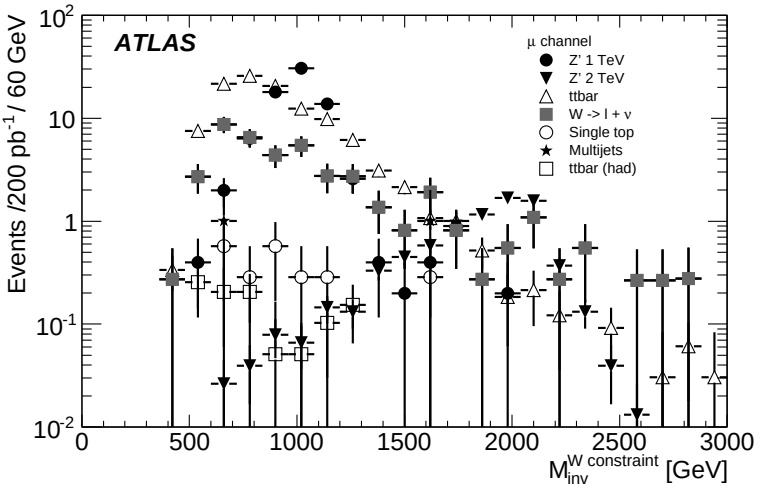

(b) Muon channel.

Figure 9.30: Invariant mass in the single lepton channels, after selection.

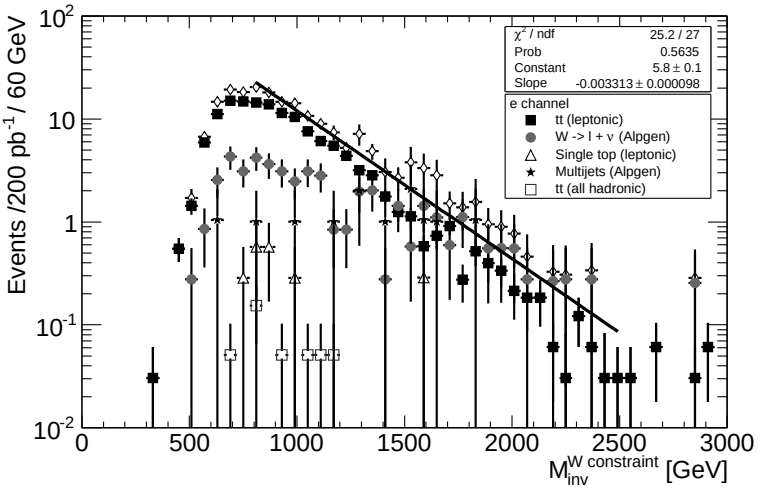

(a) Electron channel.

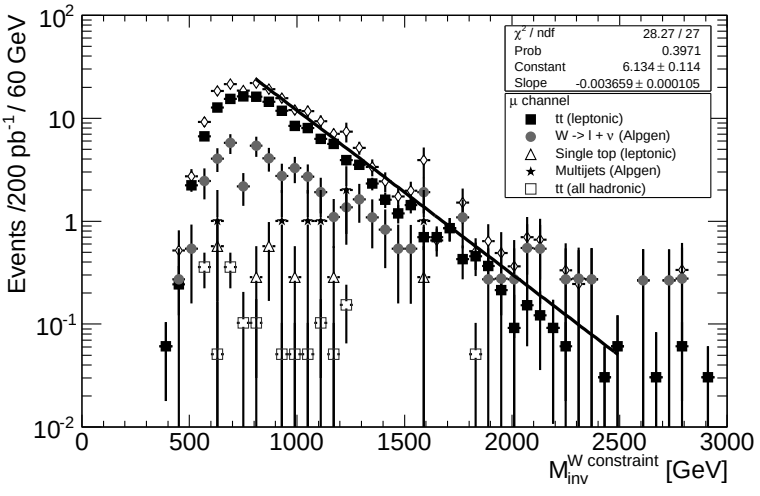

(b) Muon channel.

Figure 9.31: Invariant mass in the single lepton channels, after all selections, background only. Top-tagging using variable cuts. The backgrounds have been summed, and fitted with an exponential.

10. Estimated cross section limits

In the previous chapter, the top-tagging technique was described and its performance investigated. We saw that the background follows an exponential shape after the top-tagging selection. Now we can start to investigate how to find a signal in the invariant top mass spectrum, and how large cross sections we need in order to find the signal in 200 pb^{-1} of data from $\sqrt{s} = 10$ TeV collisions.

In this chapter, we test the signal and background hypothesis in pseudo-experiments, and extract the measured cross section for different hypothesised signal cross sections. From the different outcomes of the pseudo-experiments, the experimental sensitivity and a lower limit on the cross sections that can be seen for this particular set-up can be determined.

10.1 Cross section extraction

The cross section limits are extracted using pseudo-experiments, which are performed in the following way: we create a "data mix" from the standard model backgrounds ($t\bar{t}$, multijets, $W \to \ell\nu$, single top) and a Z' signal sample at a particular mass $1 \leq M_0 \leq 2$ TeV and a given cross section σ_{theory}. Then we draw events from a Poisson distribution, appropriate for the expected number of events at 200 pb^{-1} of integrated luminosity.

The normalised data mix is fitted with a signal-plus-background hypothesis. As background shape, we assume an exponential function, $C_\ell \cdot e^{-\lambda_\ell \cdot M_{inv}}$, which is consistent with the shape of our simulated background samples after the top-tagging selection, as shown in Figure 9.31. As signal, we use the shape of the simulated Z' sample, at the fixed mass point M_0. At this point, the mass must be fixed in order to fix the signal hypothesis. If the mass is left as a free parameter of the fit, the model tested is undefined in the absence of a signal. We fit the electron and muon channels simultaneously with an extended[1] binned maximum likelihood fit[9]. The likelihood function is transformed to a χ^2 distribution[9] for simplicity. We have five parameters of the fit: the signal cross section σ, and the parameters of the exponential backgrounds; C_e, λ_e, C_μ, λ_μ. It should be noted that we extract one single cross section from the simultaneous fit of the electron and muon channels.

[1] The *extended* binned maximum likelihood fit is used, i.e. the total number of events is Poisson distributed, since we want to measure a cross section, which is closely correlated to the total number of events observed.

For each pseudo-experiment, we get a measured cross section, σ_{meas}. By repeating the pseudo-experiments over and again, changing Poisson fluctuations, start guesses for the fit and σ_{theory}, we obtain a set of measured cross sections, from which experimental sensitivity and a cross section upper limit can be determined.

In the following sections we will explore two different ways of obtaining cross section limits: a frequentistic, and a Bayesian.

10.1.1 The frequentist's approach: Feldman-Cousins limits

A common problem when searching for a new, hitherto unknown, signal is the a priori decision on whether to make a measurement, and set a double-sided confidence limit on the parameter measured, or to set an upper limit. If this decision is left until after the data has been analysed, the consequences could be that the measured quantity ends up outside the allowed region, which renders the measurement useless (lack of *coverage*) or that an inherently worse experiment in terms of instrument performance can set a better limit than a more well-designed experiment, as pointed out in Ref. [120]. The way to handle this ambiguity is also described in Ref. [120]: instead of "flip-flopping" between single or double sided confidence levels, we extract the confidence levels from data using a Neyman construction[121], an example of which is given in Figure 10.1. We build the Neyman construction from the σ_{meas} distributions of our pseudo-experiments. For a given σ_{theory}, the distribution of σ_{meas} is Gaussian. For each σ_{meas} distribution, we compute the Gaussian mean m and Gaussian spread s. From the Feldman-Cousins prescription[120], a 95% double-sided confidence level for a $x > 0$ Gaussian is achieved if

$$m = 1.6 \cdot s. \tag{10.1}$$

We want to find the lowest σ_{theory} that gives us a distribution that fulfils Eq. 10.1. In Figure 10.1, the point $m - 1.6 \cdot s$ in each σ_{meas} distribution is indicated with a grey line. Where this line crosses the σ_{theory}-axis, we have the lowest σ_{theory} needed to just barely find a double sided 95% confidence level, which is our cross section limit for the lowest signal cross section needed for a 95% confidence level observation.

This procedure can be done for each mass point, yielding a cross section limit as a function of mass, see Figure 10.3.

10.1.2 Bayesian method

The second method to extract cross section limits is the Bayesian approach[122], where we start from the σ_{meas} distribution from the pseudo-experiments, when $\sigma_{theory} = 0$, from now on denoted σ^0_{meas}. An example distribution is shown in Figure 10.2.

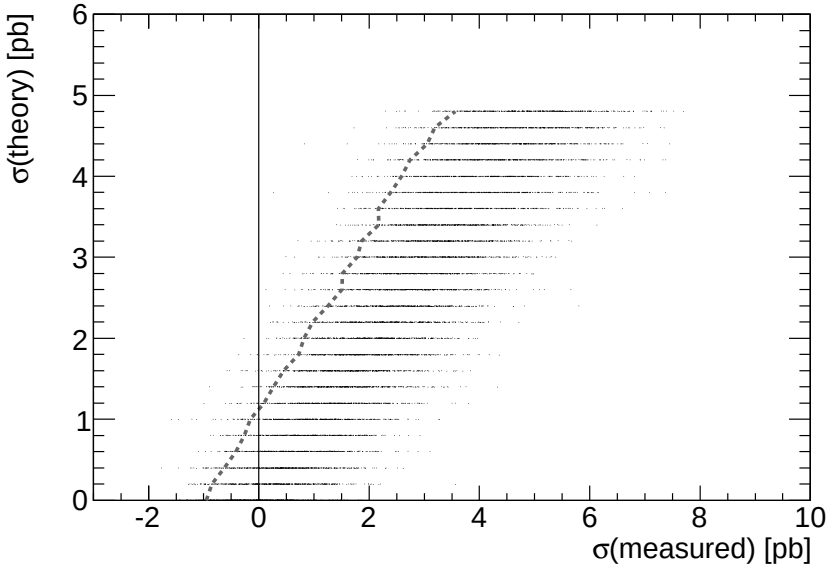

Figure 10.1: Example of the Neyman construction. Each horizontal line actually consists of a Gaussian distribution of measured cross sections. The grey dotted line indicates $< mean > -1.6 \cdot < spread >$ for each dirstribution. A double-sided 95% CL is reached when $< mean > -1.6 \cdot < spread >= 0$. In this particular example, the signal mass is 1.3 TeV and the cut-based version of the selection has been used.

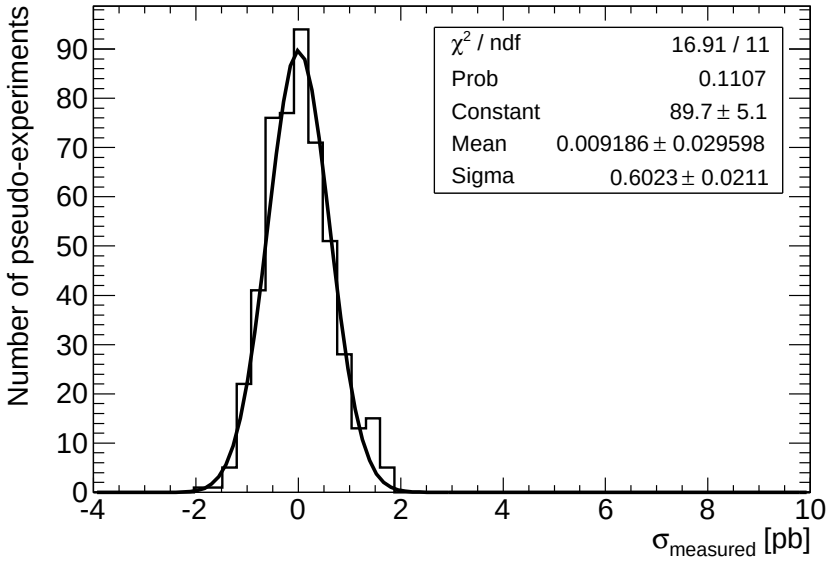

Figure 10.2: Example of a σ_{meas} distribution. In this case $M_{Z'}$ = 1.3 TeV and the cut-based selection has been used.

M (GeV)	χ^2/ndf	Prob	Gaus. mean	Gaus. sigma	σ_{Bayes} (pb)	σ_{FC} (pb)
1000	41.65/26	0.03	0.07 ± 0.08	1.55 ± 0.07	3.07 ± 0.05	2.52 ± 0.03
1100	35.67/19	0.01	0.00 ± 0.04	0.93 ± 0.03	1.81 ± 0.03	1.60 ± 0.02
1200	26.06/17	0.07	0.02 ± 0.03	0.67 ± 0.03	1.32 ± 0.04	1.24 ± 0.02
1300	16.91/11	0.11	0.01 ± 0.03	0.60 ± 0.02	1.18 ± 0.04	1.09 ± 0.02
1400	8.89/9	0.45	0.03 ± 0.02	0.52 ± 0.02	1.04 ± 0.03	0.96 ± 0.02
1500	2.78/8	0.95	0.01 ± 0.02	0.44 ± 0.01	0.85 ± 0.03	0.85 ± 0.02
1600	6.36/7	0.50	-0.03 ± 0.02	0.43 ± 0.02	0.81 ± 0.03	0.82 ± 0.02
1700	4.01/7	0.78	-0.01 ± 0.02	0.39 ± 0.01	0.71 ± 0.05	0.76 ± 0.02
1800	16.48/11	0.12	0.01 ± 0.01	0.32 ± 0.01	0.60 ± 0.04	0.65 ± 0.02
1900	19.43/12	0.08	-0.01 ± 0.01	0.29 ± 0.01	0.55 ± 0.04	0.65 ± 0.02
2000	24.64/11	0.01	-0.01 ± 0.01	0.25 ± 0.01	0.46 ± 0.03	0.61 ± 0.02

Table 10.1: Cross section limit summary for each model mass. χ^2/ndf, Prob (probability), Gaussian mean and Gaussian sigma refers to the Gaussian fit to the distribution of σ_{meas} in absence of signal, from which the Bayesian cross section limit is deived. The final column contains the Feldman-Cousins cross section limits.

Bayes theorem[123, 124] states that the probability of σ, given n, is

$$P(\sigma|n) \cdot P(n) = P(n|\sigma) \cdot P(\sigma) \tag{10.2}$$

where $P(n|\sigma)$ is the probability of n, given σ, $P(n)$ is the probability of n and $P(\sigma)$ is the probability of σ. In our case, we can interpret σ as the theoretical cross section σ_{theory} and n as our data σ_{meas}. The question of the average expected upper limit σ' for a 95% credibility limit is then answered by integrating Eq. 10.2,

$$\int_{\sigma'}^{\infty} P(\sigma|n) d\sigma = \int_{\sigma'}^{\infty} \frac{P(n|\sigma) \cdot P(\sigma)}{P(n)} d\sigma \leq 0.05 \tag{10.3}$$

where $P(n)$ now is a normalisation (essentially the integral of the σ_{meas} distribution). Since we don't know the probability $P(\sigma)$, we assume it is uniform for positive σ and vanishing otherwise (reflecting our *prior* knowledge of the cross section, i.e. only that it cannot be negative). $P(n|\sigma)$ is simply the distribution of Figure 10.2.

This integration can be performed for all the different signal masses, and reflects the experimental sensitivity of the set-up, that is how large a signal we could measure in the absence of a signal.

10.1.3 Cross section limits

In Figure 10.3 and Table 10.1, a summary of the 95% CL Bayesian and Feldman-Cousins limits are given. In the table, the parameters of the Gaus-

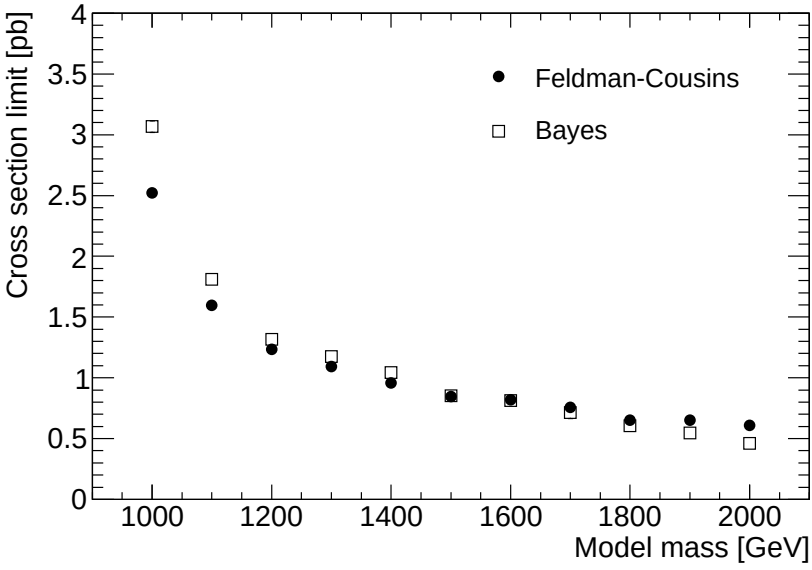

Figure 10.3: Cross section limits, 95% CL. Bayes and Feldman-Cousins limits. The cut-based selection has been used. The error bars indicate the computational errors only.

sian fits to the σ^0_{meas} distributions are given, as well as the χ^2/ndf of the fit, and the fit probability.

In Figure 10.3, it is demonstrated that the Bayesian and the Feldman-Cousins limits agree reasonably well, which indicates a robustness in the pseudo-experiments and the limit extraction.

10.2 Systematic uncertainties

So far, we have only considered the samples and cuts as fixed and given. However, there may be unknown biases and uncertainties in the data, which should be treated as systematic uncertainties[125]. In the following, we consider a jet energy scale (JES) uncertainty of 10%, a jet energy resolution (JER) smear of $25\%/\sqrt{E}+5\%$ and a luminosity shift of 20%. The jet energy scale is the correspondence between the jet energy of the simulation and the data, and the shift reflects our uncertainty of the calibration and jet acceptance in early data. The jet energy resolution has been discussed in Chapter 7. We perform an artificial worsening of the jet energy resolution by multiplying the jet energy of each event with the sum of two random numbers drawn from Gaussian distributions, one with spread $0.25/\sqrt{E}$ and the other with spread 0.05. For the jet energy scale and resolution shifts, we have shifted the model, but kept the

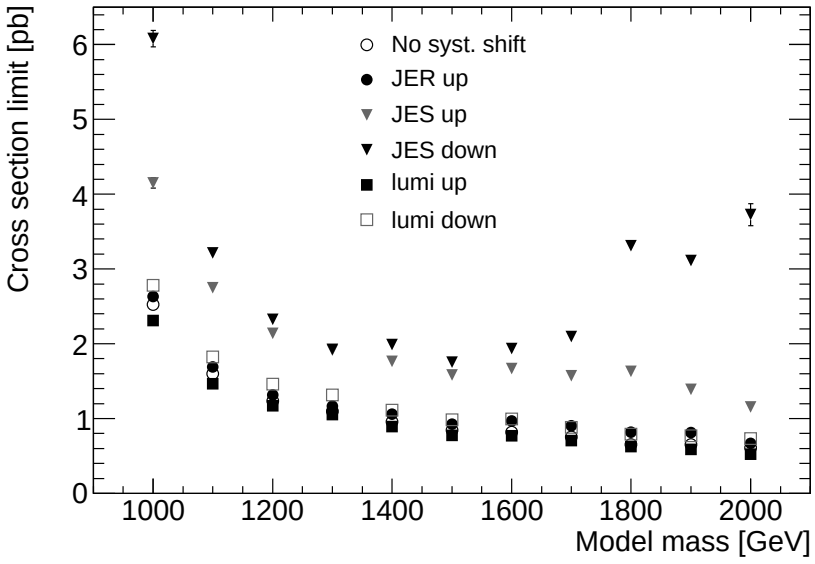

Figure 10.4: Cross section limits, 95% CL. Feldman-Cousins limits after systematic shifts. The cut-based selection has been used. Computational errors only.

signal-plus-background used in the data mix at a fixed level. In the luminosity case, the data mix is rescaled, but not the signal templates.

We compute cross sections after each shift with the Neyman construction. The signal and model must be different by the shift, otherwise we don't see the full effect of the systematics, hence the Bayesian integration wouldn't give us the correct answer here, since no signal is present in the data mix, as the integration is done on the σ_{meas} distribution when $\sigma_{theory} = 0$.

For each systematic effect, we find the corresponding Gaussian smear that has to be added to the σ^0_{meas} distribution, such that the Bayesian limit computed from the convolution is the same as the FC limits with the systematic shift. The values of the added Gaussian spreads for each mass point and systematic shift is given in Tables 10.2 (model masses $1.0 - 1.5$ TeV) and 10.3 ($1.6 - 2.0$ TeV). In the tables, u means shift up, and d means shift down. The number indicates the percentage of the shift. Hence JESu10 means a jet energy scale shift up by 10%.

For each systematic uncertainty, we obtain the cross section limit for the shift up and the shift down (except in the case of the jet energy resolution, which can only become worse). For each systematical effect, we determine which shift, up or down, gives the largest cross section limit worsening. Half the extra Gaussian spread for the worst shift of each systematical effect is added in quadrature for a combined average smearing due to the systematical uncertainty. From the combined smear, we can compute a final cross section

Mass (GeV)	Syst.	σ_{nosyst} (pb)	σ_{syst} (pb)	added spread (pb)
1000	JERu25	3.076 ± 0.005	2.630 ± 0.030	0.000 ± 0.000
1000	JESu10	3.076 ± 0.005	4.153 ± 0.071	1.448 ± 0.006
1000	JESd10	3.076 ± 0.005	6.081 ± 0.109	2.711 ± 0.002
1000	lumu20	3.076 ± 0.005	2.311 ± 0.025	0.000 ± 0.000
1000	lumd20	3.076 ± 0.005	2.783 ± 0.032	0.000 ± 0.000
	Combined		4.028 ± 0.005	1.355 ± 0.009
1100	JERu25	1.826 ± 0.005	1.693 ± 0.027	0.000 ± 0.000
1100	JESu10	1.826 ± 0.005	2.749 ± 0.035	1.047 ± 0.004
1100	JESd10	1.826 ± 0.005	3.215 ± 0.046	1.351 ± 0.002
1100	lumu20	1.826 ± 0.005	1.465 ± 0.020	0.000 ± 0.000
1100	lumd20	1.826 ± 0.005	1.824 ± 0.028	0.000 ± 0.000
	Combined		2.256 ± 0.005	0.675 ± 0.009
1200	JERu25	1.323 ± 0.005	1.315 ± 0.012	0.000 ± 0.000
1200	JESu10	1.323 ± 0.005	2.139 ± 0.028	0.861 ± 0.003
1200	JESd10	1.323 ± 0.005	2.329 ± 0.026	0.979 ± 0.003
1200	lumu20	1.323 ± 0.005	1.173 ± 0.018	0.000 ± 0.000
1200	lumd20	1.323 ± 0.005	1.461 ± 0.025	0.322 ± 0.009
	Combined		1.743 ± 0.005	0.586 ± 0.015
1300	jeru25	1.182 ± 0.005	1.165 ± 0.016	0.000 ± 0.000
1300	jesu10	1.182 ± 0.005	1.917 ± 0.032	0.769 ± 0.006
1300	jesd10	1.182 ± 0.005	1.924 ± 0.024	0.778 ± 0.003
1300	lumu20	1.182 ± 0.005	1.052 ± 0.019	0.000 ± 0.000
1300	lumd20	1.182 ± 0.005	1.316 ± 0.024	0.297 ± 0.004
	Combined		1.519 ± 0.005	0.490 ± 0.010
1400	JERu25	1.045 ± 0.005	1.058 ± 0.019	0.128 ± 0.006
1400	JESu10	1.045 ± 0.005	1.764 ± 0.028	0.734 ± 0.003
1400	JESd10	1.045 ± 0.005	1.989 ± 0.036	0.871 ± 0.003
1400	lumu20	1.045 ± 0.005	0.894 ± 0.018	0.000 ± 0.000
1400	lumd20	1.045 ± 0.005	1.115 ± 0.024	0.219 ± 0.007
	Combined		1.421 ± 0.005	0.504 ± 0.012
1500	JERu25	0.859 ± 0.005	0.927 ± 0.018	0.183 ± 0.005
1500	JESu10	0.859 ± 0.005	1.581 ± 0.034	0.678 ± 0.002
1500	JESd10	0.859 ± 0.005	1.754 ± 0.030	0.783 ± 0.003
1500	lumu20	0.859 ± 0.005	0.774 ± 0.017	0.000 ± 0.000
1500	lumd20	0.859 ± 0.005	0.982 ± 0.017	0.251 ± 0.003
	Combined		1.299 ± 0.005	0.499 ± 0.009

Table 10.2: Summary of the effect of systematic shifts on the cross section limits (Feldman-Cousins version). Model masses in the range $1.0 - 1.5$ TeV are listed.

Mass (GeV)	Syst.	σ_{nosyst} (pb)	σ_{syst} (pb)	added spread (pb)
1600	JERu25	0.830 ± 0.005	0.969 ± 0.017	0.236 ± 0.006
1600	JESu10	0.830 ± 0.005	1.669 ± 0.035	0.731 ± 0.002
1600	JESd10	0.830 ± 0.005	1.938 ± 0.032	0.888 ± 0.003
1600	LUMu20	0.830 ± 0.005	0.770 ± 0.017	0.000 ± 0.000
1600	LUMd20	0.830 ± 0.005	0.994 ± 0.022	0.260 ± 0.006
	Combined		1.396 ± 0.005	0.566 ± 0.011
1700	JERu25	0.752 ± 0.005	0.905 ± 0.021	0.250 ± 0.003
1700	JESu10	0.752 ± 0.005	1.575 ± 0.039	0.703 ± 0.002
1700	JESd10	0.752 ± 0.005	2.099 ± 0.032	0.997 ± 0.002
1700	LUMu20	0.752 ± 0.005	0.705 ± 0.015	0.000 ± 0.000
1700	LUMd20	0.752 ± 0.005	0.882 ± 0.015	0.225 ± 0.005
	Combined		1.401 ± 0.005	0.601 ± 0.007
1800	JERu25	0.625 ± 0.005	0.819 ± 0.014	0.274 ± 0.002
1800	JESu10	0.625 ± 0.005	1.632 ± 0.044	0.772 ± 0.002
1800	JESd10	0.625 ± 0.005	3.312 ± 0.054	1.660 ± 0.002
1800	LUMu20	0.625 ± 0.005	0.625 ± 0.018	0.000 ± 0.000
1800	LUMd20	0.625 ± 0.005	0.794 ± 0.020	0.254 ± 0.005
	Combined		1.885 ± 0.005	0.910 ± 0.009
1900	JERu25	0.571 ± 0.005	0.811 ± 0.022	0.292 ± 0.005
1900	JESu10	0.571 ± 0.005	1.389 ± 0.053	0.645 ± 0.002
1900	JESd10	0.571 ± 0.005	3.116 ± 0.069	1.564 ± 0.002
1900	LUMu20	0.571 ± 0.005	0.587 ± 0.016	0.061 ± 0.014
1900	LUMd20	0.571 ± 0.005	0.772 ± 0.023	0.265 ± 0.002
	Combined		1.807 ± 0.005	0.876 ± 0.009
2000	JERu25	0.483 ± 0.005	0.671 ± 0.015	0.234 ± 0.004
2000	JESu10	0.483 ± 0.005	1.158 ± 0.029	0.536 ± 0.003
2000	JESd10	0.483 ± 0.005	3.726 ± 0.146	1.885 ± 0.001
2000	LUMu20	0.483 ± 0.005	0.523 ± 0.016	0.091 ± 0.006
2000	LUMd20	0.483 ± 0.005	0.734 ± 0.019	0.277 ± 0.004
	Combined		2.036 ± 0.005	1.010 ± 0.006

Table 10.3: Summary of the effect of systematic shifts on the cross section limits (Feldman-Cousins version). Model masses in the range $1.6 - 2.0$ TeV are listed.

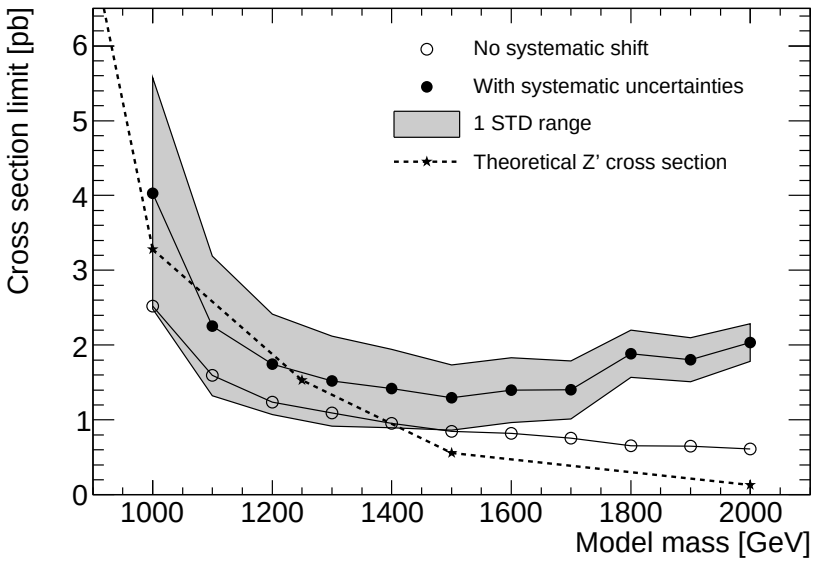

Figure 10.5: Cross section limits, 95% CL. Bayesian limits before and after adding the systematic shifts. The cut-based selection has been used. The shaded region indicate the one standard deviation interval as given by the uncertainty in the un-shifted measurement. The theoretical cross section given corresponds to a narrow leptophobic topcolour Z', as given in Refs [83, 126].

limit with the Bayesian method, as shown in Figure 10.5. The numbers are summarised in Table 10.4. Pseudo-experiments with the systematical uncertainties fully included confirm these numbers. In this figure, a theoretical cross section is also indicated, corresponding to a narrow leptophobic topcolour Z', as given in Refs [83, 126]. Although this model does not fully correspond to the one used in the analysis presented here, they are both narrow, uncoloured resonances, and a scheme to find one would also be sensitive to the other. The cross section for the leptophobic topcolour Z' is shown, since it has a fairly large predicted cross section, compared to other $t\bar{t}$ resonance models. In a sense, this is one of the most optimistic models. Figure 10.5 indicates that we could be able to discover (or exclude) a leptophobic topcolour Z' with a mass lower than about 1.2 TeV, using 200 pb^{-1} of data at $\sqrt{s} = 10$ TeV.

From Figure 10.4 we can see that a jet energy scale uncertainty is the most devastating uncertainty in the analysis, which emphasises the importance of a good understanding of the hadronic calibration and the jet corrections. It is also evident that the jet energy scale shift impact is greatest in the ends of the mass range, where the fit is inherently more sensitive to fluctuations.

The impact of the jet energy scale shift at the high-mass end of the spectrum is demonstrated in Figure 10.6, in which the mass spectrum of a $M = 2.0$ TeV Z' is drawn together with the spectrum of the same process, after the jet energy

Model mass (GeV)	$\sigma_{no\ syst}$ (pb)	σ_{syst} (pb)	1 STD (pb)
1000	2.52 ± 0.03	4.03 ± 0.01	1.55
1100	1.60 ± 0.02	2.26 ± 0.01	0.93
1200	1.24 ± 0.02	1.74 ± 0.01	0.67
1300	1.09 ± 0.02	1.52 ± 0.01	0.60
1400	0.96 ± 0.02	1.42 ± 0.01	0.52
1500	0.85 ± 0.02	1.30 ± 0.01	0.44
1600	0.82 ± 0.02	1.40 ± 0.01	0.43
1700	0.76 ± 0.02	1.40 ± 0.01	0.39
1800	0.65 ± 0.02	1.89 ± 0.01	0.32
1900	0.65 ± 0.02	1.81 ± 0.01	0.29
2000	0.61 ± 0.02	2.04 ± 0.01	0.25

Table 10.4: Summary of the cross section limits with and without the systematical uncertainties. "One standard deviation" indicates the spread of the distribution of σ_{meas} for $\sigma_{theory} = 0$, that is the underlying uncertainty in the measurement.

scale has been shifted down by 10%. The Standard Model background is also shown for comparison. In Figure 10.6, the signal cross section has been set to 2 pb. From the figure, it is clear that a jet energy scale shift also shifts the peak of the signal distribution. When the peak is shifted towards lower masses, it drowns in the background. The sharp deterioration of the cross section limits as a consequence of the jet energy scale shift that can be observed at masses higher than 1.8 TeV coincides with the point at which the number of expected background events drops below 1.

It should be noted that the treatment of the systematic uncertainties of the jet energy resolution and the jet energy scale presented here is somewhat simplified. We have assumed a fixed set of data and shifted the model of the signal fit. Such a procedure does not account for the shifts in the background spectrum that would be the result of a shift in the jet energy scale or the jet energy resolution. As the background is exponential, and the first-order effect of a jet energy scale shift is just a simple rescaling of the x-axis, the background shift per bin could be substantial. For a full treatment of the systematic uncertainties in JES and JER, the systematic shifts should be applied to the signal-plus-background data mix, while keeping the model fixed.

When the background is smeared with systematic effects, the valid region of the exponential fit can change. We have seen that the unshifted background is compatible with an exponential in the interval $800 < M_{inv} < 2500$ GeV. If the jet energy scale is shifted up by 10%, the turnover point in the invariant mass spectrum will also shift towards higher masses, and the lower limit on

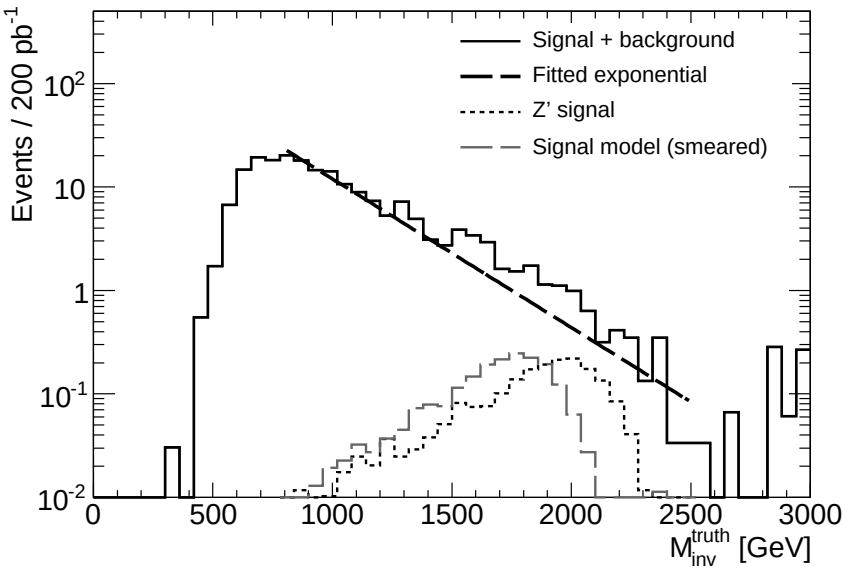

Figure 10.6: The invariant mass spectrum in the electron channel for the Standard Model background with a Z' ($M = 2.0$ TeV) signal added. The fitted function is the exponential fit to the background. The Z' signal itself is also shown, as well as the model Z' used in the fit. In the model, the jet energy scale has been shifted down by 10%. The cross section of the signal is 2 pb.

the region where the background is exponential will change. Ultimately, the sensitivity of the analysis to the 1 TeV mass peak may drastically worsen.

The two different ways of treating the systematic shifts of the jet energy scale and the jet energy resolution represents two different ways of viewing data. If we keep the data fixed, we take the data as given, "this is what we measured". On the other hand, by shifting the data mix, we account for the fact that there might be miscalibrations and other uncertainties in the data. Since shifts in the background also affect the cross section limit, although to a lesser degree than shifts in the signal, the latter approach is probably the more consistent.

A preliminary study indicates that the cross section limits with systematic uncertainties obtained by shifting the data mix are of the same order of magnitude as the limits found when viewing the data as fixed.

Considerations of other systematical uncertainties

The analysis is based on simulations, and is thus dependent on the simulations actually describing data correctly. A common way of estimating the generator uncertainty is to compare different generators. In Figure 10.7 we compare the hadronic top-tagging efficiency as a function of invariant mass for the two $t\bar{t}$ samples, the fully simulated MCATNLO sample and the PYTHIA/ATLFASTII

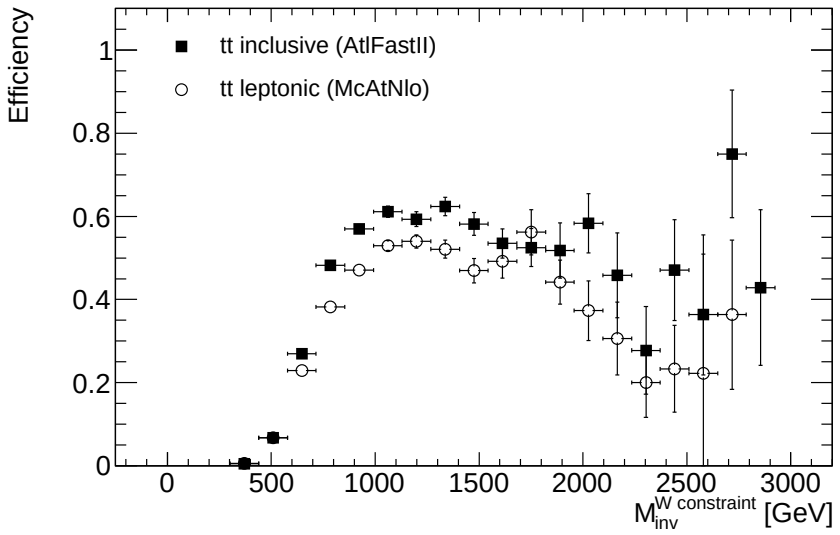

Figure 10.7: Systematic shift in the hadronic top-tagging efficiency due to different $t\bar{t}$ generators. The cut-based top-tagging selection has been used.

sample. A clear shift in the acceptance is visible, insofar that the PYTHIA sample has a generally higher efficiency for all masses, an effect which gets more pronounced at larger masses. An effect like this could affect the final result.

Another uncertainty that could arise is the composition of different Standard Model backgrounds. As a toy model, we have assumed first that the W background is 50% larger than predicted by the simulation, then that the $t\bar{t}$ background is 30% lower, and a combination of these two shifts. A final increase of the multijets background by 100% was also tried. None of these alterations of the composition of the background changes the fact that the total background is exponential, and the impact on the cross section limit is on the order of the computational uncertainty, and much smaller than the jet energy scale shift.

The sensitivity to other systematical uncertainties in the theoretical computations has partly been investigated through the comparison of HERWIG and PYTHIA hadronisation, and the difference between leading and next-to-leading order effects of the matrix element in the $t\bar{t}$ generator have also been studied, in the comparison between the MCATNLO and PYTHIA/ATLFASTII samples.

10.3 Conclusions

With the top-tagging mono-jet approach described in this and the previous chapter, we have shown that a 95% CL exclusion limit on the production cross section of a narrow uncoloured $t\bar{t}$ resonance (Z') could be set to 4.0 ± 1.6 pb ($M = 1.0$ TeV), 1.3 ± 0.4 pb ($M = 1.5$ TeV) and 2.0 ± 0.3 pb ($M = 2.0$ TeV), including systematical uncertainties in the model, assuming $\sqrt{s} = 10$ TeV collisions and 200 pb^{-1} of integrated luminosity. The top-tagging procedure facilitates the search for top quark jets at high energies, even though the top quark decay products are merged. By deliberately adding the muons to the jet clusters, we can treat the muon and the electron decay channels on an equal footing, which provides us with a powerful tool for searching in these two channels simultaneously.

The cross section result shown here is an improvement with respect to the previous official ATLAS results[92], which state a 5σ discovery limit of about 10 pb for a resonance mass of 1 TeV. In this computation, 1 fb^{-1} of integrated luminosity (that is 5 times more than we have used in the analysis) and a centre-of-mass $\sqrt{s} = 14$ TeV (which gives a substantially higher top production cross section) was used.

The CMS experiment at the LHC has also presented expected exclusion limits[126, 127] for a narrow uncoloured resonance for a resolved approach and a mono-jet search technique. For the resolved approach they report an expected cross section exclusion limit at 95% CL of $8.89^{+4.02}_{-2.23}$ pb for a 1 TeV mass resonance and $8.26^{+4.70}_{-3.18}$ pb for $M = 2$ TeV, using $\sqrt{s} = 10$ TeV and an integrated luminosity of 100 pb^{-1} and semi-leptonic top decays in the muon channel only[126]. With the mono-jet approach and an assumed integrated luminosity of 200 pb^{-1}, the CMS experiment report an expected cross section exclusion limit at 95% CL of $7.5^{+4.4}_{-2.7}$ pb at $M = 1$ TeV and a limit of $0.6^{+0.2}_{-0.1}$ pb at $M = 2$ TeV[127]. This search too, is only conducted in the muon channel. The CMS cross section limit for the 2 TeV resonance is clearly better than our limit, but at 2 TeV we are totally dominated by the systematic uncertainty in the jet energy scale. In the absence of this uncertainty, our expected limit would be below 1 pb.

Part IV:
Summary and outlook

11. Towards higher energies

> *Sometimes scientists change their minds. New developments cause a rethink. If this bothers you, consider how much damage is being done to the world by people for whom new developments do* not *cause a rethink.*
> – Terry Pratchett, Ian Stewart and Jack Cohen: "The Science of Discworld", preface to the revised edition, 2002.

Throughout this thesis, measurements of energy in different forms have been the main theme, from the studies of muons in the low-energy range and the calibration of calorimeter modules, to the suggested search for hypothetical heavy particles. The various analyses all use calorimeter signals as important ingredients, although the application of the information has been quite different.

The usage of calorimeter signals to discriminate between different particles, thus investigating the properties of very low-energy muons from pion decays, was described in Chapter 5, and it was shown that muons can be separated from the pions, even for such low energies.

The inherent difficulties in retrieving the total energy of a hadron due to the fundamental physical processes of hadronic showers was also discussed. As has been demonstrated in Chapters 4 and 7, the calibration of the calorimeter energy signal to the hadronic scale is far from trivial. The invisible energy losses of the hadronic showers, as well as their fluctuating nature, demand advanced calibration schemes in order to correctly estimate the energy. The local hadronic calibration, as described in Chapter 7, provides a method for hadronic compensation that both considers the event-by-event fluctuations and the energy dependent response of the hadronic showers.

The local hadronic calibration method has been applied to data from the combined ATLAS barrel test beam of 2004, demonstrating that a good linearity and improvements in the resolution can be achieved for real data. The method still needs some additional corrections, although the results from simulations and real data have been shown to be consistent for the levels of corrections applied.

A proposed search for $t\bar{t}$ resonances was outlined in Chapters 9 and 10. In order to find a heavy particle that decays to top quark pairs, the $t\bar{t}$ signal must be enhanced by reducing the background and the mass spectrum must be correctly reconstructed. At high energies, the standard $t\bar{t}$ reconstruction schemes fail, since the top quarks are boosted and the decay products merge.

Thus new tools must be developed for the high-energy top quarks, and in this thesis a method for selecting top mono-jets through top-tagging has been described.

The discovery (or exclusion) prospects for a narrow uncoloured $t\bar{t}$ resonance, a Z', seem good: a 95% CL exclusion on the production cross section could be set to 4.0 ± 1.6 pb ($M = 1.0$ TeV), 1.3 ± 0.4 pb ($M = 1.5$ TeV) and 2.0 ± 0.3 pb ($M = 2.0$ TeV), including systematical uncertainties in the model.

Among the systematical uncertainties studied, the results of the study indicate that the jet energy scale has the greatest impact on the final result, which further underlines that a correct jet energy scale and a good hadronic energy resolution will be crucial for the discovery of new physics at the LHC.

The first plans of the LHC were made more than twenty years ago, and now, in November 2009, we have just seen the first proton-proton collisions. It has been a long journey to get here and many physicists have devoted the major part of their careers to planning, installing, commissioning, calibrating and preparing for real data.

Now it begins.

12. Sammanfattning på svenska

Hur länge måste vi iaktta universum innan vi förstår hur det fungerar? Räcker det med några hundra år, eller krävs det tusen, tiotusen, miljoner, miljarder? Behövs det instrument som inte kan skapas med vår teknologi?
– Peter Nilsson, Stjärnvägar, 1991

Experimentell elementarpartikelfysik handlar i mångt och mycket om att försöka besvara skenbart enkla frågor, som ändå kan ha djupt komplexa svar: Vad består allting av egentligen? Hur hålls det ihop? Var började det någonstans? Den rena, grundläggande nyfikenheten är en mäktig drivkraft för mänskligheten. Viljan att se vad som finns bortom den nuvarande horisonten har skickat iväg expeditioner över haven eller genom tomma rymden, ständigt sökande efter ny kunskap. Inte sällan är svaret på den ursprungliga frågan en hel uppsättning av nya frågor. Elementarpartikelfysikens frågor besvaras ofta med hjälp av energi. I högenergetiska partikelkollisioner kan materiens innersta studeras, nya partiklar kan skapas ur kollisionsenergin och växelverkan mellan partiklarna kan undersökas med bättre och bättre precision.

Vid partikelfysiklaboratoriet CERN utanför Genève i Schweiz har partikelacceleratorn LHC (Large Hadron Collider, den stora hadronkolliderarен) byggts. I LHC accelereras protoner till hastigheter nära ljusets, för att sedan kollideras. I november 2009 skedde de första kollisionerna i LHC, som är världens mest högenergetiska partikelaccelerator. Vid LHC:s kollisionspunkter har detektorer byggts för att studera de partiklar som bildas i kollisionerna. En av dessa detektorer är ATLAS, en 7000 ton tung maskin, stor som ett femvåningshus och speciellt designad för att ta till vara på alla de möjligheter som högenergikollisionerna vid LHC erbjuder.

ATLAS fysikprogram innefattar precisionsmätningar av standardmodellen, som är den teori som för närvarande bäst beskriver materiens inre och partiklars växelverkningar, men ATLAS kommer även att användas för att förutsättningslöst leta efter ny fysik bortom standardmodellen. Ett exempel på en precisionsmätning är att studera den tyngsta kända elementarpartikeln, toppkvarken. Denna kvark är nästan lika tung som en hel guldatom och sönderfaller så snabbt att den inte hinner bilda bundna tillstånd med andra kvarkar. Toppkvarken observerades för första gången under tidigt 1990-tal vid partikelacceleratorn Tevatronen i Chicago i USA, och att göra riktigt noggranna mätningar av dess egenskaper är viktigt för att testa standardmodellen. Ett ex-

empel på sökande efter ny fysik bortom standardmodellen är att undersöka om det existerar partiklar som sönderfaller till toppkvarkar, så kallade toppresonanser. I denna avhandling beskrivs hur en sådan sökning skulle kunna gå till, och ATLAS-detektorns känslighet för sådana partiklar undersöks med hjälp av datorsimuleringar. Studien visar att en viss sorts toppresonanser, som saknar färgladdning och har en smal masstopp, skulle kunna upptäckas eller uteslutas vid LHC med 95% konfidensnivå, om de har tvärsnitten[1] 4.0 ± 1.6 pb (för en resonans med massan 1.0 TeV/c^2), 1.3 ± 0.4 pb ($M = 1.5$ TeV/c^2) eller 2.0 ± 0.3 pb ($M = 2.0$ TeV/c^2). Detta förutsätter att kollisionerna sker vid masscentrumenergin $\sqrt{s} = 10$ TeV, och att vi har en integrerad luminositet[2] på 200 pb^{-1}, vilket är realistiska data för ett års tidig datatagning med ATLAS.

Toppresonansstudien visar att en av de viktigaste begränsningarna i sökandet efter dessa partiklar är kunskapen om den detekterade energin hos sönderfallsprodukterna. Detta ansluter till avhandlingens andra studie, tester och kalibrering av ATLAS-detektorns kalorimetersystem. Kalorimetrar utgör en viktig detektorkategori, som mäter energin hos partiklar genom deras totalabsorption i kalorimetermaterialet. I avhandlingen beskrivs en metod för att kalibrera den energi som deponeras av hadroner i ATLAS centrala kalorimetrar. Kalibreringen kallas "lokal kalibrering" eftersom korrektionerna tillämpas lokalt på energikluster, baserat på kalorimetercellernas energitäthet. Kalibreringsmetoden uppvisar en linearitet inom 3% i kalorimetern, och även en rimlig överensstämmelse mellan simuleringar och data.

Avhandlingens röda tråd är energin: Kalibrering av energidepositioner och sökandet efter nya partiklar med hjälp av högenergikollisioner. Världens största partikelkolliderare, LHC, har precis startats, efter mer än tjugo år av planerande, byggande, installerande och kalibrerande, och med LHC kommer vi att kunna studera energier som aldrig tidigare frambringats i kontrollerade miljöer på jorden.

Det är nu det börjar på riktigt.

[1] I det här sammanhanget är tvärsnitt ett mått på sannolikheten att bilda en viss partikel i proton-proton-kollisionen.

[2] Den integrerade luminositeten är ett mått på den samlade mängden data. Om vi vet att det finns en partikel med produktionstvärsnittet 1 pb så kommer vi att i genomsnitt ha 200 sådana partiklar i den datamängd som motsvaras av den integrerade luminositeten 200 pb^{-1}.

Part V:
Appendices

A. Samples used in the very low-energy muon analysis

For the study presented in Chapter 6, analysis of very low-energy muons in the Tile stand-alone test beam of 2003, the data samples listed in Table A.1.

Run number	Nominal energy (GeV)	Test beam period (year)
r0360177	9	2003
r0360144	5	2003
r0360171	3	2003
r0045360	5	1999

Table A.1: Details of the data samples used for the very low-energy muon analysis

B. Numerical values of the hadronic calibration weight tables

B.1 Weight tables for the first LAr sampling layer

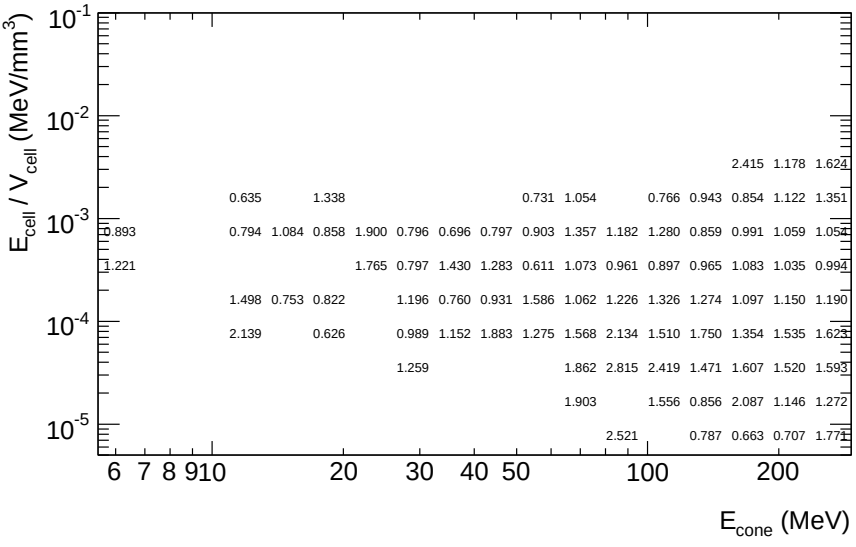

Figure B.1: Weight table for LAr first sampling layer (the strips), low E_{cone} values.

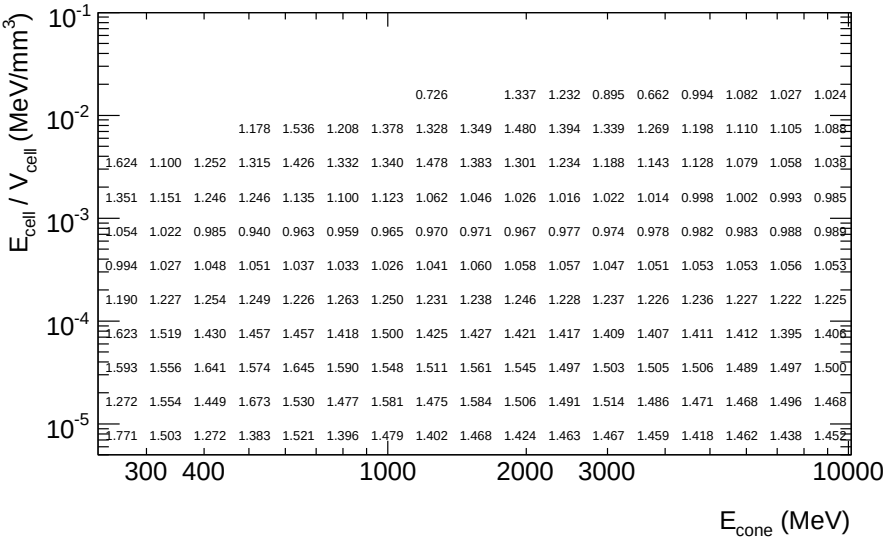

Figure B.2: Weight table for LAr first sampling layer (the strips), medium E_{cone} values.

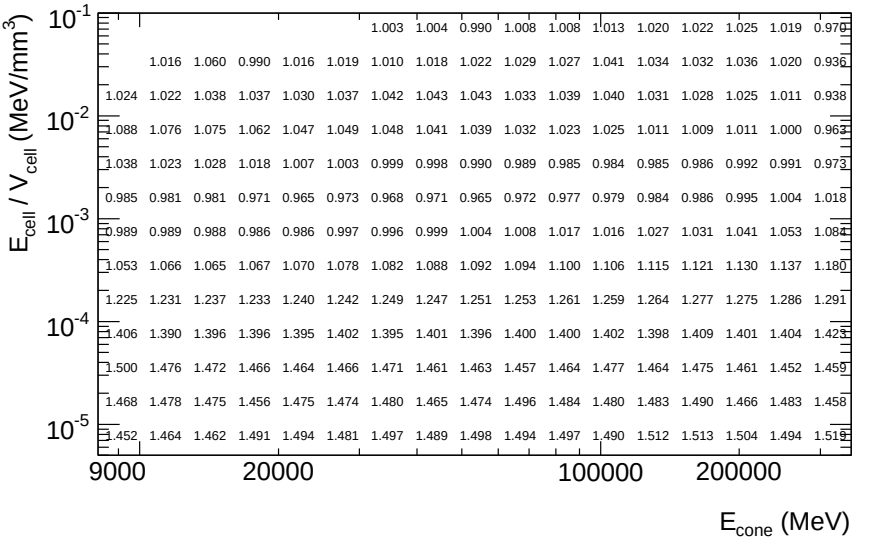

Figure B.3: Weight table for LAr first sampling layer (the strips), high E_{cone} values.

B.2 Weight tables for the second LAr sampling layer

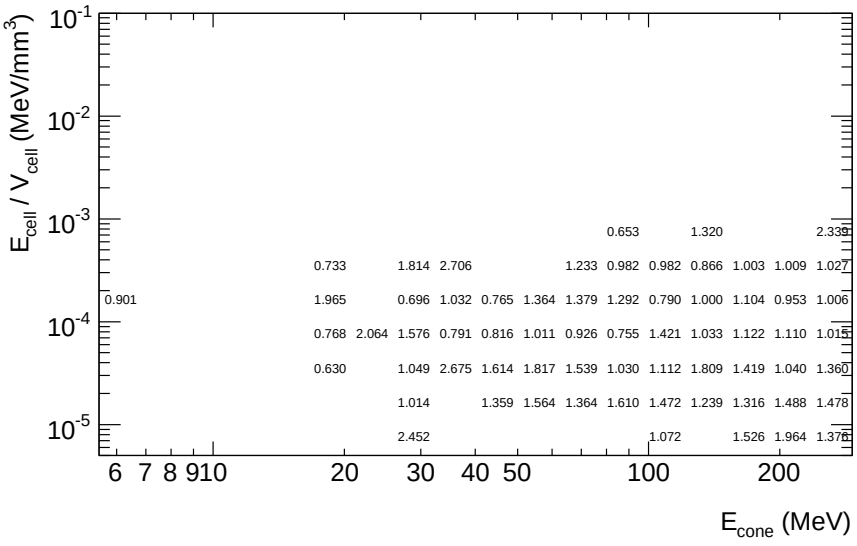

Figure B.4: Weight table for LAr second sampling layer (middle), low E_{cone} values.

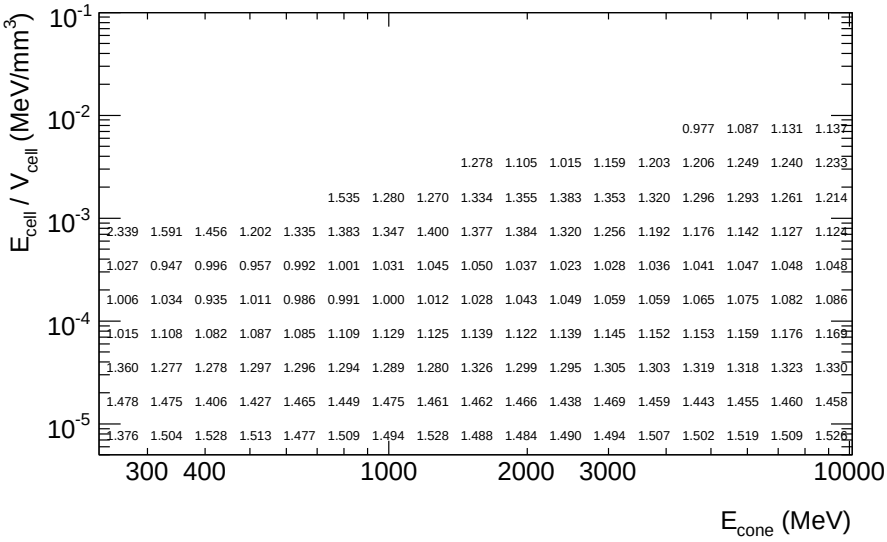

Figure B.5: Weight table for LAr second sampling layer (middle), medium E_{cone} values.

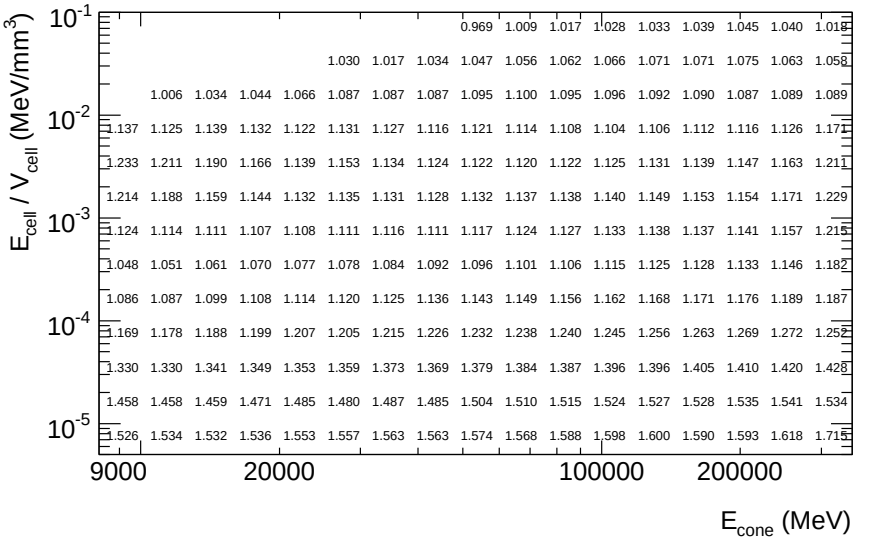

Figure B.6: Weight table for LAr second sampling layer (middle), high E_{cone} values.

B.3 Weight tables for the third LAr sampling layer

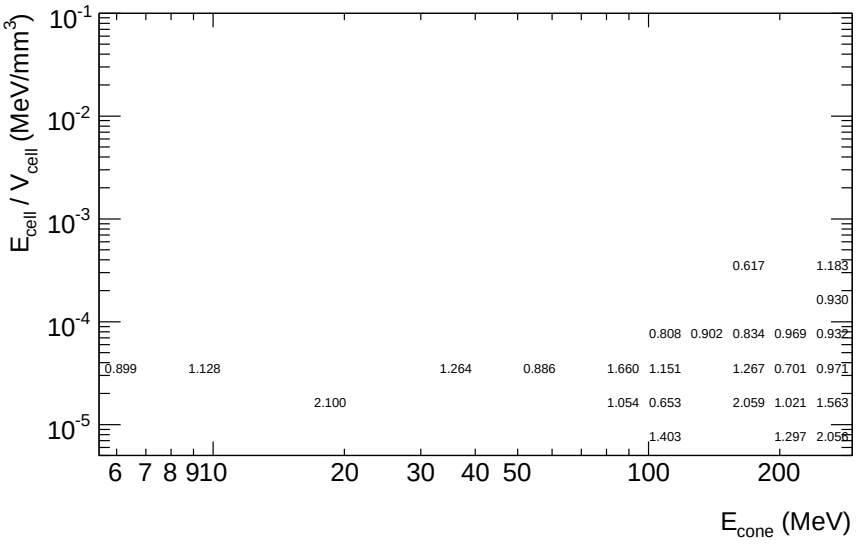

Figure B.7: Weight table for LAr third sampling layer (back), low E_{cone} values.

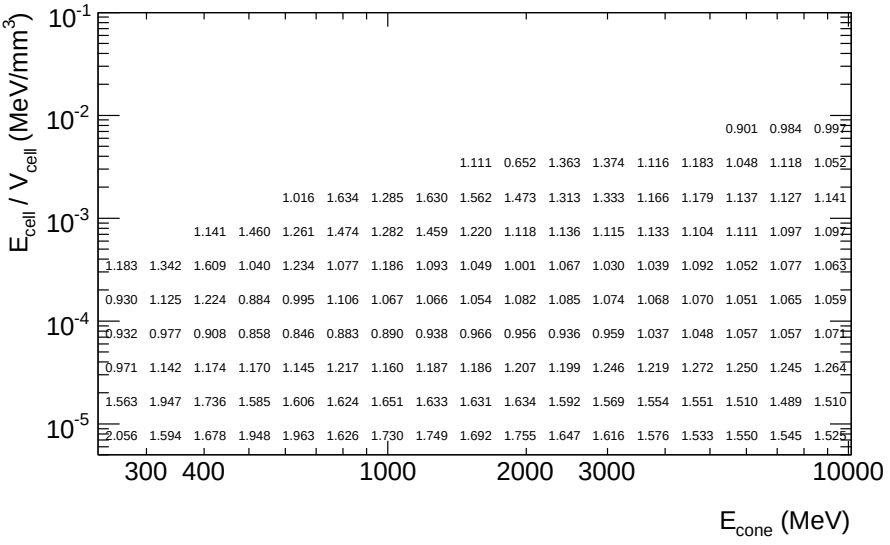

Figure B.8: Weight table for LAr third sampling layer (back), medium E_{cone} values.

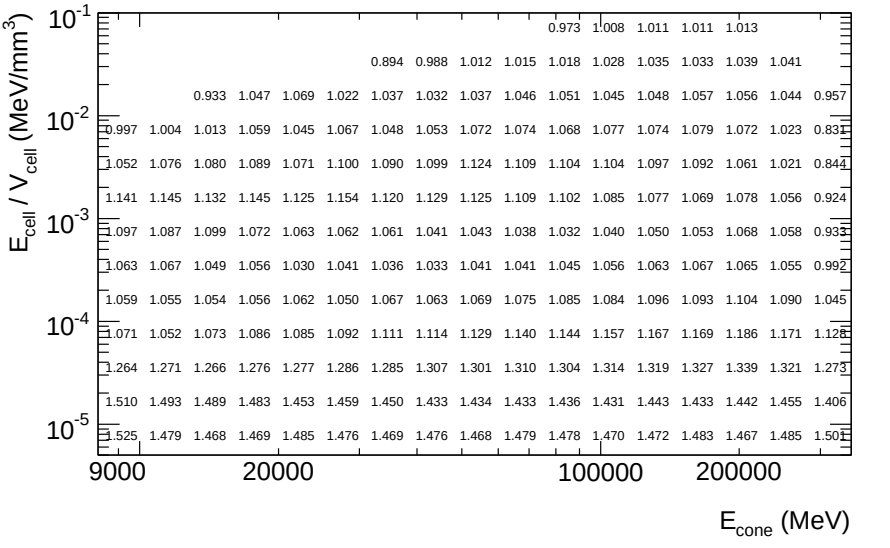

Figure B.9: Weight table for LAr third sampling layer (back), high E_{cone} values.

B.4 Weight tables for the first Tile sampling layer, the A-cells

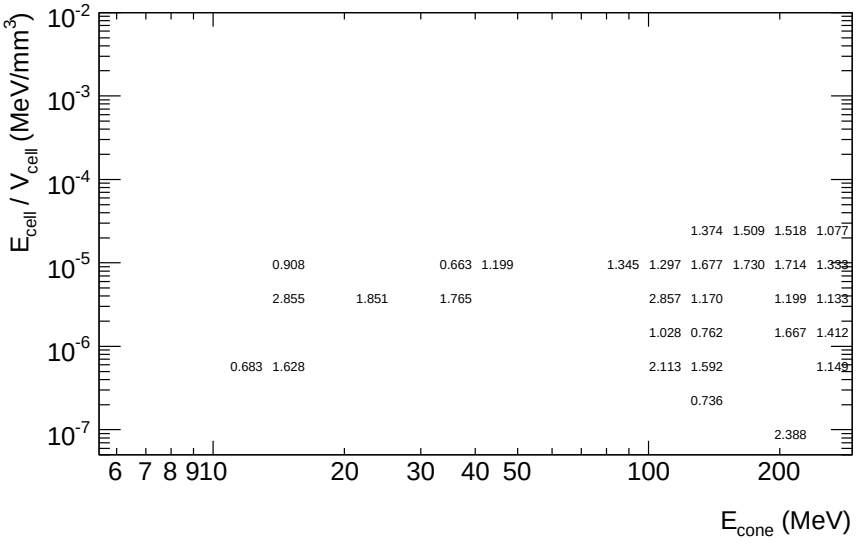

Figure B.10: Weight table for Tile first sampling layer (the A-cells), low E_{cone} values.

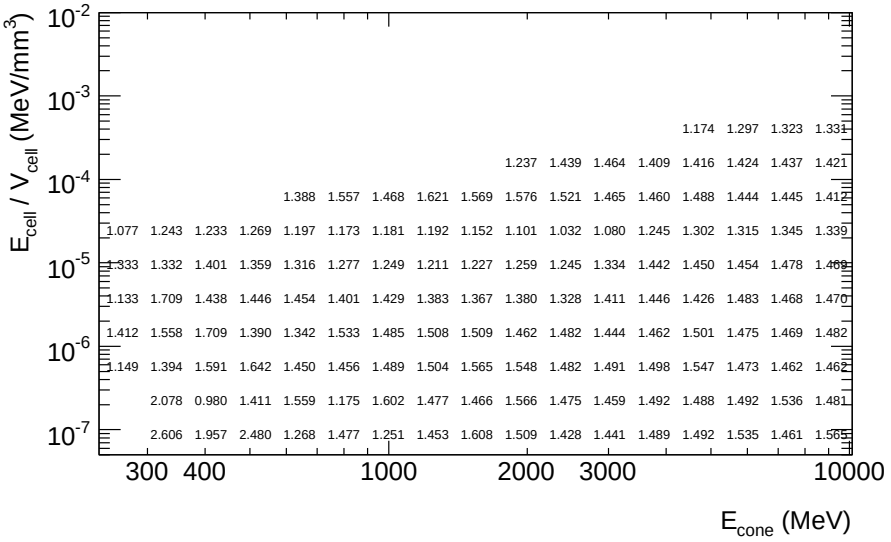

Figure B.11: Weight table for Tile first sampling layer (the A-cells), medium E_{cone} values.

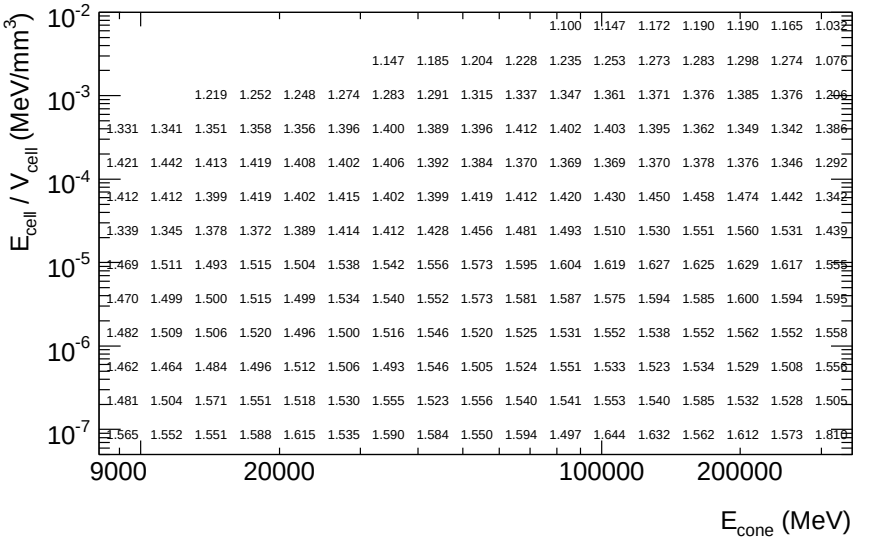

Figure B.12: Weight table for Tile first sampling layer (the A-cells), high E_{cone} values.

B.5 Weight tables for the second Tile sampling layer, the BC-cells

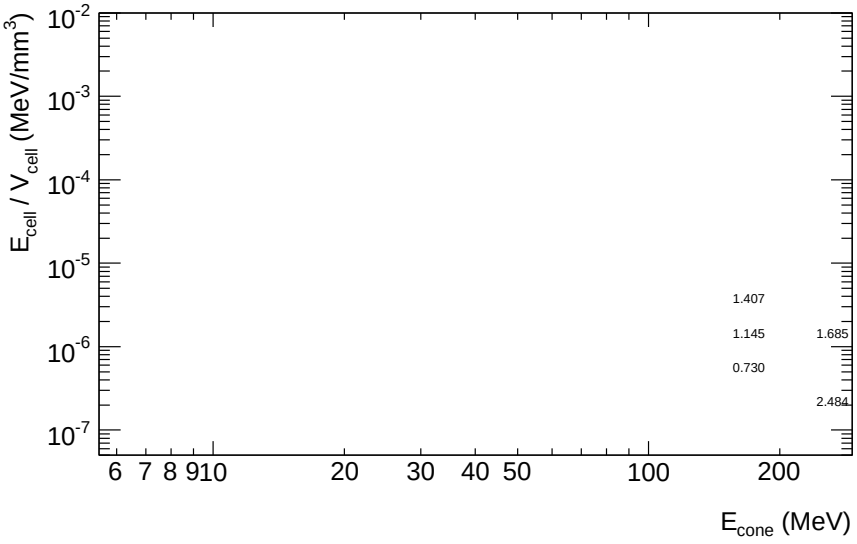

Figure B.13: Weight table for Tile second sampling layer (the BC-cells), low E_{cone} values.

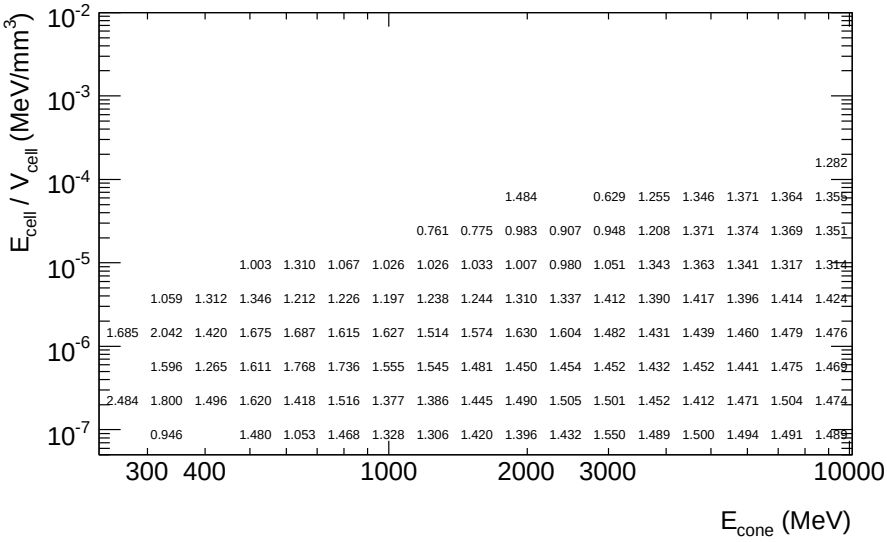

Figure B.14: Weight table for Tile second sampling layer (the BC-cells), medium E_{cone} values.

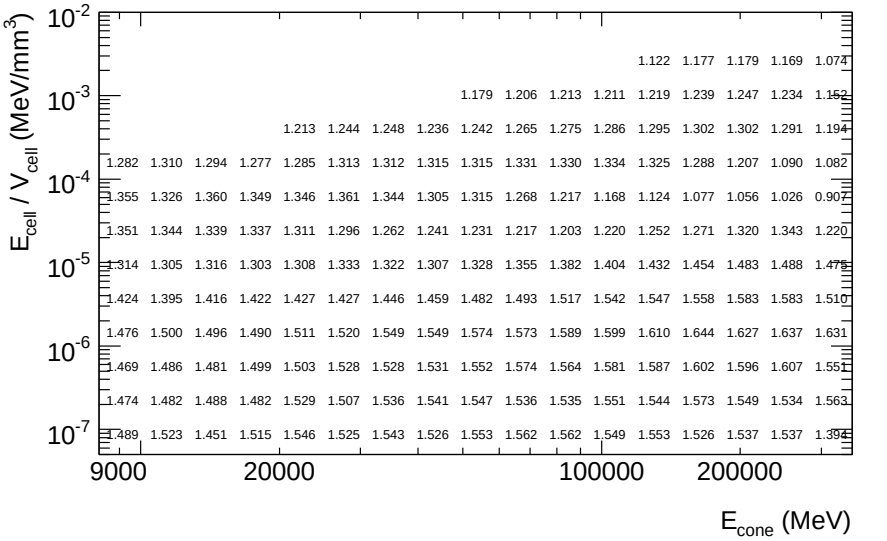

Figure B.15: Weight table for Tile second sampling layer (the BC-cells), high E_{cone} values.

B.6 Weight tables for the third Tile sampling layer, the D-cells

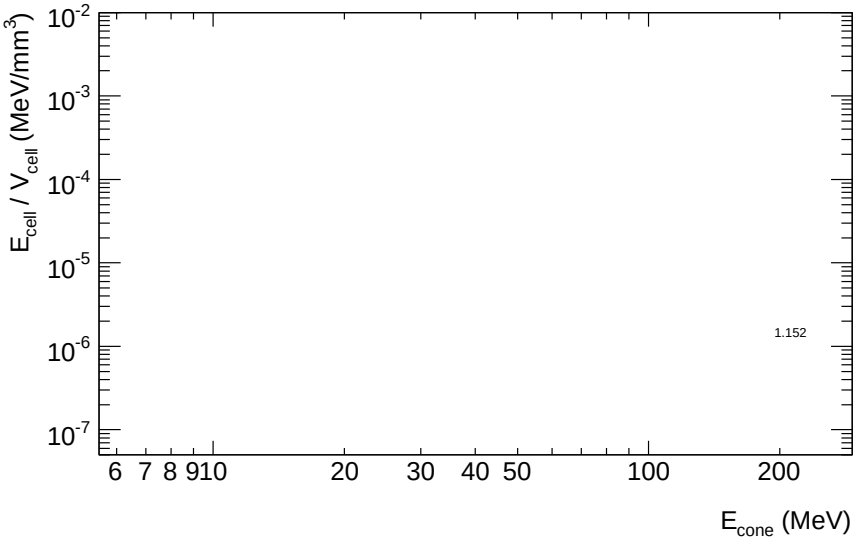

Figure B.16: Weight table for Tile third sampling layer (the D-cells), low E_{cone} values.

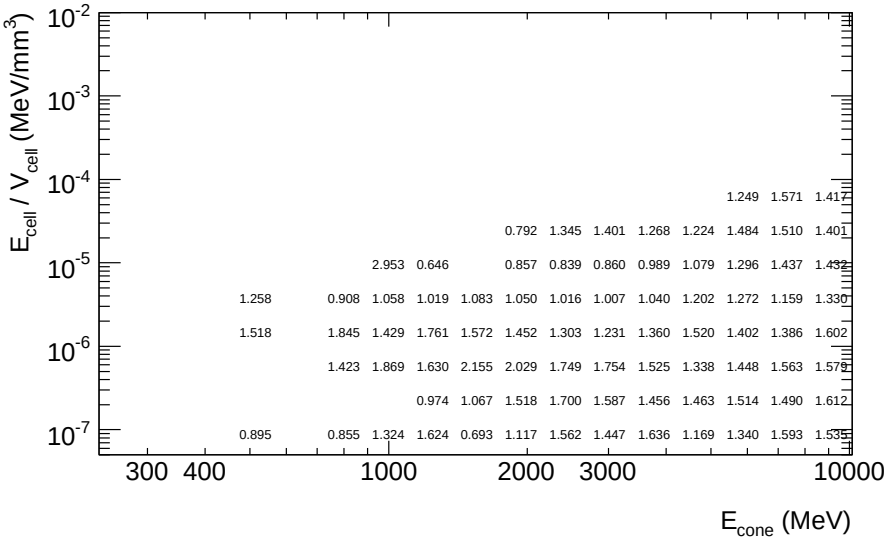

Figure B.17: Weight table for Tile third sampling layer (the D-cells), medium E_{cone} values.

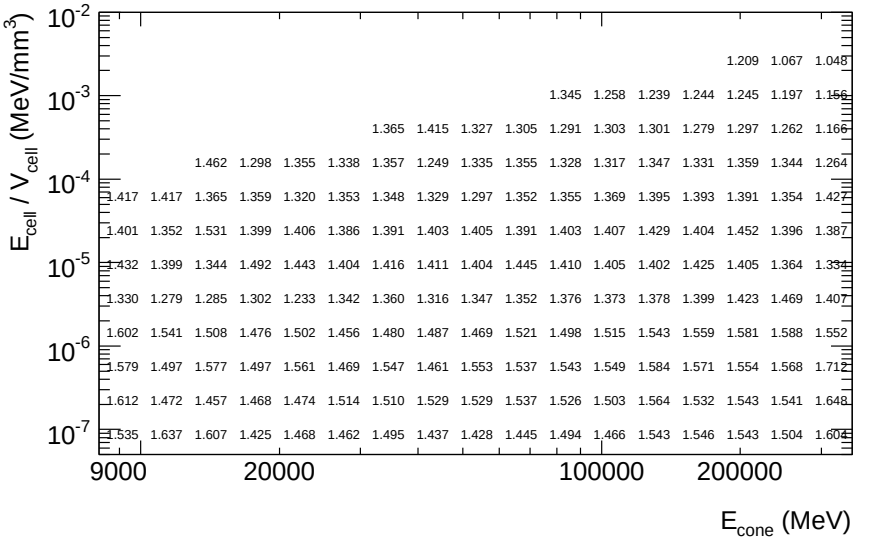

Figure B.18: Weight table for Tile third sampling layer (the D-cells), high E_{cone} values.

C. Systematic effects of hadronic calibration corrections: the dead material corrections and the electron cut

As described in Section 7.6.2, the electron removal cut will give a bias to the energy scale, which becomes significant at low energies. In Section 7.6.4, the corrections for losses in dead material were discussed, and a small bias from the correction factors not being constant with beam energy was demonstrated. In Tables C.1-C.2, the effect of the electron cut and the dead material, when applied to a pure sample of simulated pions is demonstrated. In Tables C.3-C.4, the systematic effect of the electron cut on the unweighted energy signal is given.

The statistical errors are given from the Gaussian fit to the energy distribution of the weighted and dead material corrected energy. The systematical uncertainties have been estimated using two independent samples of the simulated energy: one containing the events with odd event number (sample *A*), and one containing the even event numbers (sample *B*). The uncertainty is estimated as the difference

$$\Delta_{syst} = r_{A,\ corrected} - r_{B,\ uncorrected} \tag{C.1}$$

where r is either the resolution or the ratio E_{mean}/E_{beam}, indices A and B refer to quantities computed from the odd or even event number samples respectively, *corrected* refers to the quantity after the electron cut and dead material correction using one correction constant per region and *uncorrected* means that no electron cut was applied or the dead material corrections using beam energy dependent factors were used.

The systematic uncertainties dominate over the statistical errors for most energies. The total error exceeds 10% of the measured value at energies around 9 GeV (for the resolution) and 4 GeV (for the E_{mean}/E_{beam} ratio).

E_{beam} (GeV)	Resolution (%)	Stat. err. (%)	Syst. error DM corr. (%)	Syst. error e cut (%)	Total err. (%)
300.00	5.07	0.09	0.30	0.07	0.32
250.00	5.95	0.10	0.05	0.38	0.40
200.00	6.13	0.10	0.33	0.50	0.60
180.00	6.46	0.10	0.14	0.06	0.18
150.00	7.03	0.11	0.34	0.11	0.37
100.00	8.52	0.14	0.13	0.13	0.23
90.00	8.75	0.14	0.35	0.41	0.56
80.00	9.41	0.16	0.04	0.25	0.30
70.00	9.74	0.16	0.18	0.05	0.24
60.00	10.26	0.17	0.12	0.04	0.21
50.00	11.28	0.17	0.16	0.06	0.25
40.00	12.92	0.22	0.16	0.57	0.63
30.00	14.28	0.24	0.60	0.84	1.06
25.00	15.58	0.27	0.19	0.78	0.84
20.00	17.18	0.31	0.00	0.79	0.85
15.00	19.54	0.37	0.36	0.15	0.54
10.00	26.42	0.53	0.63	0.07	0.83
9.00	29.35	0.67	0.31	2.87	2.96
7.00	41.53	1.37	4.64	2.29	5.35
6.00	36.06	0.80	0.55	2.77	2.93
5.00	34.43	0.84	0.25	0.53	1.02
4.00	30.56	0.81	0.01	9.92	9.95
3.00	32.92	1.01	0.45	12.17	12.22
2.00	34.74	1.11	0.65	28.10	28.13
1.50	38.41	1.63	1.84	30.79	30.89
1.00	45.87	2.69	0.37	44.08	44.16
0.75	59.38	5.14	2.33	61.21	61.47
0.50	96.58	19.98	36.22	317.72	320.40

Table C.1: Systematic uncertainties in the resolution of the simulated energy signal, after weighting and dead material correction, as a consequence of the electron removal cut and the corrections for losses in dead material.

E_{beam} (GeV)	E_{mean}/E_{beam} (%)	Stat. err. (%)	Syst. error DM corr. (%)	Syst. error e cut (%)	Total err. (%)
300.00	98.28	0.09	0.39	0.14	0.42
250.00	98.61	0.10	0.31	0.06	0.33
200.00	98.39	0.10	0.13	0.08	0.19
180.00	98.33	0.10	0.01	0.10	0.14
150.00	97.90	0.11	0.51	0.03	0.53
100.00	96.89	0.14	0.94	0.42	1.04
90.00	96.48	0.14	0.85	0.14	0.87
80.00	95.93	0.15	1.05	0.37	1.12
70.00	95.29	0.16	0.94	0.01	0.95
60.00	94.58	0.16	1.33	0.60	1.47
50.00	94.44	0.18	1.73	0.09	1.74
40.00	93.48	0.21	1.46	0.84	1.70
30.00	91.57	0.23	1.60	0.45	1.68
25.00	91.25	0.25	2.33	0.21	2.35
20.00	90.00	0.28	2.83	0.25	2.85
15.00	86.78	0.32	1.99	1.63	2.59
10.00	83.25	0.44	3.22	2.85	4.32
9.00	83.90	0.51	3.70	3.80	5.33
7.00	79.11	0.91	1.19	3.49	3.80
6.00	80.26	0.68	2.77	4.15	5.03
5.00	75.72	0.65	0.76	5.35	5.44
4.00	77.62	0.60	2.62	4.95	5.63
3.00	81.43	0.75	2.19	12.76	12.97
2.00	88.94	0.99	7.85	25.97	27.14
1.50	90.58	1.34	7.24	27.55	28.51
1.00	85.64	1.94	13.05	37.68	39.93
0.75	70.05	2.80	6.84	34.38	35.17
0.50	55.67	6.70	4.37	36.35	37.22

Table C.2: Systematic uncertainties in the E_{mean}/E_{beam} ratio of the simulated energy signal, after weighting and dead material correction, as a consequence of the electron removal cut and the corrections for losses in dead material.

E_{beam} (GeV)	Resolution (%)	Stat. error (%)	Syst. err. e cut (%)	Total error (%)
300.00	10.52	0.17	0.14	0.22
250.00	10.79	0.18	0.46	0.50
200.00	11.10	0.19	0.13	0.23
180.00	11.14	0.20	0.61	0.64
150.00	12.08	0.22	0.21	0.30
100.00	12.81	0.23	0.08	0.24
90.00	12.85	0.22	0.19	0.29
80.00	13.90	0.25	0.41	0.48
70.00	14.44	0.27	0.08	0.28
60.00	14.43	0.27	0.64	0.70
50.00	14.98	0.27	0.06	0.27
40.00	16.01	0.28	0.48	0.55
30.00	16.85	0.28	0.75	0.80
25.00	18.25	0.35	0.64	0.73
20.00	19.83	0.38	0.08	0.39
15.00	21.97	0.41	0.53	0.67
10.00	29.16	0.71	1.20	1.39
9.00	33.00	0.74	2.73	2.82
7.00	32.44	0.68	2.65	2.73
6.00	31.97	0.67	1.67	1.80
5.00	30.61	0.74	2.46	2.57
4.00	30.79	0.76	8.36	8.39
3.00	36.94	1.12	9.46	9.52
2.00	40.76	1.29	24.87	24.90
1.50	41.42	1.46	33.91	33.95
1.00	54.20	2.77	31.05	31.18
0.75	65.72	4.64	53.63	53.83
0.50	101.79	22.94	517.76	518.27

Table C.3: Systematic uncertainties in the resolution ratio of the simulated energy signal, before weighting and dead material correction, as a consequence of the electron removal cut.

E_{beam} (GeV)	E_{mean}/E_{beam} (%)	Stat. error (%)	Syst. error e cut (%)	Total error (%)
300.00	76.48	0.14	0.01	0.14
250.00	75.85	0.14	0.06	0.15
200.00	75.28	0.14	0.11	0.18
180.00	75.17	0.14	0.13	0.19
150.00	74.67	0.15	0.33	0.37
100.00	73.35	0.16	0.33	0.37
90.00	73.29	0.16	0.40	0.43
80.00	72.48	0.17	0.13	0.22
70.00	72.15	0.18	0.08	0.20
60.00	71.73	0.18	0.68	0.70
50.00	70.81	0.19	0.36	0.40
40.00	70.00	0.20	0.19	0.27
30.00	68.81	0.21	0.36	0.42
25.00	68.19	0.23	0.45	0.50
20.00	66.09	0.24	0.88	0.91
15.00	63.15	0.26	0.76	0.81
10.00	58.49	0.37	1.65	1.69
9.00	57.43	0.41	1.93	1.97
7.00	58.20	0.43	2.02	2.06
6.00	57.19	0.41	1.63	1.68
5.00	55.96	0.41	0.56	0.69
4.00	58.55	0.44	1.74	1.79
3.00	61.39	0.64	7.34	7.36
2.00	65.93	0.83	14.63	14.65
1.50	65.25	0.92	17.69	17.72
1.00	56.98	1.35	16.06	16.12
0.75	49.09	2.02	16.52	16.64
0.50	38.51	5.45	33.04	33.49

Table C.4: Systematic uncertainties in the E_{mean}/E_{beam} ratio of the simulated energy signal, before weighting and dead material correction, as a consequence of the electron removal cut.

Bibliography

[1] The LHC Study Group, *The Large Hadron Collider Conceptual Design*, Tech. Rep. AC/95-05 (LHC), CERN, 20 October 1995.

[2] *The Large Hadron Collider*, http://lhc.web.cern.ch/lhc/, 2009.

[3] ATLAS Collaboration, G. Aad et al., *The ATLAS Experiment at the CERN Large Hadron Collider*, JINST **3** (2008) S08003.

[4] CDF Collaboration, F. Abe et al., *Observation of Top Quark Production in $\bar{p}p$ Collisions with the Collider Detector at Fermilab*, Phys. Rev. Lett. **74** (1995) 2626–2631, arXiv:hep-ex/9503002.

[5] D0 Collaboration, S. Abachi et al., *Observation of the top quark*, Phys. Rev. Lett. **74** (1995) 2632–2637, arXiv:hep-ex/9503003.

[6] R. Wigmans, *Calorimetry. Energy Measurement in Particle Physics*. Oxford Science Publications, Oxford, 2000.

[7] B. Martin and G. Shaw, *Particle Physics*. Wiley, second ed., 2003.

[8] B. Di Girolamo et al., *Beamline instrumentation in the 2004 combined* ATLAS *testbeam*, ATLAS technical note, ATL-TECH-PUB-2005-001, CERN, 27 July 2005.

[9] Particle Data Group Collaboration, C. Amsler et al., *Review of particle physics*, Phys. Lett. **B667** (2008) 1.

[10] Tevatron Electroweak Working Group Collaboration, *Combination of CDF and D0 Results on the Mass of the Top Quark*, arXiv:0903.2503 [hep-ex].

[11] M. Fairbairn et al., *Stable massive particles at colliders*, Phys. Rept. **438** (2007) 1–63, arXiv:hep-ph/0611040.

[12] Gargamelle Neutrino Collaboration, F. J. Hasert et al., *Observation of neutrino-like interactions without muon or electron in the Gargamelle neutrino experiment*, Phys. Lett. **B46** (1973) 138–140.

[13] Gargamelle Neutrino Collaboration, F. J. Hasert et al., *Observation of Neutrino Like Interactions Without Muon Or Electron in the Gargamelle Neutrino Experiment*, Nucl. Phys. **B73** (1974) 1–22.

[14] The UA1 Collaboration, G. Arnison et al., *Experimental observation of isolated large transverse energy electrons with associated missing energy at* $\sqrt{s} = 540$ *GeV*, Physics Letters B **122** (1983) 103–116.

[15] The UA2 Collaboration, M. Banner et al., *Observation of single isolated electrons of high transverse momentum in events with missing transverse energy at the CERN* $\bar{p}p$ *collider*, Physics Letters B **122** (1983) 476–485.

[16] The UA1 Collaboration, G. Arnison et al., *Experimental observation of lepton pairs of invariant mass around 95 GeV/*c^2 *at the CERN SPS collider*, Physics Letters B **126** (1983) 398–410.

[17] CDF Collaboration, T. Aaltonen et al., *First Observation of Electroweak Single Top Quark Production*, Phys. Rev. Lett. **103** (2009) 092002, arXiv:0903.0885 [hep-ex].

[18] D0 Collaboration, V. M. Abazov et al., *Observation of Single Top-Quark Production*, Phys. Rev. Lett. **103** (2009) 092001, arXiv:0903.0850 [hep-ex].

[19] F. Mandl and G. Shaw, *Quantum Field Theory*. Wiley, revised ed., 1993.

[20] D. N. Spergel et al., *First-year Wilkinson Microwave Anisotropy Probe (WMAP) observations: Determination of Cosmological Parameters*, Astrophysical Journal Supplement **148** (2003) 175–194.

[21] Clowe et al., *Direct Empirical Proof of Existence of Dark Matter*, Astrophysical Journal Letters **648** (10 September 2006) L109.

[22] C. Bennett et al., *First-year Wilkinson Microwave Anisotropy Probe (WMAP) observations: Preliminary Maps and Basic Results*, Astrophysical Journal Supplement **148** (2003) 1–27.

[23] L. Bergström and A. Goobar, *Cosmology and Particle Astrophysics*. Wiley, 1999.

[24] N. Arkani-Hamed, S. Dimopoulos, and G. R. Dvali, *The hierarchy problem and new dimensions at a millimeter*, Phys. Lett. **B429** (1998) 263–272, arXiv:hep-ph/9803315.

[25] L. Randall and R. Sundrum, *A large mass hierarchy from a small extra dimension*, Phys. Rev. Lett. **83** (1999) 3370–3373, arXiv:hep-ph/9905221.

[26] The ATLAS Collaboration, ATLAS *Collaboration Homepage*, http://www.atlas.ch/, October 2007.

[27] CERN. Press release, 23 November, 2009.

[28] ATLAS Collaboration, ATLAS *Technical Proposal*, Tech. Rep. LHCC94-43 LHCC/P2, CERN, 15 December 1994.

[29] LEP Working Group for Higgs boson searches Collaboration, R. Barate et al., *Search for the standard model Higgs boson at LEP*, Phys. Lett. **B565** (2003) 61–75, arXiv:hep-ex/0306033.

[30] LEP collaborations: Aleph, Delphi, L3, Opal and the LEP Electroweak Working Group, *A Combination of Preliminary Electroweak Measurements and Constraints on the Standard Model*, arXiv:0612034 [hep-ex].

[31] The ALEPH Collaboration et al., *Precision Electroweak Measurements and Constraints on the Standard Model*, arXiv:0911.2604 [hep-ex].

[32] The ATLAS Collaboration, ATLAS *Calorimeter Performance Technical Design Report*, Tech. Rep. LHCC 96-40, CERN, 13 January 1997.

[33] ATLAS Collaboration, ATLAS *Detector and Physics Performance,* ATLAS *TDR 14 Volume 1*, Tech. Rep. LHCC 99-14, CERN, 25 May 1999.

[34] The ATLAS Collaboration, G. Aad et al., *Expected Performance of the* ATLAS *Experiment - Detector, Trigger and Physics*, arXiv:0901.0512 [hep-ex]. CERN-OPEN-2008-020.

[35] R. Bock and A. Vasilescu, *The Particle Detector BriefBook*. Springer, 1998. Web version available at http://rkb.home.cern.ch/rkb/titleD.html.

[36] ATLAS Collaboration, ATLAS *detector paper wiki pages*, https://twiki.cern.ch/twiki/bin/view/Atlas/AtlasTechnicalPaper, 2007.

[37] LAr Calorimeter Collaboration, ATLAS *Liquid Argon Calorimeter Technical Design Report*, Tech. Rep. LHCC 96-41, CERN, 15 December 1996.

[38] M. Ahrrouche et al., *Response Uniformity of the ATLAS Liquid Argon Electromagnetic Calorimeter*, Nucl. Instrum. Meth. **A582** (2007) 429–455, arXiv:0709.1094 [physics.ins-det].

[39] J. Carvalho, *Calibration and monitoring of the* ATLAS *Tile calorimeter*, ATLAS note, ATL-TILECAL-PUB-2006-007, CERN, 26 July 2006.

[40] R. Achenbach et al., *The ATLAS Level-1 Calorimeter Trigger*, Journal of Instrumentation **3** (March, 2008) P03001.

[41] T. Davídek and R. Leitner, *Parametrization of the Muon Response in the Tile Calorimeter*, ATLAS note. TILECAL-NO-114, CERN, 5 March 1997.

[42] P. Adragna et al., *Testbeam studies of production modules of the ATLAS tile calorimeter*, Nucl. Instrum. Meth. **A606** (2009) 362–394.

[43] R. Wigmans, *High resolution hadronic calorimetry*, Nucl. Instrum. Meth. **A265** (1988) 273–290.

[44] R. Wigmans, *Advances in hadron calorimetry*, Ann. Rev. Nucl. Part. Sci. **41** (1991) 133–185.

[45] R. Wigmans, *On the role of neutrons in hadron calorimetry*, Rev. Sci. Instrum. **69** (November, 1998) 3723–3736.

[46] CERN, *User's manual to the beam lines in the North area*, `http://nahandbook.web.cern.ch/nahandbook/default/`.

[47] A. Gomes et al., *Cell geometry and fiber lengths of Barrel and Extended Barrel modules*, ATLAS internal note, ATL-TILECAL-2002-011, CERN, 2002.

[48] Tile Calorimeter Collaboration, ATLAS *Tile Calorimeter Technical Design Report*, Tech. Rep. LHCC 96-42, CERN, 15 December 1996.

[49] GEANT4 Collaboration, S. Agostinelli et al., *GEANT4 – a simulation toolkit*, Nucl. Instrum. Methods Phys. Res., A **506** (2003) 250–303.

[50] Private communication with Adrian Fabich and Bob Stanek. A drawing of the H8 beamline set-up for the 2003 testbeam period can be found on `http://nahandbook.web.cern.ch/nahandbook/default/common/zoneslayout/158.gif`.

[51] Ç. İşsever, K. Borras, and D. Wegener, *An improved weighting algorithm to achieve software compensation in a fine grained LAr calorimeter*, Nucl. Instrum. Methods Phys. Res., A **545** (2005) 803–812.

[52] The H1 Collaboration, G. Cozzika et al., *The H1 detector at HERA*, Nucl. Instrum. Methods Phys. Res., A **386** (1997) 310–347.

[53] R. Seuster, *Hadronic calibration of the* ATLAS *calorimeter*, AIP Conf. Proc. **867** (2006) 274–281.

[54] T. Barillari et al., *Local Hadronic Calibration*, ATLAS refereed public note ATL-LARG-PUB-2009-001, CERN 2009.

[55] ATLAS Collaboration, *ATHENA* - ATLAS *Computing framework*, `https://twiki.cern.ch/twiki/bin/view/atlas/workbook`, 2007.

[56] The ATLAS Collaboration, ATLAS *Simulation Validation*, `http://atlas-computing.web.cern.ch/atlas-computing/packages/simulation/geant4/validation/Validation.html`.

[57] S. Jorgensen Roca, *Jet reconstruction and calibration in the* ATLAS *calorimeters*, AIP Conf. Proc. **867** (2006) 433–438.

[58] ATLAS computing group, ATLAS *Computing Technical Design Report (third revision)*, Tech. Rep. LHCC-2005-022, CERN, 4 July 2005.

[59] ATLAS Liquid Argon EMEC/HEC Collaboration, C. Cojocaru et al., *Hadronic calibration of the ATLAS liquid argon end-cap calorimeter in the pseudorapidity region 1.6 < |eta| < 1.8 in beam tests*, Nucl. Instrum. Meth. **A531** (2004) 481–514, physics/0407009.

[60] C. Schwanenberger, *The jet calibration in the H1 liquid argon calorimeter*, Calorimetry in Particle Physics, Pasadena (2002) 761–766. physics/0209026.

[61] ATLAS computing group, ATLAS *Computing Technical Design Report, third revision*, Tech. Rep. LHCC-2005-022, CERN, 4 July 2005.

[62] W. Lampl et al., *Calorimeter Clustering Algorithms : Description and Performance*, Tech. Rep. ATL-LARG-PUB-2008-002, CERN, 2008.

[63] R. Brun and F. Rademakers, *ROOT: An object oriented data analysis framework*, Nucl. Instrum. Meth. **A389** (1997) 81–86. See also http://root.cern.ch/.

[64] *Combined test beam run list, period 8*, http://atlas.web.cern.ch/Atlas/GROUPS/LIQARGON/Comb_TB/CBT_Barrel/RunLists/RunListp8.txt.

[65] P. Speckmayer, C. W. Fabjan, and T. Carli, *Energy Measurement of Hadrons with the CERN ATLAS Calorimeter. oai:cds.cern.ch:1112036*. PhD thesis, Vienna, Vienna University of Technology, Vienna, 2008. Presented on 18 Jun 2008.

[66] P. Adragna et al., *Measurement of Pion and Proton Longitudinal Shower Profiles up to 20 Nuclear Interaction Lengths with the* ATLAS *Tile Calorimeter*, Refereed ATLAS public note, 2009. ATL-TILECAL-PUB-2009-009.

[67] K.-J. Grahn, *ATLAS Calorimetry: Hadronic Calibration Studies*, Licentiate thesis, KTH, Physics, 2008. http://urn.kb.se/resolve?urn=urn:nbn:se:kth:diva-9423.

[68] The ATLAS Collaboration, G. Aad et al., *Expected Performance of the* ATLAS *Experiment - Detector, Trigger and Physics*, ch. 6, *Jets and Missing Transverse Energy*, p. 261. CERN-OPEN-2008-020, 2009. arXiv:0901.0512 [hep-ex].

[69] B. Andersson, G. Gustafson, G. Ingelman, and T. Sjostrand, *Parton Fragmentation and String Dynamics*, Phys. Rept. **97** (1983) 31.

[70] S. V. Chekanov, *Jet algorithms: A mini review*, arXiv:hep-ph/0211298.

[71] G. Blazey et al., *Run II jet physics*, arXiv:hep-ex/0005012.

[72] S. Catani, Y. L. Dokshitzer, M. H. Seymour, and B. R. Webber, *Longitudinally invariant K_t clustering algorithms for hadron hadron collisions*, Nucl. Phys. **B406** (1993) 187–224.

[73] M. Cacciari, G. P. Salam, and G. Soyez, *The anti-kt jet clustering algorithm*, JHEP **04** (2008) 063, arXiv:0802.1189 [hep-ph].

[74] The CDF Collaboration, A. Pronko, *Jet fragmentation in p anti-p collisions*, Acta Phys. Polon. **B36** (2005) 451–460.

[75] T. Sjostrand, S. Mrenna, and P. Skands, *PYTHIA 6.4 Physics and Manual*, JHEP **05** (2006) 026, arXiv:hep-ph/0603175.

[76] D. Cavalli, A. Gupta, F. Paige, S. Resconi, and C. Roda, *Jet Reconstruction for Athena 12.0.4*, .

[77] M. Kaneda, *Jet Reconstruction in the* ATLAS *Calorimeters*, Joint meeting of pacific region particle physics communities (dpf-jps2006), October, 2006.

[78] T. Carli, *Summary of G4 validation results of* ATLAS *and CMS*, Talk given at the GEANT4 review 2007, cern, april 16 2007.

[79] C. T. Hill and S. J. Parke, *Top production: Sensitivity to new physics*, Phys. Rev. **D49** (1994) 4454–4462, arXiv:hep-ph/9312324.

[80] C. T. Hill, *Topcolor assisted technicolor*, Phys. Lett. **B345** (1995) 483–489, arXiv:hep-ph/9411426.

[81] T. Han, H. E. Logan, B. McElrath, and L.-T. Wang, *Phenomenology of the little Higgs model*, Phys. Rev. **D67** (2003) 095004, arXiv:hep-ph/0301040.

[82] S. González de la Hoz, L. March, and E. Ros, *Search for hadronic decays of Z_H and W_H in the Little Higgs model*, ATLAS refereed public note, January, 2006. ATL-PHYS-PUB-2006-003, Geneva, CERN.

[83] R. M. Harris, C. T. Hill, and S. J. Parke, *Cross section for topcolor Z'(t) decaying to t anti-t*, arXiv:hep-ph/9911288. Fermilab note Fermilab-FN-687.

[84] B. Lillie, L. Randall, and L.-T. Wang, *The Bulk RS KK-gluon at the LHC*, JHEP **09** (2007) 074, arXiv:hep-ph/0701166.

[85] M. Guchait, F. Mahmoudi, and K. Sridhar, *Associated production of a Kaluza-Klein excitation of a gluon with a t t(bar) pair at the LHC*, Phys. Lett. **B666** (2008) 347–351, arXiv:0710.2234 [hep-ph].

[86] M. Guchait, F. Mahmoudi, and K. Sridhar, *Tevatron constraint on the Kaluza-Klein gluon of the bulk Randall-Sundrum model*, JHEP **05** (2007) 103, arXiv:hep-ph/0703060.

[87] D0 Collaboration, *Search for $t\bar{t}$ Resonance in the Lepton+Jets Final State in $p\bar{p}$ Collisions at $\sqrt{s} = 1.96$ TeV*, D0 note 5882-conf, 16 March, 2009.

[88] CDF Collaboration, T. Aaltonen et al., *Search for resonant $t\bar{t}$ production in $p\bar{p}$ collisions at $\sqrt{s}$ = 1.96 TeV*, Phys. Rev. Lett. **100** (2008) 231801, arXiv:0709.0705 [hep-ex].

[89] CDF Collaboration, T. Aaltonen et al., *Limits on the production of narrow $t\bar{t}$ resonances in $p\bar{p}$ collisions at $\sqrt{s}$ = 1.96-TeV*, Phys. Rev. **D77** (2008) 051102, arXiv:0710.5335 [hep-ex].

[90] CDF collaboration, *A search for massive gluon decaying to top pair in lepton + jet channel*, January 15, 2008. CDF note 9164, available online at http://www-cdf.fnal.gov/physics/physics.html.

[91] CDF Collaboration, T. Aaltonen et al., *Search for New Color-Octet Vector Particle Decaying to ttbar in ppbar Collisions at $\sqrt{s} = 1.96$ TeV*, arXiv:0911.3112 [hep-ex]. Submitted to Phys. Lett. B.

[92] The ATLAS Collaboration, G. Aad et al., *Expected Performance of the* ATLAS *Experiment - Detector, Trigger and Physics*, ch. 10, *Top Quark*, p. 869. CERN-OPEN-2008-020, 2009. arXiv:0901.0512 [hep-ex].

[93] M. Bosman, R. Hawkings, and A. Shiabata, *Understanding Monte Carlo Generators for Top Physics*, Available, for ATLAS authors only, at http://cds.cern.ch, July, 2009. ATL-COM-PHYS-2009-334.

[94] The ATLAS Collaboration, G. Aad et al., *Expected Performance of the* ATLAS *Experiment - Detector, Trigger and Physics*, ch. 1, *Introduction*, p. 3. CERN-OPEN-2008-020, 2009. arXiv:0901.0512 [hep-ex].

[95] ATLAS Collaboration, ATLFASTII, Documentation wiki page, November, 2009. https://twiki.cern.ch/twiki/bin/view/Atlas/AtlfastII.

[96] T. Sjostrand et al., *High-energy physics event generation with PYTHIA 6.1*, Comput. Phys. Commun. **135** (2001) 238–259, arXiv:hep-ph/0010017.

[97] T. Sjostrand, L. Lonnblad, S. Mrenna, and P. Skands, *Pythia 6.3 physics and manual*, arXiv:hep-ph/0308153.

[98] T. Sjostrand, S. Mrenna, and P. Skands, *A Brief Introduction to PYTHIA 8.1*, Comput. Phys. Commun. **178** (2008) 852–867, arXiv:0710.3820 [hep-ph].

[99] S. Frixione and B. R. Webber, *Matching NLO QCD computations and parton shower simulations*, JHEP **06** (2002) 029, arXiv:hep-ph/0204244.

[100] S. Frixione, P. Nason, and B. R. Webber, *Matching NLO QCD and parton showers in heavy flavour production*, JHEP **08** (2003) 007, arXiv:hep-ph/0305252.

[101] G. Corcella et al., *HERWIG 6.5: an event generator for Hadron Emission Reactions With Interfering Gluons (including supersymmetric processes)*, JHEP **01** (2001) 010, arXiv:hep-ph/0011363.

[102] G. Corcella et al., *HERWIG 6.5 release note*, arXiv:hep-ph/0210213.

[103] J. M. Butterworth and J. R. Forshaw, *Photoproduction of multi - jet events at HERA: A Monte Carlo simulation*, J. Phys. **G19** (1993) 1657–1663.

[104] J. M. Butterworth, J. R. Forshaw, and M. H. Seymour, *Multiparton interactions in photoproduction at HERA*, Z. Phys. **C72** (1996) 637–646, arXiv:hep-ph/9601371.

[105] M. L. Mangano, M. Moretti, F. Piccinini, R. Pittau, and A. D. Polosa, *ALPGEN, a generator for hard multiparton processes in hadronic collisions*, JHEP **07** (2003) 001, arXiv:hep-ph/0206293.

[106] M. Cacciari and G. P. Salam, *Dispelling the N^3 myth for the k_t jet-finder*, Phys. Lett. **B641** (2006) 57–61, arXiv:hep-ph/0512210.

[107] D. E. Kaplan, K. Rehermann, M. D. Schwartz, and B. Tweedie, *Top Tagging: A Method for Identifying Boosted Hadronically Decaying Top Quarks*, Phys. Rev. Lett. **101** (2008) 142001, arXiv:0806.0848 [hep-ph].

[108] A. Hocker, P. Speckmayer, J. Stelzer, F. Tegenfeldt, and H. Voss, *TMVA, toolkit for multivariate data analysis with ROOT (version 4.0.1)*, PoSACAT:040 (2007) , arXiv:physics/0703039v5. CERN-OPEN-2007-007.

[109] J. Thaler and L.-T. Wang, *Strategies to Identify Boosted Tops*, JHEP **07** (2008) 092, arXiv:0806.0023 [hep-ph].

[110] L. G. Almeida, S. J. Lee, G. Perez, I. Sung, and J. Virzi, *Top Jets at the LHC*, Phys. Rev. **D79** (2009) 074012, arXiv:0810.0934 [hep-ph].

[111] U. Ellwanger, *The Jet Mass in Leading Log QCD*, Z. Phys. **C8** (1981) 261–263.

[112] S. V. Chekanov, *Jet algorithms: A mini review*, arXiv:hep-ph/0211298. Presented at the 14th Topical Conference on Hadron Collider Physics (HCP2002), 28 Sep - 4 Oct 2002, Karlsruhe, Germany.

[113] R. A. Fisher, *The Use of Multiple Measurements in Taxonomic Problems*, Annals of Eugenics **7** (1936) 179–188. Available online at http://digital.library.adelaide.edu.au/dspace/handle/2440/15227.

[114] B. L. Combridge, *Associated Production of Heavy Flavor States in p p and anti-p p Interactions: Some QCD Estimates*, Nucl. Phys. **B151** (1979) 429.

[115] E. L. Berger, D. DiBitonto, M. Jacob, and W. J. Stirling, *The minimum invariant mass: a technique for heavy quark searches at collider energy*, Phys. Lett. **B140** (1984) 259.

[116] V. D. Barger, A. D. Martin, and R. J. N. Phillips, *Detecting t quark pairs at anti-p p colliders usning transverse dilepton masses and jets*, Phys. Rev. **D28** (1983) 145.

[117] V. D. Barger, T. Han, and R. J. N. Phillips, *Improved transverse mass variable for detecting Higgs boson decays into Z pairs*, Phys. Rev. **D36** (1987) 295.

[118] V. D. Barger, A. D. Martin, and R. J. N. Phillips, *Perpendicular e neutrino mass from W decay*, Z. Phys. **C21** (1983) 99.

[119] V. D. Barger, A. D. Martin, and R. J. N. Phillips, *Evidence for the t Quark in anti-p p Collider Data*, Phys. Lett. **B125** (1983) 339.

[120] G. J. Feldman and R. D. Cousins, *A Unified Approach to the Classical Statistical Analysis of Small Signals*, Phys. Rev. **D57** (1998) 3873–3889, arXiv:physics/9711021.

[121] J. Neyman, *Outline of a Theory of Statistical Estimation Based on the Classical Theory of Probability*, Philosophical Transactions of the Royal Society of London. Series A, Mathematical and Physical Sciences **236** (Aug. 30, 1937) 333–380. http://www.jstor.org/stable/91337.

[122] R. D. Cousins, *Why isn't every physicist a Bayesian?*, Am. J. Phys. **63** (1995) 398.

[123] G. Cowan, *Statistical Data Analysis*. Oxford University Press, 2002.

[124] T. Bayes, *An Essay towards solving a Problem in the Doctrine of Chances. By the late Rev. Mr. Bayes, communicated by Mr. Price, in a letter to John Canton, M. A. and F. R. S.*, Phil. Trans. **53** (1 January, 1763) 370–418.

[125] J. Heinrich and L. Lyons, *Systematic errors*, Ann. Rev. Nucl. Part. Sci. **57** (2007) 145–169.

[126] CMS Collaboration, *Study of the top-pair invariant mass distribution in the semileptonic muon channel at* $\sqrt{s} = 10$ *TeV*, CMS note, 2009. CMS PAS TOP-09-009.

[127] CMS Collaboration, *Search for heavy narrow* $t\bar{t}$ *resonances in muon-plus-jets final states with the CMS detector*, CMS note, 2009. CMS PAS EXO-09-008.